University of Salford MANCHESTER

On the use of operational transmissibilities for the prediction & analysis of coupled assemblies

Acoustics Research Centre

University of Salford, United Kingdom

Author

Ramin Christopher McGee

Supervisors

Dr. Joshua Meggitt & Dr. Andrew Elliott

Submitted in partial fulfilment of the requirements for the degree Doctor of Philosophy

December 2024

Abstract

As is usually the case in many scientific disciplines, prediction and analysis techniques are firstly developed within laboratory conditions and subsequently extended to industrial settings through further studies. Within vibro-acoustics, we usually begin testing a method in a controlled environment via Experimental Modal Analysis (EMA). One example of an EMA-based method called the Round-trip (RT) method has gained traction within industry recently, a highly convenient and accurate driving-point mobility prediction technique which may be used in influence structural design. Often within various industry, the driving-point mobility may be needed at locations such as mounting points between two sub-structures coupled to one another. It is common that these areas are access limited, meaning conducting a measurement using a modal hammer can be impractical. The RT provides a solution to this by allowing the user to measure three transfer mobilities which uses force inputs on areas of the coupled structure that are much easier to apply.

However, a limitation facing EMA-based methods is that it requires any sources within the coupled system to be shut down. Additionally, if the force and measured response locations are far away from each other, this will yield data with poor signal-to-noise (SNR). This often limits the RT to smaller scale structures which can be tested in laboratory conditions. There has been a lack of investigation into incorporating an Operational Modal Analysis (OMA) approach into the RT method to circumvent these limitations. OMA similarly allows the extraction of modal properties, but does so by using ambient, unmeasured, and stochastic excitations (such as wind) and output-only

responses.

In this thesis, we show that output-only/operational transmissibilities can be used to represent two of the three transfer mobilities in the point RT identity, allowing its extension to much larger structures and uncontrolled active environments. This novel approach to the RT, termed the Operational Round-trip (ORT) method, is analysed and compared to the original technique across three experimental examples. It is shown that it too can accurately predict driving-point mobilities while adding further convenience. Additionally, this thesis has investigated an OMA-based approach for analysing transmission paths using output-only transmissibilities. It is known that by using the 'bottleneck' effect and applying the SVD to a transfer mobility of a coupled system, the singular values can be analysed to detect unaccounted flanking and the number of transmission paths. Similarly to the RT method, this EMA-based method may present challenges on larger scale structures, and/or if an active component (such as a compressor) cannot be shutdown. Instead, it is shown that by identically analysing the singular values of output-only transmissibilities instead, this method can be extended to industrial applications.

The findings in this thesis show that using output-only transmissibilities provides a more convenient means of using the vibro-acoustic prediction and analysis methods presented, while also allowing them to be used in a wider range of systems within industry. Finally, an output-only extension to these methods allows the potential to be developed into real-time monitoring tools.

Contents

List of Figures

List of Tables

List of Acronyms

DoF	Degree of Freedom
EMA	Experimental Modal Analysis
FEA	Finite Element Analysis
FFT	Fast-Fourier Transform
FRF	Frequency Response Function
ICC	Interface Completeness Criterion
LTI	Linear & Time Invariant
ORT	Operational Round Trip
OMA	Operational Modal Analysis
RT	Round Trip
SEMM	System Equivalent Model Mixing
SHM	Structural Health Monitoring
SNR	Signal to Noise Ratio
SV	Singular Value
SVD	Singular Value Decomposition
TICC	Transmissibility-based Interface Completeness Criterion
TPA	Transfer Path Analysis
VPT	Virtual Point Transformation

List of Symbols

Throughout this thesis, symbols given are most of the time in the frequency domain unless stated otherwise. Matrices and vectors are denoted uppercase and lowercase respectively, as well as being bold. A single element matrix or vector is indicated by italics, with their subscripts in the form ij denoting DoF output and input locations respectively.

Symbol	***Meaning***	***Unit***
$\mathbf{B}$	Boolean matrix	N/A
δ	Finite-difference spacing	m
$\mathbf{f}$	Force	N
$\bar{\mathbf{f}}$	Blocked force	N
$\mathcal{F}$	Fourier transform	N/A
j	Imaginary unit	N/A
k	Dynamic stiffness	$\mathrm{N/m}$
H	Frequency response function	$\mathrm{m/N}$ or $\mathrm{ms^{-1}/N}$ or $\mathrm{ms^{-2}/N}$
$\mathcal{L}$	Laplace transform	N/A
m	Mass	kg
ω	Angular frequency	$\mathrm{Radians^{-1}}$
$\angle$	Phase angle	N/A
$\mathbf{R}$	Finite-difference transformation	N/A
$\mathbf{S}$	Power spectral density	$\mathrm{W/Hz}$
σ	Individual singular value	N/A
Σ	Matrix of singular values	N/A
T	Transmissibility	N/A
$\mathbf{T}$	Generalised transmissibility	N/A
$\mathbf{v}$	Velocity	$\mathrm{ms^{-1}}$
$x(t), f(t)$	Output / Input time domain signal	m or N
$x(\omega), f(\omega)$	Output / Input frequency domain signal	m or N
$\mathbf{Y}$	Mobility	$\mathrm{ms^{-1}/N}$
$\mathbf{Z}$	Impedance	$\mathrm{N/ms^{-1}}$

Table 1: Main Symbols

Symbol	***Meaning***
a	DoF subset belonging to sub-structure A
b	DoF subset belonging to sub-structure B
c	Interface DoF subset at the connection point of a coupled system C
d	Combined DoF subsets b and c
f	Global DoF subset / Denoting a force transformation for matrix $\mathbf{R}$
u	Global DoF subset
v	Denoting a velocity transformation for matrix $\mathbf{R}$
w	Global DoF subset
x,y,z	Cartesian co-ordinates
α,β,γ	Rotational Cartesian co-ordinates

Table 2: Subscripts / co-ordinates

Acknowledgements

Firstly, I would like to express my deepest gratitude to my supervisors, Dr. Joshua Meggitt and Dr. Andrew Elliott, for their unwavering support, patience, and the wealth of knowledge they have generously shared. Their pioneering research and mentorship have profoundly shaped my career in vibro-acoustics.

I extend my sincere thanks to my industrial supervisor, Prof. John Smith, and the Defence Science and Technology Laboratory (DSTL) for their invaluable support throughout my doctoral studies. I am especially grateful to John for his unique perspective on the mathematics and physics of my research.

I am also indebted to the Acoustics Research Centre for providing an outstanding environment and state-of-the-art facilities for my experiments. A special thanks to Robbie Potter and the team at QinetiQ for their welcoming attitude and collaborative spirit during my industrial placement.

I would like to express my deep appreciation to my grandfather, Dr. Mansour Boroumand-Naini, for inspiring me to pursue doctoral studies and sharing invaluable wisdom on academic research.

Lastly, I owe an immeasurable debt of gratitude to my parents, Maman and Dad. From my earliest years, they have invested countless sacrifices to ensure I received the best possible education. I never could have imagined I would be where I am today, but their constant encouragement, love, and belief in the power of hard work have instilled in me the drive to aim higher.

Chapter 1

Introduction

This chapter begins by outlining the context behind the research conducted. Following on from this is a discussion on the topics and objectives of studies undertaken. Finally, the structure of the thesis is presented.

Contents

1.0.1 Motivation & Research Context

Analysis and prediction methods for structure-borne sound often face challenges for out of laboratory applications. This is can be due to a few reasons. Firstly, the scale of the test structure may be too large to allow the same controlled measurement method, Experimental Modal Analysis (EMA), to be used. This is suitable on smaller assemblies and in controlled conditions where the background noise level is minimal. However on an industrial size test-rig, such as a bridge or a building, it is mostly likely the data obtained via EMA will have a poor signal-to-noise ratio (SNR). Secondly, in some instances the test structure cannot be shut down operationally. A requirement for using EMA is that there are no sources of excitation other than the controlled ones

via roving hammer or shaker. For example, this may apply to a generator which is needed to generate electricity constantly. Additionally, there may be an inability to apply controlled excitations via EMA to the degrees-of-freedom (DoFs) installed on a structure - usually due to a lack of space. In all of these scenarios, the use of uncontrolled and ambient excitation is preferred. As the source will be unmeasured unlike in EMA, quantities measured in prediction and analysis methods must be generated only by the responses measured at the DoFs on the structure. This is called an output-only technique, known specifically as Operational Modal Analysis (OMA). This technique has become increasingly popular over the past 20 years, with applications seen particularly in civil engineering, as well as automotive and aerospace industries. Another beneficial attribute of the measurement process is to have the test structure coupled, or in-situ. In the past, methods for source characterisation such as Classical Transfer Path Analysis (TPA), required the decoupling the source from the receiver sub-structure. Of course this is impractical if the source is large and cumbersome. A method that is a common theme throughout this thesis, called the 'blocked force/in-situ' method, created a means of source characterisation in-situ by mathematically constraining the velocity of the interface DoFs between source and receiver to zero. This allows a blocking/reactionary force to be measured, which then may be used in predicting responses in a receiver sub-structure. This convenient method has allowed the progression of prediction and analysis methods within vibro-acoustics, which will be outlined later on this thesis. However, limited research exists in combining the conveniences of blocked force methods and OMA together. In this thesis, prediction and analysis methods which have the potential to utilise both of these areas is studied, in order to make the measurement easier and more accessible to industrial applications.

1.0.2 Thesis Topics, Aims and Objectives

A prediction method known as the Round-trip (RT) is a central topic demonstrating the combinations of the blocked force method and OMA. Specifically, the RT identity (developed by Moorhouse and Elliott [2013]) allows point or transfer mobilities to be

predicted on an coupled assembly by indirectly applying excitations at two different subsets of DoFs away from the target subset of DoFs. The concept of a mobility is useful in various contexts and will be outlined early on in this thesis, but in essence it describes a structure's motion as a result of a force. Other techniques of predicting mobilities also exist, which will be explored in the literature review, but none have quite matched the convenience and ease given by the RT method. For the last decade it has become increasingly popular with interesting new applications, such as determining the dynamic stiffness of a resilient element by employing a dual interface round trip identity shown in Meggitt et al. [2015], and applying that so one may form a virtual acoustic prototype (VAP) Meggitt and Moorhouse [2018]. The original authors of the RT method alluded to the possibility of incorporating an OMA approach, specifically, the use of output-only transmissibilities. Transmissibilities also form a central topic within this body of work. They have seen a number of applications, such as within civil engineering damage detection, as they can be calculated by operational responses alone. This concept will also be explained in greater detail, but essentially they describe a ratio between two like quantities, the most convenient of which being output-only velocities. The RT identity is made up of three mobility terms, which are measured via EMA. As it will be shown later on, transmissibilities are related to mobilities, which allows two of the the three mobilities to be replaced with a transmissibility - most conveniently a transmissibility calculated by operational responses, creating a mostly-operational approach to the RT method. This evolution of the RT forms a chapter within this thesis, and is known as the Operational Round-trip (ORT) method. Specifically within this part of the thesis, the main focus is to predict driving-point mobilities via the ORT and compare and analyse its performance against the original RT and a directly measured point mobility.

Before delving into the ORT, it is important to note that there is limited research looking into the sensitivities of the original RT method. In one chapter, its sensitivities are explored to inform the correct use of the novel ORT method later on. The accuracy of the RT is examined by its sensitivity due to the number of DoFs in certain subsets,

the positioning of those DoF subsets, the geometry of the coupled test structure, and the SNR level. This sensitivity analysis also allows an unfamiliar reader to understand the nature of the RT more generally, as it becomes a focal point again later on. Additionally, transmissibilities calculated for a sub-structure within a coupled assembly (in conjunction with the blocked force method) is also an area to investigate before delving into the ORT method. For the ORT to work correctly within a coupled assembly, the transmissibility term (which is determined by operational responses) must be 'invariant'. In the background and literature review the concept of an invariant transmissibility is presented and outlined generally, but essentially it is a transmissibility attributed solely to a particular sub-structure within a coupled assembly. This is possible due to a zero velocity constraint applied at the coupling interface DoFs between sub-structures. As long as the interface DoFs are sufficiently characterised, the transmissibility of the target sub-structure will remain the same irrespective of the dynamic influences of an adjacent sub-structure, or if a different sub-structure is coupled at the interface instead. An investigation into the invariance of transmissibilities forms another chapter preceding the presentation of the ORT. This is conducted in a number of ways, one of which is interchanging an adjacent sub-structure while calculating a transmissibility for a sub-structure of interest. Other methods for observing invariance include the locations and amount of excitations, and the responses used. In some practical industrial scenarios (for reasons that will be explained in detail later on), calculating an invariant transmissibility may not be easiest task. It requires that the interface DoFs at the connection point of the coupled assembly be "complete", which essentially means its ability to account for the full dynamic behaviour at that location. Part of this study is to inform the limits of where invariance can be observed for the case where full completeness cannot be achieved.

In the final topic of this thesis, a novel method for using output-only transmissibilities to detect transmission paths and unknown bridges within a coupled assembly is presented. When the radiated sound into a receiver sub-structure is greater than expected, this may be due to a bridge between source and receiver that has gone

undetected. In this analysis method, a bottleneck is created by the interface DoFs between the source and receiver sub-structures. A small number of DoFs at the bottleneck exists to limit the multiple excitation mechanisms of the source component to a known and reduced set of DoFs at the interface. The number of DoFs at the bottleneck DoFs are also the amount of transmission paths passing through it to the receiver component. In this chapter, the singular value decomposition (SVD) is applied to output-only transmissibilities, and it is shown that by examining its singular values (SVs), the known transmission paths through the bottleneck can be observed, as well as any mechanical bridges circumventing it. It will be shown that the SVD may also be applied to mobilities and transmissibilities calculated by EMA to do this, but its main objective is to show this is also possible using output-only transmissibilities. The aim of using the output-only versions is to allow detection in industrial applications.

With the aims and objectives outlined for the areas of research briefly outlined, the structure of the thesis is described in the next section.

1.0.3 Thesis Outline

Chapter 2 introduces a literature review for various topics related to the research undertaken, alongside background theory of foundational concepts. The chapter begins with the definition of the frequency response function (FRF) in Section 2.1, a key quantity used throughout the research. This is followed by a review of the literature on a critical assumption in FRF usage, reciprocity. This is discussed in Section 2.2. Section 2.3 introduces the theory behind a specific form of FRF employed in this study, called mobility, along with its inverse counterpart, impedance. As mentioned earlier in this introductory chapter, two main approaches to modal analysis exist: Experimental Modal Analysis (EMA) and Operational Modal Analysis (OMA). The literature and theory supporting both techniques are explored in Section 2.4. Additionally, the RT method for predicting mobilities, a key focus of this thesis, is discussed in Section 2.5, where the most common mobility prediction methods are also reviewed. Section 2.6 introduces

the concept of transmissibility, starting with its fundamental form in Single-degree-of-freedom (SDoF) systems and extending it to multi-degree-of-freedom (MDoF) systems. Following this, the topic of sub-structural invariant quantities is examined, focusing on three invariants: the blocked force in 2.7.1, transmissibilities in 2.7.2, and an example of an invariant used in practice called a damage indicator in 2.7.3. In Section 2.8 a review is conducted on two main methods for characterising interface DoFs called the Finite Difference approximation and the Virtual Point Transformation (VPT). Additionally within this section, a method for assessing the capability of the interface DoFs to mathematically apply a zero velocity constraint (completeness) is outlined - called the interface completeness criterion (ICC). In the final section of this chapter, foundational theory of the SVD is outlined in Section 2.9.

Chapter 3 explores the sensitivities of the RT method on an FE model and experimental example. Observing the potential sources of error for the RT method allows suggestions for the most optimal prediction, informing the presentation of the ORT method later on. Chapter 4 delves into detailed analysis on the nature of invariant transmissibilities. This is shown for transmissibilities determined via FRFs as well as output-only responses, and conducted across three experimental examples: a simple beam-isolator-plate model with a single resilient interface contact point in 4.2, a plate-isolator-plate model including three resilient points for the interface in 4.3, and finally in 4.4 a beam-plate model mirroring the first example except the point resilient connection is rigid. Each step demonstrates a progression in complexity. This also informs Chapter 5, which presents a mostly-operational approach to the RT method by the use of output-only transmissibilities, called the ORT method. It begins by deriving the theory of the ORT identities, followed by Section 5.2 which investigates different time block processing methods Oshana [2006] for the operational measurement of transmissibilities. In Section 5.3 the output-only transmissibility terms used in the ORT identities are compared against FRF-based ones to determine their accuracy. Section 5.4 displays the performance of the ORT driving-point mobility prediction against the original RT method and a directly measured point mobility. This is applied across

the same three experimental examples described for Chapter 4. In the final study, the method for detecting transmission paths and unknown bridges using the SVD on output-only transmissibilities is presented in Chapter 6. It begins with theory of the analysis method in Section 6.1, followed by applications of the theory on mass-spring and experimental models in Section 6.2 and 6.3 respectively.

In Chapter 7, the concluding remarks of the findings in this thesis are drawn, as well as any areas for future work.

Chapter 2

Literature review & Background theory

One of the main objectives of this chapter is to introduce the theory of dynamic quantities that are calculated on coupled assemblies. Furthermore, a review of the literature behind prediction and analysis techniques that use these quantities is outlined. The majority of the literature review will inform the history and current state of these methods, providing an understanding of methodologies used in the research presented.

Contents

In this chapter, the underlying theory and literature used for the research presented in this thesis is introduced. We begin by introducing the theory of frequency response functions (FRFs) in Section 2.1, a concept which some of the quantities used in this research are derived from. This is outlined on a single-degree-of-freedom (SDoF) mass-spring model, its most fundamental form. Some theory of quantities that are based on FRFs is presented in Section 2.3, mobilities and impedances. The former concept will be used throughout this document. Following on from this is a widely used assumption in many areas of physics, the idea of reciprocity. The literature behind reciprocity is explored in Section 2.2; important for the use of mobilities. In Section 2.4 we introduce the theory of modal analysis for Multi-Degree of Freedom (MDoF) systems. This analytical method is essential for identifying dynamic characteristics of a mechanical system and can be split up into two approaches. We begin with the literature behind Experimental Modal Analysis (EMA), a method of calculating FRFs,

followed by Operational Modal Analysis (OMA) which calculates the dynamics of a structure using output-only methods. In Section 2.5 the literature and theory behind a number of methods used for prediction of FRFs is presented. One of which called the Round-trip (RT) method, is central to a couple of chapters in this thesis. Another important concept used in much of the research presented is a transmissibility. We begin introducing the theory of transmissibilities in its most basic form via an SDoF mass-spring system in Section 2.6.1. This is followed by a generalised form of the theory that extends it to MDoF systems, shown in Section 2.6. Much of the work presented in this thesis builds upon on research based on the in-situ/blocked force method, a fundamental technique to many of the dynamic quantities determined for coupled assemblies. These quantities are known as sub-structural 'invariants'. Examples of these are introduced in Section 2.7, such as transmissibilities, damage indicators, and of course blocked forces. An essential consideration when calculating sub-structural invariants is the blocking constraints at the interface between sub-structures. Theory of two of the most commonly used interface characterisation methods are outlined in Section 2.8, the Finite Difference Method and the Virtual Point Transformation. In Section 2.8.3, the theory of a technique used to determine how complete the characterisation of interfaces is outlined, called the Interface Completeness Criterion. Finally in Section 2.9, we cover uses of the Singular Value Decomposition (SVD) by reviewing the literature on the mathematical technique within the field of vibro-acoustics, followed by its theory which will be important later on for the final study of this thesis.

2.1 Frequency response functions

Frequency response functions (FRFs) relate an input force to an output response in the frequency domain. Its main use is to determine the mode shapes, resonances and damping of a mechanical linear and time invariant (LTI) systems. You may come across a very similar definition called a transfer function (Tse et al. [1978]). In many academic works the two terms are used interchangeably, but their definitions do differ

slightly. The theory of these concepts can be found in many textbooks such as Macduff and Curreri [1958], Dimentberg et al., and Jr. [2016]. Essentially, they both are mathematical expressions of a system's input-output relationship. A transfer function is defined as the Laplace transform (s-domain) of input and out time-domain functions $f(t)$ and $x(t)$ respectively,

$$\mathcal{L}\{x(t)\} = X(s) = \int_{-\infty}^{\infty} x(t)e^{-st}\,dt \tag{2.1}$$

$$\mathcal{L}\{f(t)\} = F(s) = \int_{-\infty}^{\infty} f(t)e^{-st}\,dt \tag{2.2}$$

The output and input time-domain functions have turned into complex frequency domain functions, $X(s)$ and $Y(s)$ respectively. On the other hand, a FRF is defined as taking the Fourier transform of output and input time domain signals $x(t)$ and $f(t)$. It should be noted that when taking the Fourier transform, the real part of the s-domain is zero and is evaluated along the imaginary axis, meaning $s = j\omega$. Thus, the functions for the input and output are defined as,

$$\mathcal{F}\{x(t)\} = X(\omega) = \int_{-\infty}^{\infty} x(t)e^{-j\omega t}\,dt \tag{2.3}$$

$$\mathcal{F}\{f(t)\} = F(\omega) = \int_{-\infty}^{\infty} f(t)e^{-j\omega t}\,dt \tag{2.4}$$

Note that the response $X(\omega)$ represents the displacement output. You may also refer to the response in terms of velocity $\dot{X}(\omega)$ or acceleration $\ddot{X}(\omega)$, but in this example we will use displacement.

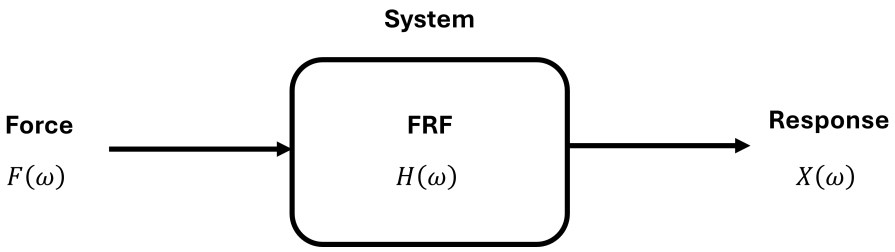

Figure 2.1: Schematic of a calculated FRF for a single input-output system.

The diagram above is usually seen in most vibro-acoustics textbooks to illustrate the relationship between the complex spectra quantities in Eq.2.5 and 2.6.

$$X(\omega) = H(\omega) \cdot F(\omega) \tag{2.5}$$

$$H(\omega) = \frac{X(\omega)}{F(\omega)} \tag{2.6}$$

In the context of single input-output systems, in this example the FRF $H(\omega)$ is defined as the ratio between the complex response spectra $X(\omega)$ and the complex excitation spectra $F(\omega)$. As we the output is a displacement, $H(\omega)$ is a known as a compliance or receptance. If a velocity $\dot{X}(\omega)$ or acceleration $\ddot{X}(\omega)$ is used instead, this results in a different form of FRF known as mobility and accelerance respectively. Accelerance is perhaps considered the default measurement of FRFs in much of the literature and within industry, because acceleration is usually the quantity directly measured experimentally. However in this thesis, we will keep in line with the ISO standard definition (ISO 7626-1:2011), which uses mobility.

For the remainder of this section, an FRF will be derived on a SDoF mass-spring system (its most fundamental form) using equations of motion. An influential academic work by Ewins [2000] forms the basis of the theory that will be covered in this section.

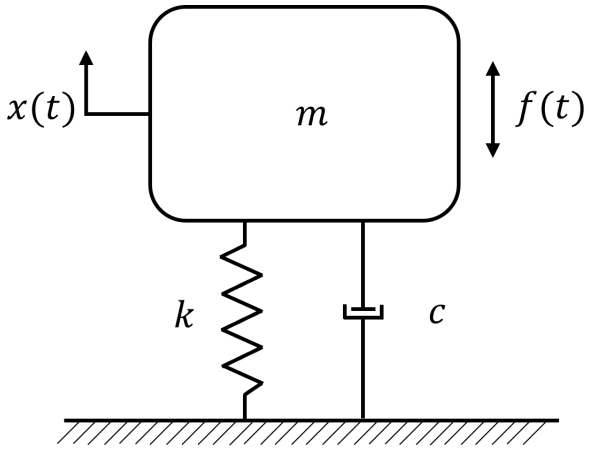

Figure 2.2: SDoF mass-spring system

In Fig.2.2 a SDoF structure with mass m is supported by viscous damping c and spring with stiffness k. In the first example for this system we will take the undamped free vibration scenario, meaning there will be no viscous damping c, yielding the equation of motion as:

$$m\ddot{x} + kx = 0 \tag{2.7}$$

Therefore the solutions for the external force and response are as follows respectively,

$$f(t) = Fe^{jwt} \tag{2.8}$$

$$x(t) = Xe^{jwt} \tag{2.9}$$

To satisfy the displacement solution the following definition must be made in order to obtain a single mode of vibration with natural frequency $\bar{\omega}_0$,

$$(k - \omega^2 m) = 0 \tag{2.10}$$

The reasoning for this definition is made clearer after taking the second derivative of

Eq.2.9 and substituting in the equation of motion, which yields,

$$(k - \omega^2 m)x = 0 \tag{2.11}$$

While the mass is oscillating with displacement x, the bracketed term must equal zero so that the definition is true as being equal to zero. We now are able to define our equation of motion as,

$$(k - \omega^2 m)Xe^{jwt} = Fe^{jwt} \tag{2.12}$$

By rearranging for the division of complex displacement and force scalars, we may obtain the frequency response function $H(\omega)$,

$$H(\omega) = \frac{X}{F} = \frac{1}{k - \omega^2 m} \tag{2.13}$$

Let' set the mass m to 0.05 kg, and stiffness k to 10000 N/m.

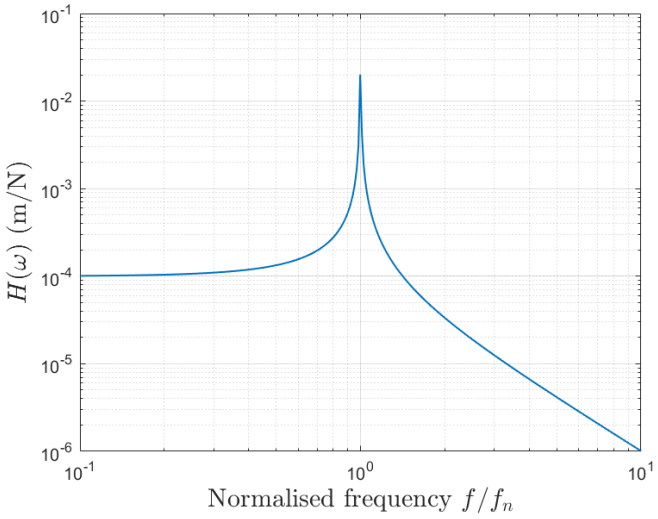

Figure 2.3: FRF of undamped SDoF mass-spring system

Fig.2.3 represents the magnitude of this system's FRF against frequency for an undamped SDoF mass-spring system.

In the case where viscous damping is considered, the equation of motion is defined as,

$$m\ddot{x} + c\dot{x} + kx = 0 \tag{2.14}$$

When taking the force response and displacement solutions as shown in Eq.2.8 and Eq.2.9, the equation of motion is defined as,

$$(-m\omega^2 + jc\omega + k)Xe^{j\omega t} = Fe^{j\omega t} \tag{2.15}$$

Therefore the receptance FRF $H(\omega)$ is defined as,

$$H(\omega) = \frac{X}{F} = \frac{1}{-m\omega^2 + jc\omega + k} \tag{2.16}$$

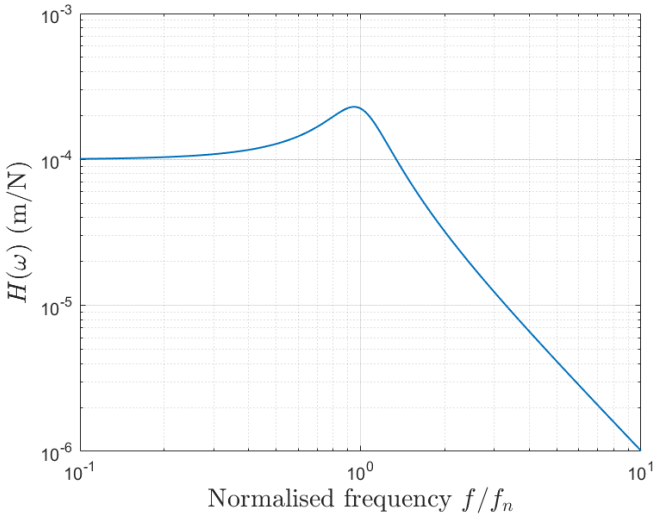

Figure 2.4: FRF of undamped SDoF mass-spring system

In the above figure, the magnitude of the receptance FRF on a damped SDoF mass-spring system is presented. Mass m and stiffness k have been kept the same from the undamped example, only now a damping coefficient c of 10 Ns/m is included in the definition made in Eq.2.16.

2.2 Reciprocity

Reciprocity is a principle that is relevant to central to the analysis of LTI systems. Originally, the concept was applied to the field of optics by Helmholtz [1867], but its expression has been extended into other areas of physics, such as acoustic and electromagnetic branches (Rayleigh [1878]). Rayleigh is quoted as stating:

"If in a space filled with air, which is partly bounded by finitely extended fixed bodies and is partly unbounded, sound waves be excited at any point a, the resulting velocity potential at a second point b is the same both in magnitude and phase, as it would have been at a, had b been the source of sound."

The first person that is often credited with its relation to the field of vibro-acoustics is Betti in 1872, known as the Maxwell-Betti Reciprocal Work Theorem Maxwell [1864]. Betti's principle is based on an earlier form of the reciprocal theorem by Maxwell. It states for a linearly elastic structure that:

"The linear displacement at point a due to a unit load applied at point b is equal in magnitude to the linear displacement at point b due to a unit load applied a point a."

This key assumption will be used throughout in the majority of the research presented in this thesis.

2.3 Mobility and impedance concepts

Mobilities and impedances are essentially a form of FRF. The theory behind these concepts can be found in most vibro-acoustic textbooks. Some popular examples include O'Hara [1967], Ewins [2000], Vigran [2008], Fahy and Gardonio [2007]. They are central quantities in much of the research presented in this thesis, therefore it is essential to provide their definitions. When either is determined for a component within in a coupled assembly, they must be calculated in a way that ensures their independence. The method of how this is carried out for each quantity will be covered

in the following subsections.

2.3.1 Mobility

Mobility is defined as the ratio between a force and velocity response,

$$\mathbf{v} = \mathbf{Y}\mathbf{f}, \qquad Y_{ij} = \left.\frac{v_i}{f_j}\right|_{f_{i\neq j}=0} \tag{2.17}$$

where Y_{ij} is the ijth entry of the mobility matrix $\mathbf{Y}$, f_j is the jth term of the applied force vector $\mathbf{f}$, and v_i is the ith term of the velocity vector $\mathbf{v}$.

Note that terms denoted as uppercase represent a matrix, while lowercase indicates a vector. If the quantity is in bold, this states there are multiple elements. Terms in italic represent just one element. Finally, within the subscript the first letter denotes the subset of a response, while the second indicates the subset of a force.

For every excitation and response DoF juxtaposed, $i = j$, meaning $\mathbf{Y} = \mathbf{Y}^{\mathrm{T}}$, which satisfies the concept of reciprocity. It is important that each applied force at DoFs of interest are conducted one at a time. Additionally, the structure should be permitted to respond without restrictions by applying a zero force constraint to all other points of interest. It is apparent that Eq.2.17 is very similar to the definition of the admittance FRF in Eq.2.5. To translate the definition from the SDoF to a MDoF system, the admittance FRF will defined using displacement s. Often the terms admittance, mobility, and accelerance are used interchangeably due to the measured displacement, velocity and acceleration being analogous.

2.3.2 Impedance

In most cases, a mobility will be measured instead of impedance (Snoeys et al. [1987]). As we cover the theory in this subsection, it will be made clear as to why this is the case. Put simply, impedance is the inverse of mobility and describes a system's resistance to motion. It is defined as as,

$$\mathbf{Zv} = \mathbf{f}, \qquad Z_{ij} = \left.\frac{f_i}{v_j}\right|_{v_{i\neq j}=0} \tag{2.18}$$

where Z_{ij} is the ijth entry of the impedance matrix $\mathbf{Z}$, f_i is the ith term of the force vector $\mathbf{f}$, and v_j is the jth term of the velocity vector $\mathbf{v}$. For every excitation and response juxtaposed, $i = j$, meaning $\mathbf{Z} = \mathbf{Z}^{\mathrm{T}}$, which satisfies the concept of reciprocity. When carrying out an impedance measurement, the velocity at all other DoFs should be constrained to zero while a velocity is applied to each point. In practice this is extremely difficult, and in the vast majority of cases impossible. This is why the mobility is the preferred quantity to measure directly. The impedance can be determined indirectly by inverting a measured mobility. If displacement or acceleration is used instead of velocity, then we call this the dynamic stiffness or effective mass, respectively.

2.4 Modal analysis

Modal analysis is a technique utilised for the identification of modal parameters on mechanical systems. These dynamic characteristics include natural frequencies, modes shapes, and damping ratios; usually with the main objectives of prediction or mitigation of resonances, improving experimental structural design by verifying analytical results of a Finite-Element (FE) model, and structural health monitoring (SHM). It may be applied to structures exhibiting linear (Veletsos and Ventura [1986]) or non-linear behaviour (Kerschen et al. [2013]). However, the main focus in this literature review will be on the former, as the coupled assemblies used in the research presented later on are assumed as LTI. Many industrial applications exist for modal analysis, such as in automotive (Panza [2015]), civil engineering (Roesset et al. [1973], Cunha and Caetano [2006]), and aerospace (Aykan and Çelik [2009]).

In general, modal analysis can be broken down into three steps:

- Excitation - where the structure is under load to induce vibrations. This can either be controlled by impact hammer/ shaker, or by ambient forces such as an operational source/wind.
- Measurement - where the vibrational response is obtained by using accelerometers or strain gauges.
- Data analysis - the processing of measured data to determine the dynamic characteristics, either by analysing FRFs or operational responses with signal processing.

The different methods of carrying out the above three steps can be split up into methods of modal analysis; Experimental Modal Analysis (EMA) and Operational Modal Analysis (OMA). These two techniques will be covered in the following subsections.

2.4.1 Experimental modal analysis

EMA is often uses controlled laboratory conditions to extract modal parameters. In this scenario, the support condition of the test structure can be free, unrestrained, grounded, or in-situ. Experimental and FE models examples used for the research in this thesis will focus mainly on the in-situ condition. Some reports in the past have suggested EMA as being the most reliable technique (Magalhães et al. [2010]), despite EMA and OMA being theoretically as reliable as each other. In one experimental study on a laboratory test plate (Orlowitz and Brandt [2017]), it was concluded there was little difference in the modal parameters obtained by either route. What actually effects the reliability is usually down to the proportions of the structure and its setting. In EMA, a controlled measured force input via roving hammer or shaker is applied, resulting in a response measured on the structure. This force input is only insufficient when the test structure is large, such as a bridge or a building. In laboratory conditions, this is not an issue due to the test structure being smaller, meaning the excitation and response positions are localised. The vibratory energy due to the excitation can be picked up by the sensors sufficiently above the noise floor before dissipating. Additionally, the

noise floor in laboratory conditions is usually much lower than in real world cases due to the ideal conditions set. For a large structure, the distance for the input force signal to be picked up by a response is too large, and would require an extremely large force input to yield an FRF with an acceptable signal-to-noise-ratio (SNR). This is why in civil engineering applications, EMA is usually avoided. Despite this, EMA has seen a lot of use in other industries where the scale of the test structure is much smaller, such as in automotive. As pointed out earlier in this section, the final stage of modal analysis is the processing of measured data. This is known as data acquisition, and in EMA the analogue data for the input (force) and output (response) time domain signals is collected using a Data Acquisition System (DAS). The acquired signals are digitised and then subject to signal conditioning - the process of removing noise and artifacts using filters to improve the SNR, and amplification of signals with a low response amplitude. Time synchronisation of excitation and response signals is applied to ensure correlation between them, as well as windowing so that spectral leakage is avoided. In the final stage of EMA data analysis, the Fourier transform is applied to the time domain signals to calculate FRFs. In the remainder of this section, the theory of how these FRFs are determined via EMA will be presented; with works by Ewins [2000], Rao [2004], Maia and Silva [2003], and Brandt [2011] forming the basis.

Let's recall the Fourier transform definitions made earlier on the input force and output response time domain signals in Section 2.1, Eq.2.4 and 2.3 respectively. We have already established the Fourier transform of these two signals forms the definition of an FRF, shown in Eq.2.6. However, this equation is often prone to noise, which can be circumvented by the use of spectral densities. Specifically, the auto-spectral density and the cross-spectral density are taken. Beginning with the cross-spectral density $S_{xf}(\omega)$, it is defined as,

$$S_{xf}(\omega) = \frac{1}{N}\sum_{i=1}^{N} X_i^*(\omega)F_i(\omega) \tag{2.19}$$

A * in the superscript denotes the complex conjugate. $S_{xf}(\omega)$ calculates the correlation

between the input $f(t)$ and output $x(t)$, essentially capturing the system dynamics. Note that an average is taken, where N represents the number of measurements. Additionally, the auto-spectral density of the input $S_{ff}(\omega)$ and output $S_{xx}(\omega)$ signals are defined respectively as,

$$S_{ff}(\omega) = \frac{1}{N}\sum_{i=1}^{N} F_i^*(\omega)F_i(\omega) \tag{2.20}$$

$$S_{xx}(\omega) = \frac{1}{N}\sum_{i=1}^{N} X_i^*(\omega)X_i(\omega) \tag{2.21}$$

$S_{ff}(\omega)$ is basically a normalisation by the input force power, while $S_{xx}(\omega)$ informs the power of the output signal. With these definitions the FRF may now be derived, beginning with the FRF $H_1(\omega)$, which is defined as,

$$H_1(\omega) = \frac{S_{xf}(\omega)}{S_{ff}(\omega)} \tag{2.22}$$

$H_1(\omega)$ is often used when the input is applied by roving hammer. It also ensures the minimisation of noise on the output. Additionally, another FRF $H_2(\omega)$ can be defined,

$$H_2(\omega) = \frac{S_{xx}(\omega)}{S_{xf}^*(\omega)} \tag{2.23}$$

$H_2(\omega)$ is often used when the input is applied by a broadband and continuous force such as shaker. This definition makes sure noise on the input is minimised.

2.4.2 Operational modal analysis

OMA is an alternative approach to EMA, which is often utilised in the field of civil engineering. As mentioned previously, applying a known force input via EMA on say, a wind turbine, is impractical due to the size and testing conditions. OMA provides a much more suitable means for identification of modal parameters for structures such

as this as no explicit knowledge of input forces are required, and the modal parameters are determined solely by measured operational responses. This has been particularly advantageous in the field of SHM where it is perhaps used the most. Examples where structural integrity is assessed using OMA, sometimes continuously by constant measurement of responses, include wind turbines (Devriendt et al. [2014]), concrete dams (Li et al. [2022]), and historical masonry-type buildings (Ramos et al. [2010]). Assumptions made in OMA can be split into three areas:

- Input forces are unknown, stochastic in nature, and broadband (Guassian white noise).
- The system analysed is LTI, meaning the magnitude of the measured response is proportional to the input forces, and the dynamic characteristics do not change with time.
- Observability has been achieved, which essentially means how well the sensor layout is across the structure to capture modes correctly and to avoid nodes.

For many years OMA was considered as a technique with potential but unreliable. It was only up until the late 1990s and early 2000s when influential methods such as the Stochastic Subspace Identification (SSI) Peeters and Roeck [1999] and Frequency Domain Decomposition (FDD) Brincker et al. [2001] were introduced, that OMA saw much broader use. Both differ in that the former uses time domain data directly, while the latter is based on the SVD of a Fourier transform spectral density matrix. Operational measurements in this thesis will be mostly based off the frequency Domain Decomposition.

For the remainder of this section, we will derive the theory of OMA using works by Rainieri and Fabbrocino [2014] as the foundational understanding. Let's recall the definition for the auto-spectra density $S_{xx}(\omega)$ in Eq.2.21. In this case, N represents the number of time-blocks, which will ensures the spectral density is robust to noise. By substituting the definition of an FRF made in Eq.2.5 into the definition for $S_{xx}(\omega)$, the following definition is obtained,

$$S_{xx}(\omega) = \frac{1}{N}\sum_{i=1}^{N}\big(H(\omega)F_i(\omega)\big)^*\big(H(\omega)F_i(\omega)\big) \tag{2.24}$$

which expands to,

$$S_{xx}(\omega) = H(\omega)H^*(\omega)\cdot\frac{1}{N}\sum_{i=1}^{N}F_i^*(\omega)F_i(\omega) \tag{2.25}$$

and it has already been established that $\frac{1}{N}\sum_{i=1}^{N}F_i^*(\omega)F_i(\omega)$ is the input auto-spectral density $S_{ff}(\omega)$. As a result, the fundamental definition of OMA is made,

$$S_{xx}(\omega) = H(\omega)H^*(\omega)S_{ff}(\omega) \tag{2.26}$$

Assuming the input is constant, I.e. Guassian white noise, $S_{xx}(\omega)$ is directly proportional to the squared magnitude of the FRF matrix,

$$S_{xx}(\omega) \propto |H(\omega)|^2 \tag{2.27}$$

To summarise this section, the differences between OMA and EMA are provided in the table below.

Properties	***EMA***	***OMA***
Input force $F(t)$	Measured, Controlled	Not measured, Stochastic, Broadband
Spectral functions	$S_{ff}(\omega)$, $S_{fx}(\omega)$, $S_{xx}(\omega)$	$S_{xx}(\omega)$
FRF	Obtained by measured input and output	Estimation solely by operational response
Modal parameter extraction	Modal decomposition, FRF-based curve fitting	FDD, SSI

Table 2.1: Comparison of EMA and OMA techniques.

2.5 FRF prediction methods

In this section, a literature review of the different methods for estimating FRFs is presented. As already pointed in the previous section, one form of EMA requires applying a controlled and collocated roving hammer excitation to DoFs installed on the test structure. Within industry, obtain a $M \times M$ FRF matrix directly (across all sensors/DoFs installed on the structure) can be impractical. As a result a number of methods have been proposed for prediction. Some use spectral estimation algorithms (Allemang et al. [2022]), but in this section the focus will be on FRF reconstruction at DoFs of interest using measured data. Examples of these techniques include modal shape extraction, System Equivalent Model Mixing (SEMM), the round-trip method; and will be reviewed in the following subsections. Reasons for predicting FRFs experimentally can be due to:

- Inaccessibility of DoFs, meaning a roving hammer excitation is not possible.
- Many DoFs installed on the structure, making the direct measurement process time consuming.
- Combining limited experimental data to update or validate numerical models.

We will begin introducing one of the earliest methods of FRF reconstruction using measured data, synthesis by modal shape extraction.

2.5.1 Modal shape extraction synthesis

Often within industry, it can be difficult to obtain accurate driving-point FRFs on particular areas of a system that are inaccessible to excite via roving hammer. This problem has lead to research into reconstructing an $M \times M$ FRF matrix without needing to apply excitations at all M response positions. In response, modal shape extraction techniques that enable the synthesis of a full FRF matrix by using only a single excitation one M DoF position have arisen. Works by Maia et al. [1997], Ashory [1998], Ashory [1999], and Silva et al. [2000] demonstrated this is certainly possible. Essen-

tially, these methods use the mass loading of sensors to their advantage to generate a series of equations with repeated tests to generate FRFs at the unmeasurable DoFs. As reported by Moorhouse and Elliott [2013], this approach is sensitive to measurement error. For example, if there is a significant amount of loading from the sensor, the magnitude of resonant frequencies will be lower than it should be. Before these methods had arisen, in the 1980s Ewins [1980] had shown that FRF reconstruction using a force at only a single DoF was achievable without repeated tests. Reasons why the mass-loading methods had arisen was because Ewin's method required modal decomposition (extracting resonances and mode shapes) across all DoFs, which is impractical on structures such as beams which have theoretically an infinite number of modes. went onto show that reconstruction was possible without repeated tests, but was proven to be impractical for systems with multiple modes.

2.5.2 System equivalent model mixing

SEMM was first introduced by Klaassen et al. [2018], and is a relatively recent method that combines frequency-based experimental and numerical models to build a hybrid model. Examples of where it has been applied include the identifying the dynamic parameters of vehicle components (Pasma et al. [2018]), and joint identification between a blade and disk (Saeed et al. [2020]). Another implementation is to predict quantities such as FRFs at points on a structure where DoFs do not exist in the experimental model. This is achieved by combining the measured FRF from the limited DoF-space of an experimental model, and using that data to extrapolate FRFs to the expanded DoF-space of an equivalent numerical model. Alternatively, it has been used to estimate mobilities by mixing two experimental models instead (Ocepek et al. [2021]).

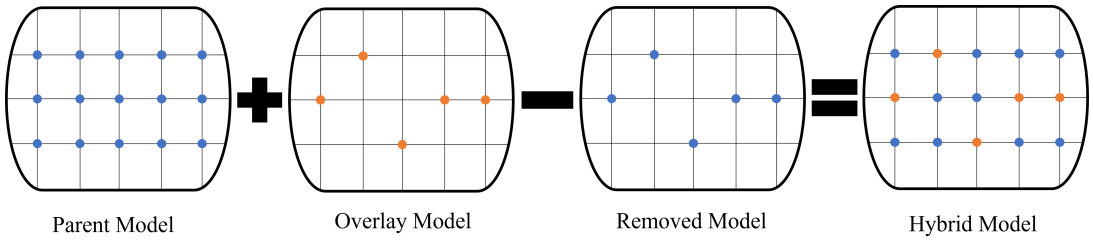

Figure 2.5: Processing of models used in SEMM, resulting in a hybrid model.

There are 3 models used in determining the final and 4th hybrid model. As demonstrated by Fig.2.5, they are the parent, overlay, and removed models. The parent model provides the full DoF structure (usually by an FE-model), while the overlay model (which has a smaller DoF space and usually experimental) will provide the FRFs in relation to those DoFs. The mobility FRFs of the overlay model $\mathbf{Y}^O$ are enforced by removing the parent model mobilities $\mathbf{Y}^P$ at the subset of DoFs that correspond to the overlay model. This results in another mobility matrix $\mathbf{Y}^R$ of the removed model. Essentially this method uses a primal dynamic sub-structuring approach. For the remainder of this section, a brief outline of how SEMM works mathematically is presented, with Klaassen and der Seijs [2018] providing the basis of this understanding. Let's recall the definition of the mobility FRF in Eq.2.17. Our new definition becomes,

$$\mathbf{v} = \mathbf{Y}(\mathbf{f} - \mathbf{g}) \tag{2.28}$$

where the matrix of mobilities $\mathbf{Y}$ is defined as,

$$\begin{bmatrix} \mathbf{Y}^P & 0 & 0 \\ 0 & -\mathbf{Y}^R & 0 \\ 0 & 0 & \mathbf{Y}^O \end{bmatrix} \tag{2.29}$$

and the vectors of velocities $\mathbf{v}$, external forces $\mathbf{f}$, and connecting forces $\mathbf{g}$ are defined as,

$$\mathbf{v} = \begin{pmatrix} \mathbf{v}^P \\ \mathbf{v}^R \\ \mathbf{v}^O \end{pmatrix}, \mathbf{f} = \begin{pmatrix} \mathbf{f}^P \\ \mathbf{f}^R \\ \mathbf{f}^O \end{pmatrix}, \mathbf{g} = \begin{pmatrix} \mathbf{g}^P \\ \mathbf{g}^R \\ \mathbf{g}^O \end{pmatrix} \tag{2.30}$$

where the superscripts denote the model at which the velocity or force vector is attributed to, I.e. in the same fashion as the mobility terms covered.

Note that the equation of motion (Eq.2.28), has a minus sign between the external force and connecting force vectors. This is showing $\mathbf{Y}^R$ being removed.

The parent model informs internal and boundary DoFs, i and b respectively. To achieve coupling, b DoFs are used to coincide with the overlay model. On the other hand, the i DoFs of the parent model will be unique. As a result the definitions of the mobility matrices of the models are given,

$$\mathbf{Y}^P = \begin{bmatrix} \mathbf{Y}_{ii} & \mathbf{Y}_{ib} \\ \mathbf{Y}_{bi} & \mathbf{Y}_{bb} \end{bmatrix} \quad , \quad \mathbf{Y}^O = \mathbf{Y}^O_{bb} \quad , \quad \mathbf{Y}^R = \mathbf{Y}^P_{bb} \tag{2.31}$$

Compatibility of velocities yields the following definition,

$$\mathbf{v}^P_b = \mathbf{v}^R = \mathbf{v}^O \tag{2.32}$$

meaning,

$$\mathbf{v}^P_b - \mathbf{v}^R = 0 \tag{2.33}$$

$$\mathbf{v}^R - \mathbf{v}^O = 0 \tag{2.34}$$

using a Boolean matrix $\mathbf{B}$, this condition can be applied as,

$$\mathbf{B}\mathbf{v} = 0 \quad , \quad \mathbf{B} \begin{bmatrix} \mathbf{I} & -\mathbf{I} & 0 \\ 0 & \mathbf{I} & -\mathbf{I} \end{bmatrix} \tag{2.35}$$

where $\mathbf{I}$ represents an identity matrix. To apply the equilibrium of forces, the connecting

forces must be equal and opposite,

$$\mathbf{g}_b^P = \mathbf{g}^R = \mathbf{g}^O \tag{2.36}$$

which similarly when using a Boolean matrix $\mathbf{B}$, and the connecting forces are denoted as Lagrange multipliers vector λ yields,

$$\mathbf{g} = -\mathbf{B}^{\mathrm{T}}\lambda \tag{2.37}$$

In the original text, Klassen solves what is called the Lagrange Multiplier Frequency Based Sub-structuring problem, which yields the mobility matrix of the hybrid model $\mathbf{Y}^{SEMM}$,

$$\mathbf{Y}^{SEMM} = \mathbf{Y}_{gg} - \mathbf{Y}_{gb}^P\big(\mathbf{Y}_{bb}^R\big)^{-1}\big(\mathbf{Y}_{bb}^R - \mathbf{Y}_{bb}^O\big)\big(\mathbf{Y}_{bb}^R\big)^{-1}\mathbf{Y}_{bg}^P \tag{2.38}$$

where g denotes the combination of i and b DoFs, i.e. describing a global DoF.

2.5.3 Round-trip identity reconstruction

Moorhouse et al. [2011] showed that the indirect measurement of point mobilities at the interface DoFs (installed at the connection point between sub-structures) is possible by applying excitations at two subsets of 'remote' DoFs, within each sub-structure. This is to measure three mobility terms, which when combined can be used to predict the interface point mobility. Specifically, the authors validated the method experimentally for point mobilities, but alluded to the fact a transfer mobility may also be predicted by rearranging the RT identity and using the same subsets of DoFs. The RT method was later generalised by Wienen et al. [2021].

This section is designed to be brief and give a general overview of what the RT method, as a full comprehensive explanation will be presented in the Chapter 3. The reason for why it is called the round-trip will be made clearer win that chapter, but essentially to

reconstruct the interface point mobility you must measure transfer mobilities for each sub-structure as well as the transfer mobility across the coupled assembly. It is also the first method to reconstruct driving-point mobilities without directly exciting the DoFs of interest. This is a very beneficial attribute for various applications where a lack of room limits modal testing. Often for industrial test rigs, the area around the connection point between sub-structures (perhaps isolator mounts) is an area where sensors can be placed but cannot be excited by say a modal hammer. The round-trip method makes use of indirect excitations at 'remote' sets of DoFs to reproduce driving point FRFs at those locations. It should be noted that traditional methods require free-suspension of the system, so the in-situ nature of the round-trip method is also hugely beneficial for time and cost.

2.6 Transmissibility

Transmissibilities are quantities that provide an understanding of how energy is transferred through a system. It is defined as a ratio between two measurements of the same quantity that are measured at different locations on a mechanical system, and may be calculated in terms of velocity, acceleration, displacement or force. It is particularly useful when measuring the first three quantities, as it allows a transmissibility calculation just by measuring the output/response on a structure. There are different names across various academic works for this type of transmissibility. Usually it is named after the quantity used, i.e. displacement transmissibility when using displacements, but in this thesis it will be termed as a response transmissibility. If forces are used instead, this is simply termed as the force transmissibility. The concept has been known for many years, and was mostly limited to SDoF systems. It was only until the beginning of the 2000s that its generalisation to MDoF systems was introduced by Ribeiro et al. [2000]. In this section, the most fundamental definition of a transmissibility will be derived through a SDoF mass-spring model. This will be followed by a derivation of the generalised transmissibility (MDoF systems).

2.6.1 Single-degree-of-freedom transmissibility

The transmissibility concept can be found in most vibro-acoustic textbooks. Texts by Preumont [2018] and Vigran [2008] will be used as references for its derivation on a SDoF system.

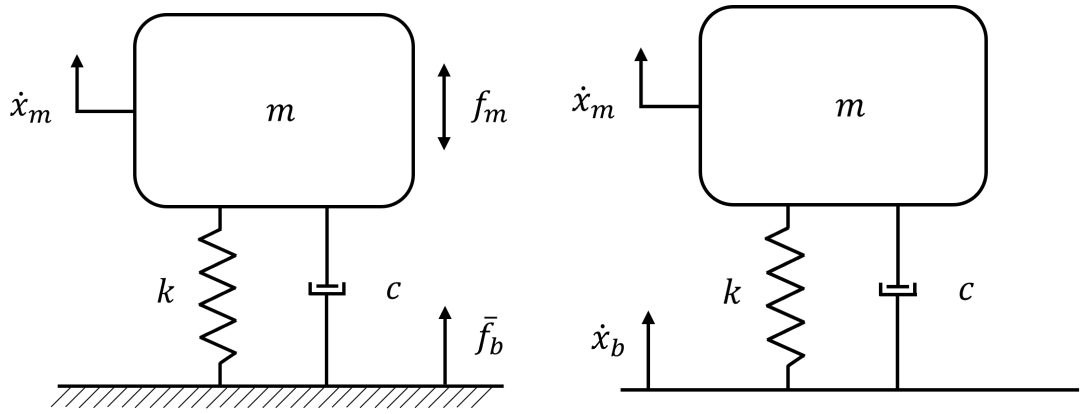

(a) Mass excitation causing a force f_m (b) Base excitation causing a velocity $\dot{x}_b$

Figure 2.6: SDoF mass-spring-damper system under different excitation scenarios.

Fig.2.6 introduces a diagram of a SDoF mass-spring-damper system under two excitation scenarios. In Fig.2.6a a force f_m is generated by the mass m and propagated to the base via the supporting structure (k and c). This causes a reaction force $\bar{f}_b$ but can also be interpreted as a blocking force, hence the bar. For example this scenario may correspond to an engine, creating oscillations that are transmitted through a supporting structure such as a resilient mount. Fig. 2.6b represents a base excitation scenario, causing a velocity $\dot{x}_b$. The kinetic energy caused by the base is transferred to the supporting structure, which in turn causes the mass to oscillate with velocity $\dot{x}_m$. The mass can be interpreted as piece of sensitive equipment such as a telescope, isolated by a resilient mount.

Firstly lets describe the above system in terms of equations of motion. Note this definition is applied to both scenarios despite the excitation location.

$$\begin{pmatrix} f_m \\ f_b \end{pmatrix} = \begin{bmatrix} m & 0 \\ 0 & 0 \end{bmatrix} \begin{pmatrix} \ddot{x}_m \\ \ddot{x}_b \end{pmatrix} + \begin{bmatrix} c & -c \\ -c & c \end{bmatrix} \begin{pmatrix} \dot{x}_m \\ \dot{x}_b \end{pmatrix} + \begin{bmatrix} k & -k \\ -k & k \end{bmatrix} \begin{pmatrix} x_m \\ x_b \end{pmatrix} \tag{2.39}$$

$\ddot{x}$, $\dot{x}$, x are defined as acceleration, velocity, and displacement respectively. Force, damping and stiffness are represented by f, c, and k respectively. Subscripts denote a location either at the mass m or base b. This definition mirrors Eq. 2.18, and made clearer when Eq.2.39 is rewritten in terms of complex impedance terms and rearranged,

$$\begin{pmatrix} f_m \\ f_b \end{pmatrix} = \left(j\omega \begin{bmatrix} m & 0 \\ 0 & 0 \end{bmatrix} + \begin{bmatrix} c & -c \\ -c & c \end{bmatrix} + \tfrac{1}{j\omega} \begin{bmatrix} k & -k \\ -k & k \end{bmatrix} \right) \begin{pmatrix} \dot{x}_m \\ \dot{x}_b \end{pmatrix} \tag{2.40}$$

The second round bracketed term on the RHS of Eq. 2.40 represents an impedance matrix of the system.

$$\begin{pmatrix} f_m \\ f_b \end{pmatrix} = \begin{bmatrix} jwm + c + k & -c - k \\ -c - k & c + k \end{bmatrix} \begin{pmatrix} \dot{x}_m \\ \dot{x}_b \end{pmatrix} = \begin{bmatrix} Z_{mm} & Z_{mb} \\ Z_{bm} & Z_{bb} \end{bmatrix} \begin{pmatrix} \dot{x}_m \\ \dot{x}_b \end{pmatrix} \tag{2.41}$$

Firstly lets examine the force transmissiblity T^f_{mb} for Fig. 2.6a. A blocking force $\bar{f}_b$ is considered due to a mass excitation f_m. The blocking constraint at the base defines the velocity as $\dot{x}_b = 0$, thus defining Eq. 2.41 as,

$$\begin{pmatrix} f_m \\ \bar{f}_b \end{pmatrix} = \begin{bmatrix} Z_{mm} & Z_{mb} \\ Z_{bm} & Z_{bb} \end{bmatrix} \begin{pmatrix} \dot{x}_m \\ 0 \end{pmatrix} \tag{2.42}$$

Taking both rows of Eq.2.42, equating and substituting for $\dot{x}_m$,

$$Z_{bm} f_m = -Z_{mm} \bar{f}_b \rightarrow -\frac{\bar{f}_b}{f_m} = \frac{Z_{bm}}{Z_{mm}} = T^f_{bm} \tag{2.43}$$

Similarly we can define the response transmissibility T^r_{mb}. Let's consider a base excitation scenario, as shown in Fig.2.6b. The force at the mass must therefore be defined as $f_m = 0$. This turns Eq. 2.41 into,

$$\begin{pmatrix} 0 \\ f_b \end{pmatrix} = \begin{bmatrix} Z_{mm} & Z_{mb} \\ Z_{bm} & Z_{bb} \end{bmatrix} \begin{pmatrix} \dot{x}_m \\ \dot{x}_b \end{pmatrix} \tag{2.44}$$

Taking both rows of Eq. 2.44 we arrive at the following equation,

$$Z_{mm}\dot{x}_m = -Z_{mb}\dot{x}_b \rightarrow \frac{\dot{x}_m}{\dot{x}_b} = -\frac{Z_{mb}}{Z_{mm}} = T^r_{mb} \tag{2.45}$$

Using the definitions made in Eq. 2.43 and Eq. 2.45, we are now able to calculate the force and response transmissibilities respectively.

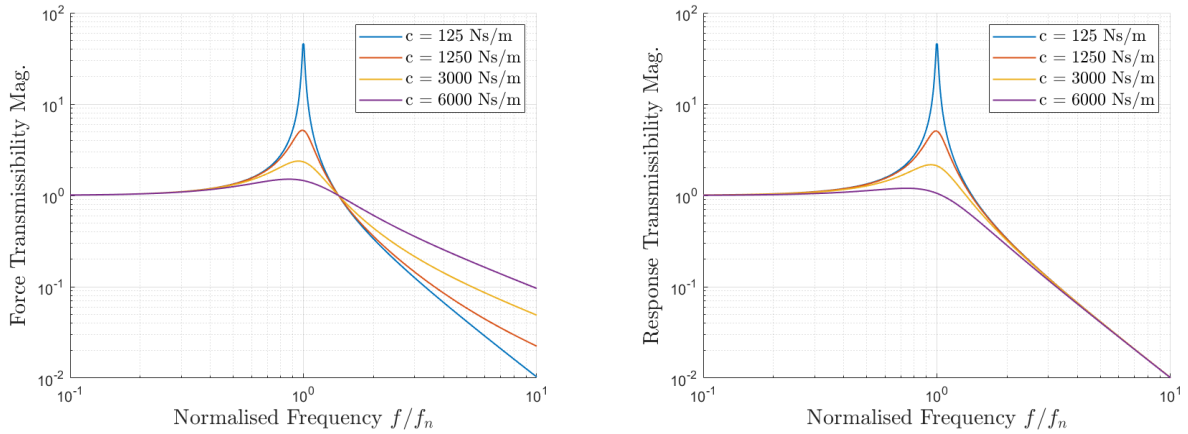

(a) T^f_{bm} due to mass excitation.

(b) T^r_{mb} due to base excitation.

Figure 2.7: Force and velocity transmissibilities of SDoF system for when different amounts of damping is applied.

It's important to understand what the value of a transmissibility actually represents in order to tell what kind of dynamic behaviour the system is under. A value below 1 indicates the mass response is less than the response measured at the base. Conversely, a value above 1 tells us the response of the mass is greater than the base response. A transmissibility that tends to 1 specifies the mass of the system is oscillating with an equal amplitude and phase, i.e. direct transmission.

In Fig.2.7 we can see that the force and response transmissibilities are very similar in their characteristics. They have also been calculated with various amounts of

damping c to demonstrate the difference in magnitude at the critical frequency f_c. Both response and force transmissibilities begin with a direct transmission between the base and mass. The difference between forces or velocities increases at varying rates approaching the critical frequency. At f_c we see the greatest difference between quantities, indicating a maximum amplification of the transmissibility.

2.6.2 Generalised Transmissibility

While the transmissibility concept for SDoF systems was established for many decades, it was only until the 1980s when Magrans [1981] laid the theoretical ground work for its extension to MDoF systems, providing a demonstration via an experimental electrical system. One of the first to present the concept on an MDoF mass-spring system was by Liu and Ewins [1998]. This was followed by a definitive exposition for the generalisation of the transmissibility concept to MDoF systems in 2000 (Ribeiro et al. [2000]). Technically its generalisation was presented by the author at the *NATO-ASI Modal Analysis and Testing* conference in 1998, but a formal publication to the journal *Mechanical Systems and Signal Processing* was made 2 years later and often the most cited text. In this section, the theory behind the generalised transmissibility will be derived in the context of a global structure (its original form for MDoF systems). Further theory for its application to coupled assemblies will be covered later in Section 2.6.2. Following the derivations in this section, a review on the properties and uses of generalised transmissibilities is provided.

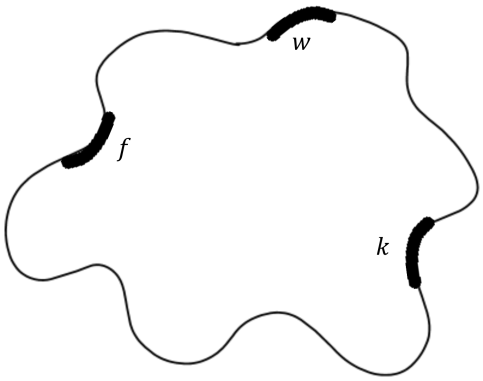

Figure 2.8: Arbitrary LTI MDoF system with response DoF subsets u and w, and force DoF subset f.

Similarly to the SDoF transmissibilities, generalised transmissibilities can represent a relationship between two responses due to some load, or between applied forces and reaction forces. In this section, the theory for both of these generalised transmissibilities (response and force respectively) will be derived. Ribeiro et al. [2000] and Maia et al. [2001] defined the fundamental formulation via mobilities as well as measured responses (output-only) for a response transmissibility. In Fig.2.8 we there are 3 subsets of DoFs. f represents the location of applied forces, while u and w are two DoF subsets of responses. As shown earlier in Section 2.17, we may define the relationship between the velocity responses at u and w due to an applied force at f,

$$\mathbf{v}_u = \mathbf{Y}_{uf}\mathbf{f}_f \tag{2.46}$$

$$\mathbf{v}_w = \mathbf{Y}_{wf}\mathbf{f}_f \tag{2.47}$$

yielding the mobility FRFs $\mathbf{Y}_{uf}$ and $\mathbf{Y}_{wf}$. One can clearly see Eq.2.46 and 2.47 can be combined,

$$\mathbf{v}_u = \mathbf{Y}_{uf}\mathbf{Y}_{wf}^{-1}\mathbf{v}_w \tag{2.48}$$

Note that for this example $\mathbf{Y}_{wf}$ can be inverted as it is a square matrix. In this case

as we are assuming the number of applied force DoFs in f is equal to the number of response DoFs in w. It is required that $w_n \geq f_n$, where n indicates the number of DoFs within the subset. In most practical cases $\mathbf{Y}_{wf}$ is rectangular, and a pseudo-inverse Penrose [1955] $^+$ will be taken. By having more applied forces than responses there we create a least-mean-square problem that minimises error. This known as over-determination. In this thesis, examples will be shown where inverting a square matrix increases noise and error within measurements.

Eq. 2.48 relates velocities at u and w, which means the two mobility terms equate to a transmissibility,

$$\mathbf{T}_{uw}^{r,f} = \mathbf{Y}_{uf}\mathbf{Y}_{wf}^{-1} \tag{2.49}$$

Note that in the superscript of $\mathbf{T}_{uw}^{r,f}$ the first term indicates the type of transmissibility, followed by location of the applied force. The subscripts of the response transmissibility, denote the locations of velocities measured. Likewise if a force transmissibility is used, the subscripts denote the locations of forces. This is differs to the mobility notation; where the subscripts denote locations of response and force. For transmissibilities the locations are of the same quantity. Technically, $\mathbf{T}_{uw}^{r,f}$ can be thought as a form of FRF, because it relates responses at u and w. Eq.2.48 can be rewritten as,

$$\mathbf{v}_u = \mathbf{T}_{uw}^{r,f}\mathbf{v}_w \tag{2.50}$$

A final note is that response transmissibility does not require the location of forces to coincide with a subset of response DoFs. While the location of the applied force must be known, the magnitude of it is not needed. As we can see from the above derivation, this is because the force vector f_f has cancelled out. As pointed out in Section 2.3, mobility and impedance are related by inverse, meaning an alternative definition of the response transmissibility by impedances can be made (Ribeiro et al. [2005]).

As already mentioned earlier in the context of SDoF systems, a force transmissibility

can also be defined. It's generalisation to MDoF systems was presented by Maia et al. [2006], and shows how the inverse problem can be used to estimate blocking (or reaction) forces from applied forces.

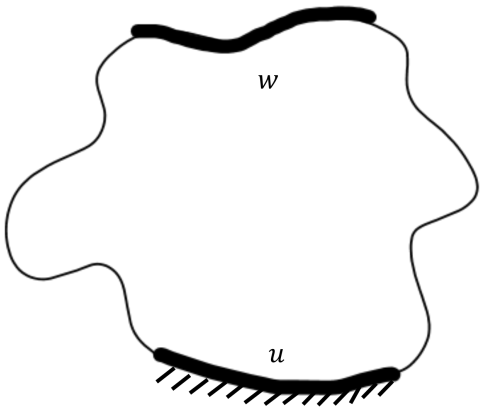

Figure 2.9: Arbitrary LTI MDoF system with force DoF subsets u and w.

In reference to the above figure, w represents a DoF subset of applied forces while u denotes a DoF subset of blocking forces. A reaction force at u means the velocity at at subset must 0, $\mathbf{v}_u = 0$. Firstly, the equations of motion for this system are defined as,

$$\mathbf{v}_u = -\mathbf{Y}_{uu}\bar{\mathbf{f}}_u \tag{2.51}$$

$$\mathbf{v}_u = \mathbf{Y}_{uw}\mathbf{f}_w \tag{2.52}$$

where $\bar{\mathbf{f}}_u$ represents the blocking force at the blocking DoFs u, and $\mathbf{f}_w$ indicating an applied force at DoF w. Combining these two equations yields,

$$-\bar{\mathbf{f}}_u = \mathbf{Y}_{uu}^{-1}\mathbf{Y}_{uw}\mathbf{f}_w \tag{2.53}$$

therefore the force transmissibility must be,

$$\mathbf{T}_{uw}^{f,w} = \mathbf{Y}_{uu}^{-1}\mathbf{Y}_{uw} \tag{2.54}$$

and Eq.2.53 may be rewritten as,

$$-\bar{\mathbf{f}}_u = \mathbf{T}_{uw}^{f,w}\mathbf{f}_w \tag{2.55}$$

Similarly to the response transmissibility, the force transmissibility may be calculated by mobilities, which also means $\mathbf{T}_{uw}^{f,w}$ can also be determined using impedances. With the generalised response and force transmissibilities now derived, the rest of this section will review the literature behind the concept, outlining its applications and properties.

Generalised transmissibilities have been used in various fields, some of which are not necessarily related to the research conducted in this body work. However, it is important to show the versatility of using the concept, as it will be applied in two different ways for the research presented in this thesis. Applications include: damage detection in SHM (Sampaio et al. [1999], Chesné and Deraemaeker [2013], Maia et al. [2011a]), estimating responses (Law et al. [2011]), finite element model updating (Steenackers et al. [2007]), predicting FRFs (Urgueira et al. [2008], Almeida et al. [2010], Urgueira et al. [2011]), and in-situ transfer path analysis (TPA) (Meggitt et al. [2021]). As we've already seen from the derivation, the generalised response transmissibility does not depend on the magnitude of applied forces, and can be determined either by output-only or mobility approaches. The output-only property is a particularly useful one, and is central later on for the research presented in Chapter 5. It was shown first by Ribeiro et al. [2002] that generalised transmissibilities (in this particular case a response transmissibility) can also be determined using stochastic forces, I.e. ambient excitations. This is beneficial for systems that can only be analysed by OMA, such as those that cannot be shut down operationally, or that using an applied force via EMA is impractical. The force transmissibility may also be calculated via OMA, but indirectly. In the theory derived later in Chapter 4, it will be made clear how this is possible. For a general overview of generalised transmissibilities, Maia et al. [2011b] provides a very useful guide for those who are perhaps unfamiliar with the concept.

2.7 Sub-structural invariants

A sub-structural invariant quantity in the context of coupled assemblies, is defined as a measured property that is intrinsic to a sub-structure found in-situ. Invariants may also be determined by uncoupling the sub-structure of interest and measuring with free-interface conditions. This can be conducted by suspending the component using soft connections. However, in some situations this is impractical. For example, let's consider an automotive application. Components such as a compressor or engine are usually mounted on compact isolator mounts, which will have some amount of pre-load. By having a free-interface condition, the pre-load will not be replicated and the measured invariant will not be the true value than if it were measured in-situ. Another reason is that some components within industry may be so large and cumbersome that decoupling it is impractical or impossible. This begs the question: "How do you determine a property that is unique to a particular sub-structure in-situ?". The answer to this is a mathematical one; by applying a 0 velocity constraint to a discrete subset of DoFs installed at a coupling connection, creating a 'theoretical' blocked force. In the past, a highly rigid blocking mass would be attached to a decoupled sub-structure to achieve a zero velocity constraint. Along with the limit to a narrow frequency range, it was rather unpractical to carry out such measurements. Bobrovnitskii [2001] was the first to contribute to the more viable use of blocked forces. However, advances by Moorhouse et al. [2009] which independently derived Bobrovnitskii's equivalent field theorem, established that the blocked force could be found experimentally through an in-situ FRF-based inversion. This was shown in the context of a source characterisation, that a blocked force (one example of an invariant) can be obtained while coupled to a receiver sub-structure. This finding has led to advances in applications such as TPA (Elliott et al. [2013], van der Seijs et al. [2016]), component modification (Elliott et al. [2019], Meggitt et al. [2020], Meggitt et al. [2021]), condition monitoring (Moorhouse [2012]), prediction of FRFs (Moorhouse and Elliott [2013]), and virtual acoustic prototyping (VAP) (Moorhouse et al. [2022]). This research has had a impacted industrial applications, that an ISO standard has been made for it (ISO 20270:2019). In this

section, different examples of invariants will be introduced, beginning with the most obvious one - the blocked force.

2.7.1 Blocked force

In the context of a global structure it was shown in Section 2.6.2 that a blocked force (or reaction force) is the force required rigidly constrain a discrete subset of DoFs so that their velocity is 0. On the other for a coupled assembly, we may define the blocked force as the reaction force exerted by a coupled (and theoretically infinitely rigid) adjacent sub-structure.

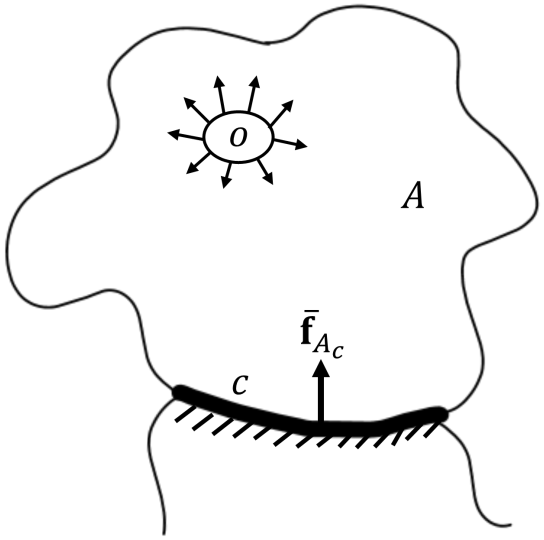

Figure 2.10: Diagram showing the blocked force of a source sub-structure, due to a rigid constraint at the interface c DoFs.

Let's consider a coupled assembly where a source sub-structure A has some operating mechanisms located at o. The blocked force $\bar{\mathbf{f}}_{A_c}$ is defined as the contact force $\mathbf{f}_c$ needed to fix the velocity at the interface DoF subset c to zero, $\mathbf{v}_c = 0$.

$$\bar{\mathbf{f}}_{A_c} = \mathbf{f}_c\Big|_{\mathbf{v}_c=0} \tag{2.56}$$

In methods such as Classical TPA (Verheij [1982]) the source is operational and coupled to determine interface forces, but to predict a response in the adjacent sub-

structure it requires decoupling the receiver to determine the mobility between the interface and receiver DoF subset via EMA. This can be especially challenging if the receiver is cumbersome. Using the blocked force TPA method provided a means of describing independent source activity, in other words without the an adjacent receiver component influencing it, while also being able to measure the mobility between the interface and receiver DoFs in-situ. This is why it is also referred to as the in-situ method. An important assumption when using the blocked force in a mechanical coupled assembly, is that the blocked force and operational forces reproduce the same response field in the receiver (Moorhouse and Seiffert [2006]). The way this assumption is used for the measurement of a response in a receiver by using the blocked force will be demonstrated.

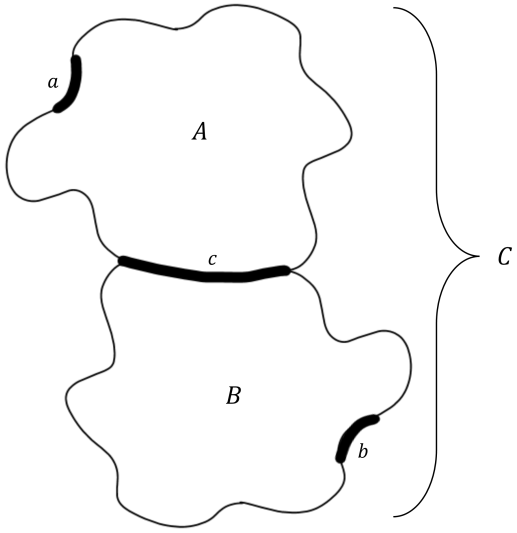

Figure 2.11: Model of an arbitrary structure divided by a user defined interface, c, making two sub-structures A and B.

A key equation shown by Moorhouse et al. [2009] which uses the mentioned assumption states that,

$$\mathbf{v}_{C_b} = \mathbf{Y}_{C_{bc}} \bar{\mathbf{f}}_{A_c} \tag{2.57}$$

Eq.2.57 relates the blocked force of the source to a velocity measured at the receiver DoF subset b for the coupled assembly C, denoted $\mathbf{v}_{C_b}$. $\mathbf{Y}_{C_{bc}}$ is the transfer mobility

between the interface DoFs c and the receiver DoFs b. These two quantities are readily measurable, but the blocked force $\bar{\mathbf{f}}_{A_c}$ is unknown. To calculate it the inverse problem must be solved, which is performed by pre-multiplying both sides of the equation by $\mathbf{Y}_{C_{bc}}$, yielding,

$$\bar{\mathbf{f}}_{A_c} = \mathbf{Y}_{C_{bc}}^{-1}\mathbf{v}_{C_b} \tag{2.58}$$

This key equation allows the use of a theoretically infinitely rigid test-bench to be avoided. To conduct this measurement, $\mathbf{v}_{C_b}$ is calculated while the source is operational. Following this, $\mathbf{Y}_{C_{bc}}$ is measured in-situ while the source is shut down. It was established earlier in Section 2.2 that the principle of reciprocity can be use, meaning that if the mobility cannot be measured by applying an applied force and the interface (such as via roving hammer), then it can transposed so the force is applied at b and the response is measured at c, i.e. $\mathbf{Y}_{C_{bc}}^{\mathrm{T}}$.

2.7.2 Transmissibility

In this section, response and force transmissibilities will be derived to show how they too are invariant.

The force transmissibility T_{ij}^{f} is defined as the relationship between an applied force f_j at the DoF j, and the blocking force $-\bar{f}_i$ at the DoF i, whilst all DoFs except for i and j are subject to a zero force constraint $f_{k\neq i,j} = 0$.

$$\begin{pmatrix} -\bar{f}_1 \\ \vdots \\ -\bar{f}_N \end{pmatrix} = \begin{bmatrix} T_{11}^{f} & \dots & T_{1M}^{f} \\ \vdots & \ddots & \vdots \\ T_{N1}^{f} & \dots & T_{NM}^{f} \end{bmatrix} \begin{pmatrix} f_1 \\ \vdots \\ f_M \end{pmatrix}, \qquad T_{ij}^{f} = \left.\frac{-\bar{f}_i}{f_j}\right|_{f_{k\neq j}=0}. \tag{2.59}$$

For Eq.2.59, the excitation and blocking force DoFs belong to different groups of DoFs. If more than one blocking DoF is used then a constraint of $v_{i\in N} = 0$ is applied to those DoFs. The generalised response transmissibility T_{ij}^{r}, it is defined as,

$$\begin{pmatrix} \bar{v}_1 \\ \vdots \\ \bar{v}_M \end{pmatrix} = \begin{bmatrix} T^r_{11} & \dots & T^r_{1N} \\ \vdots & \ddots & \vdots \\ T^r_{M1} & \dots & T^r_{MN} \end{bmatrix} \begin{pmatrix} v_1 \\ \vdots \\ v_N \end{pmatrix}, \qquad T^r_{ij} = \left. \frac{\bar{v}_i}{v_j} \right|_{v_{k\neq j}=0} . \tag{2.60}$$

In terms of individual elements, the response transmissibility T^r_{ij} is defined as the ratio between an applied velocity v_j of DoF j, and response velocity $\bar{v}_i$ of DoF i. Note that in the same way as the force transmissibility, the two velocity DoFs belong to different sets, where j belongs to the set N, and i is part of the set M. Additionally, all DoFs except the one corresponding to j are rigidly constrained. In some works, the transmissibilities defined in Eq.2.59 and 2.60 are termed *blocked* or *direct transmissibilities* Guasch et al. [2013] Jové and Guasch [2017]. This is in opposition to global transmissibilities, which do not have blocking constraints.

Now the response and force transmissibilities are defined, one may notice the similarities between them. Both require rigidly constraining the blocking DoFs to zero when measuring at or between distinct DoFs. This is an important requirement, as the author explains in detail in Meggitt and Moorhouse [2020a], if the blocking DoFs which separate the coupled system into two distinct sub-structures, the obtained transmissibility will be an 'invariant' property of the sub-structure across which it was measured. Essentially this means the blocking constraints have removed the effect of an adjacent sub-structure, making the transmissibility calculated on the target sub-structure solely a property of that sub-domain. Additionally, it has already been established in Section 2.6.2 may be calculated by the product of two FRFs, which means they too are invariant for a transmissibility calculated on a sub-structure (Meggitt and Moorhouse [2020b]). The invariance property can be useful in the contexts of updating particular areas of a numerical models using measured in-situ data Meggitt and Moorhouse [2020b], or localising damage in within a coupled assembly (Meggitt and McGee [2024]). Perhaps unsurprisingly, given their similar blocking constraints, the two transmissibilities are related through simple matrix operations Lage et al. [2014]. The theory of this relation will covered in the theory section of Chapter 4.

2.7.3 Damage indicator

Within the field of SHM, a sub-structural invariant quantity called a damage indicator can be used to determine the integrity of a structure or its coupled components. While this is not related exactly to the work of this thesis, the purpose of this sub-section is demonstrate the breadth of what can be defined as a sub-structural invariant. An FRF or transmissibility measured on a structure that is damaged, will differ to when that quantity was measured without damage. A damage indicator is a value that compares the baseline and damaged FRFs/transmissibilities; which if invariant, means the damage indicator is also an invariant. Furthermore, this is a way of localising damage as the damage indicator will an inherent property of a sub-structure (Meggitt and McGee [2024]). While observing the difference between FRFs or transmissibilities visually via a plot is possible, it is more practical to quantify the magnitude of a structural fault by using a damage indicator. When a structural fault occurs there is a change in stiffness or damping. This effect shifts resonances of the system. Quantifying the difference between baseline and damaged FRFs/transmissibilities can be done in different ways, such as by: difference (Schulz et al. [1997], Sampaio et al. [2016]), correlation (Maia et al. [2011a]), and coherence methods (Haeussler et al. [2020]).

2.8 Interface representation

There are three common ways in which an interface is represented: the Finite Difference Approximation, Single Point Connection (SPC), and Virtual Transformation Point (VPT). An interface tends to resemble a surface or line in practice. In theory representing an interface like this would require an infinite amount of DoFs and is obviously impractical. In Finite Element Modelling (FEM) the interface is characterised by nodes, and for practical tests the interface is usually defined discretely. This allows for direct comparison and validation.

SPC does not represent an interface sufficiently as it doesn't include rotational DoFs. Elliott and Moorhouse [2008] showed how including the rotational DoFs is important

for coupled sub-structures. As for VPT exact knowledge of sensor placement and orientation due to the virtual point is needed, which can be time consuming but does allow one to characterise an interface sufficiently. Both the finite difference and VPT methods are explained so that one may understand the process of fully defining an interface for rigidly coupled systems.

2.8.1 Virtual Point Transformation

The Virtual Point Transformation (VPT) method (der Seijs et al. [2014]) relates local translational response sensors and excitation forces to a virtual point (VP) or node, i.e. a conceptual point, on a structure. Like all other interface presentation methods, the VPT assumes rigid connections between sensors and the virtual point. This is essential in estimating translational and rotational DoFs at the VP based on sensor measurements.

By taking a virtual point on a rigid interface, the dynamics of it are simplified to a set of coordinates that are related to the rigid interface deformation modes, resulting in a node with 6 DoFs. Essentially, VPT relates the dynamics of a local group of DoFs to a virtual point. These DoFs are usually 3 tri-axial accelerometers accounting for 9 DoFs. When performing an interface characterisation measurement one will obtain a 9$\times$9 mobility matrix. This becomes a 6$\times$6 mobility matrix after Interface Deformation Mode (IDM) filtering, consisted of all translations x, y, z and rotations α, β, γ. The advantage of using a virtual point is the ability to compare the virtual point interface to a node in an identical FE model. However the VPT's downfall is that precise knowledge of sensor placement and orientation due to the virtual point is needed. This can be time consuming as it can require some planning ahead of measurement.

2.8.2 Finite Difference Method

This method originally published by Sattinger [1980] requires a set of two translational placed apart from each other at a known distance δ to the centre. By taking the two

translational excitations and responses at these two points, an approximation of the rotational excitations and responses (moment and angular velocity) is acquired. Later on Elliott et al. [2008] went onto develop the method, providing a rapid means of obtaining said rotational quantities. A demonstration of the measurement is shown by Fig.2.12. When conducting the in-situ blocked force method it is essential to include all DoFs for full characterisation of an interface, so that the dynamic properties of each coupled sub-structure can be accurately distinguished. This section will outline how to perform the finite difference method but for a simple 2D beam.

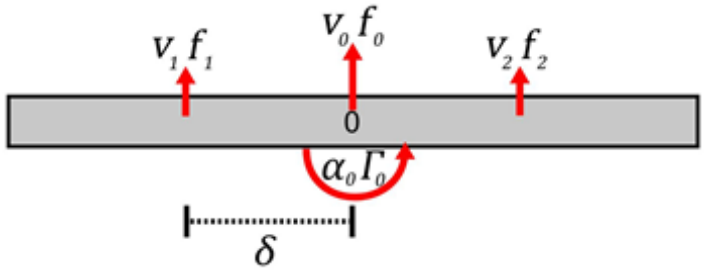

Figure 2.12: Finite Difference approximation taken from two transnational components spaced by δ from the centre line. The resultant point where translational and rotational DoFs are calculated for are at centre, 0

For the following derivation, a simple structure shown in Fig.2.12 will be denoted as C,

$$\mathbf{Y}_{C_{00}} = \begin{bmatrix} Y_{C_{v_0 f_0}} & Y_{C_{v_0 \alpha_0}} \\ Y_{C_{\Gamma_0 f_0}} & Y_{C_{\Gamma_0 \alpha_0}} \end{bmatrix} \tag{2.61}$$

Eq.2.61 is defined as the point mobility matrix. It is made up of mobilities that are related to the translational and rotational force and response components. Each of these elements are defined as,

$$\hat{Y}_{v_0 f_0} \approx \frac{Y_{v_1 f_1} + Y_{v_2 f_1} + Y_{v_1 f_2} + Y_{v_2 f_2}}{4} \tag{2.62}$$

$$\hat{Y}_{\alpha_0 f_0} \approx \frac{-Y_{v_1 f_1} + Y_{v_2 f_2}}{4\delta} \tag{2.63}$$

$$\hat{Y}_{v_0\Gamma_0} \approx \frac{-Y_{v_1f_1} + Y_{v_2f_2}}{4\delta} \tag{2.64}$$

$$\hat{Y}_{\alpha_0\Gamma_0} \approx \frac{Y_{v_1f_1} - Y_{v_2f_1} - Y_{v_1f_2} + Y_{v_2f_2}}{4\delta^2} \tag{2.65}$$

v and f are the translational velocity and force components, while α and Γ are the angular velocity and moment force. $\hat{\mathbf{Y}}$ represents the mobility approximation via the finite difference method.

A convenient way in which Eq.2.61 can be represented is in the form,

$$\hat{\mathbf{Y}} \approx \mathbf{RYR}^{\mathrm{T}} \tag{2.66}$$

$\mathbf{R}$ represents the finite difference transformation matrix, and is pre-multiplied with mobility matrix $\mathbf{Y}$. This row operation will determine the translational and angular velocities. Next is the post-multiplication of $\mathbf{R}^{\mathrm{T}}$, which conducts a column operation. This determines the translational and moment forces. Eq.2.66 in shown in terms of individual elements is shown as,

$$\begin{bmatrix} Y_{C_{v_0f_0}} & Y_{C_{v_0\alpha_0}} \\ Y_{C_{\Gamma_0f_0}} & Y_{C_{\Gamma_0\alpha_0}} \end{bmatrix} \approx \begin{bmatrix} \frac{1}{2} & \frac{1}{2} \\ \frac{-1}{2\delta} & \frac{1}{2\delta} \end{bmatrix} \begin{bmatrix} Y_{v_1f_1} & Y_{v_1f_2} \\ Y_{v_2f_1} & Y_{v_2f_0} \end{bmatrix} \begin{bmatrix} \frac{1}{2} & \frac{-1}{2\delta} \\ \frac{1}{2} & \frac{1}{2\delta} \end{bmatrix} \tag{2.67}$$

Before using the finite difference mobility approximation in calculating the blocked force, the finite difference method must be applied to the velocity response matrix as well,

$$\hat{\mathbf{v}} \approx \mathbf{Tv} \tag{2.68}$$

$\mathbf{v}$ is the translational velocity response, while $\hat{\mathbf{v}}$ is the finite difference approximation velocities. Therefore the blocked force approximation $\hat{\mathbf{f}}$ is as follows,

$$\hat{\mathbf{f}} = \hat{\mathbf{Y}}^{-1}\hat{\mathbf{v}} \tag{2.69}$$

An experimental validation, error analysis, and full derivation of the finite difference equations are shown by Elliott et al. [2012]. It is worth noting that in their error analysis findings, for an analytical beam such as that in Fig.2.12 the overall error is inversely proportional to the magnitude of the mobility. Furthermore, it was found that the error is also proportional to frequency and the separation distance δ. These two factors limit measurements to a certain bandwidth so that one may yield reliable results. For frequencies above the bandwidth δ is similar to the bending wavelength, resulting in large errors due to decreased rigidity. Below the bandwidth there will be accurate mobility results, but due to finite difference noise will be introduced.

2.8.3 Interface completeness criterion

If an interface isn't characterised correctly, i.e. the blocking constraints are insufficient, then the dynamic quantities determined for a sub-structure such as transmissibility, blocked forces, mobility etc. are not invariant. Instead they are related to the coupled structure as a whole, rather than the sub-structure of interest. For invariance to exist, the coupling interface must take into account the relevant DoFs, depending on the nature of the interface. For example if the interface is a resilient mount, then 1 DoF facing the direction of attenuation by the resilient mount will usually suffice. If the interface is a rigid point connection, the interface must be characterised by 3 translational DoFs x, y, z and as well as rotational DoFs α, β, γ. This is much more involved and time consuming than the resilient interface. It is certainly possible in this case that one may be unsure the characterisation of c is sufficient. This is where the Interface Completeness Criterion (ICC) is supposed to help identify at what frequencies invariance may break down. The term 'completeness' is used in assessing the capability of the blocking DoFs c at applying a zero velocity constraint. A tool such as the ICC may be helpful in determining the reliability of dynamic quantities determined for a sub-structure in an

industrial setting. For example, an engineer may conduct a measurement for a transmissibility across a sub-structure. Often in industry heavy and/or large structures such as machinery may be inaccessible in areas such as the mounts. Often the mounting points are where the blocking constraints will be applied. This means that defining an interface completely by the relevant number of DoFs can be impractical.

In this section, the theory behind two versions of the ICC will be outlined. Firtstly the correlation-based ICC by Meggitt and Moorhouse [2020a] is defined as,

$$\mathbf{ICC}_{ab} = \frac{\left| \underset{\rightarrow}{\mathbf{Y}}_{C_{ab}} \left(\underset{\rightarrow}{\hat{\mathbf{Y}}}_{C_{ab}} \right)^{\mathrm{H}} \right|^2}{\underset{\rightarrow}{\mathbf{Y}}_{C_{ab}} \left(\underset{\rightarrow}{\mathbf{Y}}_{C_{ab}} \right)^{\mathrm{H}} \underset{\rightarrow}{\hat{\mathbf{Y}}}_{C_{ab}} \left(\underset{\rightarrow}{\hat{\mathbf{Y}}}_{C_{ab}} \right)^{\mathrm{H}}} \tag{2.70}$$

H in the superscipt refers to a conjugate transpose, while the under arrow $\underset{\rightarrow}{\ }$ indicates a column-wise vectorisation. Another formulation of the ICC, most commonly referred to as the coherence-based ICC by Haeussler et al. [2020], is defined as,

$$\mathbf{ICC}_{ab} = \frac{\left(\hat{\mathbf{Y}}_{C_{ab}} + \mathbf{Y}_{C_{ab}} \right) \left(\mathbf{Y}^*_{C_{ab}} + \hat{\mathbf{Y}}^*_{C_{ab}} \right)}{2 \left(\hat{\mathbf{Y}}_{C_{ab}} \hat{\mathbf{Y}}^*_{C_{ab}} + \mathbf{Y}_{C_{ab}} \mathbf{Y}^*_{C_{ab}} \right)} \tag{2.71}$$

Terms in Eq.2.71 with a * in the superscript denotes complex conjugate. Additionally, both mobility terms must be averaged over the indices in the subscripts.

In the above equations, the measure of completeness is judged between the direct transfer mobility $\mathbf{Y}_{C_{ab}}$, and reconstructed transfer mobility via the round-trip method $\hat{\mathbf{Y}}_{C_{ab}}$. The round-trip identity will be covered in the next chapter in further detail, but essentially to reconstruct the transfer mobility, $\mathbf{Y}_{C_{ac}}$, $\mathbf{Y}_{C_{cc}}$, and $\mathbf{Y}_{C_{cb}}$ must be measured. If the interface description is complete, then $\mathbf{Y}_{C_{ab}} = \hat{\mathbf{Y}}_{C_{ab}}$, and therefore $\mathbf{ICC}_{ab} = 1$. For an incomplete characterisation of the interface, $\mathbf{ICC}_{ab} < 1$. In reality, Eq.2.70 is not sensitive to changes in amplitude. Instead, Eq.2.71 is used for a more accurate

representation of interface completeness,

2.9 Singular Value Decomposition

The singular value decomposition (SVD) is a mathematical technique used in various fields of science such as image compression, and model reduction in control theory. Within vibro-acoustics it is used widely as a method of regularisation for ill-conditioned matrices due to the inverse problem Janssens et al. [1999] . Later in this thesis (Chapter 6), a different application of the SVD is presented; detecting transmission paths and mechanical bridges between source and receiver sub-structures within a coupled assembly. For its most common application (regularisation) the SVD takes a high dimensional signal that has a high degree of variability and reduces it to a lower dimensional signal where the structure is ordered from the highest variation to the lowest. A form of the SVD called the truncated SVD (TSVD) is particularly advantageous for noise reduction, as it ignores variation at a particular threshold, resulting in a reduced data set.

Mathematically speaking, the SVD uses a linear algebra theorem that states any square or rectangular matrix $\mathbf{A}$ can be split up into the product of three matrices $\mathbf{U}$, $\mathbf{\Sigma}$, $\mathbf{V}^{\mathrm{H}}$ (where $^{\mathrm{H}}$ represents the Hermitian, or conjugate transpose).

$$\mathbf{A} = \mathbf{U}\mathbf{\Sigma}\mathbf{V}^{\mathrm{H}} \tag{2.72}$$

$\mathbf{U}$ is an orthogonal matrix where $\mathbf{U} = [u_1, u_2, ..., u_m]$ is an $m \times m$ matrix that is unitary, i.e. $\mathbf{U}^{\mathrm{H}}\mathbf{U} = 1$ and contains the left singular vectors. It captures how the rows of the original matrix are related to each other and shows the underlying structure and relationships in the data. $\mathbf{\Sigma}$ is a $m \times n$ if $\mathbf{A}$ is rectangular or $m \times m$ if square, and is a diagonal matrix where $\mathbf{\Sigma} = \mathbf{diag}(\sigma_1, \sigma_2, ...\sigma_n)$ and its entries contain non-negative real numbers along the diagonal and are known as the singular values (SVs) of $\mathbf{A}$. Σ describes the importance of each SV from most important being σ_1 descending to

least important σ_n. Finally, $\mathbf{V}^{\mathrm{H}}$ is a $n \times n$ orthogonal matrix, or $m \times m$ if A is square. It has the form $\mathbf{V}^{\mathrm{H}} = [v_1, v_2, ..., v_n]$, is unitary, and described as the complex conjugate transpose of the right singular vectors. It reveals how the columns of the original matrix are related to each other.

The rank r of matrix $\mathbf{A}$ describes the number of rows or columns that are linearly independent, i.e are unique and are not made of other rows or columns. r is dependent on the number of non-zero singular values in the matrix $\mathbf{\Sigma}$, and if it is less than the smallest dimension of Σ it is rank deficient and does not satisfy Jacques Hadamard's condition of uniqueness for a 'well-posed' problem. In some instances $\mathbf{A}$ can appear full rank due to linear dependencies when it is actually rank deficient, resulting in a large condition number and therefore an ill-conditioned matrix. The condition number can checked by applying the following equation:

$$c(\mathbf{A}) = \frac{\sigma_{max}}{\sigma_{min}} \tag{2.73}$$

Let's assume that matrix $\mathbf{A}$ is a matrix of FRFs or transfer functions. Commonly used analysis methods within vibro-acoustics such a transmission path analysis (TPA) require to invert this, also known as an inverse problem. Let us assume $\mathbf{A}$ is rectangular, a generalisation of the matrix inverse operation by means of least squares is applied, called the Penrose [1955] pseudo-inverse. Consequently notated $\mathbf{A}^+$, Eq.2.72 can be written as:

$$\mathbf{A}^+ = \mathbf{V}\mathbf{\Sigma}^+\mathbf{U}^{\mathrm{H}} \tag{2.74}$$

It is likely in an experimental setting that $\mathbf{\Sigma}^+$ will have some singular values that are small and mostly composed of measurement error and noise. Including these singular values can lead to incorrect solutions. To combat this issue the truncated singular value decomposition technique is used. This introduces a threshold to each singular value, which we will call t. This will keep t amount of the largest singular values and

thus t number of columns and rows of $\mathbf{U}$ and $\mathbf{V}^{\mathrm{H}}$ respectively. Eq.2.74 can now be rewritten as:

$$\tilde{\mathbf{A}}^{+} = \mathbf{V}_t \boldsymbol{\Sigma}^{+}{}_t \mathbf{U}_t^{\mathrm{H}} \tag{2.75}$$

The caveat to using the TSVD is that the threshold must be determined appropriately for the data set at hand, so to preserve all of the main relationships within $\mathbf{A}$.

Chapter 3

Sensitivity analysis on the round-trip method

In this Chapter the sensitivities of both point and transfer mobility predictions via the round-trip method are explored with respect to the number of remote DoFs and their positioning, the number of interface DoFs and their positions, the geometry of the structure, and noise. This is demonstrated mainly on a numerical model, followed by some analysis on an experimental example. This research is to inform those that use the round-trip of what conditions lead to an optimum prediction.

Contents

Round-trip method theory

In the beginning of this chapter, we explore the concept of the RT method in greater detail. In addition, mathematical derivations on the RT identity are provided to inform the reader of areas for analysis on its sensitivities. The RT theory was first proposed by Moorhouse et al. [2011] through simulations, and soon after validated experimentally in Moorhouse and Elliott [2013]. The round-trip method constructs an $\mathbf{M} \times \mathbf{M}$ FRF matrix at a coupling interface $\mathbf{Y}_{cc}$ without needing to excite the DoFs along it directly. Rather, the RT method reconstructs the point FRF by using two subsets of remote DoFs on either side of the coupling interface that are more accessible to excite. Modal synthesis techniques have also proved to have some success, by reconstructing the interface matrix with measured responses at all c positions while applying only a single excitation to one DoF within the c subset. Early examples include Ashory [1998], Ashory [1999], and Silva et al. [2000], which used repeated tests with varying mass loading. However this approach appeared to be prone to error if there is only a small change in mass loading. One of the earliest bodies of work to show theoretically reconstruction was possible without repeated tests was by Ewins [1980]. It was Maia et al. [1997] that built on Ewin's work, presenting a similar method that cancelled the effect of transducer masses. The RT method is different as it does not follow the trend of reconstruction by modal synthesis, but instead by a new means based off a generalisation of the 'cavity equation' by Draeger and Fink [1999].

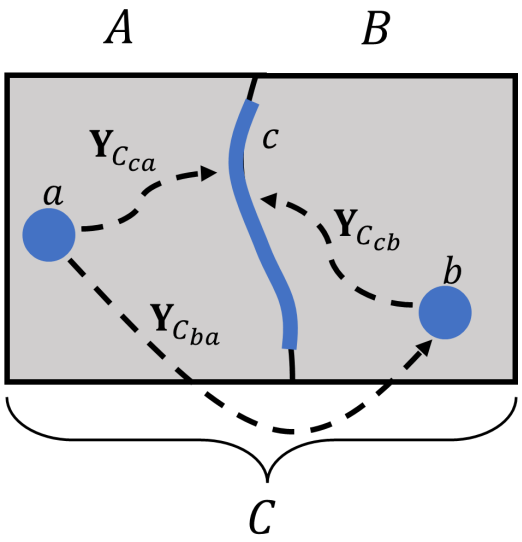

Figure 3.1: Diagram specifying the measured mobilities needed when using the round-trip method.

Consider an arbitrary coupled structure such as Fig.3.1. It consists of two sub-domains A and B, which have multiple DoF subsets installed on each, a and b respectively. In addition, DoFs are also located at the interface between the sub-structures denoted c. Moorhouse and Elliott [2013] states $n_a \geq n_b \geq n_c$ must be satisfied for a unique solution, where n_a, n_b, and n_c are the number of DoFs for subsets a, b, and c respectively. Firstly let's apply excitations at subset b, called $\mathbf{f}_b$. As a result the velocities at subset a and c are defined as,

$$\mathbf{v}_a = \mathbf{Y}_{C_{ab}}\mathbf{f}_b \tag{3.1}$$

$$\mathbf{v}_c = \mathbf{Y}_{C_{cb}}\mathbf{f}_b \tag{3.2}$$

As we are applying the blocked force at c, defining the velocity at the interface requires taking the reaction force measured at c. I.e. The negative blocked force at the interface $-\bar{\mathbf{f}}_c$, is equal to the applied force at b, $\mathbf{f}_b$. This implies $-\bar{\mathbf{f}}_c$ and $\mathbf{f}_b$ form the same velocity field in sub-structure A. Thus, the velocity at c may also be defined as,

$$\mathbf{v}_c = -\mathbf{Y}_{C_{cc}}\bar{\mathbf{f}}_c \tag{3.3}$$

In this example there is an applied force in B, and therefore the velocity in the receiver sub-structure A with our blocked force definition may now be defined,

$$\mathbf{v}_a = -\mathbf{Y}_{C_{ac}}\bar{\mathbf{f}}_c \tag{3.4}$$

If we take Eq. 3.1 and 3.2, rearrange them for $\mathbf{f}_b$ so the applied force terms cancel we arrive at,

$$\mathbf{v}_c = \mathbf{Y}_{C_{cb}}\mathbf{Y}_{C_{ab}}^{-1}\mathbf{v}_a \tag{3.5}$$

A requirement of the round-trip is that the number of DoFs in the subset of the receiver sub-structure should be more than or equal to the number of DoFs in the source subset. In this case where n represents the number of DoFs, $n_a \geq n_b$. Taking our definitions due to a blocked force made in Eq. 3.3 and 4.20 and substituting them into Eq. 4.13, we have the following definition,

$$\mathbf{Y}_{C_{cc}}\bar{\mathbf{f}}_c = \mathbf{Y}_{C_{cb}}\mathbf{Y}_{C_{ab}}^{-1}\mathbf{Y}_{C_{ac}}\bar{\mathbf{f}}_c \tag{3.6}$$

Then by post multiplying by the inverse of $\bar{\mathbf{f}}_c$ we get rid of the blocked force terms and we obtain the point mobility round-trip identity,

$$\mathbf{Y}_{C_{cc}} = \mathbf{Y}_{C_{cb}}\mathbf{Y}_{C_{ab}}^{-1}\mathbf{Y}_{C_{ac}} \tag{3.7}$$

Equally by reciprocity,

$$\mathbf{Y}_{C_{cc}} = \mathbf{Y}_{C_{cc}}^{T} = \mathbf{Y}_{C_{ca}}\mathbf{Y}_{C_{ba}}^{-1}\mathbf{Y}_{C_{cb}}^{T} \tag{3.8}$$

$\mathbf{Y}_{C_{cc}}$ is an $M \times M$ matrix of the reconstructed point mobility at DoF subset c. It may be calculated using Eq.3.7, but its most convenient form by the Maxwell-Betti reciprocal theorem is with Eq. 3.8, as it does not require a controlled excitation at c. The mobility terms in the latter equation are the ones represented by the arrows in Fig.3.1, which should now make it a bit clearer as to why this method is termed 'round-trip'. Note that the mobility $\mathbf{Y}_{C_{cc}}$ is to be determined for linear systems (as well as time invariant ones), and that the inverted terms within the above two equations should be represented by a pseudo-inverse instead if $n_a \geq n_b$. Eq.3.8 represents the same equation that satisfies Maxwell-Betti reciprocal theorem. $\mathbf{Y}_{C_{ab}}$ is defined as a mobility relating a response in a due to excitations in b and is referred to as the reconstructed transfer mobility. The reconstructed transfer mobility equation as presented by Moorhouse and Elliott [2013] is a rearrangement of the indirect measurement of mobility at the interface as proposed by Moorhouse et al. [2011]. The round-trip method may be used to reconstruct this transfer mobility, however this out of the scope of this thesis and will be analysed in future studies. To determine the transfer mobility simply apply a rearrangement for $\mathbf{Y}_{C_{ab}}$ or $\mathbf{Y}_{C_{ba}}$,

$$\mathbf{Y}_{C_{ab}} = \mathbf{Y}_{C_{ac}} \mathbf{Y}_{C_{cc}}^{-1} \mathbf{Y}_{cb} \tag{3.9}$$

or by reciprocity,

$$\mathbf{Y}_{C_{ba}} = \mathbf{Y}_{C_{bc}} \mathbf{Y}_{C_{cc}}^{-1} \mathbf{Y}_{ca} \tag{3.10}$$

In this chapter, a series of analyses is conducted investigating the sensitivities of the round-trip identities of point mobility $\mathbf{Y}_{C_{cc}}$ and transfer mobility $\mathbf{Y}_{C_{ba}}$ via Eq.3.7 and Eq.3.9 respectively. Two plate models are used to carry this out: FE and experimental for $\mathbf{Y}_{C_{cc}}$, and only FE for $\mathbf{Y}_{C_{ba}}$. The FE model (3D elastic) represents a steel plate, while the experimental example is made up of aluminium. A part of the investigation is to validate whether some sensitivities that exist on the FE plate are seen in a practical

case for the point mobility prediction. Firstly, the point mobility is analysed in Section3.1, with the series of analyses comprising of: changing the number of remote and interface DoFs, the aspect ratio of the plate model, the positioning of the remote DoFs, and the sensitivity to noise. In the final part of the point mobility prediction analysis, the experimental model in Section.3.1.2 will present the error of the round-trip prediction against the direct measurement with respect to the number of remote DoFs used.

The second half of the chapter will similarly analyse the round-trip prediction of the transfer mobility $\mathbf{Y}_{C_{ba}}$. The prediction is tested by looking at its accuracy with respect to the location of remote DoFs included in the calculation. This is firstly done by using the Monte-Carlo method, which randomly chooses the positions of A and B DoFs within each sub-structure 50 times. From this a standard error across the frequency range is observed. In addition to this, the positioning of remote points is tested by picking 4 different scenarios of A and B locations. Each of these cases will show the round-trip transfer mobility vs. the direct measurement, and from these plots any resonances which are not in line with the direct measurement are looked into further. In order to understand what is occurring structurally on the model at these resonances, a plot of amplitude across the plate for that given frequency is compared against error contours which are overlayed. Following on from this, the performance of the RT is tested when the number of interface DoFs included in calculating the prediction is changed and compared against a direct mobility. Furthermore, the FRF data obtained from the model is 'spoiled' with varying amounts of noise. Using the MATLAB function "Specspoil.m" the SNR is chosen at 4 different intervals, and compared against the direct mobility for each. The function has the structure: $\mathbf{FRF}_{noise} = Specspoil(Input, L, N, Type)$. *Input* represents the FRF that is to be contaminated with noise, *L* is the signal-to-noise ratio level, *N* is the number of averages, and finally *Type* is the nature of random noise being applied which can be either linear or quadratic. Finally, the initial remote positioning analysis where the error was observed against the amplitude across the FE plate is applied to the experimental plate.

The way FE and experimental models are set up is explained in further detail within

Section3.1 and Section3.1.2, but in essence they are both split along the width side by a line of discretised responses known as the interface c subset of DoF/accelerometers. A zero velocity constraint is imposed along this interface, and either side of it exists a sub-structure A and B which both have 'remote' subsets of DoFs denoted a and b respectively. All subsets of DoFs are uniaxial and face towards the vertical z-axis (perpendicular from the face of the plate). This does not lead to a complete interface description, but there are a couple of reasons for this decision. Firstly, this is to mirror a practical test where uniaxial accelerometers are likely to be used as they are cheaper than triaxial, while also only a limited amount of sensors will be used to define the line interface. This does not allow rotations to be determined, but because both model examples will have forces acting in z-axis the most dominant component at the responses will be in the same plane. Therefore this makes the x and y-axes contributions to the responses small in comparison. Sensitivity analysis on the RT method is conducted on a regularly spaced grid of points for FE and experimental models. Additionally, analysis is conducted on the random positioning of remote or interface DoFs for the FE model.

3.1 Point mobility

A finite-element model representing a steel plate is constructed in which the structural responses are calculated via modal summation. Firstly, a regular grid of discretised points are formed on the surface. Similarly to Fig.2.11, Fig.3.2a shows how the FE model's grid is divided into two remote sub-domains A and B, due to an interface c.

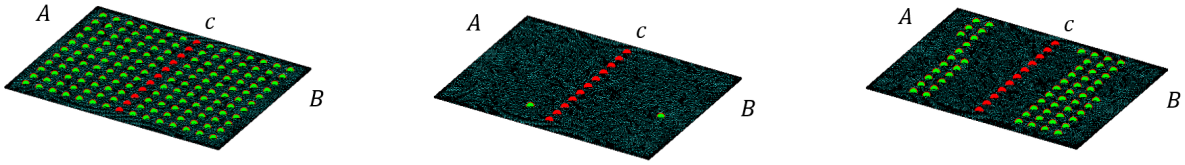

(a) All discretised points of a regular grid.

(b) Randomly selected single remote points from regular grid.

(c) 20 a and 40 b points on the regular grid for remote positions.

Figure 3.2: FE diagram of steel plate, divided into substructures A and B, divided by an interface c.

3.1.1 FE-model example

Accuracy due to the number of DoFs included

Fig.3.3a, Fig.3.3b, and Fig.3.3c correspond to the sub-figures in Fig.2 respectively. All results within Fig.3 show the reconstructed point mobility is not sensitive to the number of interface positions used. Only one result is visible because all prediction scenarios where the interface DoFs are changed are stacked on one another. In Fig.3.3a all remote positions are included in calculating the reconstructed point mobility and appears identical (up to 1kHz) to the direct interface point mobility. For Fig.3.3b a random DoF within A and B was selected, and indicates a rather inaccurate result over all of the frequency range. However it should be noted that numerous resonances are accounted for in this prediction. Lastly Fig.3.3c shows a prediction where 20 DoFs within A and 40 within B are selected. For the vast majority of the frequency range the prediction shows good agreement to the direct measurement, and in some respects performs better than the case where all remote DoFs are accounted for in Fig.3.3a over the full frequency range. Fig.3.3c shows a more accurate prediction after 1kHz while Fig.3.3a performs better between 1Hz-1kHz, an identical result to the direct measurement. It is clear from all sub-figures in Fig.3.3 the reconstructed interface point mobility is unaffected by the number of interface DoFs, but sensitive to the number of remote DoFs accounted for.

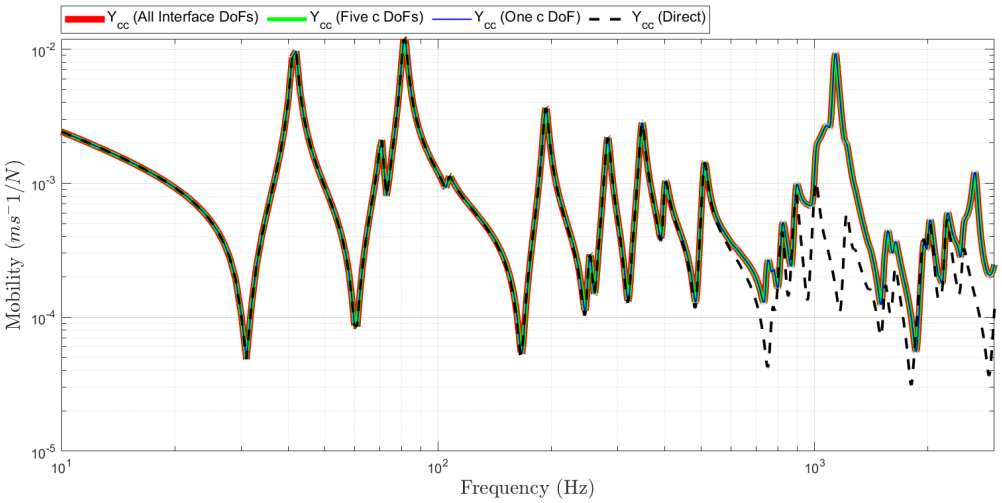

(a) Changing number of interface c DoFs, while including all a and b positions.

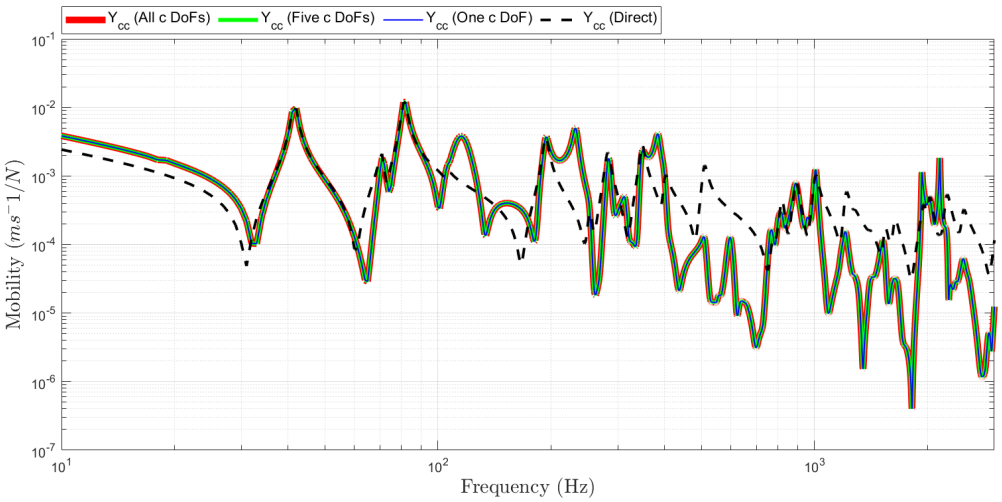

(b) Changing number of interface c DoFs, while including only one a and b position.

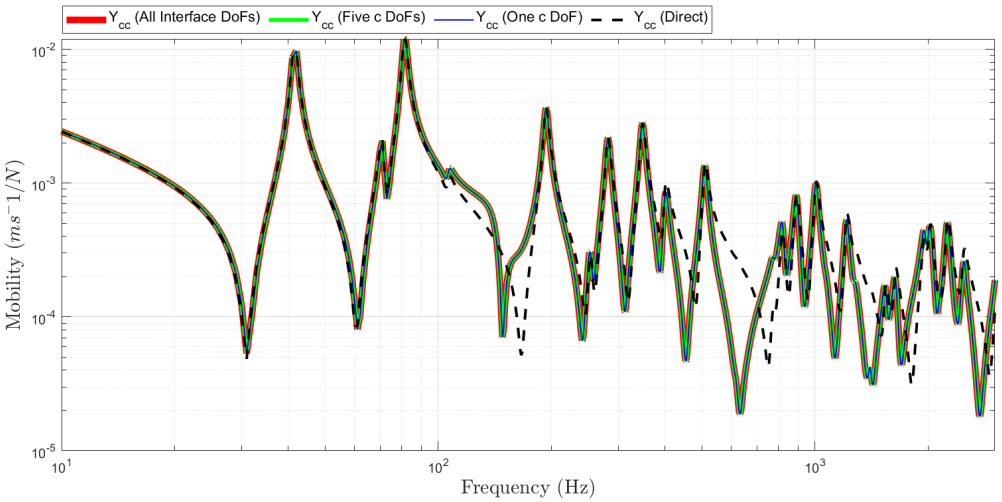

(c) Changing number of interface c DoFs, while including 20 a and 40 b positions.

Figure 3.3: Round-trip prediction of the interface point mobility when c DoFs are changed in different scenarios. From top to bottom, these cases correspond to the number of a and b DoFs shown in Fig.3.2a, 3.2b, and 3.2c respectively.

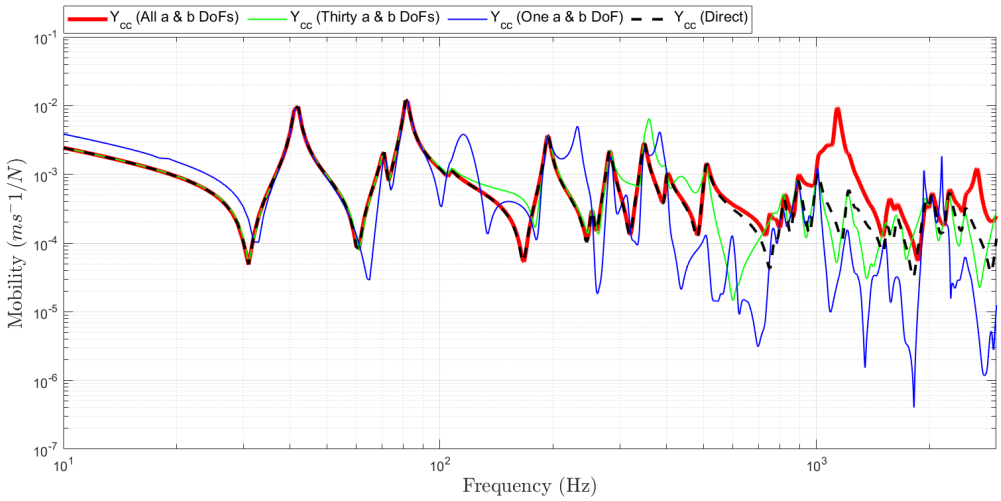

(a) Changing number of a and b DoFs, while including all interface c DoFs.

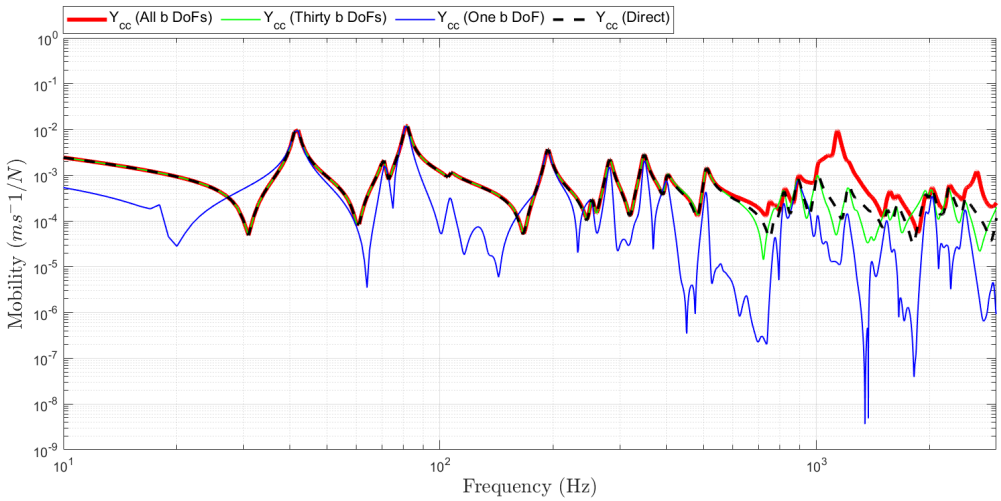

(b) Changing b DoFs, while including all a and c points.

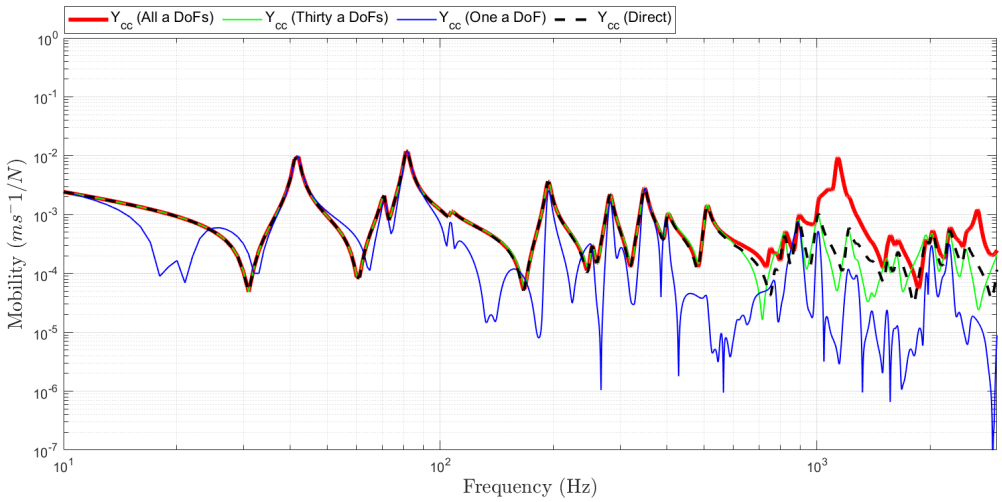

(c) Changing a DoFs, while including all b and c points.

Figure 3.4: Round-trip prediction of the interface point mobility when the number of remote DoFs (a and b) have changed.

In the next set of sub-figures within Fig.3.4 the prediction is observed for when both sets of remote DoFs and one set of remote DoFs are changed. Fig.3.4a presents a case where both remote sides in A and B are altered together. The prediction where one selected a and b position shows the least accurate result, is consistent with the previous result in Fig.3.3b. While being inaccurate at the anti-resonances and for its overall magnitude, almost all resonances correspond to the direct point mobility with similar magnitude. The result where 30 a and b DoFs are accounted for shows a significant boost in accuracy from 1-700Hz. Fig.3.4a shows that if fewer remote positions are accounted for in the reconstructed point mobility, the greater the inaccuracy to the direct point mobility.

The next test of accuracy due to the number of remote positions used is conducted by changing just one set of remote DoFs while including all interface DoFs and the other set of remote positions. The results for this test are displayed in Fig.3.4b and Fig.3.4c. All cases except for where only one remote point is used shows good agreement to the directly measured point mobility up 1kHz. After this only the cases which include all DoFs, and thirty points perform well and stay close to the direct measurement. From these figures it is not made clear as to why the case that uses all remote DoFs is less accurate after 1kHz. However, this will be made clearer in Fig.3.5. Before moving forward onto that, a comment must be made about the sub-figures Fig.3.4c and Fig.3.4b. In the scenarios where one remote position is used, there are differences in accuracy at distinct frequencies. This is because the one remote DoF scenarios are present at different locations on the plate and thus will have dissimilar structural responses.

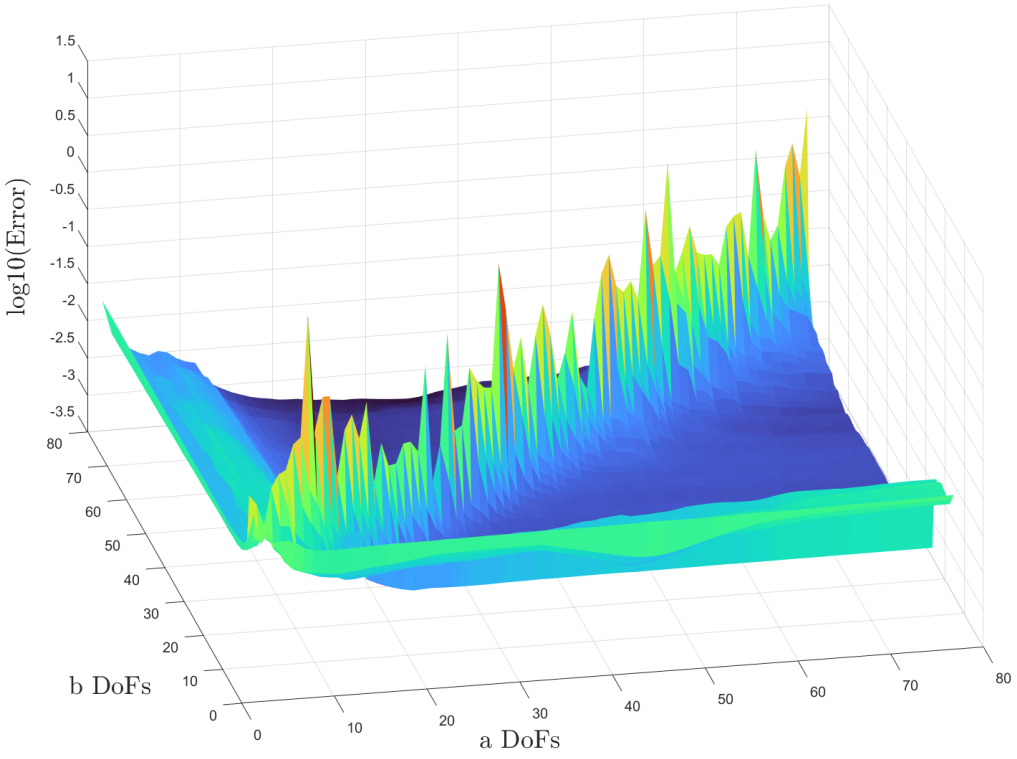

Figure 3.5: $\log_{10}(\text{Error})$ plot for FE plate due to the number of a vs b DoFs accounted for in calculating the interface point mobility. Error calculated up to 1kHz.

Fig.3.5 shows the 'why' for the scenarios where both sets of remote DoF are the same. By calculating the difference between the prediction and direct measurement of the interface point mobility the error is obtained. In order to plot to plot this error between remote points all point mobilities along the interface had to be averaged. It is more significant when less remote positions are used, which corresponds to the inaccurate reconstruction shown in Fig.3.4a where the remote DoFs are equal. The source of the diagonal spike in error is not yet fully understood. In Section 3.3 possible causes of this $a = b$ error is discussed. It can be inferred from Fig.3.5 that an optimal prediction would lie either side of this diagonal spike. The figure also explains why the case that uses all remote DoFs does not agree with the direct measurement above 1kHz, despite having an almost perfect result below 1kHz.

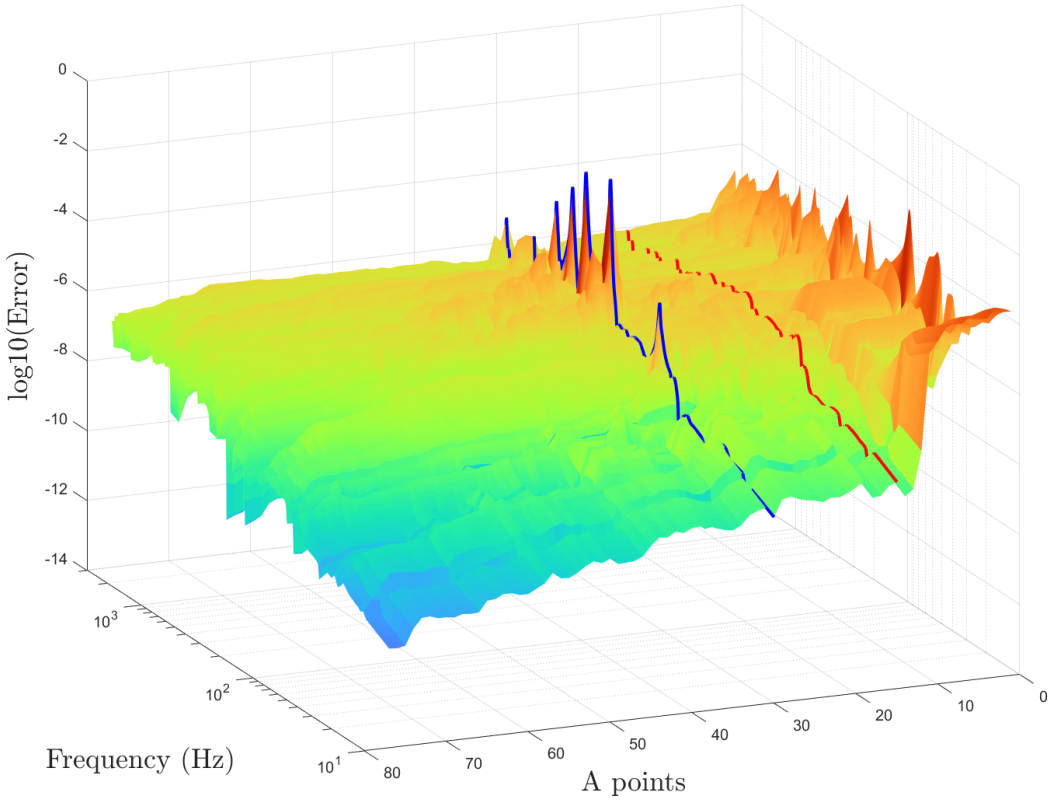

(a) $\log_{10}(\text{Error})$ plot for FE plate. Varied number of a DoFs vs. fixed 30 b DoFs.

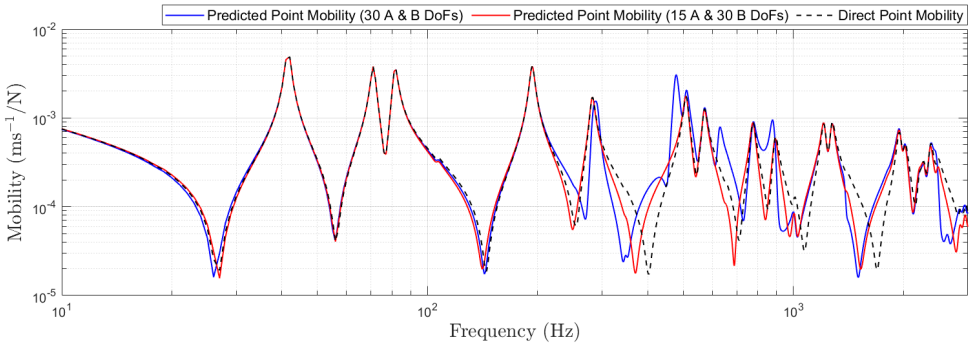

(b) Direct vs. predicted interface point mobilities. The round-trip mobilities are calculated using 30 a and b points, and 15 a and 30 b points.

Figure 3.6: Error of the reconstructed interface point mobility, with a comparison to the direct measurement.

Fig.3.6a represents the $\log_{10}(\text{Error})$ against frequency and the number of a DoFs being used in the RT prediction. In order to plot this figure, a fixed number of b DoFs had to be chosen. For this case, 30 b DoFs were selected. In a similar fashion to Fig.3.5, a spike in error occurs when there are the exact same number of remote DoFs (a's and

b's) being used in the RT prediction. Fig.3.6a shows a blue line representing the error of the reconstructed point mobility when 30 b DoFs and 30 a DoFs are used in the RT identity. Upon further inspection of Fig.3.6a, one will notice a considerable decline in error after 10 a DoFs between 10-40Hz. Furthermore, Fig.3.6b shows a difference emerging between the direct and RT point mobility predictions as frequency increases. In particular, the RT point mobility using the same number of a's and b's is the worst case out of the two predictions. This is reflected in the spikes that can be seen for the blue line in Fig.3.6a.

Accuracy due to plate geometry

The next point of the investigation is to test whether the aspect ratio of the plate has an effect on the error of the round-trip method. Fig.3.7 shows a 3:1 aspect ratio plate. It is the original plate taken from Fig.3.2 (4:3 ratio) but the length has been extended to achieve this aspect ratio.

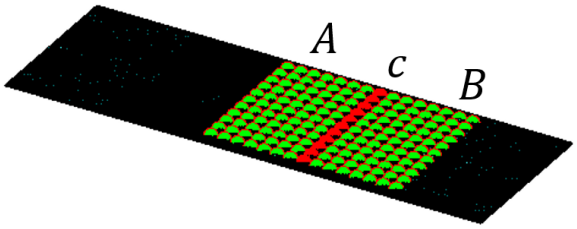

Figure 3.7: FE diagram of 3:1 aspect ratio steel plate, divided into sub-domains A and B which are discretised into a regular grid. Sub-domains A and B are divided by the interface c.

The grid is discretised the exact same to the previous plate, however it has been shifted so that the interface is off centre from the middle of the plate. Fig.3.2's interface cuts across exactly in the middle of the plate. The grid is implemented in this way to observe whether a reduction in error occurs due to symmetry by the interface.

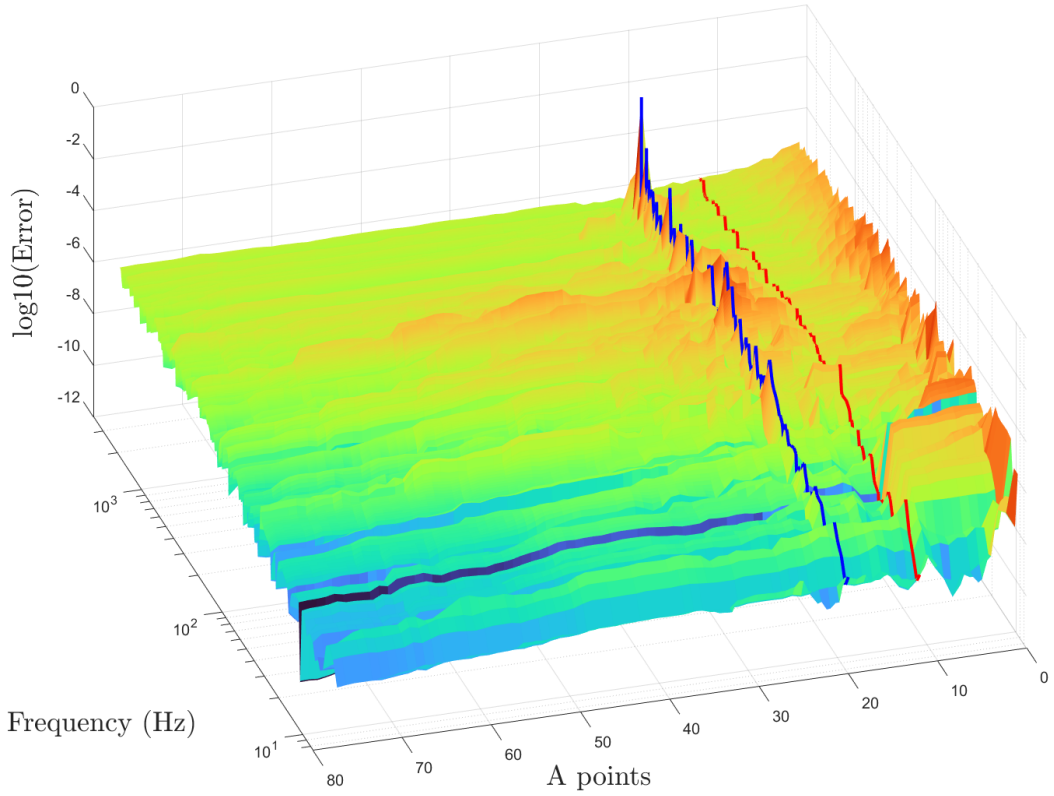

(a) $\log_{10}(\text{Error})$ plot for 3:1 ratio FE plate.Varied number of a DoFs vs. fixed 20 b DoFs.

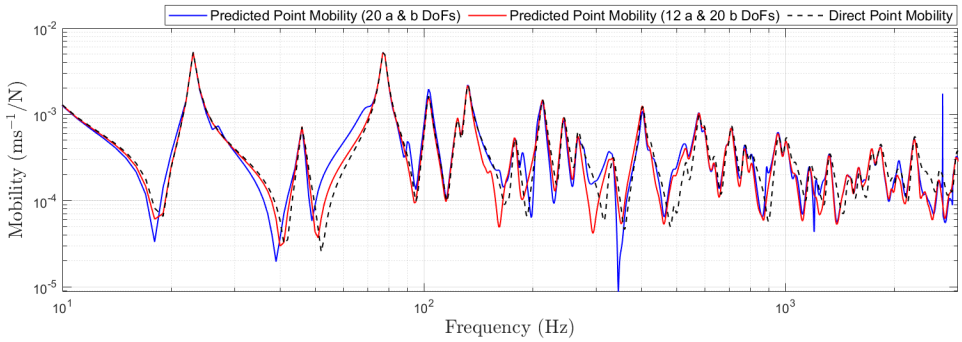

(b) Direct vs. two round-trip derived interface point mobilities. The round-trip mobilities are calculated using 20 a and b points, and 12 a and 20 b. points.

Figure 3.8: Error of the reconstructed interface point mobility for 3:1 ratio plate, with a comparison to the direct measurement.

Fig.3.8a shows a similar overall trend to Fig.3.6a where a spike in error occurs when $a = b$. This figure also suggests that symmetry has no noticeable effect.

Accuracy due to remote DoF positioning

To investigate the accuracy of the round-trip method due to the positioning of remote sensors, the Monte-Carlo method is applied. The round-trip prediction is calculated for 50 iterations of the randomly positioned DoFs within A and B. One of the randomly selected DoF iterations is shown in Fig.3.9.

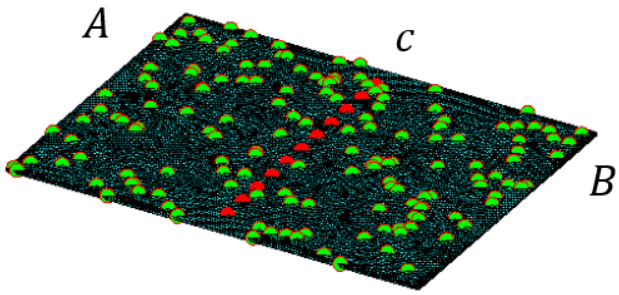

Figure 3.9: Diagram of original 4:3 aspect ratio plate with randomly selected remote positions. Diagram represents one iteration of one hundred.

The number of DoFs of interest was kept consistent with the same number used in the regular grid in Fig.3.2a. 77 points each on the remote sides, and the 11 interface points in the same location. Fig.3.10 shows the top subplot of every round-trip interface point mobility conducted in the Monte-Carlo loop, and a below sub-figure showing the direct point mobility against the upper and lower bounds of the operation.

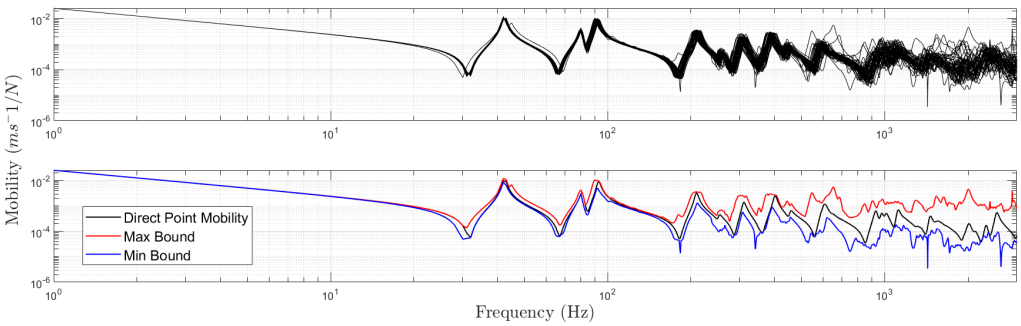

Figure 3.10: Top sub-figure shows every interface point mobility with each iteration, bottom sub-figure shows the direct point mobility plotted against the upper and lower bounds of the prediction.

When viewing the error bounds one can see occasional spikes in low frequencies from the direct interface point mobility shown in black. If compared to the top sub-figure it is obvious that these spikes are due to two anomalous iterations.

3.1.2 Experimental model example

The following diagram in Fig.3.11 shows a 2D top-down view of the experimental plate used for analysing the RT point mobility prediction. The results that follow are due to the defined remote and interface structures in the diagram. The remote accelerometer positions in A and B are marked in green, while the interface accelerometers are in red. The plate is made of aluminium, with 3 vinyl strips stuck to the accelerometer side for damping (marked light blue). The experiment was set up to simulate free-free conditions by supporting the plate on foam pads. This means the plate is analysed in an unconstrained state (identically to the FE model), allowing it to move freely in all six DoFs (three translational and three rotational). The dimensions are 0.7m $\times$ 0.9m $\times$ 0.0025m.

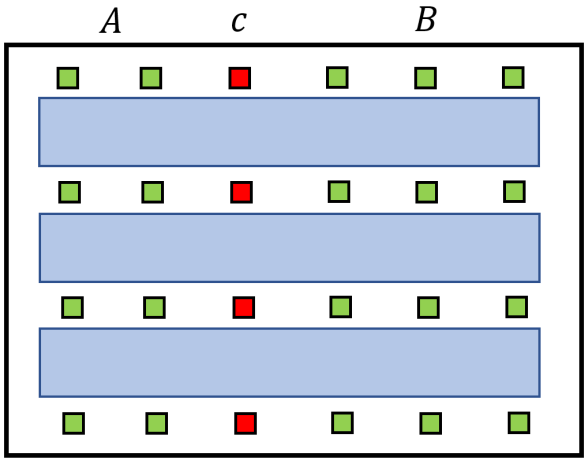

Figure 3.11: Top-view 2D diagram of experimental plate, accelerometers discretised in a regular grid.

An analysis of the interface point mobility prediction is made by observing the $\log_{10}(\text{Error})$, plotted against A DoFs and frequency with a fixed number of 5 randomly selected B

DoFs. Two predictions are calculated for comparison against the directly measured interface point mobility shown in Fig.3.12b. One prediction utilises 5 a and b DoFs marked in blue, and the other 3 a and 5 b DoFs marked in red.

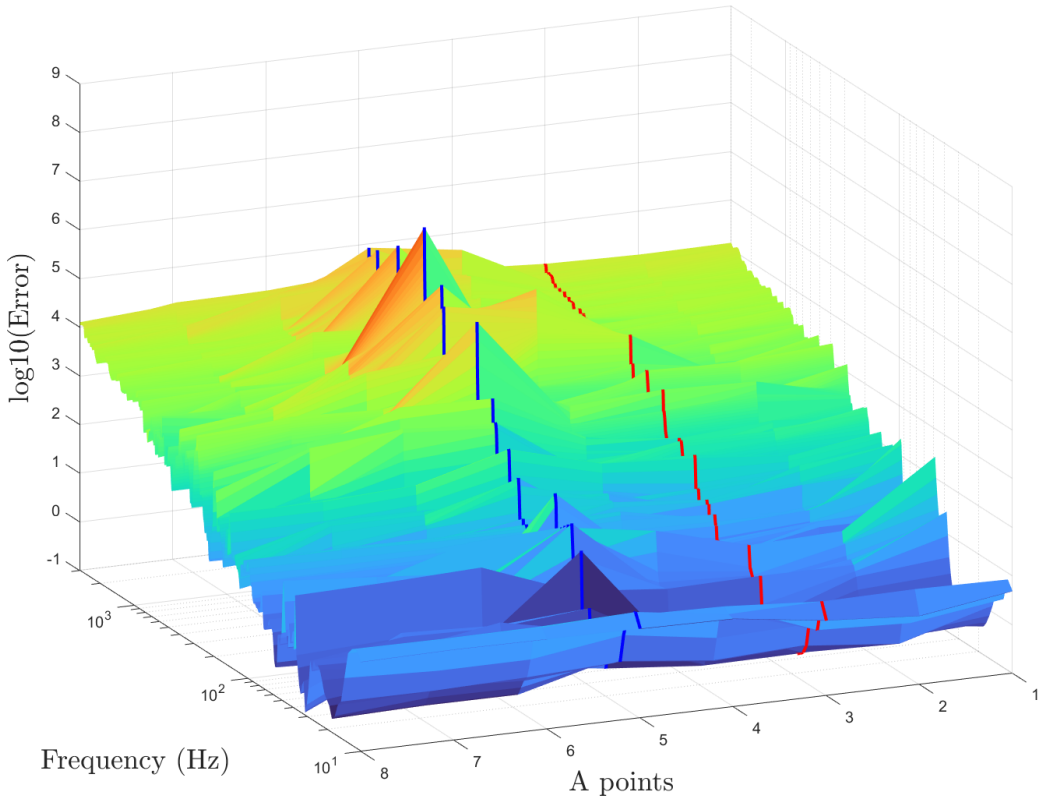

(a) $\log_{10}(\text{Error})$ plot for experimental plate. Varied number of a DoFs vs. fixed 5 b DoFs

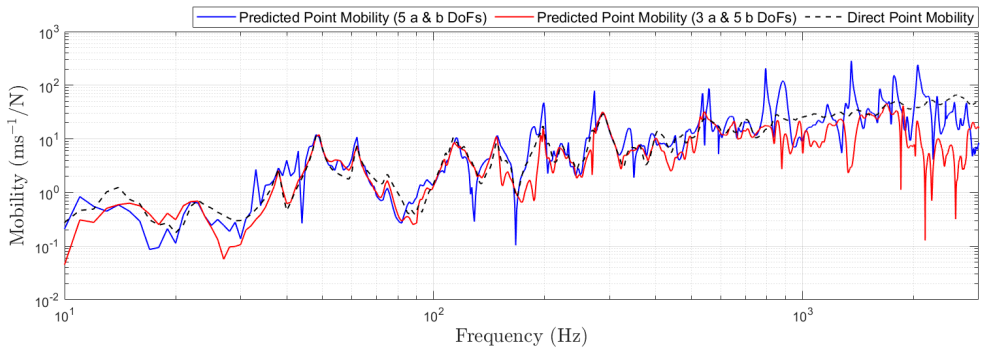

(b) Direct vs. Round-trip derived interface point mobilities. The mobilities are calculated using 5 a and b points, and 3 a and 5 b points.

Figure 3.12: Error of the reconstructed interface point mobility for an experimental plate. A comparison to the direct measurement is made for two cases of the round-trip prediction.

Between 20Hz - 2kHz the experimental case conveys a reasonable prediction in both

cases (5 a's & b's, and 3 a's & 5 b's) when compared against the direct measurement, as shown in the above figure. The overall error across the frequency range is clearly higher than the FE model case, with the smallest error being $\log_{10}(-0.93)$ at 30Hz. As frequency increases, it is clear that both predictions begin to stray away from the direct measurement (from around 1kHz and upwards), which is likely attributed to the rotational components at the interface DoFs c not being accounted for (as shown by Meggitt and McGee [2024]). In summary, it is clear that the spike in error that occurs when $a = b$ is also apparent in the experimental case study.

3.2 Transfer mobility

The same FRF matrix obtained from the FE model for the reconstructed point mobility is used in analysing the reconstructed transfer mobility. In this section the accuracy of the RT transfer mobility is analysed due the location of a and b subsets in the regular grid as shown by Fig.3.2a, as well as the application of noise and the geometry of the plate.

3.2.1 FE-model example

Accuracy due to the location of remote DoFs

In this section the reconstructed transfer mobility $\mathbf{Y}_{C_{ab}}$ is calculated via Eq.3.9 and compared against the directly measured transfer mobility. In fact, four different transfer mobilities are calculated via the round-trip equation that have different combinations of remote points being observed which are shown in Fig.3.13. The goal of this part of the study is to observe if there is a change in accuracy depending on which remote points are used in the reconstructed transfer mobility. It is expected there are worse case than others, but by picking four distinctly different mobilities it is possible to achieve a general overview of its performance against their directly measured counterparts.

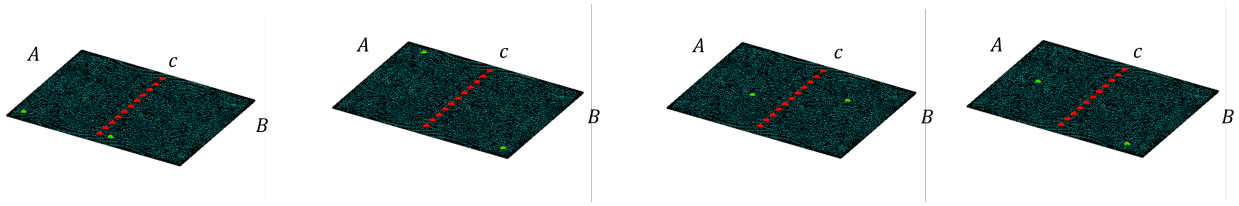

(a) $\mathbf{Y}_{C_{a_1,b_1}}$ (b) $\mathbf{Y}_{C_{a_{22},b_{67}}}$ (c) $\mathbf{Y}_{C_{a_{49},b_{41}}}$ (d) $\mathbf{Y}_{C_{a_{28},b_{56}}}$

Figure 3.13: Diagrams of the indices used on the FE steel plate for calculating the reconstructed transfer mobility.

Fig.3.13a was chosen to observe a transfer mobility that is between two points that are on the same side as each other. Furthermore, Fig.3.13b is selected to observe what the round-trip yields for two points almost opposite from each other, Fig.3.13c are for two points that are more central, and finally Fig.3.13d where one point is central and the other is near an edge.

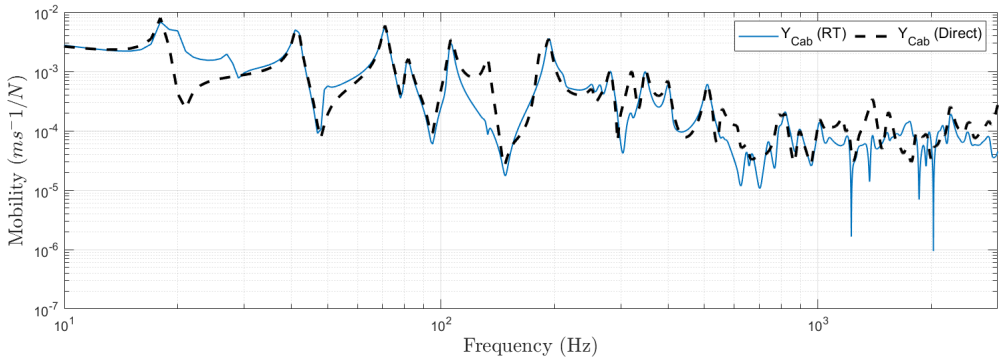

Figure 3.14: RT vs. direct $\mathbf{Y}_{C_{a_1,b_1}}$.

Fig.3.14 shows the reconstructed transfer mobility between the first a and first b DoF against a direct measurement. It is clear that the round-trip approximation is accurate for the vast majority of the frequency range, with some exceptions between 1-2kHz and at some distinct resonances such as 132Hz, 320Hz, and 560Hz. In addition there is an anti-resonance at 22Hz which is not true to the direct mobility.

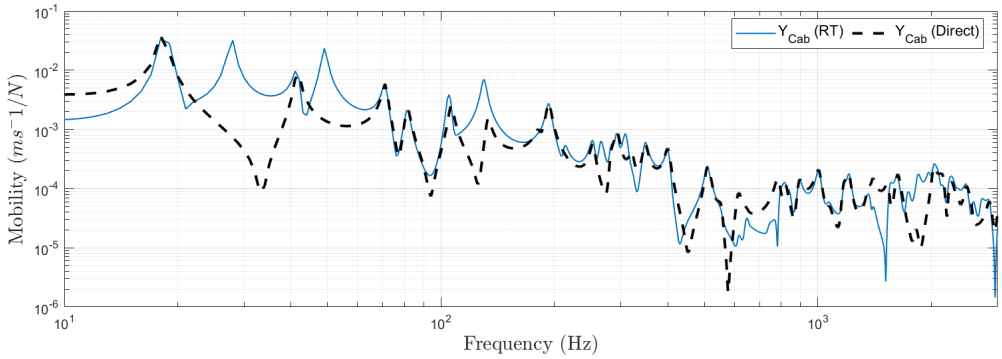

Figure 3.15: RT vs. direct $\mathbf{Y}_{C_{a_{22},b_{67}}}$.

A similar trend can be seen in Fig.3.15 where the round-trip prediction is quite accurate for most of the frequency range. The areas where the prediction loses precision to the measured result differ from Fig.3.14, which is expected as the DoFs used in A and B are quite different in location. This is due to certain resonances not being accurately captured if the excitation is not applied at the critical locations associated with their modes. There are two frequencies where $\mathbf{Y}_{C_{a_{22},b_{67}}}$ shows a resonance that is not present in the direct measurement at 28Hz and 49Hz. Furthermore there are resonances where the reconstructed transfer mobility loses accuracy such as 615Hz, 780Hz, and 1.4kHz.

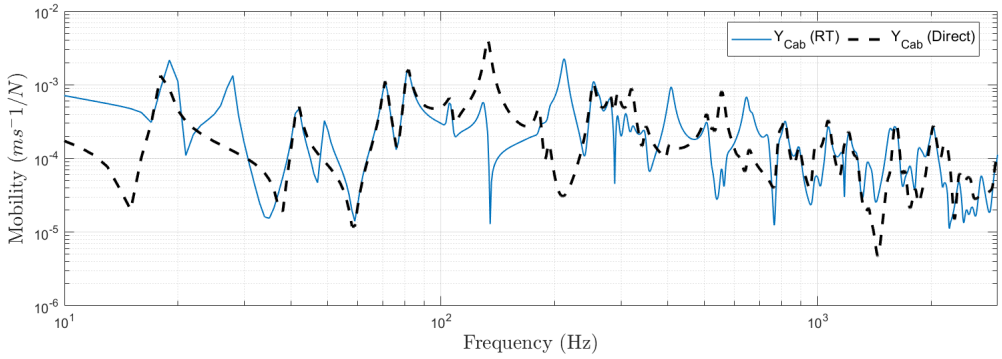

Figure 3.16: RT vs. direct $\mathbf{Y}_{C_{a_{49},b_{41}}}$.

The reconstructed result in Fig.3.16 shows itself to be the least accurate prediction thus far. There are parts of the frequency range which have good accuracy such as between 40-105Hz and 780Hz-1.3kHz. In addition there are resonances that agree well such as at 250Hz, 280Hz, 505Hz, 1.6kHz, and 2kHz. The inaccuracies present

can be observed in a few areas: between 10-17Hz there is a large difference while also the resonance at 18Hz in the direct measurement being shifted slightly and increased in magnitude, there are resonances present in the prediction but are not in the direct measurement at 28Hz, 50Hz, 210Hz, and 2.7kHz. In addition, There are resonances where the magnitude is poorly predicted at 130Hz, between 290-350Hz, 405Hz, 560Hz, 650Hz, 1kHz, and 1.3kHz. This particular case of where the excitation and response DoFs are more centred on the plate has so far yielded the least accurate round-trip prediction.

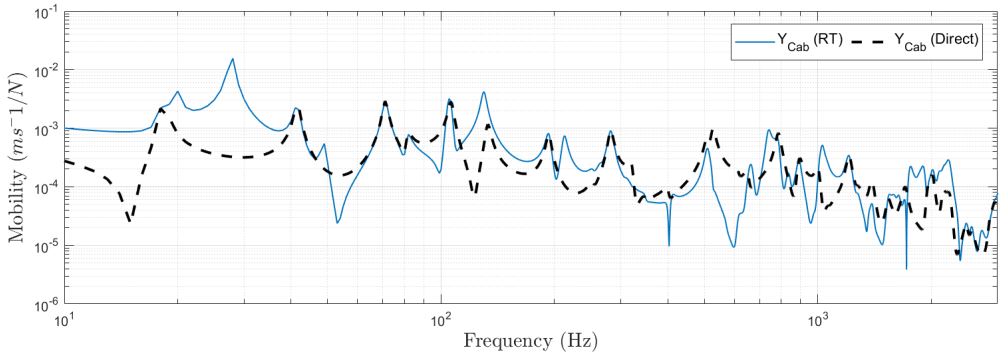

Figure 3.17: RT vs. direct $\mathbf{Y}_{C_{a_{28},b_{56}}}$

In the final result where the mobility is due to an excitation near the edge of the plate and a response more central in Fig.3.17 yields a slightly more accurate prediction than Fig.3.16 at resonances, but similar in the amount of inaccuracies present. The resonances which are represented accurately in the prediction can be seen at 40Hz, 70Hz, 82Hz, 105Hz, 193Hz, 280Hz, 780Hz, 900Hz, 1.2kHz, and 2.5kHz. The resonances which are poorly predicted exist at 18Hz, 135Hz, 320Hz, 650Hz, 1kHz, 1.4kHz, 1.5kHz, 1.7kHz, and 2.16kHz. In addition there are resonances present in the prediction that are not seen in the direct measurement at 28Hz, 49Hz, 210Hz, 1.76kHz, 1.9kHz, and 2.7kHz. The similarity between this plot and Fig.3.16 is the inaccurate prediction of resonances that present in both direct measurements at 650Hz and 1kHz. So far these plots have shown that the least accurate transfer mobility predictions have occurred when the response DoF has been more central.

Taking only 4 cases of the round-trip prediction can give a rough overview of the per-

formance of the transfer mobility round-trip prediction but is not enough to conclude its accuracy in detail. Thus for the remainder of this section an error analysis on the DoF positioning is conducted. Firstly let's analyse a particular resonant frequency that isn't accurately represented by the round-trip prediction. For example this is the case at 320Hz for Fig.3.14 and Fig.3.16.

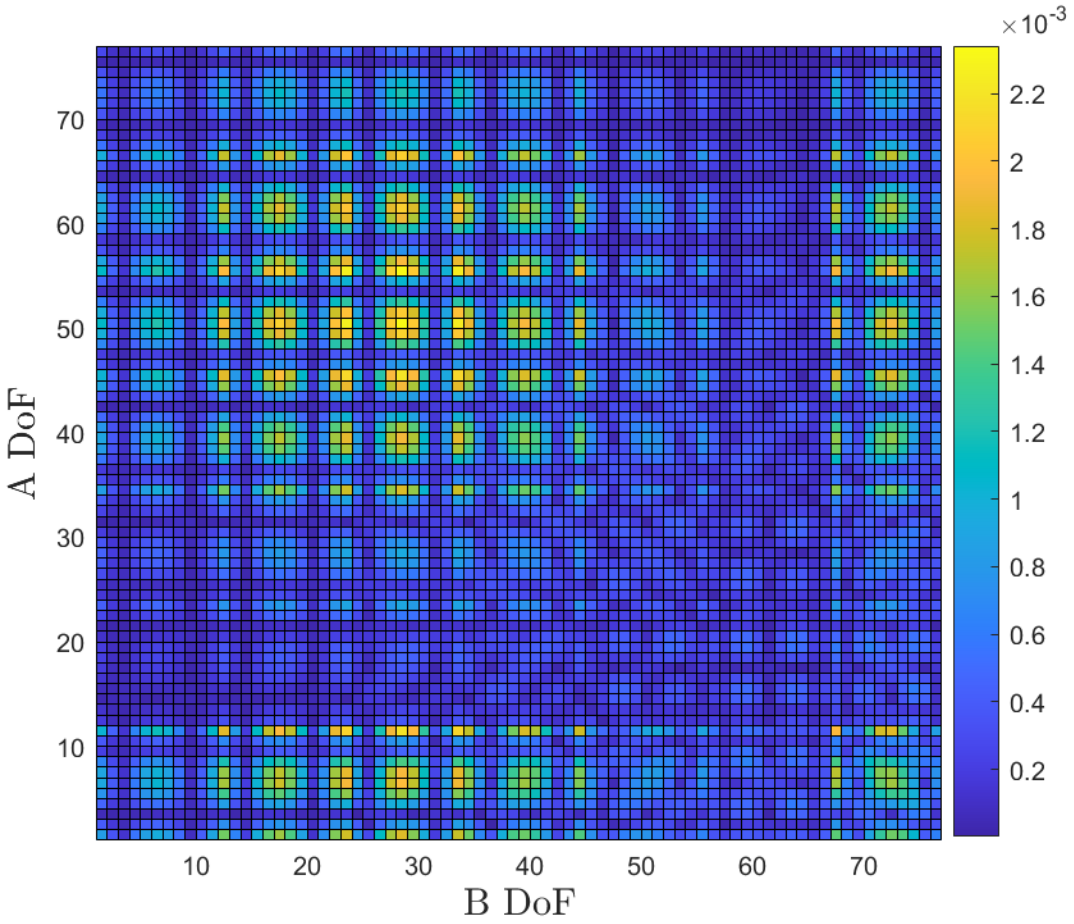

Figure 3.18: Error at 320Hz, B excitation DoF vs A response DoF.

The plot in Fig.3.18 represents the error of the round-trip prediction, with the response DoF index in A on the y-axis vs the excitation DoF index in B on the x-axis. Take the round-trip prediction in Fig.3.14 where the first A and B DoFs are used, one can see an increased error when compared to the darker blue error values surrounding it, which is at a value of around 1×10^{-3}. While not the largest error that exists on the plot it is about middle of the park, and suggests there is an increased error using the response of the 1st A DoF which is in the corner of the plate. In order to achieve a

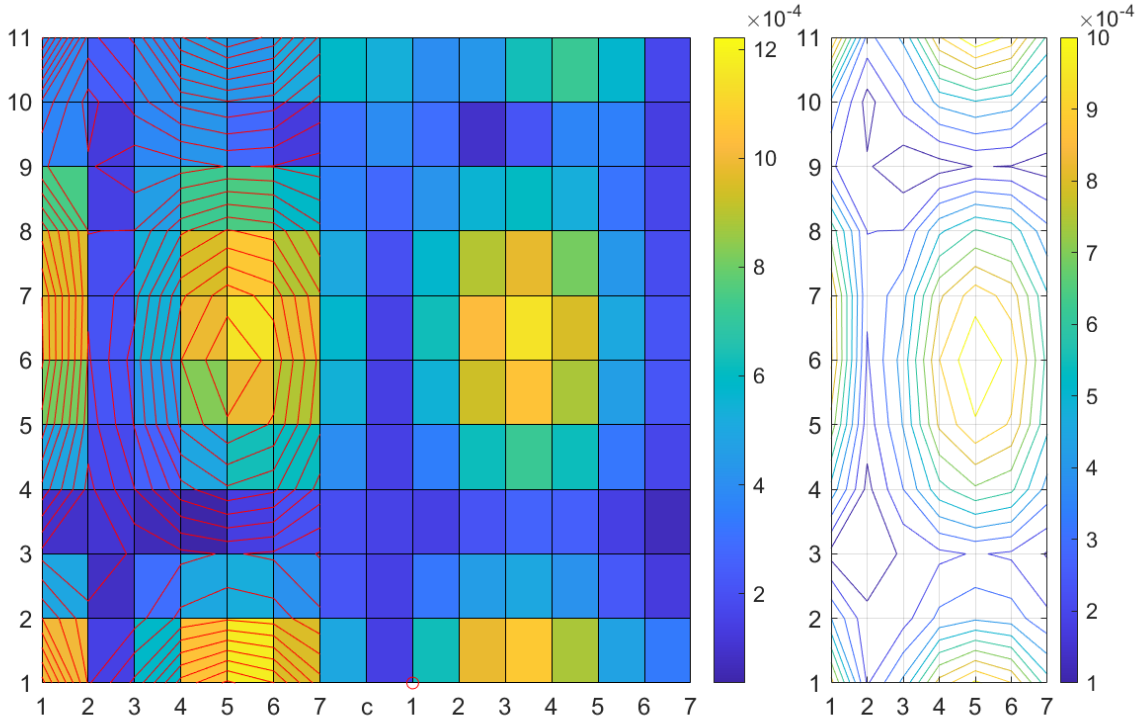

Figure 3.19: Amplitude of plate at mode corresponding to 320Hz vs. error, due to excitation at b_1

greater understanding of the dynamics of the plate and its relation to error, Fig.3.19 is made to observe any correlations with the maxima/minima of the mode in relation to 320Hz.

This figure is made up of two sub-figures where the larger one of the left represents a top down view of the plate. Along the x-axis the column number of DoFs are related to each sub-structure, i.e. the first 1-7 columns represent the first 7 columns in A, then followed by the interface column c, which is then followed by the next 7 columns of DoFs in B. Along the y-axis denotes which row of DoFs in the grid, labelled 1-11. At each intersection of a row and column lies a DoF. In between each DoF a rectangle is formed with a colour which denotes the amplitude of that part of the plate for a given mode. The contour lines on the left hand sub figure show the error of across A, but sadly the figure editing did not allow for the colour map to be imposed on this sub figure, so it is repeated in the right hand sub figure to show the error. The circle marker in red on the left hand sub figure shows the location of the excitation DoF. As

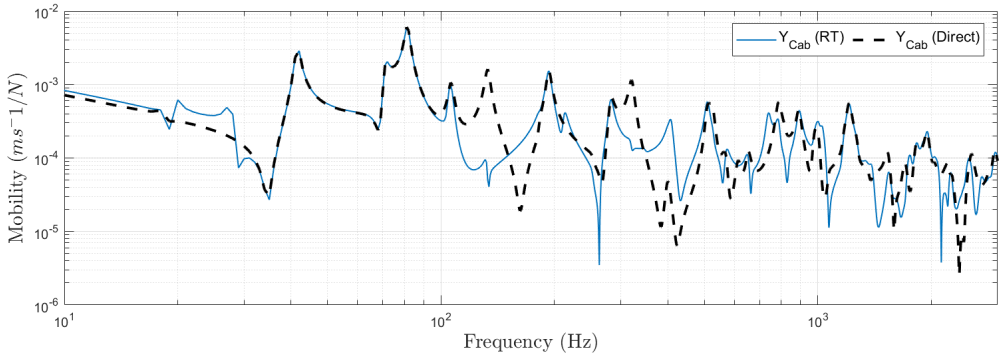

Figure 3.20: RT vs. direct $\mathbf{Y}_{C_{a_{50},b_1}}$.

we are looking at the mobility $\mathbf{Y}_{C_{a_1,b_1}}$, one can see on Fig.3.19 that the red circle is on the first DoF in B. This mobility's response DoF location is the first in A, where one can tell that the amplitude is relatively high. When comparing this to the right hand sub figure, the colour map of the contour lines show an increased error of around 1×10^{-3}, which is the same as shown previously by Fig.3.18. So far these results show there is a correlation between the increased amplitude of a mode corresponding to 320Hz occurring at response DoF a_1. Then this DoF is used in determining the mobility $\mathbf{Y}_{C_{a_1,b_1}}$ its error is increased.

On the 6th row and 5th column (DoF no. 50 in A) one can also see an area of increased amplitude on the left hand sub figure, while also on the right hand sub figure the contour lines show an increased error. To check that this correlation is still true, a comparison of the direct and round-trip prediction is conducted as shown in Fig.3.20. While this round-trip prediction stays true to the direct measurement rather well, it can be seen at 320Hz there is a large difference between the two. In addition, a look back at Fig.3.18 also shows that at the 1st B DoF and the 50th A DoF there is a relatively increased error.

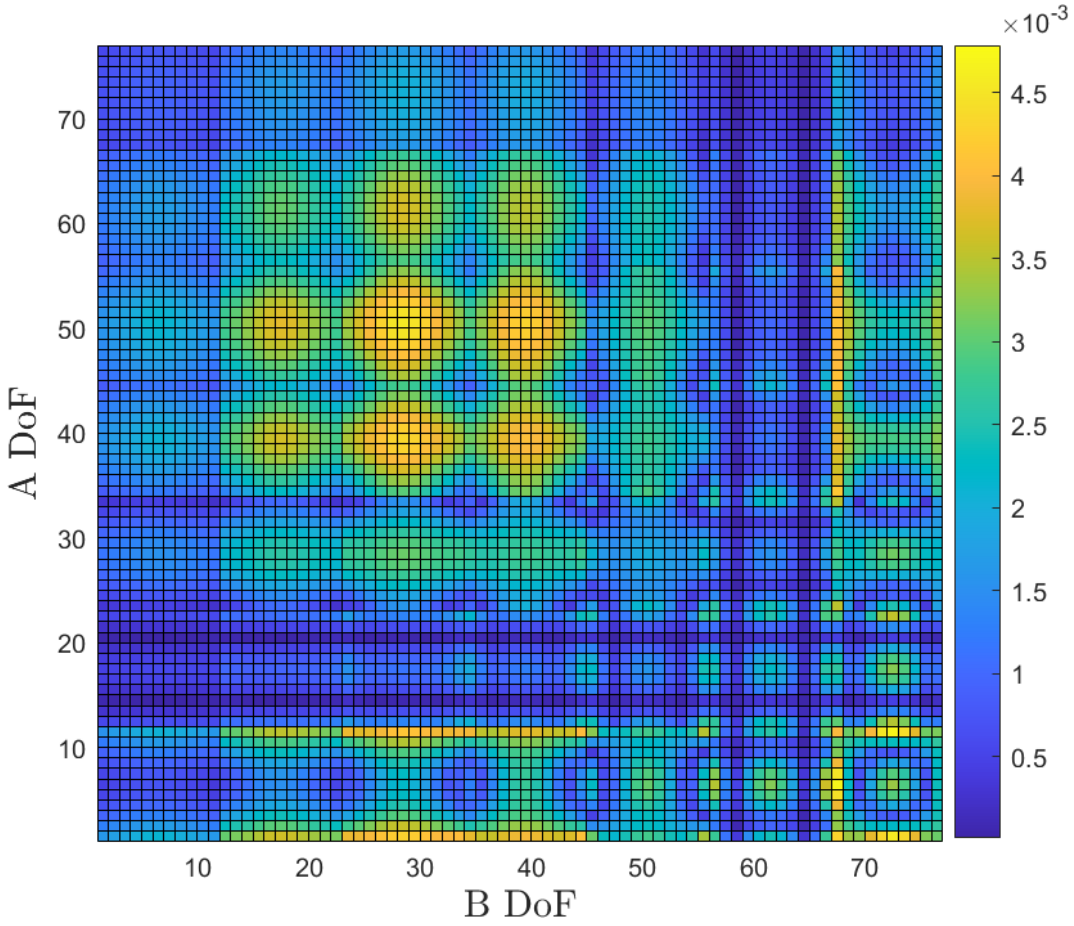

Figure 3.21: Error at 135Hz, B excitation DoF vs A response DoF.

One more resonant frequency is chosen to check this is true at other resonant frequencies apart from 320Hz. For example, let's take a look at Fig.3.17 where there are differences at resonances approximately 135Hz and 2.2kHz. Taking a plot of A vs B DoFs in Fig.3.21 one can see at 135Hz there is a relatively increased error for the round-trip mobility between the 28th A and 56th B, with a value of approximately 2×10^{-3}. Inspecting this plot further shows there are areas of the plate with increased error, such as at A DoF 40 and B DoF 40 marked in yellow with an approximate value of 4×10^{-3}.

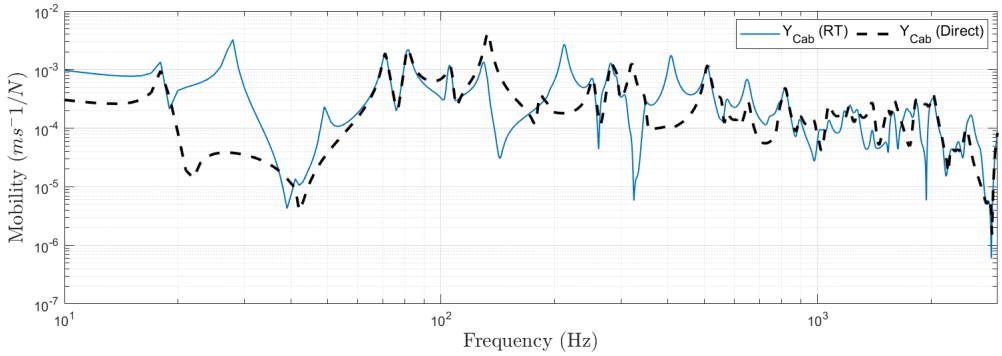

Figure 3.22: RT vs direct $Y_{C_{a_{40}b_{40}}}$

Fig.3.22 shows that at 135Hz the difference between the prediction and direct measurement is rather large. By taking a plot of error against the amplitude of the plate, we may now check if this correlates to a larger amplitude at the mode corresponding to the 135Hz resonance.

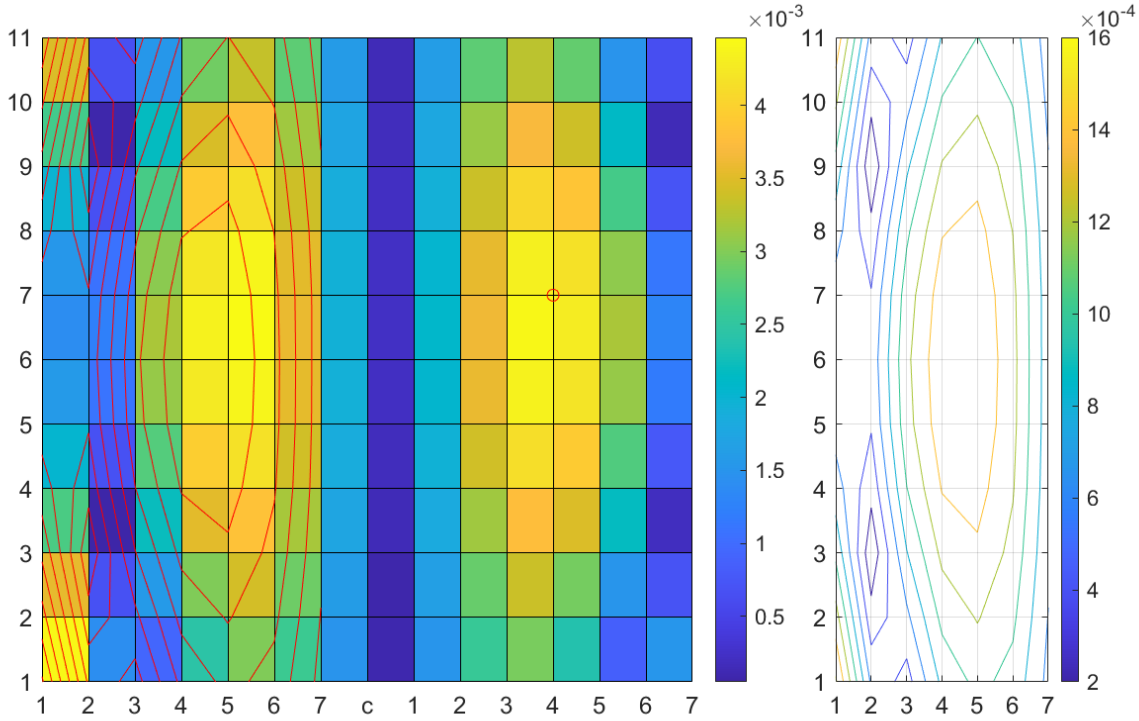

Figure 3.23: Amplitude of plate for mode corresponding to 135Hz vs. error, due to excitation at b_{40}

There is a maximum value in amplitude at a_{40} in Fig.3.23 of around 4×10^{-3}, corresponding to a maximum error value of about 15×10^{-4}. Therefore it can be said when

predicting $\mathbf{Y}_{C_{a_{40},b_{40}}}$, an increased maximum amplitude correlates with maximum error to a resonance or mode at 135Hz.

Accuracy due to the location of interface DoFs

In this section, the reconstructed transfer mobility is analysed when the interface DoFs c is randomly distributed along the centre line. Using the Monte-Carlo method, the reconstructed transfer mobility is calculated 50 times, where each iteration has different randomised locations of c. Remote subsets a and b have been kept in the regular grid form. The goal of this is to examine the accuracy of the RT prediction when the interface DoFs are not evenly distributed.

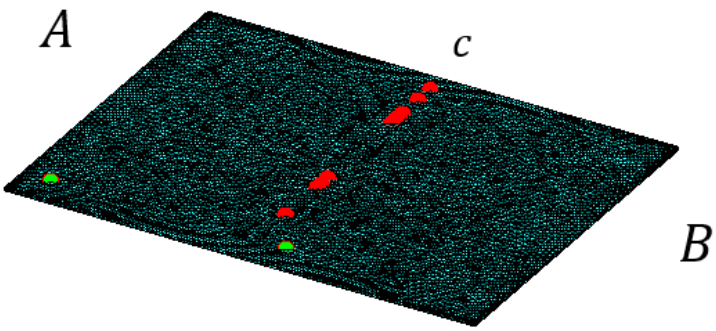

Figure 3.24: Random distribution of interface c DoFs for one iteration of the $\mathbf{Y}_{C_{a_1,b_1}}$ prediction Monte-Carlo loop.

In the above figure is an example of how the c DoFs are randomly distributed in one of the fifty iterations within the Monte-Carlo loop to calculate $\mathbf{Y}_{C_{a_1,b_1}}$.

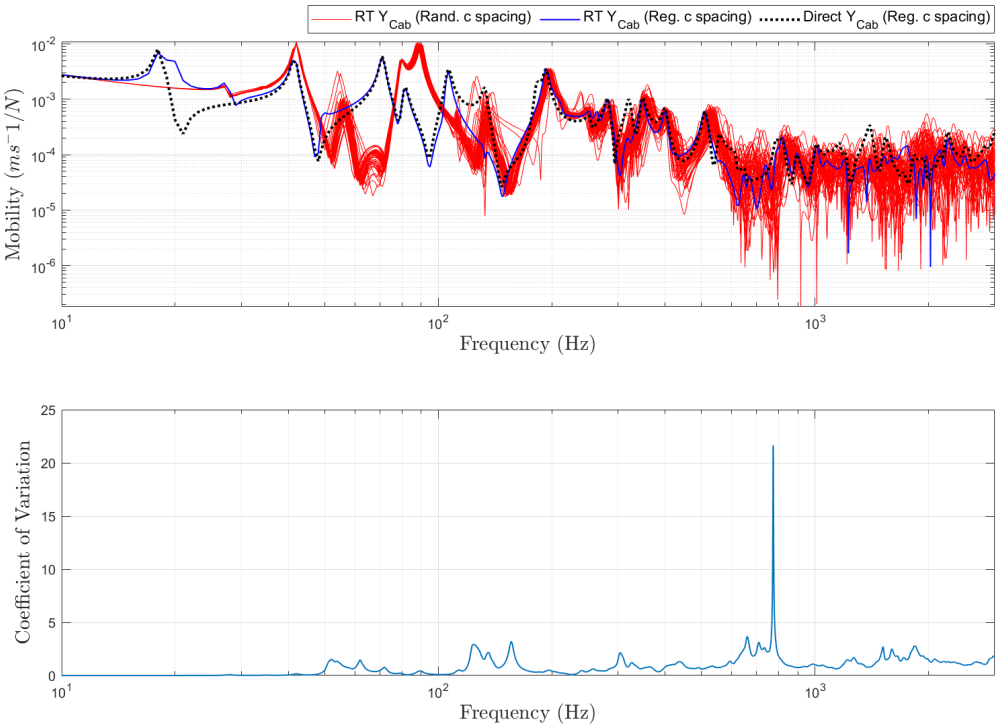

Figure 3.25: Top sub-figure: every iteration of $\mathbf{Y}_{C_{a_1,b_1}}$ prediction when distribution of c DoFs is randomised (red), vs. prediction with regular c DoF spacing and a direct measurement. Bottom sub-figure: Coefficient of variation for $\mathbf{Y}_{C_{a_1,b_1}}$ prediction when c DoF positions are randomised.

In Fig.3.25 all 50 iterations of the Monte-Carlo loop are plotted in the top sub-figure, alongside direct and round-trip $\mathbf{Y}_{C_{a_1,b_1}}$ when the c DoFs are regularly spaced. In the bottom sub-figure the coefficient of variation is calculated for all 50 iterations of the RT prediction when c is randomly spaced. When c is randomly distributed, some differences to the direct and the regularly spaced RT prediction are apparent between 50-130Hz. This is understandable as the low frequency performance is affected most when there is insufficient blocking. As you can see in Fig.3.24, there can be large gaps between c DoFs which means there is not sufficient blocking for parts along the centre line. Furthermore, the coefficient of variation is almost zero for most of the low frequencies. This suggests that despite not being accurate in this region, there is a consistent lack of blocking in parts along the centre line. From 130-510Hz the 50 iterations follow the direct and RT prediction with regular c spacing quite closely. In this region the coefficient of variation is most of the time below 1, with a couple exceptions at 130Hz and

156Hz rising to 3.2 and 0.85 respectively. Above this range the coefficient increases slowly until a sharp spike at 780Hz with a value of 21.65. When comparing to the top sub-figure, this spike occurs at an anti-resonance. Above 780Hz, the coefficient is between 0.85 and 2.50. This suggests there is variation between each $\mathbf{Y}_{C_{a_1,b_1}}$ iteration in the high frequencies, which is corroborated with the top sub-figure when comparing to the direct measurement.

Accuracy due to the number of the interface points included

In this section, the accuracy of $\mathbf{Y}_{C_{ab}}$ is observed as the amount of interface DoFs changes. In theory, less DoFs should make the prediction less accurate as the blocking constraints at the interface will be incomplete. This study takes the same mobility predictions shown in Fig.3.14, 3.15, 3.16, 3.17, but compares them against the same prediction where only 1 interface point is used in the round-trip equation (Eq.3.9). The reason for this is to observe how well the prediction is implemented in a 'worst case' scenario. As stated by Moorhouse et al. [2011], a difficulty in the round-trip prediction is "the need to account for all degrees of freedom at a rigid interface", and attributes this in particular to studies that tested coupled beams where in-plane shear forces and moments were neglected due to their difficulty in measurement, but were found to contribute significantly to the dynamics of the structure. In this FE-model example however, the applied forces are all perpendicular to the surface with the responses acting in the same z-axis. While moments will be present, they will be a much smaller contributor to the overall dynamics of the plate compared to the z-axis applied forces, thus they are neglected in this study. However if forces were applied in x-axis and y-axis planes, then there would be a need to characterise the interface in terms of moments. Choosing to neglect these moments will cause a small error in the prediction, while also in theory altering the $\mathbf{Y}_{C_{cc}}^{-1}$ term in Eq.3.9 should yield the largest source of error in the equation due to its inversion.

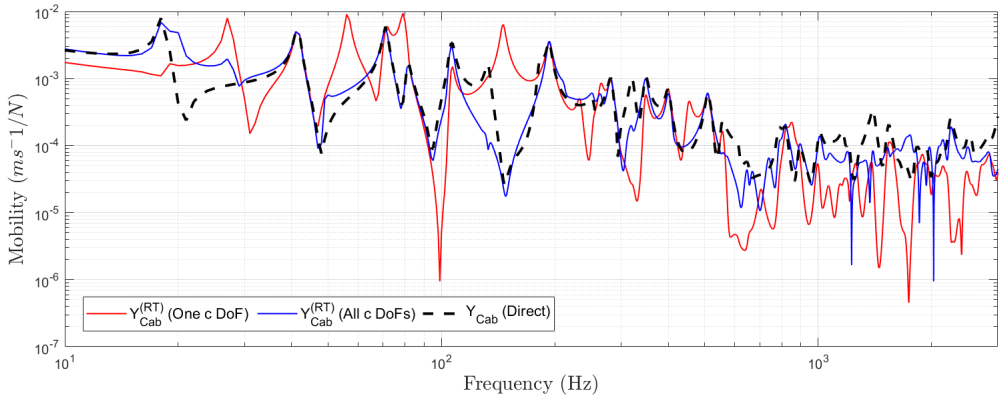

Figure 3.26: Performance of the transfer mobility prediction in the presence of 1 interface DoF vs. all interface DoFs vs. direct transfer mobility for $\mathbf{Y}_{C_{a_1,b_1}}$.

It is clear that Fig.3.26 shows the performance of the RT prediction is best when all interface DoFs are included. While it is true the all interface DoFs case lacks precision at certain points; for example between 1-2kHz and at some distinct resonances such as 132Hz, 320Hz, and 560Hz; the 1 interface DoF prediction is shown to have a lower accuracy throughout the majority of the frequency range. There are some exceptions where it performs well such as at the resonance at 42Hz and between 190-560Hz. While the all interface case starts to reduce in accuracy at points past 1kHz, the 1 interface DoF prediction starts to break down earlier around 560Hz and onwards.

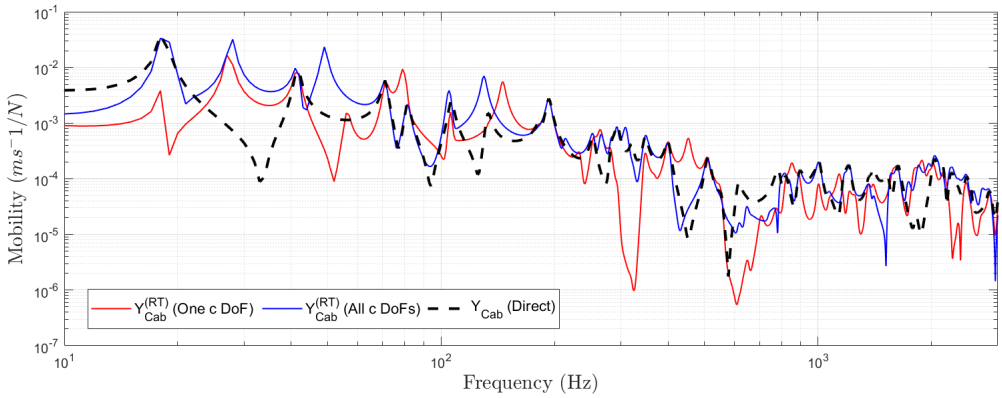

Figure 3.27: Performance of the transfer mobility prediction in the presence of 1 interface DoF vs. all interface DoFs vs. direct transfer mobility for $\mathbf{Y}_{C_{a_{22},b_{67}}}$.

For the prediction displayed in Fig.3.27, where only one c DoF is used, a worse result is visible overall. For example at resonances 18Hz, 80Hz, and 350Hz there is

a significant difference between prediction and direct measurement. Furthermore a large error can be seen at 280-350Hz where a large anti-resonance is present in the prediction but not in the direct measurement. Between approximately 580-810Hz both predictions have low accuracy, but the 1 c DoF case falls short even more so. Lastly for this result, between 810Hz-1.35kHz the All c DoF prediction performs reasonably well while the 1 c DoF case does not. However, the trend of a worse performance in the 1 c DoF prediction is not shown to be the same for the next mobility in Fig.3.28.

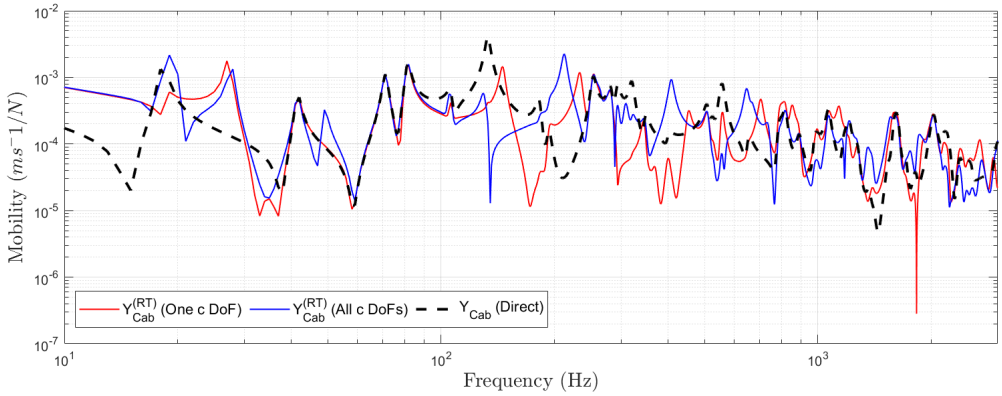

Figure 3.28: Performance of the transfer mobility prediction in the presence of 1 interface DoF vs. all interface DoFs vs. direct transfer mobility for $\mathbf{Y}_{C_{a_{49},b_{41}}}$.

In this result both predictions are quite similar to one another, and have errors in similar areas of the frequency range. For example, between 10-110Hz both predictions are nearly as accurate as each other. From 110-800Hz both lose accuracy, with the 1 c DoF case being slightly worse between 280-340Hz but on the other hand the all c DoF case is worse at 515-650Hz. Lastly, between 765Hz-2.3kHz both predictions are reasonably true to the direct measurement. Thus from this particular case where the prediction wasn't the best case scenario, both 1 c DoF and all c DoF cases performed similar to each other.

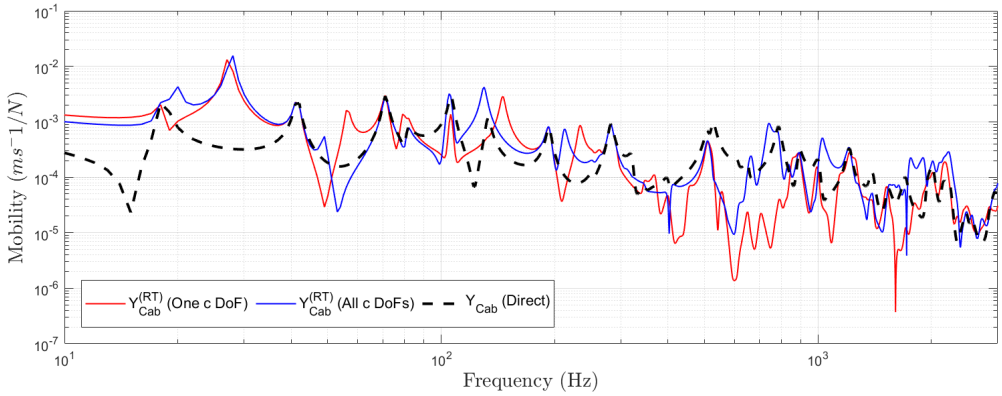

Figure 3.29: Performance of the transfer mobility prediction in the presence of 1 interface DoF vs. all interface DoFs vs. direct transfer mobility for $\mathbf{Y}_{C_{a_{28},b_{56}}}$.

For Fig.3.29 the predictions are similar to each other in certain parts of the frequency range, but there are parts where the one c DoF case performs worse. Overall the all c DoF prediction is closer to the direct measurement.

Accuracy due to noise

In this study varying amounts of noise is added to the FRF matrix obtained from the FE-model shown in Fig.3.2a. The MATLAB function *Specspoil* is used to contaminate data with random noise for varying signal-to-noise-ratio (SNR). Earlier in this chapter the function was described in terms of its inputs. We will now explain in greater detail how the function operates using those inputs. This study adds noise using the linear *Type* and therefore the explanation for the quadratic method is omitted. Firstly, we take the sum of the absolute values in the *Input* FRF matrix to obtain its total magnitude, and then scale it by the user's desired SNR level *L*. We then generate an array matching the size of *Input*, which has random amplitudes between 0-1 and phase between 0-2π. The noise matrix is normalised to match the power of the total magnitude of *Input* to ensure the desired SNR level is met, and then added to the original FRF and averaged over *N*. The purpose of this study is to simulate measurement noise that is regularly seen in an experimental test, and observing the performance of the round-trip prediction with varying noise in order to inform what may be seen in the FRF data in an experimental setting. A SNR of 45dB is chosen to the begin with (a good case

scenario) and reduced gradually by 5dB till an SNR of 30dB, which is near the limit of an acceptable amount of noise in an experimental setting.

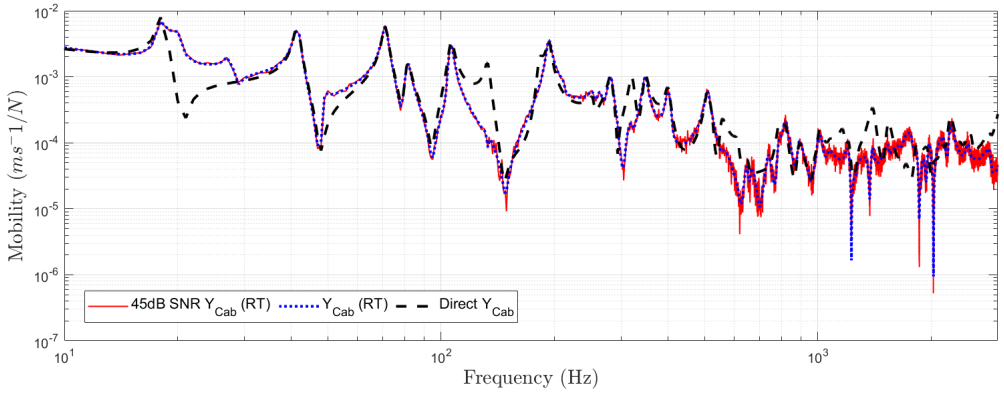

Figure 3.30: RT $\mathbf{Y}_{C_{a_1,b_1}}$ vs. RT $\mathbf{Y}_{C_{a_1,b_1}}$ with 45dB SNR vs. direct $\mathbf{Y}_{C_{a_1,b_1}}$.

A 45dB SNR applied to the FRF data shows the round-trip prediction performing very well for the frequency range observed as seen in Fig.3.30. It shows for $\mathbf{Y}_{C_{a_1,b_1}}$ that this level of SNR certainly yields an acceptable prediction.

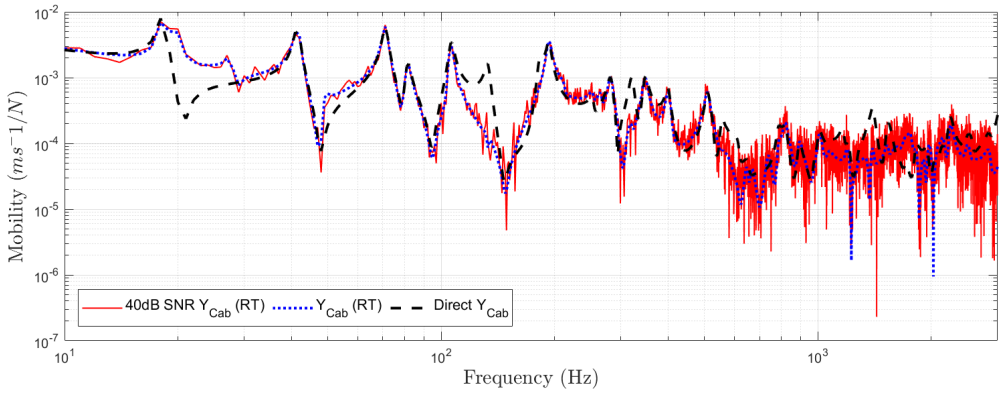

Figure 3.31: RT $\mathbf{Y}_{C_{a_1,b_1}}$ vs. RT $\mathbf{Y}_{C_{a_1,b_1}}$ with 40dB SNR vs. direct $\mathbf{Y}_{C_{a_1,b_1}}$.

Fig.3.31 shows the prediction's accuracy is similar to Fig.3.30 but starts to show an increased amount of noise after 1kHz. The overall shape of the mobility past this point does follow the trend of the direct measurement the caveat is that more artefacts are present. Much like the previous case the low frequency part of the range (roughly 10-550Hz) shows little or next to no noise. It is only approaching 1kHz that the noise starts to dominate and then gradually gets worse as the frequency increases past the

1kHz. If the SNR is reduced to 35dB the prediction proves to be even worse after 1kHz a shown in Fig.3.32.

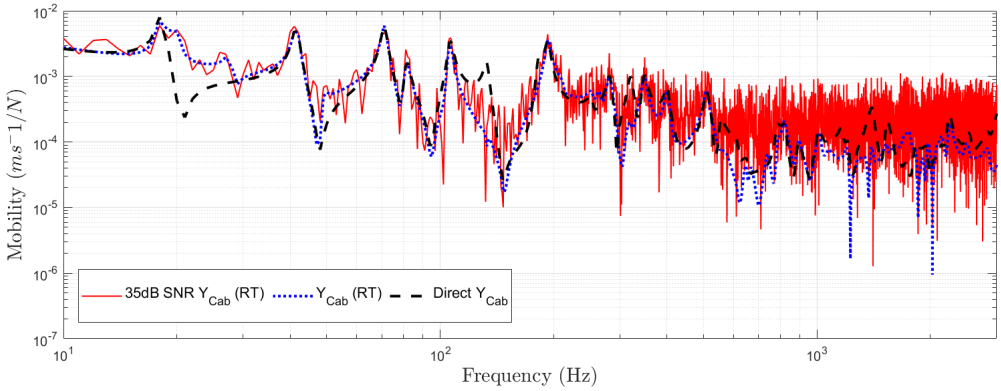

Figure 3.32: RT $\mathbf{Y}_{C_{a_1,b_1}}$ vs. RT $\mathbf{Y}_{C_{a_1,b_1}}$ with 35dB SNR vs. direct $\mathbf{Y}_{C_{a_1,b_1}}$.

Similarly to Fig.3.31, a 35dB SNR has shown to have a small amount of noise in lower frequencies but starts to become more prominent from 400Hz onwards. Essentially the point at which the noise becomes a dominating factor of the prediction has started earlier by around 150Hz. After the resonance at approximately 460Hz onwards the noise starts to make the prediction unintelligible. While it is present within the range of the direct measurement, it has become extremely difficult to discern any resonances or anti-resonances, making the prediction unusable in the higher end of the frequency range. This is also true for a SNR of 30dB as shown in Fig.3.33.

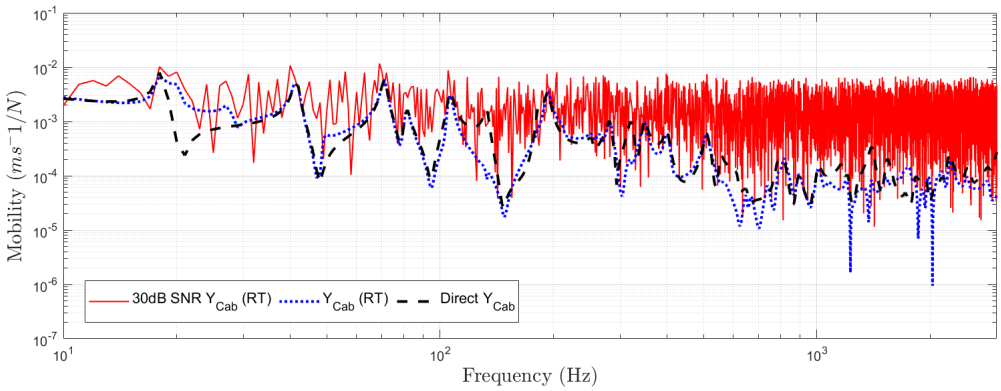

Figure 3.33: RT $\mathbf{Y}_{C_{a_1,b_1}}$ vs. RT $\mathbf{Y}_{C_{a_1,b_1}}$ with 30dB SNR vs. direct $\mathbf{Y}_{C_{a_1,b_1}}$.

In fact the prediction above the resonance at 460Hz performs much worse, and is not within the bounds of the direct measurement at all. The noise is extremely dominant,

to the point where it has caused the level of the mobility to be greatly increased by roughly one factor. On the other hand the prediction shows to be following the trend of the direct measurement quite well with an exception at the anti-resonance present at approximately 160Hz. It is only now that the noise is more visible in the very low frequencies (roughly 100Hz and below), which was not so in the previous cases.

3.3 Discussion

3.3.1 Point mobility Round-trip

Fig.3.5, 3.6a, 3.8a, and 3.12a show clear optimal conditions concerning the number of measurement DoFs. Fig.3.5 distinctly indicates a large spike in error for when $a = b$. Avoiding this situation achieves an accurate prediction. An optimal result is more obvious in Fig.3.6a, and Fig.3.8a. This plot shows that for the FE model example when using 30 b DoFs, the best result occurs when a was at it's maximum 77 DoFs as shown by the error decreasing at very low frequencies. However using this many DoFs is likely impractical for experiments and only achieves a small increase in the accuracy of the prediction. As shown by the red lines in figures 3.6a, 3.8a and 3.12a, the most practical round-trip prediction lies below the large error spike. In other words having less DoFs in one of the remote sub-domains. The most optimal prediction in these examples occurred when $a = b/2$ or $b = a/2$.

The source of error for when $a = b$ is likely due to two reasons. A common theme that will occur through this body of work is when a square matrix is inverted, the error increases on the output. This occurs when the matrix being inverted is ill-conditioned, or in other words it is close to being singular (non-invertible). When a matrix like this is inverted, small errors on the input are amplified significantly. Another possible explanation could be down to 'controllability' and 'observability' of the round-trip method as described by Wienen et al. [2021]. Controllability essentially describes whether enough excitations have been applied to replicate excitations elsewhere in the system

while observability describes whether enough sensors and enough positions are sufficient for explaining excitations. In the paper it is said in order to gain full controllability and observability the round-trip must satisfy the condition of $n_a \geq n_b \geq n_c$ for Eq.3.7. For the case of the transposed equation Eq.3.8 it must satisfy $n_b \geq n_a \geq n_c$.

In the FE model investigation it was found that altering the aspect ratio of the plate had no noticeable effect on the results. The surf error plots for both plate geometries conveyed a similar trend in error.

It was found that the error plot of the experimental case had no decrease in the low frequency region when the number of a DoFs was increased, as seen in the FE model example. The reasoning for this is likely due to the resolution of DoFs in A on the experimental example. The FE model has many more remote positions spread across the plate, and therefore able to account for more modes on the structure more accurately.

Both finite-element and experimental examples show good agreement with each other when observing the error plots in Fig. 3.6a, 3.8a, and 3.12a. The same large spike in error occurs in all of these cases for when $a = b$. When observing their counterpart mobility plots in Fig.3.6b and 3.8b their optimal results shown in red agree with each other for when the remote side has around half as many DoFs as the other. In Fig.3.12a the red line shows a better result than the blue line where the spike occurs, but when observing Fig.3.12b there does not seem to be as significant difference to the worst case scenario marked in blue when compared to the FE model examples Fig.3.6b and 3.8b. Further investigation is needed experimentally by using more remote DoFs, as this could be the large error observed for low amounts of remote DoFs as seen in Fig.3.5.

In summary:

- The FE examples show that if more remote (a and b) points are included the more accurate the prediction of the interface point mobility. However it is only valid if an unequal number of remote points are used, otherwise a large error will occur

in the prediction.

- The interface point mobility prediction was thought by Moorhouse and Elliott [2013] to be sensitive to the number of interface DoFs included, however this study suggests otherwise as demonstrated by Fig.3.3a, 3.3b,3.3c.
- The experimental example shows agreement with the FE model. A spike in error is observed experimentally for when $a = b$. However, a further experimental test is needed with more remote DoFs to improve the resolution. The large spacing between DoFs on the experimental model means certain modes are not picked up, and the modes that are picked up may be at a node.

3.3.2 Transfer mobility Round-trip

The reconstructed transfer mobility was firstly predicted by choosing 4 distinct pairs of remote DoF locations, as shown by Fig.3.13. These pair of DoFs were chosen in the following scenarios: central in one sub-structure and near to the interface in the other, far from the interface and towards the edge of the plate, or a mix of both of these cases. Analysis was conducted by observing the plots of these predictions and investigating resonances which did not match the directly measurement transfer mobility. For example Fig.3.14 and 3.16 show a common loss in accuracy occurs at a resonance of 320Hz. To gain a better understanding as to why this occurs, Fig.3.19 was constructed to observe how the error at 320Hz corresponds to the dynamics of the FE-plate. The response DoF for the mobility $\mathbf{Y}_{C_{a_1,b_1}}$ is the first DoF in A and shows there is an increased amplitude there. Furthermore the error contour line shows the error has increased at this same location. Furthermore, inspecting the rest of A shows it is not only at response DoF 1 where an increase in error occurs. Observing the rest of A shows the error increases in other parts of the sub-structure that have increased amplitude. To check this was correct the mobility $\mathbf{Y}_{C_{a_{50},b_1}}$ was chosen for prediction via the round-trip and plotted in Fig.3.20, where the 50th response DoF in A showed increased amplitude and error at 320Hz. As predicted it displayed at 320Hz a large

discrepancy.

Further understanding was required see what the most optimum prediction was at particular problematic resonances. Fig.3.18 and 3.21 were constructed to show the error at those resonances depending on which A and B DoFs were chosen. Fig.3.20 showed that a difference also occurs between round-trip prediction and direct transfer mobility at 135Hz. Observing Fig.3.21 shows for the mobility $\mathbf{Y}_{C_{a_{50},b_1}}$ an error of 2×10^{-3}, and is on the less extreme side of other pairs that could be chosen. For example it shows using DoFs a_{40} and b_40 to predict $\mathbf{Y}_{C_{a_{40},b_{40}}}$ has an error twice that of $\mathbf{Y}_{C_{a_{50},b_1}}$. On the other hand the DoFs chosen showing minimum error are any mix of a_{20} or a_{14} with any b DoF, as well as b_{58} or b_{64} with any a DoF.

Chapter 4

Investigation into the invariance of transmissibilities

In this chapter, the property known as sub-structural 'invariance' is analysed for generalised transmissibilities. Outlined in Chapter 2, an invariant dynamic quantity is solely attributed to a sub-structure within a coupled assembly, and unaffected by adjacent sub-structures due to the blocking constraint at their connecting interface. The invariance of a transmissibility for a component is analysed in a number of ways. One example is by interchanging an adjacent coupled sub-structure and observing whether the transmissibility of the target component has stayed the same. Another way is by changing the positioning of excitation when determining the transmissibility of the target sub-structure and observing whether it remains the same. Additional analysis methods are explored and explained in more detail further on. While many quantities can be invariant, the main focus in this chapter is on transmissibilities. The reason for this is to inform the next chapter which introduces the Operational Round-trip (ORT) method. It uses operational invariant transmissibilities to predict driving-point FRFs within a coupled assembly. This information should not only inform the correct applicability of the ORT method, but also any vibro-acoustic analysis and prediction methods

that use transmissibilities within coupled assemblies.

Contents

In Chapter 2, generalised force and response transmissibilities (Eq.2.59 and Eq.2.60 respectively), were defined as sub-structural invariant quantities due to the blocking constraints in their definitions. Specifically in the context of coupled assemblies, transmissibilities are invariant when sufficient blocking constraints are applied to the subset

of DoFs installed at the connection point between sub-structures, c. This is convenient as a transmissibility for a sub-structure can be determined without decoupling. If no sufficient blocking is applied here, the transmissibility calculated will be a property of the coupled system instead. Also in the case there is an active sub-structure coupled to a target passive sub-structure, the dynamic behaviour of the active component will be blocked at the interface, and thus unable to influence transmissibilities measured for the passive conponent. An example for this application can be in automotive test rigs where the force generating mechanisms by the engine or compressor, can be blocked at the mounting points when calculating a transmissibility of a passive component within the vehicle.

While Meggitt and Moorhouse [2020b] demonstrate transmissibilities are invariant in the context of FE-model updating, this chapter seeks to build on that work experimentally and to analyse the sensitivities of invariant transmissibilities. This investigation is broken down into three experiments, where each adds a layer of complexity. In Section 4.2, we have a preliminary experiment which consists of a beam which is resiliently mounted at one point to a large plate. Here it is observed for the simplest case whether the transmissibility of the plate remains unchanged when the beam is changed or removed completely. Additionally, a comparison is made between two transmissibilities which have different excitation positions. Following this in Section 4.3, the second experimental example has a plate which is coupled at three points by three resilient mounts to the same large plate. The same analyses from the preliminary experimental example is also applied here. Sensitivity analysis on their invariance is also conducted by changing the amount of excitations and responses used in calculation. Lastly for this three-mount example, invariance is analysed by using the transposition relation between force and response transmissibilities and observing whether they remain the same irrespective of being determined operationally or via FRFs. In the final part of this chapter analysis is conducted on a more complex version of the preliminary experiment in Section 4.4. The single resilient mount has been replaced with a rigid connection instead. The same analyses from the previous section is applied to this

case study. However due to the rigid connection, the interface must be characterised by additional DoFs to ensure an invariant transmissibility. Analysis is conducted on the sensitivity of transmissibilities as the DoFs at the rigid connection are altered. For the preliminary experiment only FRF-based transmissibilities are analysed, but as we progress to the three-resilient mount and rigid connection experimental studies, analysis is conducted on FRF-based and operational transmissibilities.

4.1 Invariant transmissibility theory

Following on from Section 2.7.2, we delve into the theory on invariant transmissibilities more comprehensively.

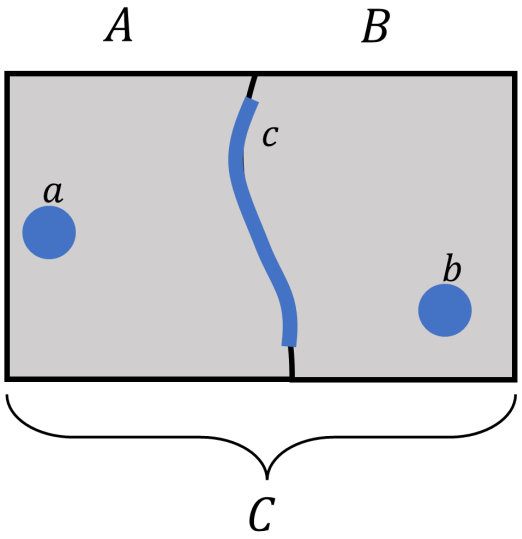

Figure 4.1: Diagram of a coupled assembly C, consisting of sub-structure A which has a subset of DoFs within it denoted a, and sub-structure B with subset b. At the connection point lies another subset of DoFs denoted c.

For example, let us consider a coupled assembly as shown in Fig.4.1. The equations of motion for subsets b and c, defined in terms of impedance are,

$$\begin{pmatrix} f_b \\ f_c \end{pmatrix} = \begin{bmatrix} Z_{B_{bb}} & Z_{B_{bc}} \\ Z_{B_{cb}} & Z_{B_{cc}} + Z_{A_{cc}} \end{bmatrix} \begin{pmatrix} v_b \\ v_c \end{pmatrix} \tag{4.1}$$

Within the above coupled mechanical impedance matrix $\mathbf{Z}_C$, is the interface impedance matrix $Z_{C_{cc}}$, defined by the $Z_{B_{cc}} + Z_{A_{cc}}$ element. It is clear that the other elements $Z_{B_{bb}}$ and $Z_{B_{bc}} = Z_{B_{cb}}^T$ are an invariant property of B. As detailed in earlier in Section 2.3.2, direct measurement of these quantities are problematic experimentally as it requires a zero velocity constraint to all DoFs on the system, except for the DoF where the excitation is applied. Thus, the alternative approach of measuring them indirectly by the inverse of $\mathbf{Y}_C$ is taken to acquire these invariants,

$$\begin{bmatrix} Z_{B_{bb}} & Z_{B_{bc}} \\ Z_{B_{cb}} & Z_{B_{cc}} + Z_{A_{cc}} \end{bmatrix} = \begin{bmatrix} Y_{C_{bb}} & Y_{C_{bc}} \\ Y_{C_{cb}} & Y_{C_{cc}} \end{bmatrix}^{-1} \tag{4.2}$$

Inverting $\mathbf{Y}_C$ has the effect of a zero force constraint to all DoFs other than the one with the applied excitation. However this is only the case if the interface c has a complete interface characterisation and that all DoFs applicable to $\mathbf{Y}_C$ are included. The implication of this matrix inversion is well known Hansen [1998], if $\mathbf{Y}_C$ is ill-conditioned (its condition number is very large), it is close to being singular (non-invertible). In other words, any small errors on the inputs are amplified significantly when inverted.

To take a blocking force at the interface c for Eq.4.1, a zero velocity constraint is applied, which removes the influence of A. Thus our definitions become,

$$\begin{pmatrix} f_b \\ -\bar{f}_{B_c} \end{pmatrix} = \begin{bmatrix} Z_{B_{bb}} & Z_{B_{bc}} \\ Z_{B_{cb}} & Z_{B_{cc}} + Z_{A_{cc}} \end{bmatrix} \begin{pmatrix} v_b \\ 0 \end{pmatrix} \tag{4.3}$$

By substituting the first row into the second, we can see a force transmissibility defined via mechanical impedances emerge,

$$-\bar{f}_{B_c} = Z_{B_{bc}} Z_{B_{bb}}^{-1} f_b \tag{4.4}$$

It is clear that the impedance terms represent a transmissibility between applied force f_b and the negative blocking force $-\bar{f}_{B_c}$,

$$\mathbf{T}_{cb}^{f,b} = \mathbf{Z}_{B_{cb}}\mathbf{Z}_{B_{bb}}^{-1} \tag{4.5}$$

As it was stated earlier, the terms $\mathbf{Z}_{B_{cb}}$ and $\mathbf{Z}_{B_{bb}}$ clearly invariant quantities as denoted in the uppercase subscript. As the transmissibility $\mathbf{T}_{cb}^{f,b}$ is the product of two invariant impedances, it is also an invariant of B.

4.1.1 Response transmissibility

Having introduced the general definitions of invariant force and response transmissibilities in Section 2.7.2, the mobility relations for the specific sets of DoFs (a, b and c) illustrated in Fig. 4.1 will now be derived.

Consider an external force applied within B, at DoFs b. The responses at each subset of DoFs due to this applied force are defined as,

$$\mathbf{v}_a = \mathbf{Y}_{C_{ab}}\mathbf{f}_b, \qquad \mathbf{v}_c = \mathbf{Y}_{C_{cb}}\mathbf{f}_b, \qquad \mathbf{v}_b = \mathbf{Y}_{C_{bb}}\mathbf{f}_b \tag{4.6}$$

Equating the forces $\mathbf{f}_b$ between $\mathbf{v}_a$ and $\mathbf{v}_c$, we obtain,

$$\mathbf{v}_a = \mathbf{Y}_{C_{ab}}\mathbf{Y}_{C_{cb}}^{-1}\mathbf{v}_c = \mathbf{T}_{ac}^{r,b}\mathbf{v}_c \tag{4.7}$$

To help visualise what these transmissibilities “look” like, a diagram of $\mathbf{T}_{ac}^{r,b}$ is provided below.

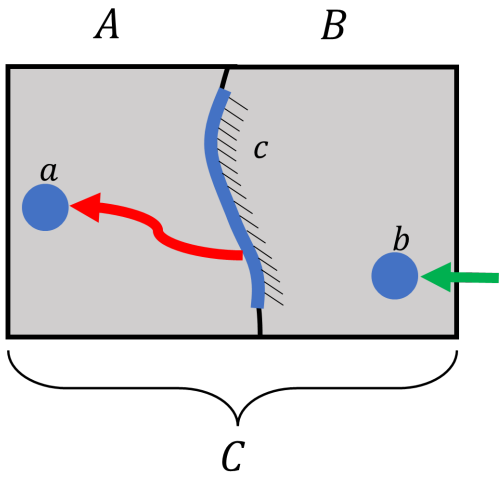

Figure 4.2: Visualisation of an invariant transmissibility for sub-structure A, $\mathbf{T}_{ac}^{r,b}$, relating responses at c and a, due an applied force at b.

$\mathbf{T}_{ac}^{r,b}$ is an invariant response transmissibility between c and a, or in other words of sub-structure A. Note that the direction of the transmissibility goes from c and a (shown by the red arrow). The number of force DoFs should be equal to the number of interface DoFs c such that $\mathbf{Y}_{C_{cb}}$ is invertible. Additional forces can be included (over-determination), in which case a pseudo-inverse $^+$ replaces the inverse operation. Combining the definitions in Eq.4.6 of $\mathbf{v}_c$ and $\mathbf{v}_b$, we similarly obtain,

$$\mathbf{v}_c = \mathbf{Y}_{C_{cb}} \mathbf{Y}_{C_{bb}}^{-1} \mathbf{v}_b = \mathbf{T}_{cb}^{r,b} \mathbf{v}_b. \tag{4.8}$$

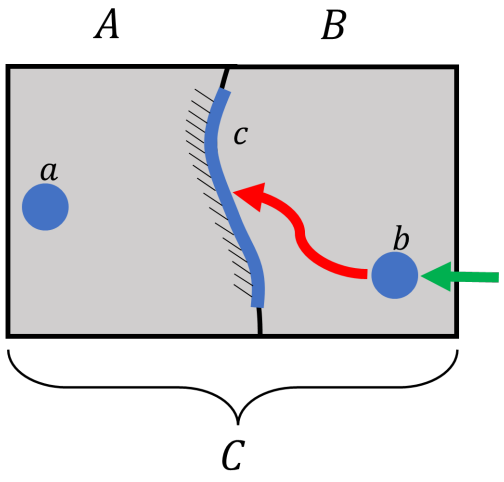

Figure 4.3: Visualisation of an invariant transmissibility for sub-structure B, $\mathbf{T}_{cb}^{r,b}$, relating responses at b and c, due an applied force at b.

Considering an external force applied to the interface DoFs c instead, we can compute the velocity at a, c or b.

$$\mathbf{v}_a = \mathbf{Y}_{C_{ac}}\mathbf{f}_c, \qquad \mathbf{v}_c = \mathbf{Y}_{C_{cc}}\mathbf{f}_c, \qquad \mathbf{v}_b = \mathbf{Y}_{C_{bc}}\mathbf{f}_c \tag{4.9}$$

Using the above we obtain the following transmissibility relations,

$$\mathbf{v}_a = \mathbf{Y}_{C_{ac}}\mathbf{Y}_{C_{cc}}^{-1}\mathbf{v}_c = \mathbf{T}_{ac}^{r,c}\mathbf{v}_c \tag{4.10}$$

$$\mathbf{v}_b = \mathbf{Y}_{C_{bc}}\mathbf{Y}_{C_{cc}}^{-1}\mathbf{v}_c = \mathbf{T}_{bc}^{r,c}\mathbf{v}_c \tag{4.11}$$

If one instead considers an external force within A at DoFs a, we compute the velocities at a, c or b as,

$$\mathbf{v}_a = \mathbf{Y}_{C_{aa}}\mathbf{f}_a, \qquad \mathbf{v}_c = \mathbf{Y}_{C_{ca}}\mathbf{f}_a, \qquad \mathbf{v}_b = \mathbf{Y}_{C_{ba}}\mathbf{f}_a \tag{4.12}$$

and the following transmissibility relations are obtained,

$$\mathbf{v}_c = \mathbf{Y}_{C_{ca}}\mathbf{Y}_{C_{aa}}^{-1}\mathbf{v}_a = \mathbf{T}_{ca}^{r,a}\mathbf{v}_a \tag{4.13}$$

$$\mathbf{v}_b = \mathbf{Y}_{C_{ba}}\mathbf{Y}_{C_{ca}}^{-1}\mathbf{v}_c = \mathbf{T}_{bc}^{r,a}\mathbf{v}_c \tag{4.14}$$

4.1.2 Force transmissibility

It can be shown that the response field within a domain (say B) can be reproduced identically by applying the so-called (negative) blocked force along its connecting interface, in place of the original excitation Bobrovnitskii [2001]. That is, given an external force applied within A, $\mathbf{f}_a$, we can express the velocity at b in the following form,

$$\mathbf{v}_b = -\mathbf{Y}_{C_{bc}}\bar{\mathbf{f}}_c \tag{4.15}$$

In the case of an external force applied within B, the velocity at a is therefore,

$$\mathbf{v}_a = -\mathbf{Y}_{C_{ac}}\bar{\mathbf{f}}_c \tag{4.16}$$

In both external force cases, the velocity at the interface DoFs c is defined as,

$$\mathbf{v}_c = -\mathbf{Y}_{C_{cc}}\bar{\mathbf{f}}_c \tag{4.17}$$

where $\bar{\mathbf{f}}_c$ is the force required to restrain the interface motion generated by the external force $\mathbf{f}_a$. Equating Eq.4.15 and 4.12c we obtain,

$$\mathbf{v}_b = -\mathbf{Y}_{C_{bc}}\bar{\mathbf{f}}_c = \mathbf{Y}_{C_{ba}}\mathbf{f}_a \tag{4.18}$$

which rearranges to,

$$-\bar{\mathbf{f}}_c = \mathbf{Y}_{C_{bc}}^{-1}\mathbf{Y}_{C_{ba}}\mathbf{f}_a = \mathbf{T}_{ca}^{f,a}\mathbf{f}_a \tag{4.19}$$

where $\mathbf{T}_{ca}^{f,a}$ is the force transmissibility between a and c. Similarly, equating equation 4.17 and 4.12b we obtain,

$$\mathbf{v}_c = -\mathbf{Y}_{C_{cc}}\bar{\mathbf{f}}_c = \mathbf{Y}_{C_{ca}}\mathbf{f}_a \tag{4.20}$$

which rearranges to,

$$-\bar{\mathbf{f}}_c = \mathbf{Y}_{C_{cc}}^{-1}\mathbf{Y}_{C_{ca}}\mathbf{f}_a = \mathbf{T}_{ca}^{f,a}\mathbf{f}_a \tag{4.21}$$

Considering an external force applied within B at the DoFs b, a similar pair of transmissibility relations can be obtained,

$$-\bar{\mathbf{f}}_c = \mathbf{Y}_{C_{ac}}^{-1}\mathbf{Y}_{C_{ab}}\mathbf{f}_b = \mathbf{T}_{cb}^{f,b}\mathbf{f}_b \tag{4.22}$$

$$-\bar{\mathbf{f}}_c = \mathbf{Y}_{C_{cc}}^{-1}\mathbf{Y}_{C_{cb}}\mathbf{f}_b = \mathbf{T}_{cb}^{f,b}\mathbf{f}_b \tag{4.23}$$

4.1.3 Force and response transmissibility relation

Inspecting the transmissibilities derived above, it can be seen that the force and response transmissibilities are directly related. For example, let us take the definitions of Eq.4.14 and 4.22 respectively. They are related through a matrix transpose operation,

$$\mathbf{T}_{bc}^{r,a} = \mathbf{Y}_{C_{ba}}\mathbf{Y}_{C_{ca}}^{-1}, \qquad \mathbf{T}_{cb}^{f,b} = \mathbf{Y}_{C_{ac}}^{-1}\mathbf{Y}_{C_{ab}}$$

$$\mathbf{T}_{cb}^{f,b} = (\mathbf{T}_{bc}^{r,a})^{\mathrm{T}} \tag{4.24}$$

Similarly, by taking the definitions of Eq.4.11 and 4.23,

$$\mathbf{T}_{bc}^{r,c} = \mathbf{Y}_{C_{bc}}\mathbf{Y}_{C_{cc}}^{-1}, \qquad \mathbf{T}_{cb}^{f,b} = \mathbf{Y}_{C_{cc}}^{-1}\mathbf{Y}_{C_{cb}}$$

$$\mathbf{T}_{cb}^{f,b} = (\mathbf{T}_{bc}^{r,c})^{\mathrm{T}} \tag{4.25}$$

Also if we take Eq.4.7 and 4.19,

$$\mathbf{T}_{ac}^{r,b} = \mathbf{Y}_{C_{ab}}\mathbf{Y}_{C_{cb}}^{-1}, \qquad \mathbf{T}_{ca}^{f,a} = \mathbf{Y}_{C_{bc}}^{-1}\mathbf{Y}_{C_{ba}}$$

$$\mathbf{T}_{ca}^{f,a} = \left(\mathbf{T}_{ac}^{r,b}\right)^{\mathrm{T}} \tag{4.26}$$

Finally for Eq.4.10 and 4.21,

$$\mathbf{T}_{ac}^{r,c} = \mathbf{Y}_{C_{ac}} \mathbf{Y}_{C_{cc}}^{-1}, \qquad \mathbf{T}_{ca}^{f,a} = \mathbf{Y}_{C_{cc}}^{-1} \mathbf{Y}_{C_{ca}}$$

$$\mathbf{T}_{ca}^{f,a} = (\mathbf{T}_{ac}^{r,c})^{\mathrm{T}} \tag{4.27}$$

The force transmissibility from DoFs i to j due to an external force at DoF a, $\mathbf{T}_{ji}^{f,a}$, is equal to the transpose (i.e. reverse) of the response transmissibility from DoFs j to i with external force at b, $\mathbf{T}_{ij}^{r,b}$. Given that the location of the a and b DoFs is arbitrary, either can be collocated with the interface DoFs c and the same transmissibility obtained, for example $\mathbf{T}_{ij}^{r,b} = \mathbf{T}_{ij}^{r,c}$. This is validated experimentally later on in Section 4.2.2.

This relation between the force and response transmissibility is well known, with its exact form depending on the precise definition of the transmissibility. For example Lage et al. [2014] includes a negative sign. Here, this negative sign is attached to the blocked force vector, and so does not appear in the transmissibility relation explicitly. Furthermore, they provide the necessary relation as an inverse transpose. This was based on the definition of the force and response transmissibilities in the same direction, i.e. $\mathbf{T}_{ca}^{f,c}$ and $\mathbf{T}_{ca}^{r,c}$. Here we have derived the transmissibilities in the direction away from the external excitation, i.e. from c to a if excitation is in b, or c to b if excitation is in a. Inversion of a transmissibility matrix has the effect of reversing its direction, $(\mathbf{T}_{ca}^{r,c})^{-1} = \mathbf{T}_{ac}^{r,c}$. The important fact is that the force transmissibility can be obtained directly from the response transmissibility which, as will be shown in Section 4.1.4, can be obtained using output-only measurements.

4.1.4 Operational transmissibility

Consider component A or B as active, containing some internal force-generating mechanisms, e.g. gear meshing or bearing forces within a gearbox. In this case, it is possible to estimate the response transmissibility from output-only measurements. To do so

we consider N linearly independent operational states of the active component. For each state, we obtain a force vector $\mathbf{f}_N$ which can be arranged to form a force matrix $\mathbf{F}$.

$$\mathbf{F} = \Big[\mathbf{f}_1, \mathbf{f}_2, \dots \mathbf{f}_N\Big] \tag{4.28}$$

Consequently, all response vectors become response matrices $\mathbf{V}$, where each column represents the complex Fourier spectra of the operational response; corresponding to the same force vector column in $\mathbf{F}$. As a result, the velocity and force vectors for our transmissibility definitions, $\mathbf{v}$ and $\mathbf{f}$ respectively, are now replaced by $\mathbf{V}$ and $\mathbf{F}$. Take for example N internal forces within A. Our definitions become,

$$\mathbf{V}_a = \mathbf{Y}_{C_{aa}}\mathbf{F}_a, \qquad \mathbf{V}_c = \mathbf{Y}_{C_{ca}}\mathbf{F}_a, \qquad \mathbf{V}_b = \mathbf{Y}_{C_{ba}}\mathbf{F}_a \tag{4.29}$$

Equating Eq.4.29b and Eq.4.29c we obtain,

$$\mathbf{V}_b = \mathbf{Y}_{C_{ba}}\mathbf{Y}_{C_{ca}}^{-1}\mathbf{V}_c = \mathbf{T}_{bc}^{r,a}\mathbf{V}_c \tag{4.30}$$

thus yielding the operational transmissibility definition,

$$\mathbf{T}_{bc}^{r,a} = \mathbf{V}_b\mathbf{V}_c^{-1} \tag{4.31}$$

It is important that the first column of $\mathbf{V}_b$ is measured at the same time as the first column of $\mathbf{V}_c$ to ensure the velocity measurements at both DoF subsets are time aligned. Similarly take the definitions from Eq4.6 for an excitation applied at subset b,

$$\mathbf{V}_a = \mathbf{Y}_{C_{ab}}\mathbf{F}_b, \qquad \mathbf{V}_c = \mathbf{Y}_{C_{cb}}\mathbf{F}_b, \qquad \mathbf{V}_b = \mathbf{Y}_{C_{bb}}\mathbf{F}_b \tag{4.32}$$

Equating Eq.4.32a and Eq.4.32b we obtain,

$$\mathbf{V}_a = \mathbf{Y}_{C_{ab}} \mathbf{Y}_{C_{cb}}^{-1} \mathbf{V}_c = \mathbf{T}_{ac}^{r,b} \mathbf{V}_c \tag{4.33}$$

thus yielding,

$$\mathbf{T}_{ac}^{r,b} = \mathbf{V}_a \mathbf{V}_c^{-1} \tag{4.34}$$

It must be noted the inverted velocity matrices in the definitions above have been denoted as such assuming they are square. Over-determination may be carried out by including additional operational states such that the inverted matrices become rectangular, thus replacing the matrix inverse with a pseudo-inverse. If possible, over-determination is encouraged as it reduces sensitivity to noise. Note that to calculate the response transmissibilities shown in Eq.4.34 and 4.31, inversion of a velocity matrix is required. To guarantee the invertibility of these matrices, it is necessary to apply adequate forces that are also linearly independent; otherwise, the velocity matrix will be rank-deficient and singular.

4.2 Beam-isolator-plate experimental example

In order to demonstrate the invariance of transmissibilities, a simple experiment was conducted where a beam component A was interchanged with another beam of different dimensions. If the interface DoFs c is completely characterised, the transmissibility of sub-structure B (resiliently coupled in this case) is invariant and should remain the same. The first experimental example to demonstrate this is a simple beam-isolator-plate case, illustrated by Fig.4.4. All of the system's sensors are uni-axial, and orientated in the vertical plane (z-axis). As we are conducting EMA via roving hammer, the excitations applied at DoFs a are also in z-axis. As the isolator is dominated by motion mostly in the z plane, in most cases it is likely that a single c DoF facing the z-axis is sufficient for a complete interface description Meggitt and McGee [2024]. All other translations and rotations contribute very little to the overall dynamics and are thus deemed negligible for this assembly.

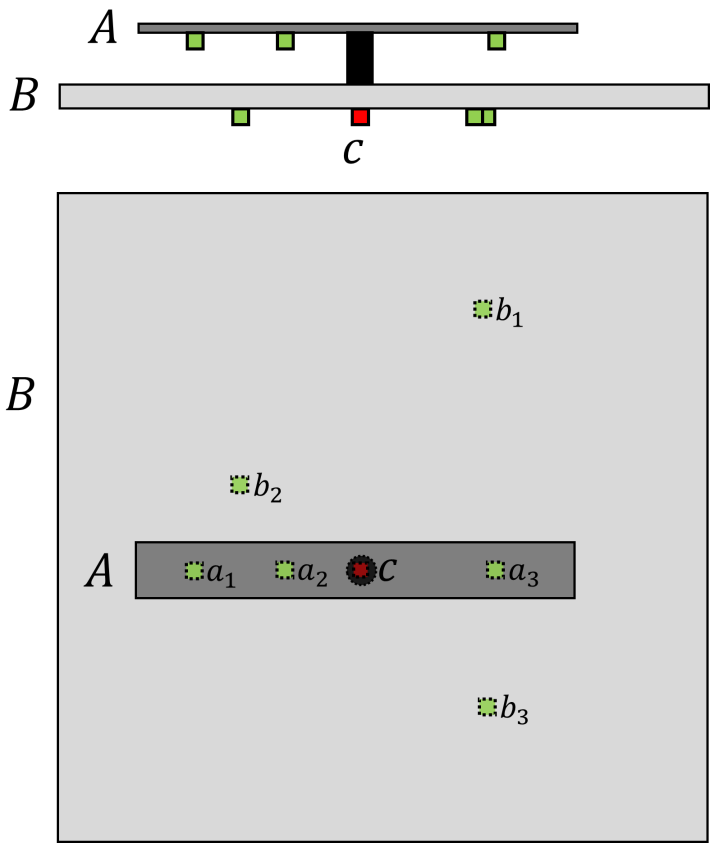

Figure 4.4: 2D diagram of Beam-isolator-plate experiment. Above is side-on, below is top-down view.

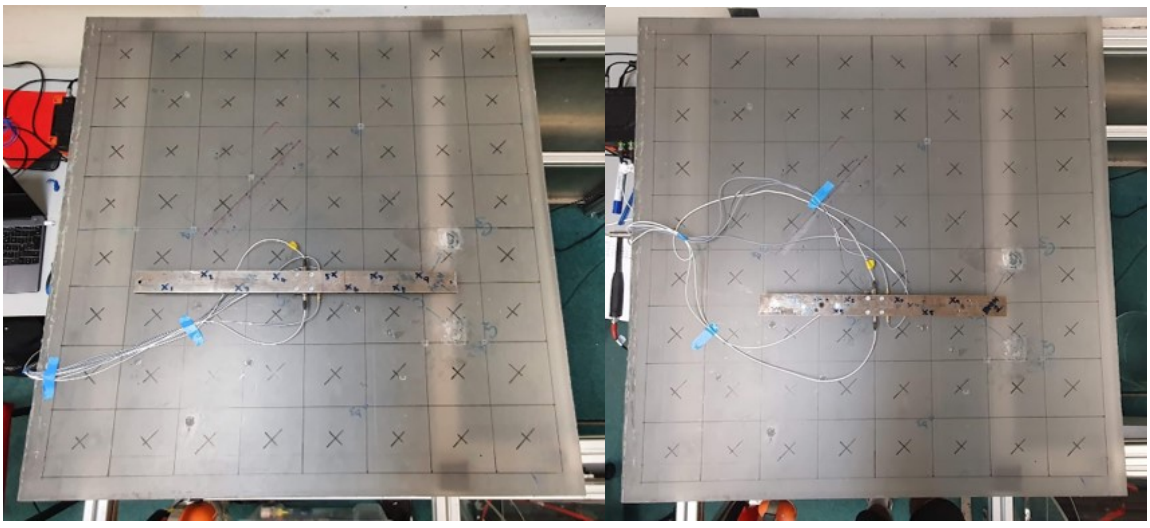

(a) Photograph of Beam 1 coupled in whole system.(b) Photograph of Beam 2 coupled in whole system.

Figure 4.5: A components beams 1 and 2, coupled to plate B, via a single resilient mount.

4.2.1 Interchanging coupled component

Force and response transmissibilities, $\mathbf{T}_{cb}^{f,b}$ and $\mathbf{T}_{bc}^{r,c}$, are determined for B (via Eq. 4.23 and 4.11 respectively) while A is interchanged with beams shown in Fig.4.5. In addition, the transmissibilities are also calculated for when no beam is coupled to the system I.e. no A. In theory if the blocking DoF c is sufficiently characterised, the transmissibility calculated when A is not coupled to the assembly will be identical to the transmissibilities where it is coupled. Both beams used in the experiment are made of steel but differ in length. The dimensions of Beam 1 and 2 are 56x4x1cm and 44x4x1cm respectively.

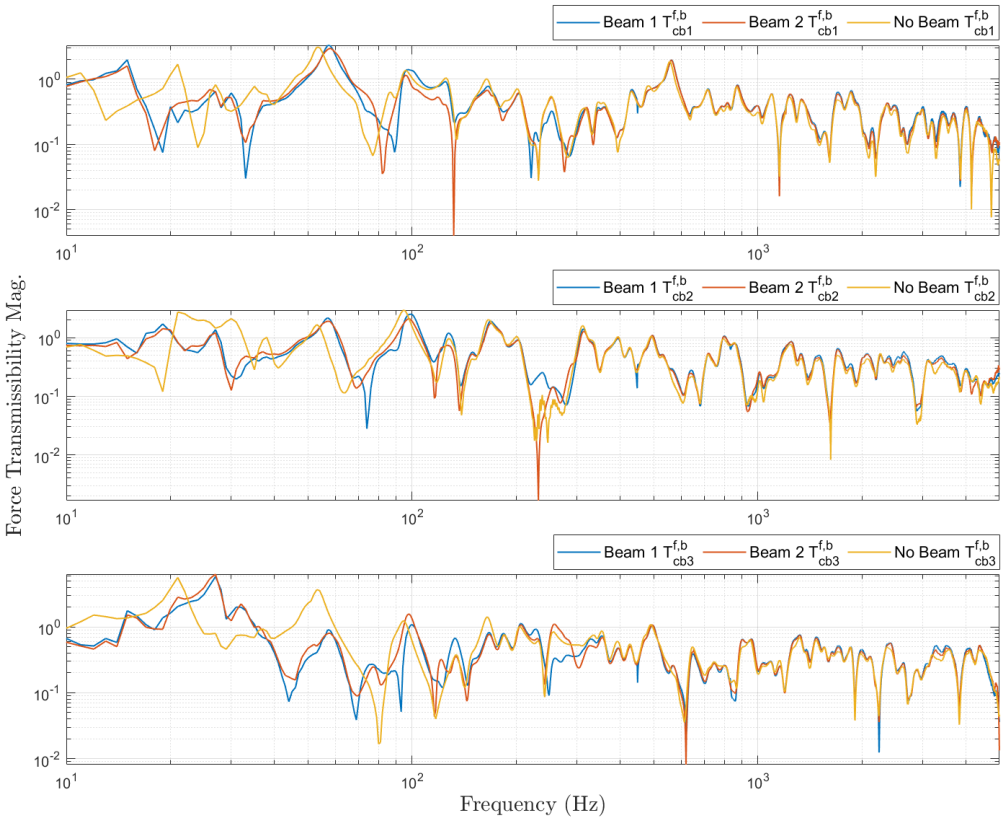

Figure 4.6: $\mathbf{T}_{cb}^{f,b}$ due to A component Beam 1 or 2, and no beam. In reference to test rig Fig.4.4

Firstly, let's observe the invariance of $\mathbf{T}_{cb}^{f,b}$ in Fig.4.6. The three sub-figures plot the force transmissibility between the single interface DoF c and to each of the response DoFs in subset b. I.e. the top sub-figure corresponds to $\mathbf{T}_{cb_1}^{f,b}$, the middle $\mathbf{T}_{cb_2}^{f,b}$, and the

bottom $\mathbf{T}_{cb_3}^{f,b}$. Within each sub-figure, there are two plots where either beam 1 or 2 is coupled, as well as no A component. All show good agreement to one another for the majority of the frequency range. Some discrepancies are observed in the 10-150Hz range for the no beam case. This is likely due to the lack of mass loading onto the system, which is why it causes the lower frequencies to be affected the most.

Now let us observe $\mathbf{T}_{bc}^{r,c}$ for invariance.

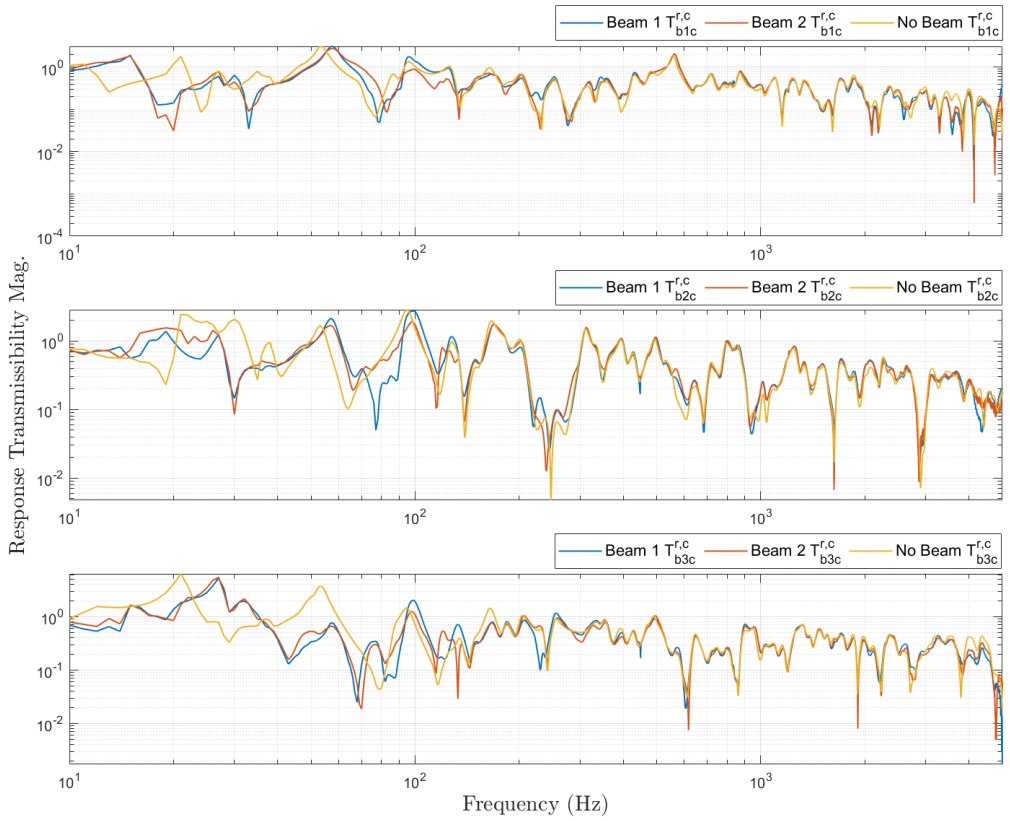

Figure 4.7: $\mathbf{T}_{bc}^{r,c}$ due to A component Beam 1 or 2, and no beam. In reference to test rig Fig.4.4

Similarly to $\mathbf{T}_{cb}^{f,b}$, Fig.4.7 shows that the response transmissibility shows invariance. The same discrepancies in the low frequency range for the 'No Beam' case are also present. Furthermore, all transmissibilities appear to be very similar to each across the rest of the frequency range. For this experimental example, the single z-axis DoF c has sufficiently blocked the dynamic behaviour of either A component, and displays transmissibilities that are invariant.

4.2.2 Transmissibility excitation positioning

For this analysis, let us consider A as an active component and B as a passive one. The transmissibility of the passive sub-structure (between interface c and remote subset b), due to an external force applied within the active sub-structure at DoF subet a, should in theory, be identical to the transmissibility obtained when external forces are applied at the interface c instead. Both of these external forces are applied within A, but differ in location. As an example, the two response transmissibilities of B, $\mathbf{T}_{bc}^{r,c}$ and $\mathbf{T}_{bc}^{r,a}$, should be the same. Using Eq.4.11 and Eq.4.14 we calculate these two transmissibilities respectively.

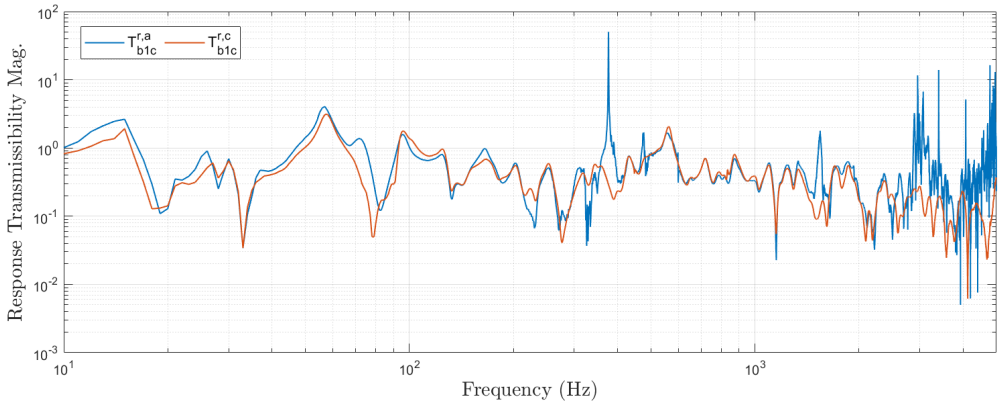

Figure 4.8: $\mathbf{T}_{b1c}^{r,c}$ vs. $\mathbf{T}_{b1c}^{r,a}$. In reference to single-interface test rig, Fig.4.4

Shown in Fig.4.8 are the transmissibilities $\mathbf{T}_{bc}^{r,a}$ and $\mathbf{T}_{bc}^{r,c}$ obtained using their FRF formulations. We obtain good agreement across the majority of the frequency range, though between 3-5kHz some discrepancies begin to emerge. We suspect the disagreement at high frequencies is due to attenuation induced noise through the resilient connections. This only occurs when excitations are made above the mount, i.e. at a. For $\mathbf{T}_{bc}^{r,c}$ excitations are applied below the mount, and so no attenuation is introduced. Of course, some of this error could also be attributed to the lack of rotational DoFs, which for resilient connections have been shown to become important at high frequencies (Meggitt and McGee [2024]). In addition to the broadband error above 3kHz, some localised errors are seen around 400Hz and 1050Hz. These errors are likely a result of inconsistencies in the measured FRF matrix, which have been shown to introduce

spurious errors in other analysis methods (Rixen [2008]). The large scale of such errors may be attributed to the matrix inversion taking place; it is well known that matrix inversion operations have an amplifying effect on noise and other measurement errors.

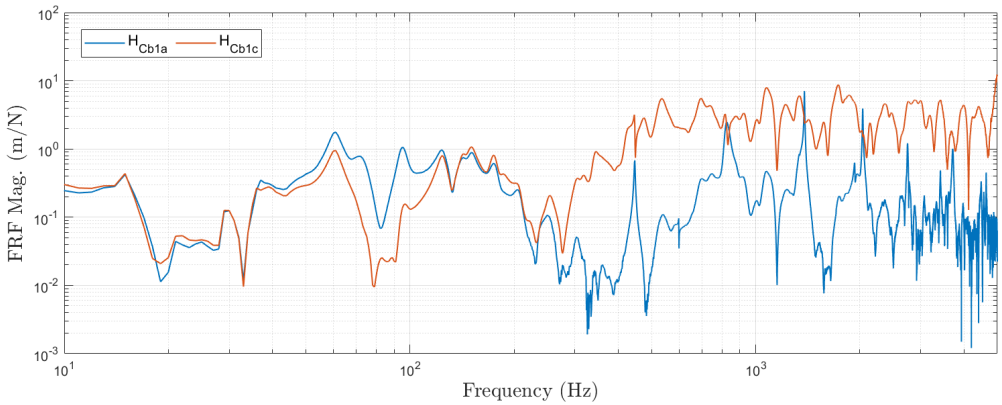

Figure 4.9: $\mathbf{H}_{C_{b1a}}$ vs. $\mathbf{H}_{C_{b1c}}$. In reference to single-interface test rig, Fig.4.4

To illustrate the point further that transmissibilities are similar irrespective of the external force location in the active component, a comparison of FRFs is shown in Fig. 4.9. $\mathbf{H}_{C_{ba}}$ and $\mathbf{H}_{C_{bc}}$ both relate the same b response but use external forces applied at a and c respectively. It is clear that these FRFs are different from one another, especially from 300Hz-5kHz.

4.3 Plate-isolator-plate experimental example

Having demonstrated experimentally that transmissibilities are an invariant property of a passive sub-structure in a coupled system, this section will test the limits of invariance by altering certain parameters. This is demonstrated on a more complex case compared to the preliminary experiment. Instead of a single resilient point interface, there are three in this case.

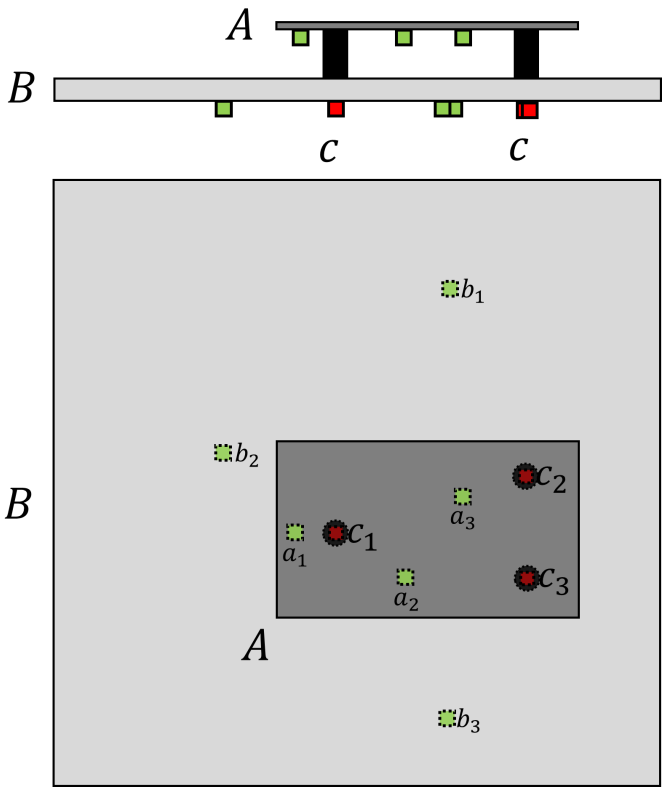

Figure 4.10: 2D diagram of coupled assembly consisting of a resilient 3 point interface connection.

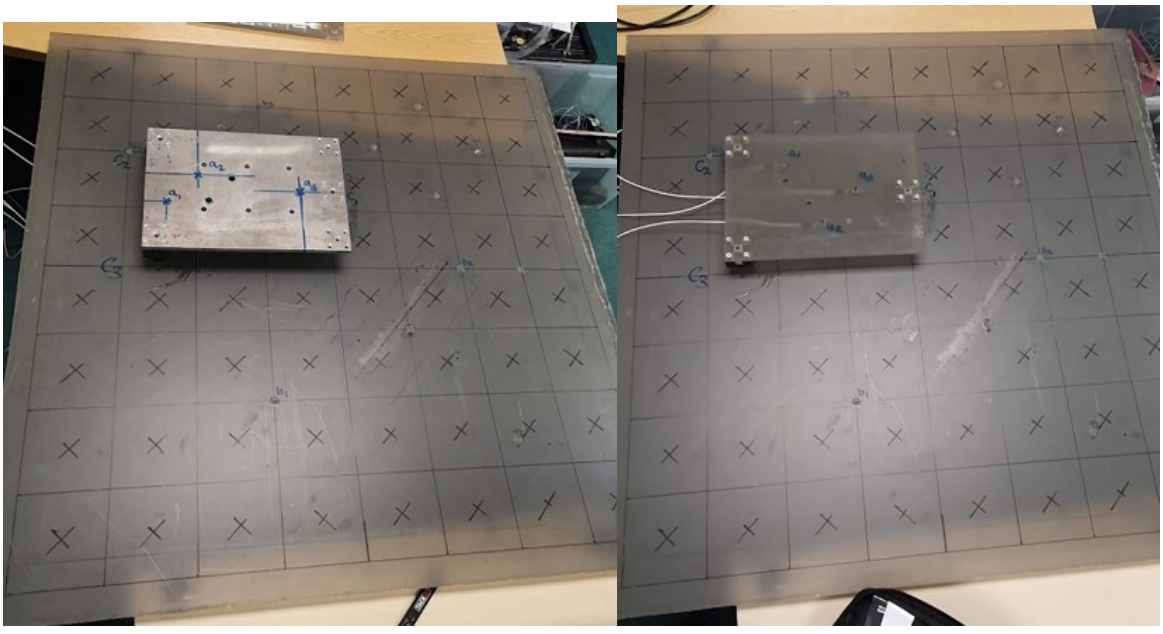

(a) Photograph of Plate 1 coupled.

(b) Photograph of Plate 2 coupled.

Figure 4.11: A component plates 1 and 2 coupled to B plate via three resilient mounts.

4.3.1 Interchanging coupled component

Firstly it is demonstrated for Fig.4.10 that $\mathbf{T}_{cb}^{f,b}$ and $\mathbf{T}_{bc}^{r,c}$ were invariant as they showed to be very similar when A had been interchanged. A was changed by its dimensions, as well as by its mass (No beam attached) which presented a challenge at very low frequencies. For this particular test rig, we interchange A plates of different materials. Pictured in Fig.4.11, Plate 1 is made of steel while Plate 2 is made of acrylic perspex. These were chosen as the damping they provide is very different, presenting a different challenge. Firstly let us observe transmissibilities calculated via mobilities via Eq.4.23 and 4.11.

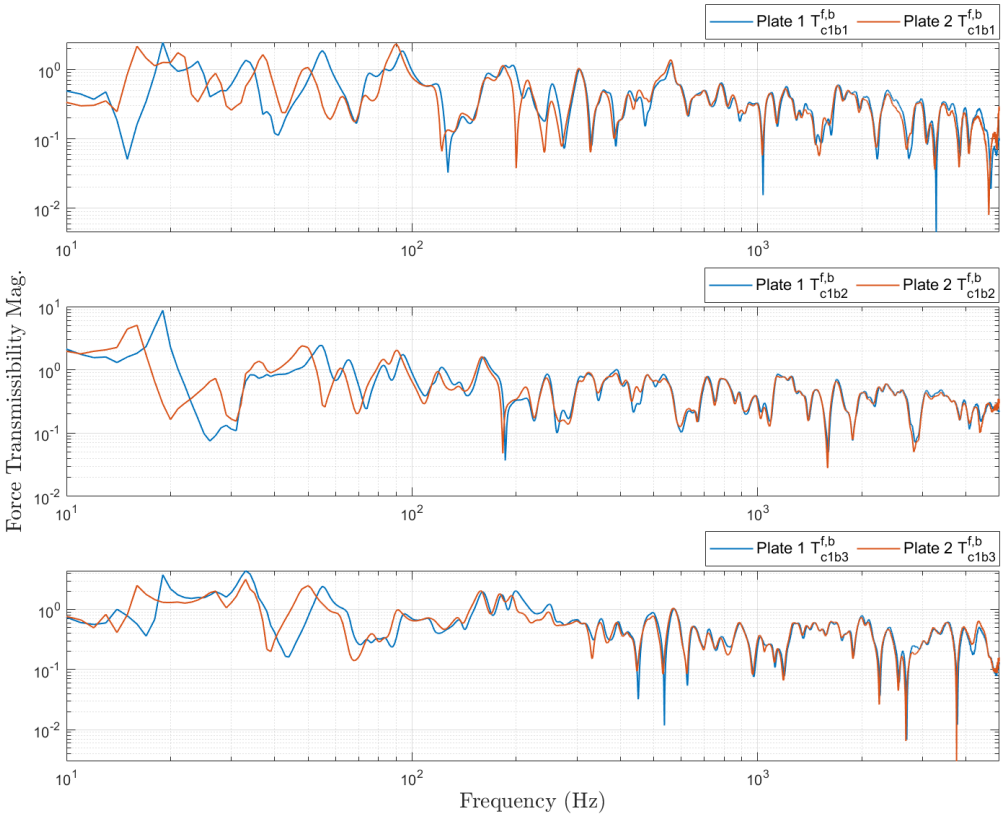

Figure 4.12: Mobility-based $\mathbf{T}_{cb}^{f,b}$ with either plate 1 or 2 coupled to the assembly.

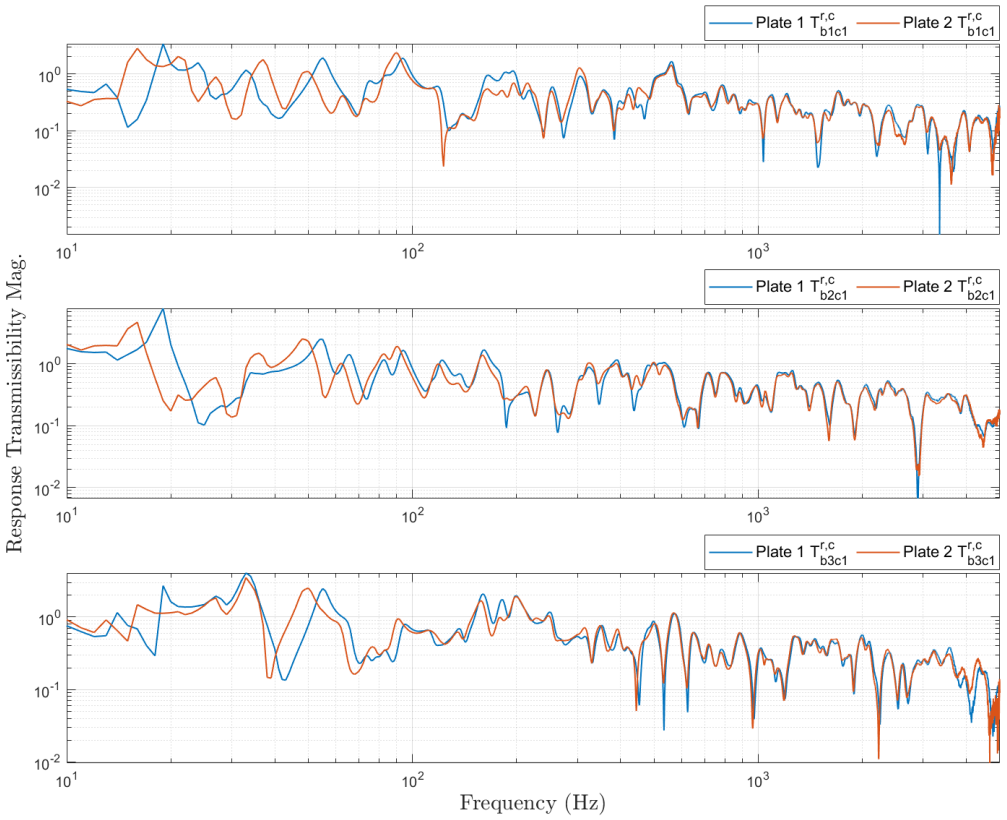

Figure 4.13: Mobility-based $\mathbf{T}_{bc}^{r,c}$ with either plate 1 or 2 coupled to the assembly.

In Fig.4.12 and 4.13 $\mathbf{T}_{cb}^{f,b}$ and $\mathbf{T}_{bc}^{r,c}$ are plotted respectively due to the different A plates coupled to the assembly. For $\mathbf{T}_{cb}^{f,b}$ all three excitation DoFs were used at subset b, while $\mathbf{T}_{bc}^{r,c}$ is calculated using the single DoF in subset c. The top sub-figures show the transmissibilities between c_1 and b_1, the middle c_1 and b_2, and the bottom c_1 and b_3. Overall there is good agreement between Plate 1 and 2 cases for both transmissibilities. A difference is visible consistently below 100Hz for both transmissibility figures, however above this frequency the transmissibilities are shown to be almost identical. As we had already established in the previous study, changing the mass of A affected the low frequencies. In this study it appears changing the damping of A also presents a challenge at low frequencies.

Analysis is also conducted on these transmissibilities when calculated by operational velocities. Examples of transmissibilities were derived in the beginning of this chapter. For the response transmissibility $\mathbf{T}_{bc}^{r,c}$ this is calculated via Eq. 4.11 and turning the

velocity vectors into matrices due to N amount of operational states. Thus we yield,

$$\mathbf{V}_b = \mathbf{Y}_{bc}\mathbf{Y}_{cc}^{-1}\mathbf{V}_c \tag{4.35}$$

As we already know that the product of $\mathbf{Y}_{bc}\mathbf{Y}_{cc}^{-1}$ equals $\mathbf{T}_{bc}^{r,c}$, the following operational definition of this response transmissibility is,

$$\mathbf{T}_{bc}^{r,c} = \mathbf{V}_b\mathbf{V}_c^{-1} \tag{4.36}$$

As $\mathbf{T}_{bc}^{r,c}$ and $\mathbf{T}_{cb}^{f,b}$ are related by transposition, we also yield the following operational definition for the force transmissibility,

$$\mathbf{T}_{cb}^{f,b} = (\mathbf{V}_b\mathbf{V}_c^{-1})^{\mathrm{T}} \tag{4.37}$$

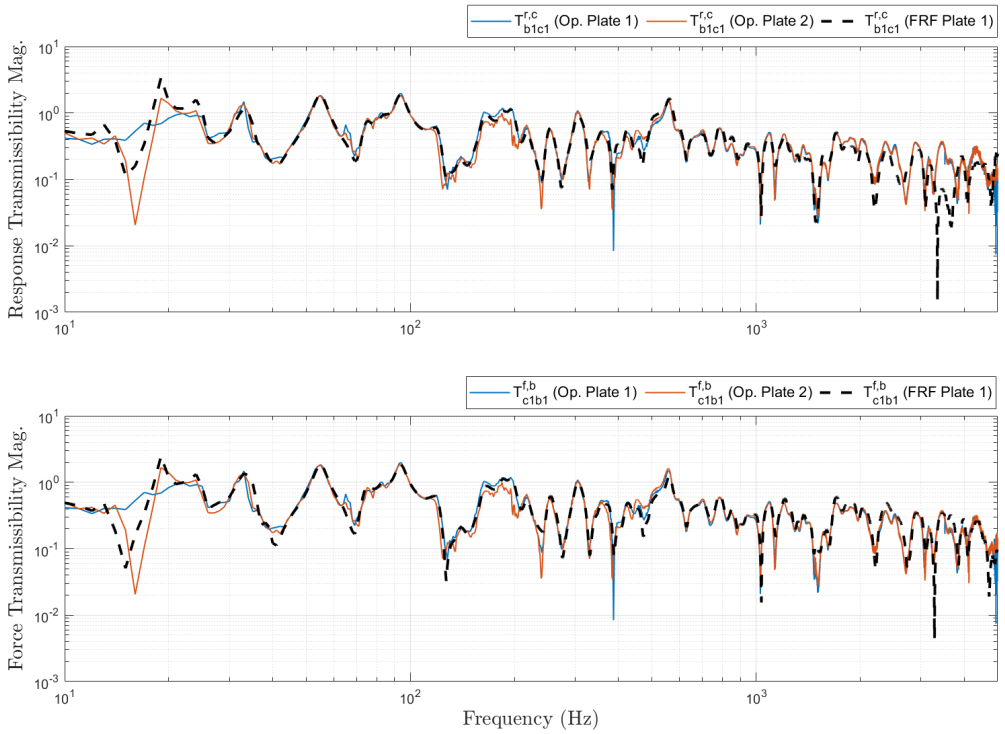

Figure 4.14: Operational $\mathbf{T}_{bc}^{r,c}$ and $\mathbf{T}_{cb}^{f,b}$, compared against validation FRF measurement.

In Fig.4.14 the operational response and force transmissibilities are compared against the FRF measurement when plate 1 was coupled to the assembly, and serves to validate the operational test. Indicated previously in Fig.4.29 and 4.13, FRF-based transmissibilities of B when either plate or 2 are coupled to the system, have shown to be almost identical (when ignoring very low frequencies). Thus for clarity reasons when displaying the figure, our benchmark to compare is only the FRF-based transmissibilities when plate 1 was coupled. It should be noted, the output-only transmissibilities are determined by taking the averaged cross-spectrum across 20 time windows, each 1 second long. Analyses on different processing of time windows will be explored in Chapter 5. The above figure shows good agreement between the output-only transmissibilities and the validation plot. In addition, the operational transmissibilities are almost identical (except between 10-20Hz), irrespective of which A plate is coupled to the assembly. Thus it is strongly indicated the operational transmissibilities are indeed invariant.

4.3.2 Transmissibility excitation positioning

Similarly to the previous experimental case study in Section 4.2.2, let us assume A is active and B is passive. One may argue at first glance for the single interface experimental example (Fig.4.4), that because B is exposed to a single DoF excitation through one interface point, the transmissibility between c and b will always be the same. By introducing more than one interface point, the transmissibility can be observed from each c point to a single response position in subset b.

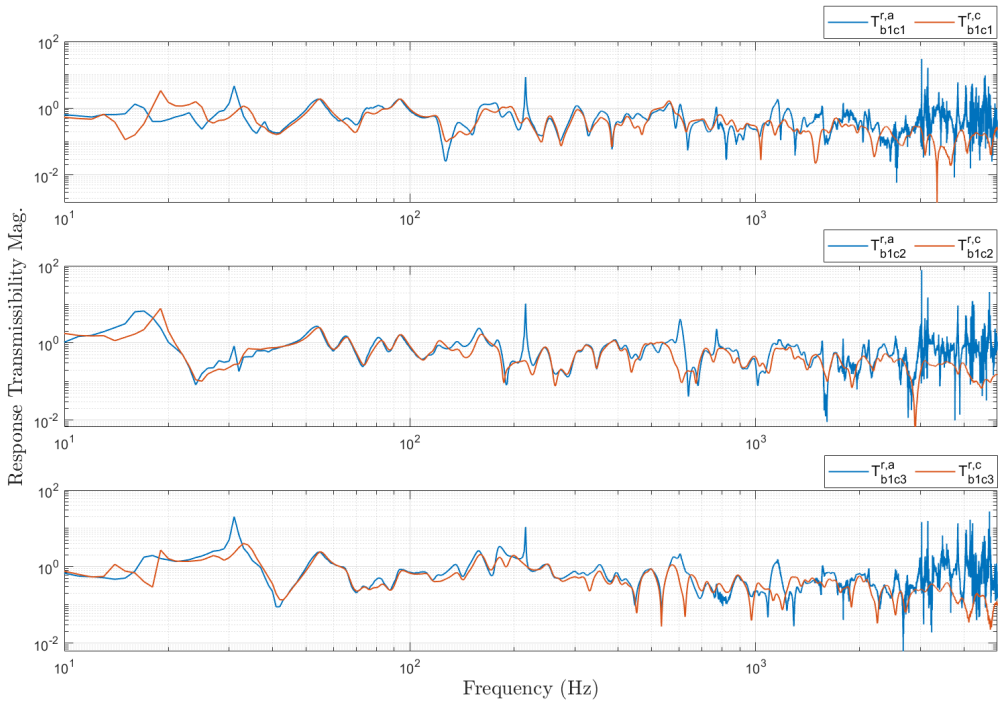

Figure 4.15: Mobility-based $\mathbf{T}_{bc}^{r,c}$ vs. $\mathbf{T}_{bc}^{r,a}$. Each sub-figure shows the transmissibility between each interface point and one b response. In reference to three-interface test rig, Fig.4.10.

Fig.4.15 presents three sub-figures, where the transmissibilities were determined between each interface DoF and b_1. The top sub-figure represents $\mathbf{T}_{b_1c_1}^{r}$, the middle $\mathbf{T}_{b_1c_2}^{r}$, and the bottom $\mathbf{T}_{b_1c_3}^{r}$. Each sub-figure plots $\mathbf{T}_{bc}^{r,a}$ and $\mathbf{T}_{bc}^{r,c}$. Similarly to Fig.4.8, this result indicates despite where the excitation is located within the active component, the transmissibility remains the same (within error). Like the single DoF interface example, there is an increase in noise from around 3kHz upwards. Being another resilient connection, this error can be attributed to attenuation-induced noise floor. Below 3kHz the transmissibilities appear to be similar.

Let us observe these transmissibilities when calculated via operational responses. It was shown in the previous subsection that $\mathbf{T}_{bc}^{r,c}$ is determined via Eq.4.36, and in Section 4.1.4 $\mathbf{T}_{bc}^{r,a}$ was calculated using Eq.4.31.

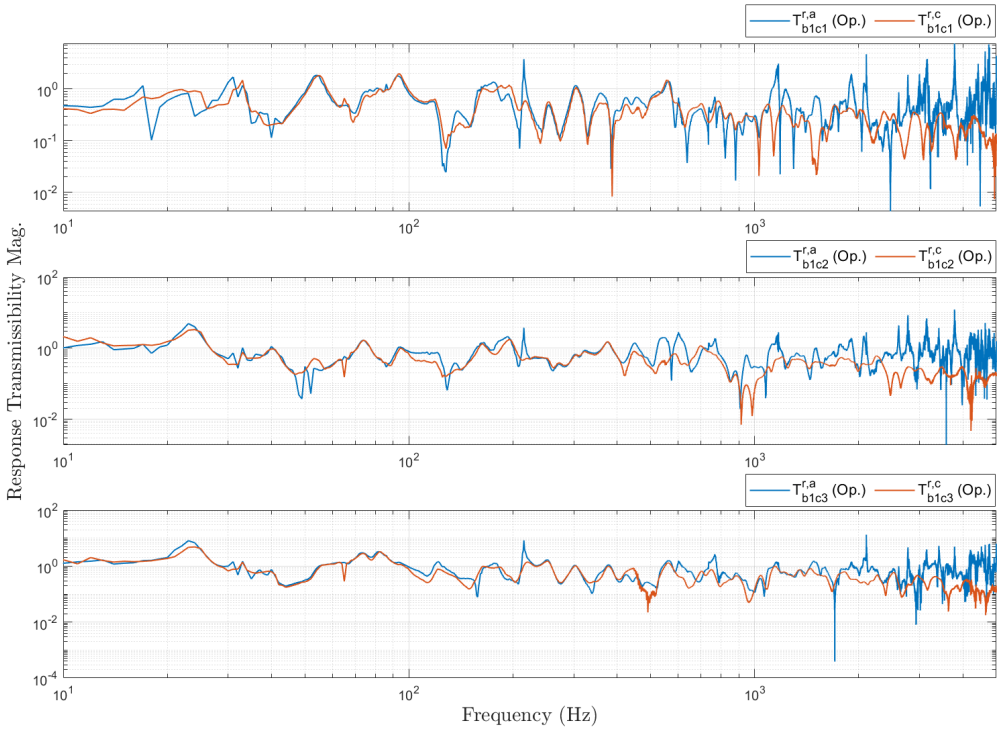

Figure 4.16: Operational $\mathbf{T}^{r,c}_{bc}$ vs. $\mathbf{T}^{r,a}_{bc}$. Each sub-figure shows the transmissibility between each interface point and one b response. In reference to three-interface test rig, Fig.4.10.

For each sub-figure in Fig.4.16, there is good agreement overall between the two transmissibilities. It is only in the higher frequencies where differences begin to emerge. $\mathbf{T}^{r,c}_{b_1c_2}$ and $\mathbf{T}^{r,a}_{b_1c_2}$ show the difference earliest in the frequency range (from 900Hz), and $\mathbf{T}^{r,c}_{b_1c_1}$ and $\mathbf{T}^{r,a}_{b_1c_1}$ from 1.1kHz. $\mathbf{T}^{r,c}_{b_1c_3}$ and $\mathbf{T}^{r,a}_{b_1c_3}$ is the best case, with differences emerging the latest at around 1.9kHz. The attenuation-induced noise effect also appears for $\mathbf{T}^{r,a}_{bc}$ from 3kHz.

4.3.3 Excitations and responses used in transmissibility calculation

The significance of how many excitations and responses are used in preserving invariant transmissibilities is analysed. A requirement which is pointed out by Maia et al. [2011b], is that the number of remote DoFs (in a or b) must be greater than or equal to the number of interface DoFs c. If not carried out as such, the accuracy of the transmis-

sibilities decreases. In this section, analysis is conducted to see whether invariance can still exist to an acceptable level below the number of DoFs set by this requirement. For example, while conducting the modal hammer test to measure mobilities, the number of external forces applied to each DoF in subsets a, b, and c (three). $\mathbf{T}_{cb}^{f,b}$ and $\mathbf{T}_{bc}^{r,a}$ are calculated from this modal test, while discarding a certain number of excitations and responses. $\mathbf{T}_{cb}^{f,b}$, defined by Eq. 4.23, has excitations applied at two subsets, c and b. This force transmissibility is analysed when both of the force DoFs have been reduced. On the other hand, $\mathbf{T}_{bc}^{r,a}$, defined by Eq. 4.11, excitations are applied only at c, therefore invariance is analysed for when applied forces are reduced only at that subset. Note in this section the transmissibilities have been determined while only plate 1 is coupled to the assembly. No interchanging of component A is carried out.

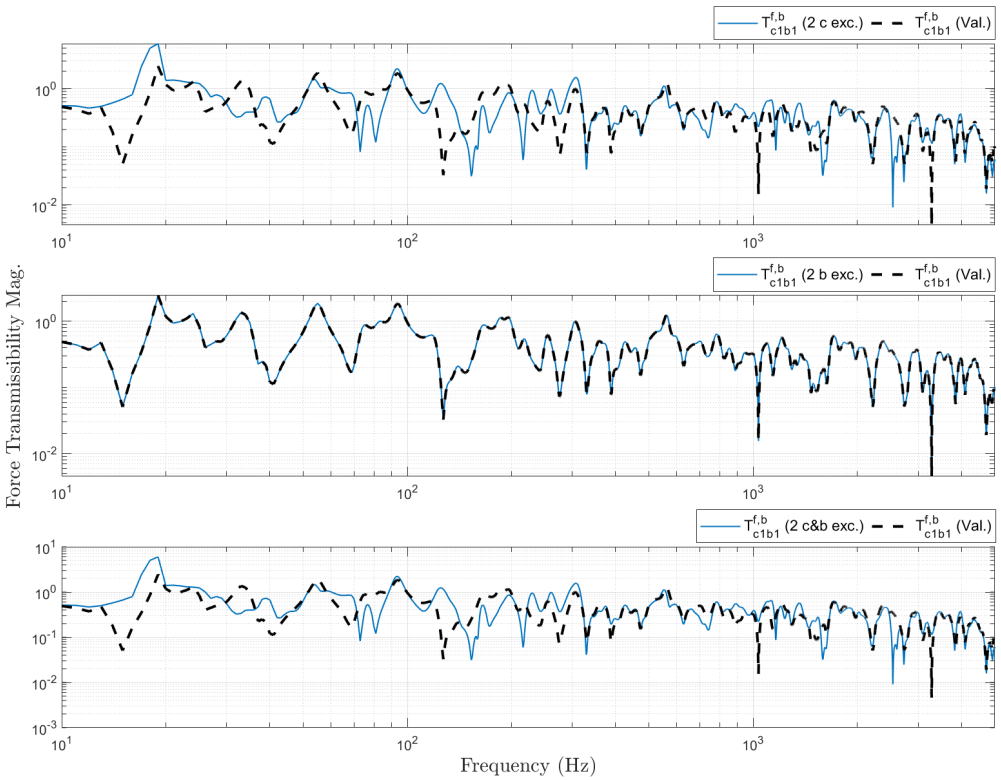

Figure 4.17: Mobility-based $\mathbf{T}_{cb}^{f,b}$. From top to bottom the force transmissibility is observed for one c excitation discarded, one b excitation discarded, and one excitation discarded from both c and b. This is compared to the validation plot where all excitations have been included.

In Fig.4.17, $\mathbf{T}_{cb}^{f,b}$ is calculated when two out of the three excitations are used. In the top

sub-figure the force transmissibility is calculated with two c excitation while all three are used in subset b. In the middle sub-figure, we have all three c excitations but two from b. Finally in the bottom sub-figure both c and b have two out of the three excitations used in testing. By reducing the number of c excitations by 1 in the top sub-figure, it shows invariance breaking down. We know this because the validation plot in this figure (where all three excitations are used in c and b) is the Plate 1 plot in Fig.4.12 which is almost identical to the plot for when Plate 2 was used. Thus it is indicated that the validation plot is invariant, and that deviations from this plot show invariance breaking down. Meanwhile the middle sub-figure, which discards one b excitation while keeping all three at c, shows little to no deviation from the validation plot. For the bottom sub-figure where one excitation was removed for both c and b, the transmissibility appears deviate from the validation plot almost identically to the top sub-figure. This indicates that altering the number of b excitations does not have a significant effect on calculating this force transmissibility, and that altering the number of excitations at c causes an error. The reason for this is because invariance comes from the blocking constraint applied at the interface DoFs c and not b. Additionally, changing the dimensions of the inverted $\mathbf{Y}_{cc}$ term in Eq. 4.23 causes additional errors. In other words, $\mathbf{Y}_{cc}$ is ill-conditioned, meaning it is very sensitive to input changes.

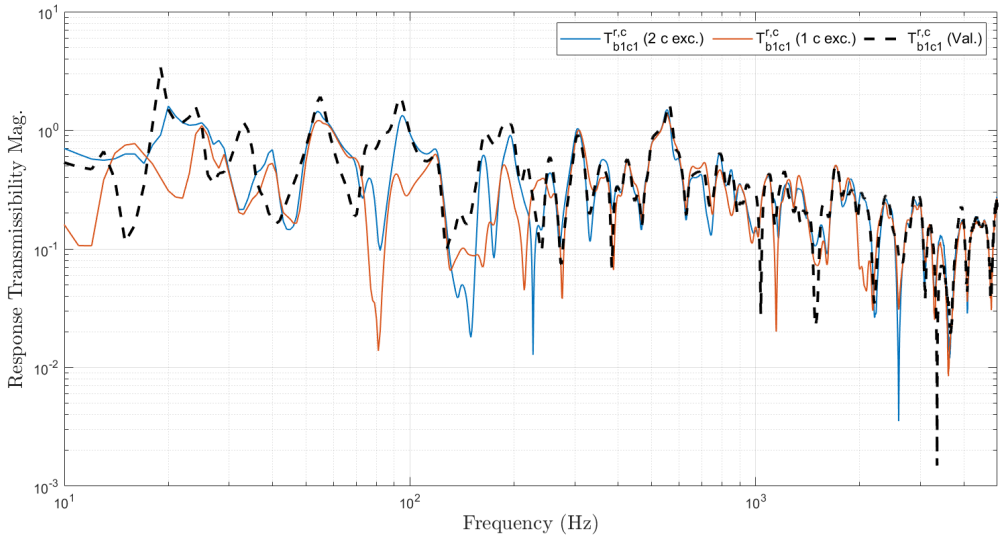

Figure 4.18: Mobility-based $\mathbf{T}^{r,c}_{bc}$. Response transmissibility is observed for 2 c excitations and 1 excitation. This is compared to the validation plot where all 3 excitations have been included.

Fig.4.18 shows the response transmissibility, calculated via Eq.4.11, when only one or two c excitations are used out of the three measured. It shows both scenarios deviating significantly from the validation plot between 10-275Hz, with the one c excitation case performing the worst in this region. However above 275Hz, both of these transmissibilities perform well and show reasonable precision to the validation transmissibility. There are only two particular frequencies in this 275Hz-5kHz region that show the largest error (resonances at 950Hz and 1.55kHz). Otherwise both plots show invariance in this frequency range.

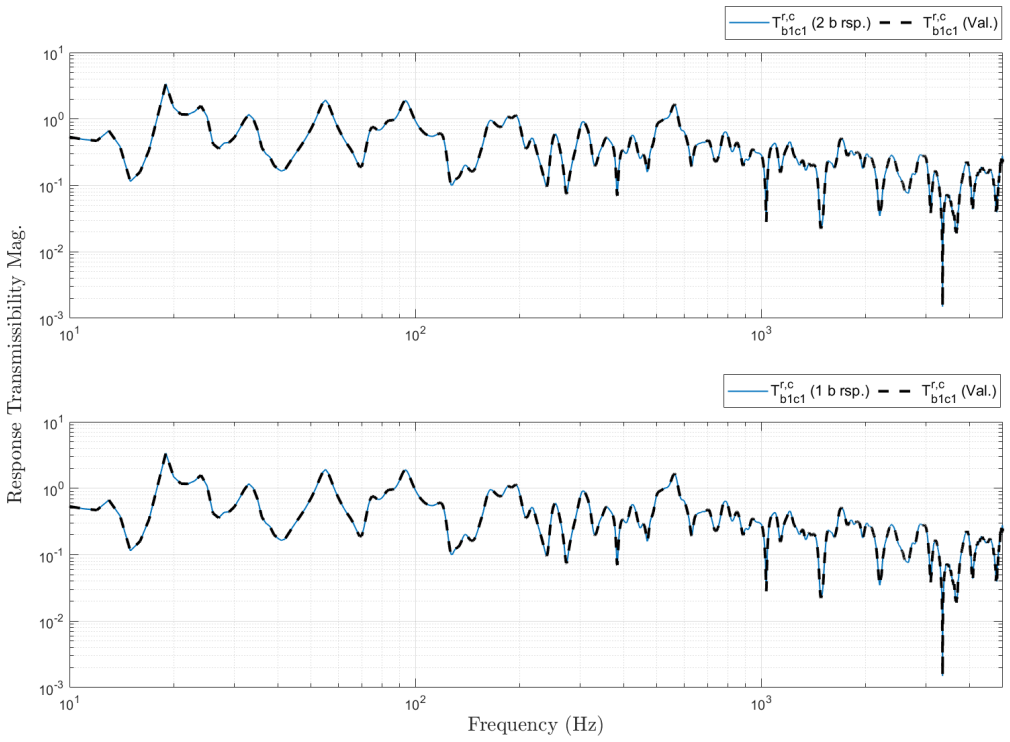

Figure 4.19: Mobility-based $\mathbf{T}^{r,c}_{bc}$, plotted when one or two b responses are used in calculation. Compared to the validation plot where all three b responses are included.

As explained earlier in this section, transmissibilities appear to be affected most when the inputs of the inverted mobility terms are altered, or if the blocking constraints at interface DoFs c have been altered by changing the number of DoFs within the subset. To highlight this further, Fig.4.19 presents $\mathbf{T}^{r,c}_{bc}$ when only one or two b responses out of the three are used. In Eq.4.11 the inverted term $\mathbf{Y}^{-1}_{cc}$ affected the accuracy of the response transmissibility when the c excitations were reduced, as demonstrated in Fig.4.18. Fig.4.19 shows the transmissibility is identical to the validation plot when the b responses have been reduced in calculation. This is because the mobility term $\mathbf{Y}_{bc}$ is not inverted, therefore matrix inversion error does not exist in this scenario, as well as there being no blocking constraint applied to subset b.

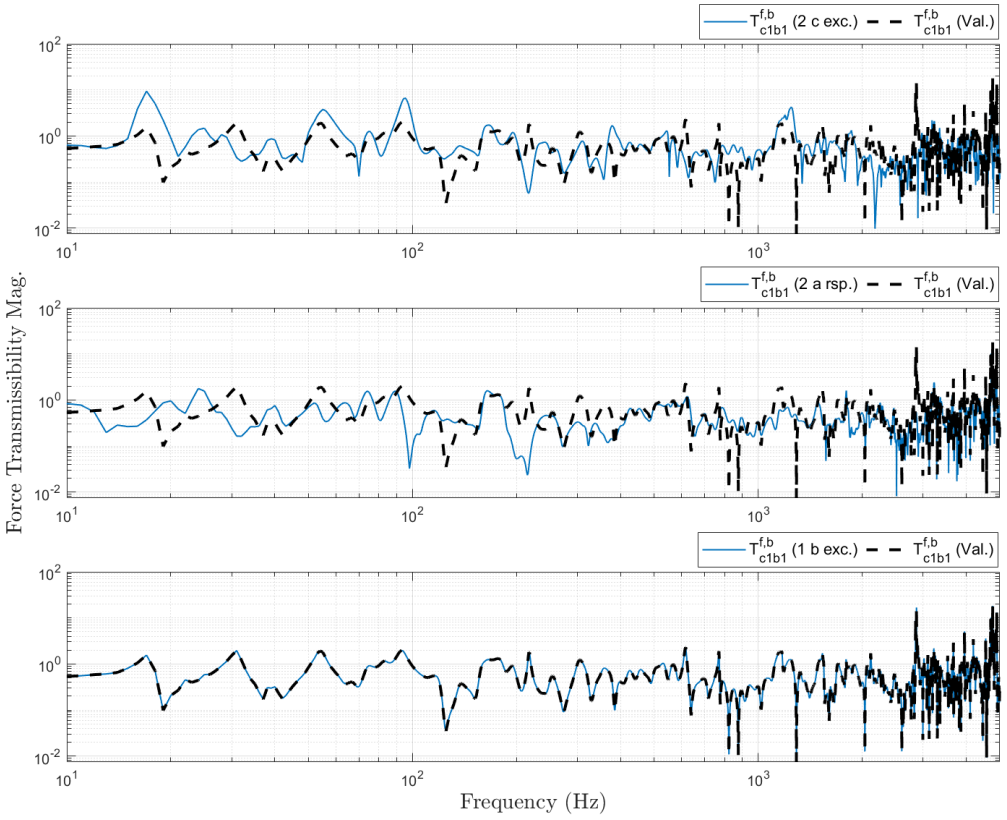

Figure 4.20: Mobility-based $\mathbf{T}_{cb}^{f,b}$, plotted when one or two b responses are used in calculation. Compared to the validation plot where all three b responses are included.

For example in Eq.4.22, another definition for $\mathbf{T}_{cb}^{f,b}$ exists that uses different mobilities. If one were to use this definition, which has the inverted term $\mathbf{Y}_{ac}^{-1}$ instead of $\mathbf{Y}_{cc}^{-1}$ in Eq.4.23, the force transmissibility will become less accurate by altering the c excitations as well as the a responses. This is demonstrated in the top and middle sub-figures within Fig.4.20 respectively. Both show deviation from the validation plot where all three a and c DoFs are used. Meanwhile in the bottom sub-figure the force transmissibility is calculated using only one b excitation being used. This affects the mobility term $\mathbf{Y}_{ab}$ in Eq.4.22 which is not inverted and has no blocking constraints within its definition, therefore appearing identical to the validation transmissibility.

Analysis is also conducted for the operational variant of $\mathbf{T}_{bc}^{r,c}$. Firstly, we observe the affect on the transmissibility when the number of b responses used in Eq.4.36 is altered.

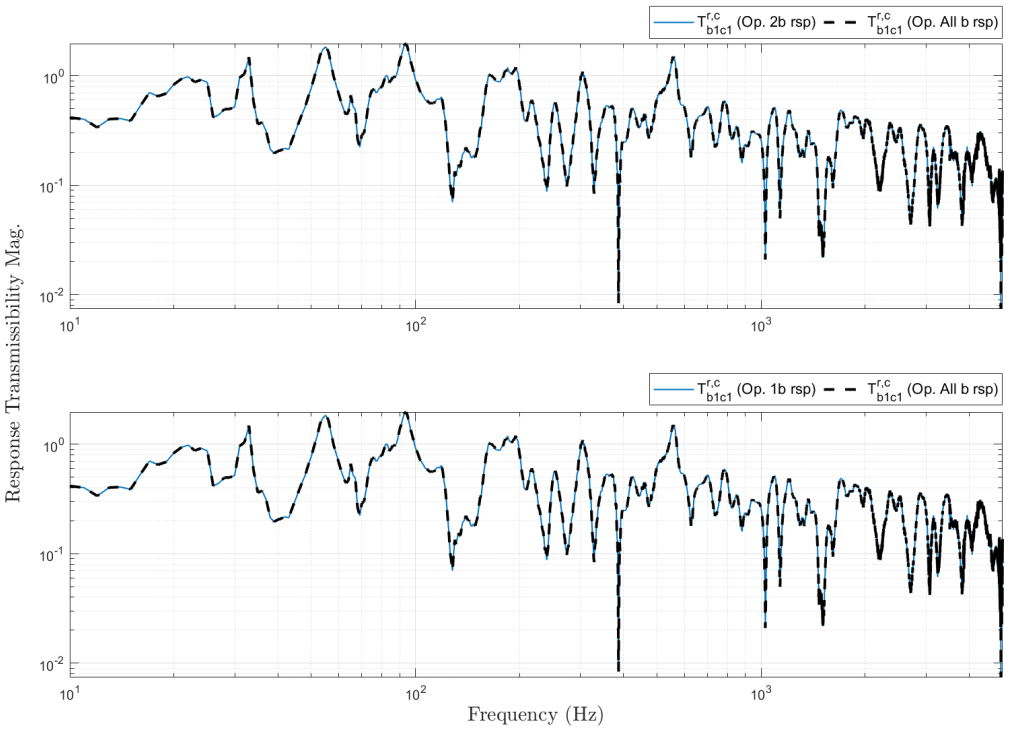

Figure 4.21: Operational $\mathbf{T}^{r,c}_{bc}$ for when one or two b responses are used in calculation. Compared to $\mathbf{T}^{r,c}_{bc}$ where all three b responses are included.

In the top and bottom sub-figures of Fig.4.21, $\mathbf{T}^{r,c}_{bc}$ is calculated using one or two b responses respectively and compared against the same transmissibility where all three have been used. It is clear that changing the dimensions of the term $\mathbf{V}_b$ in Eq.4.36 does not have any discernable effect on the transmissibility, similarly to Fig.4.19. If the number of responses is altered for the interface DoFs c, it is likely there would be a change to the transmissibility. This is because the term $\mathbf{V}_c$ has the blocking constraints applied and inverted, meaning small changes in the input will most likely have a large effect on the output. This was also shown previously for the mobility-based transmissibilities in Fig.4.18 and 4.20, where altering the number of DoFs in the inverted terms changed the transmissibilities.

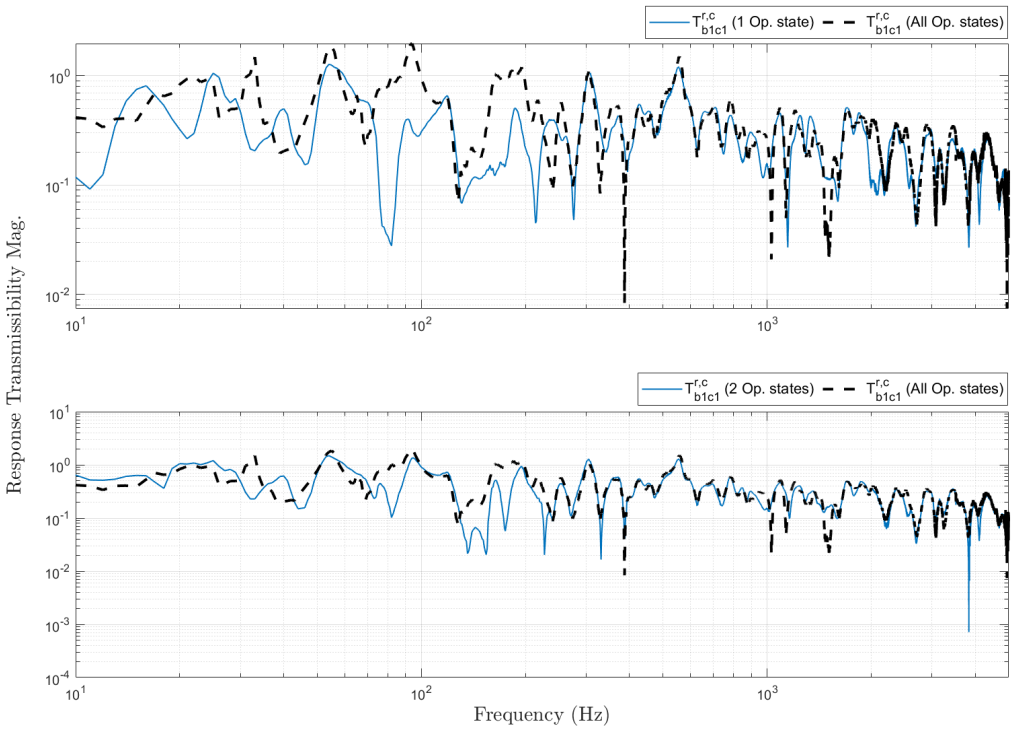

Figure 4.22: Changing operational states in output-only $\mathbf{T}_{bc}^{r,c}$. Compared to $\mathbf{T}_{bc}^{r,c}$ where all available operational states are included.

$\mathbf{T}_{bc}^{r,c}$ is analysed for when the number of operational states has been reduced. It is required that the number of operational states is equal to or more than the number of responses for both DoF subsets being used in calculation. Fig.4.22 shows when this is not followed, with the top and bottom sub-figures displaying $\mathbf{T}_{bc}^{r,c}$ for when one or two operational states are used respectively, and compared against the same transmissibility when all three operational states included. The three operational state transmissibility is used as a validation plot, as we know from Fig.4.14 it is very much in line with the FRF-based transmissibility, which is probably the most accurate means of measuring $\mathbf{T}_{bc}^{r,c}$. For the case using one operational state, there is good agreement for the majority of the frequency range. However it is in the lower frequencies (10-250Hz) where it does not follow all operational states $\mathbf{T}_{bc}^{r,c}$ well. The transmissibility with two operational states shows a much better performance overall, especially in the lower frequency range. As $\mathbf{V}_c$ has the blocking constraints applied to the c DoFs, and affecting the operational state input changes as it is inverted, has as expected changed the

transmissibility.

4.3.4 Force and response transmissibility relation

Lage et al. [2014] demonstrate force and response transmissibilities are related via an inverse transpose operation. This is because of the way their transmissibility notation is defined. In this case the inverse matrix operation changes the direction of the transmissibility. However in the alternative definitions made in Section 2.7.2 where the direction is included in the notation, only a transpose operation is needed. With this in mind, this section will show that it should be possible to observe invariance when applying the transpose of a transmissibility, I.e. the transposed transmissibility will be similar to that of the original transmissibility which has already been deemed invariant. One may recognise from the previous figures that $\mathbf{T}_{cb}^{f,b}$ and $\mathbf{T}_{bc}^{r,c}$ plots look similar to one another. This is because they are related by a transpose operation, which was derived earlier in Eq.4.25.

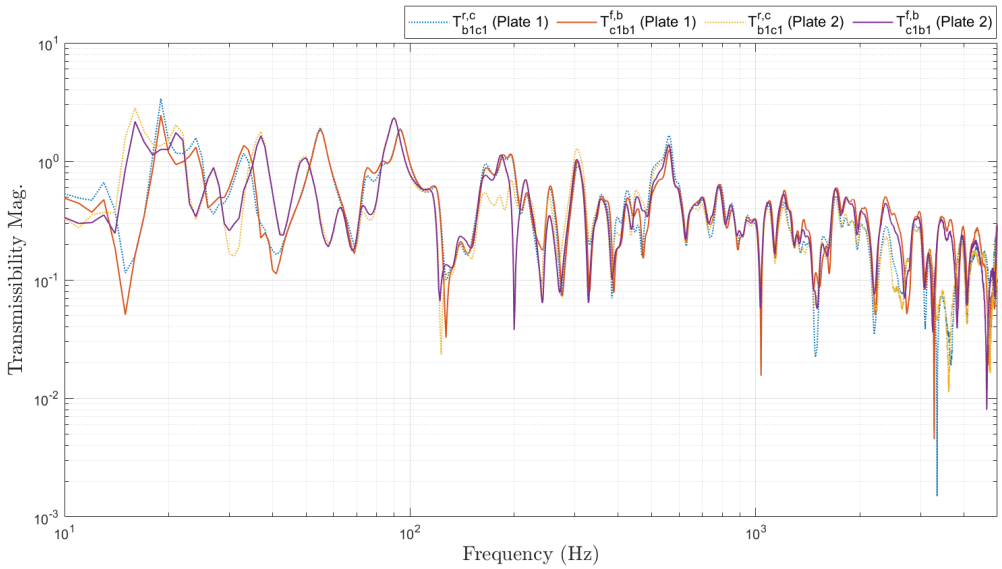

Figure 4.23: Mobility-based $\mathbf{T}_{cb}^{f,b}$ and $\mathbf{T}_{bc}^{r,c}$ for either A plate coupled to the assembly.

Fig.4.23 shows overall that $\mathbf{T}_{cb}^{f,b}$ and $\mathbf{T}_{bc}^{r,c}$ are similar for both A plates coupled to the assembly. Between 10-100Hz it is clear that the response and force transmissibilities for a particular plate scenario align with each other, but do not correspond to the trans-

missibilities determined for the other plate. I.e. Within this frequency range $\mathbf{T}_{cb}^{f,b}$ and $\mathbf{T}_{bc}^{r,c}$ for plate 1 are similar, but do not match with $\mathbf{T}_{cb}^{f,b}$ and $\mathbf{T}_{bc}^{r,c}$ determined for plate 2. This is likely due to differing amounts of loading provided by plate 1 and 2. Plate 1 is made of steel which is much heavier than plate 2 which is perspex. Furthermore, there are particular resonances where the transmissibility of one plate aligns with the same transmissibility from the other, I.e. $\mathbf{T}_{cb}^{f,b}$ for plate 1 and 2, as well as $\mathbf{T}_{bc}^{r,c}$ for plate 1 and 2 being similar. This is observed at 2.4kHz and 3.5kHz.

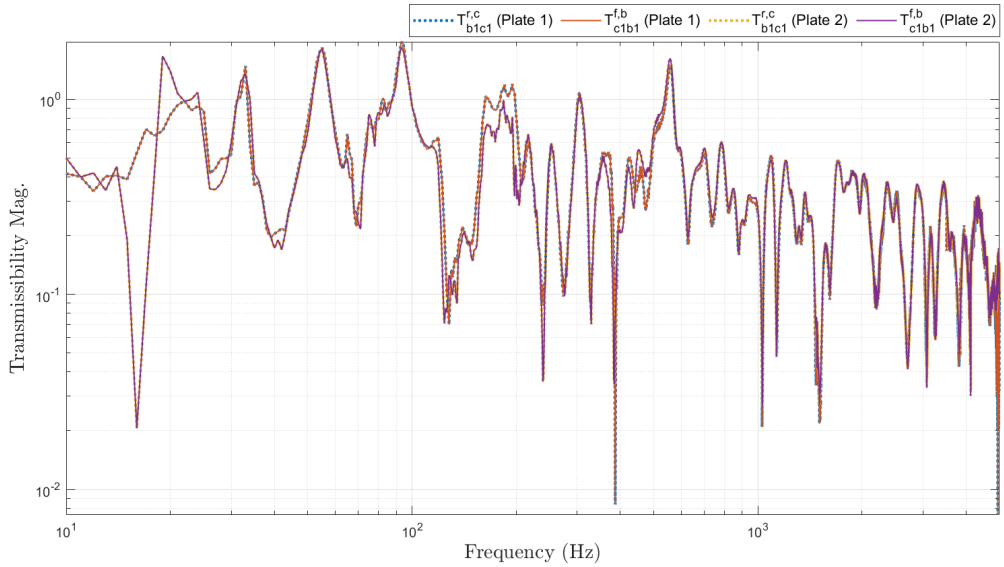

Figure 4.24: Operational $\mathbf{T}_{cb}^{f,b}$ and $\mathbf{T}_{bc}^{r,c}$ for either A plate coupled to the assembly.

Analysis is also conducted on the relation between operational $\mathbf{T}_{cb}^{f,b}$ and $\mathbf{T}_{bc}^{r,c}$. Fig.4.24 shows the transpose relation between $\mathbf{T}_{cb}^{f,b}$ and $\mathbf{T}_{bc}^{r,c}$ for a particular plate coupled is identical, i.e for plate 1 $\mathbf{T}_{cb}^{f,b}$ and $\mathbf{T}_{bc}^{r,c}$ are the same, as well as for plate 2. While the transmissibilities were very similar to each for the mobility-based transmissibilities, they weren't as closely related like the operational ones. Overall, all transmissibility plots are very closely aligned to one another, with some slight differences between plate cases between 10-200Hz. From 200Hz and above all plots follow each other very closely.

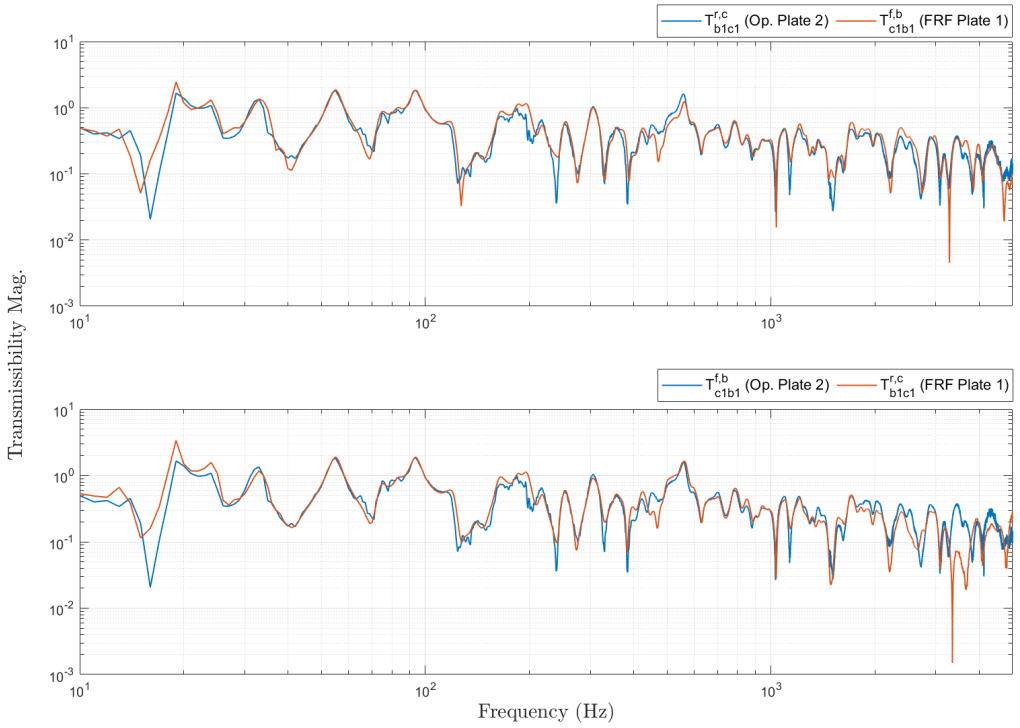

Figure 4.25: Comparison between $\mathbf{T}^{f,b}_{cb}$ and $\mathbf{T}^{r,c}_{bc}$ when calculated operationally or by FRFs. Additionally, different A components are coupled for each transmissibility calculation.

In Fig.4.25 a comparison is made between force and response transmissibilities by the way they were calculated (Output-only or FRF), as well as by which A plate is coupled to the assembly. For example in the top-figure, $\mathbf{T}^{r,c}_{bc}$ is determined operationally using plate 2, and compared against $\mathbf{T}^{f,b}_{cb}$ which is calculated using mobilities and with plate 1 coupled to the assembly. In the bottom sub-figure, a similar comparison is made where $\mathbf{T}^{f,b}_{cb}$ is determined operationally with plate 2 coupled, versus $\mathbf{T}^{r,c}_{bc}$ which is calculated using mobilities and plate 1. Both sub-figures show the transposition relation between these transmissibilities irrespective of which A component is coupled, or if they are determined operationally or by mobilities. Thus it is indicated invariance can be observed when comparing two related transmissibilities, whether they have been calculated using operational responses or FRFs.

4.4 Beam-plate experimental example

Invariance of transmissibilities is analysed on another experimental setup similar to that shown in Fig.4.4. The interchanged beam components represented by A, and plate B are kept the same. DoF subsets b and c are also the same locations, but there are no a sensors installed. For the FRF measurement, 20 excitations are applied within A in all translational planes (10 in z, 8 in y, and 2 in x), in addition to the ones applied to each sensor in subsets b and c. The single resilient mount at c has been interchanged with a rigid connection.

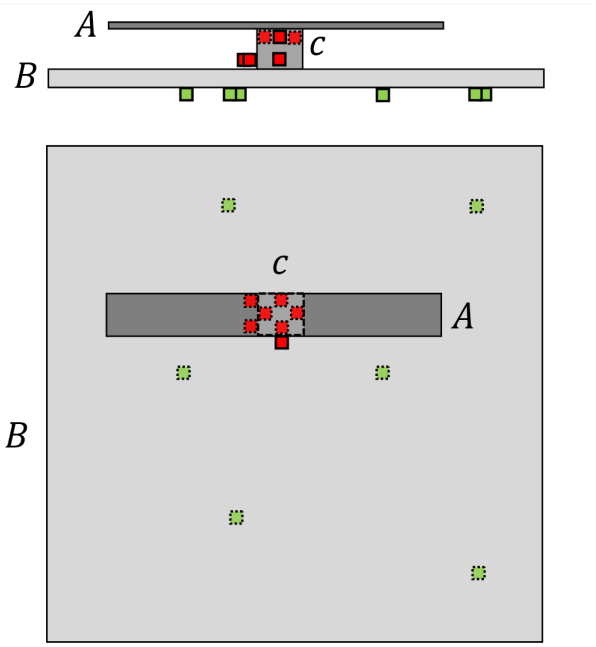

Figure 4.26: 2D diagram of rigid point connection case between beam A and plate B.

This adds a layer of complexity. In the previous experimental examples, the interface motion was dominated mostly in the z-axis. Other translational and rotational DoFs are dampened significantly and deemed negligible. This is why only a single response at c facing the z-axis is used at the resilient connections. However, evidence shown by Meggitt and McGee [2024] suggests an increase in error can occur at higher frequencies, which is attributed to the lack of rotational DoFs. This is perhaps a reason for the divergence between plots in the higher frequencies for Fig. 4.15 and 4.16. For an experimental case with a rigid mount as shown in Fig.4.26, multiple DoFs must be

factored in when characterising the interface c. Experimentally and data processing-wise, it is more involved to determine all six degrees of motion: translational x, y, z and rotational α, β, and γ. Analyses on the invariance of transmissibilities is similar to the previous experimental examples, with the addition of observing the extent invariance exists while translational and rotational DoFs are discarded at the interface c. It must be noted that the most significant DoFs at c are not universally applicable, and most likely will differ for experimental setups of a different nature. The purpose of this part of the study is to examine the extent invariance can be observed, while interface DoFs are incrementally discarded.

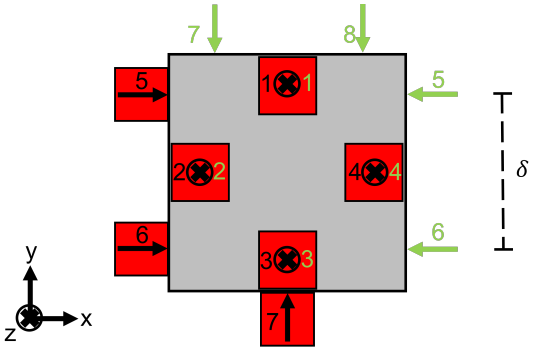

Figure 4.27: Diagram of fully characterised point interface used in the rigid connection beam-plate experimental example.

The finite-difference method was used to characterise the rigid interface mount c for Fig.4.26. The derivation made in Section 2.8.2 was in reference to a 2 dimensional beam, but for this experimental example we must derive the approximation in 3 dimensions. A diagram of how this was conducted experimentally on the rigid interface test rig is illustrated in Fig.4.27. Red squares represent uni-axial sensor positions. Black arrows and numbers show the order and direction of responses, while the ones in green show the order and direction of excitations. The finite-difference approximation of the interface point mobility, $\hat{\mathbf{Y}}_{cc}$, is calculated via,

$$\hat{\mathbf{Y}}_{cc} \approx \mathbf{R}_v \mathbf{Y}_{cc} \mathbf{R}_f^{\mathrm{T}} \tag{4.38}$$

In matrix form, the finite difference approximation of the interface point mobility is given,

$$\hat{\mathbf{Y}}_{cc} = \begin{bmatrix} \hat{Y}_{xx} & \hat{Y}_{xy} & \hat{Y}_{xz} & \hat{Y}_{x\alpha} & \hat{Y}_{x\beta} & \hat{Y}_{x\gamma} \\ \hat{Y}_{yx} & \hat{Y}_{yy} & \hat{Y}_{yz} & \hat{Y}_{y\alpha} & \hat{Y}_{y\beta} & \hat{Y}_{y\gamma} \\ \hat{Y}_{zx} & \hat{Y}_{zy} & \hat{Y}_{zz} & \hat{Y}_{z\alpha} & \hat{Y}_{z\beta} & \hat{Y}_{z\gamma} \\ \hat{Y}_{\alpha x} & \hat{Y}_{\alpha y} & \hat{Y}_{\alpha z} & \hat{Y}_{\alpha\alpha} & \hat{Y}_{\alpha\beta} & \hat{Y}_{\alpha\gamma} \\ \hat{Y}_{\beta x} & \hat{Y}_{\beta y} & \hat{Y}_{\beta z} & \hat{Y}_{\beta\alpha} & \hat{Y}_{\beta\beta} & \hat{Y}_{\beta\gamma} \\ \hat{Y}_{\gamma x} & \hat{Y}_{\gamma y} & \hat{Y}_{\gamma z} & \hat{Y}_{\gamma\alpha} & \hat{Y}_{\gamma\beta} & \hat{Y}_{\gamma\gamma} \end{bmatrix} \tag{4.39}$$

The measured point mobility is given by,

$$\mathbf{Y}_{cc} = \begin{bmatrix} Y_{v_1f_1} & Y_{v_1f_2} & Y_{v_1f_3} & Y_{v_1f_4} & Y_{v_1f_5} & Y_{v_1f_6} & Y_{v_1f_7} & Y_{v_1f_8} \\ Y_{v_2f_1} & Y_{v_2f_2} & Y_{v_2f_3} & Y_{v_2f_4} & Y_{v_2f_5} & Y_{v_2f_6} & Y_{v_2f_7} & Y_{v_2f_8} \\ Y_{v_3f_1} & Y_{v_3f_2} & Y_{v_3f_3} & Y_{v_3f_4} & Y_{v_3f_5} & Y_{v_3f_6} & Y_{v_3f_7} & Y_{v_3f_8} \\ Y_{v_4f_1} & Y_{v_4f_2} & Y_{v_4f_3} & Y_{v_4f_4} & Y_{v_4f_5} & Y_{v_4f_6} & Y_{v_4f_7} & Y_{v_4f_8} \\ Y_{v_5f_1} & Y_{v_5f_2} & Y_{v_5f_3} & Y_{v_5f_4} & Y_{v_5f_5} & Y_{v_5f_6} & Y_{v_5f_7} & Y_{v_5f_8} \\ Y_{v_6f_1} & Y_{v_6f_2} & Y_{v_6f_3} & Y_{v_6f_4} & Y_{v_6f_5} & Y_{v_6f_6} & Y_{v_6f_7} & Y_{v_6f_8} \\ Y_{v_7f_1} & Y_{v_7f_2} & Y_{v_7f_3} & Y_{v_7f_4} & Y_{v_7f_5} & Y_{v_7f_6} & Y_{v_7f_7} & Y_{v_7f_8} \end{bmatrix} \tag{4.40}$$

Response and applied force transformation matrices, $\mathbf{R}_v$ and $\mathbf{R}_f$ respectively, are in the form,

$$\mathbf{R}_v = \begin{bmatrix} 0 & 0 & 0 & 0 & \frac{1}{2} & \frac{1}{2} & 0 \\ 0 & 0 & 0 & 0 & 0 & 0 & 1 \\ \frac{1}{4} & \frac{1}{4} & \frac{1}{4} & \frac{1}{4} & 0 & 0 & 0 \\ \frac{1}{\delta} & 0 & -\frac{1}{\delta} & 0 & 0 & 0 & 0 \\ 0 & \frac{1}{\delta} & 0 & -\frac{1}{\delta} & 0 & 0 & 0 \\ 0 & 0 & 0 & 0 & \frac{1}{\delta} & -\frac{1}{\delta} & 0 \end{bmatrix} \tag{4.41}$$

$$\mathbf{R}_f = \begin{bmatrix} 0 & 0 & 0 & 0 & -\frac{1}{2} & -\frac{1}{2} & 0 & 0 \\ 0 & 0 & 0 & 0 & 0 & 0 & \frac{1}{2} & \frac{1}{2} \\ \frac{1}{4} & \frac{1}{4} & \frac{1}{4} & \frac{1}{4} & 0 & 0 & 0 & 0 \\ \frac{1}{\delta} & 0 & -\frac{1}{\delta} & 0 & 0 & 0 & 0 & 0 \\ 0 & \frac{1}{\delta} & 0 & -\frac{1}{\delta} & 0 & 0 & 0 & 0 \\ 0 & 0 & 0 & 0 & \frac{1}{\delta} & -\frac{1}{\delta} & 0 & 0 \end{bmatrix} \tag{4.42}$$

Columns in $\mathbf{R}_v$ and $\mathbf{R}_f$ indicate the response or excitation DoFs indices respectively. Rows correspond to translational and rotational DoFs. The order from row 1 to 6 goes x, y, z, α, β, γ. The first three rows: x, y, z, are translational DoFs. Rows four to 6: α, β, γ are rotational DoFs. Due to the 7 responses at this mounting point, $\mathbf{R}_v$ is a 6 $\times$ 7 matrix, while $\mathbf{R}_f$ is a 6 $\times$ 8 matrix due to 8 applied excitations.

4.4.1 Interchanging coupled component

In this section $\mathbf{T}_{bc}^{r,c}$ and $\mathbf{T}_{cb}^{f,b}$ are calculated when either beam 1 or 2 is used as component A. Beams 1 and 2 differ in dimensions, and are the exact ones used in the preliminary experimental example shown in Fig.4.5. In theory, by characterising the interface c by all translational and rotational DoFs, the transmissibilities of component B will be identical for either A beam coupled to the assembly.

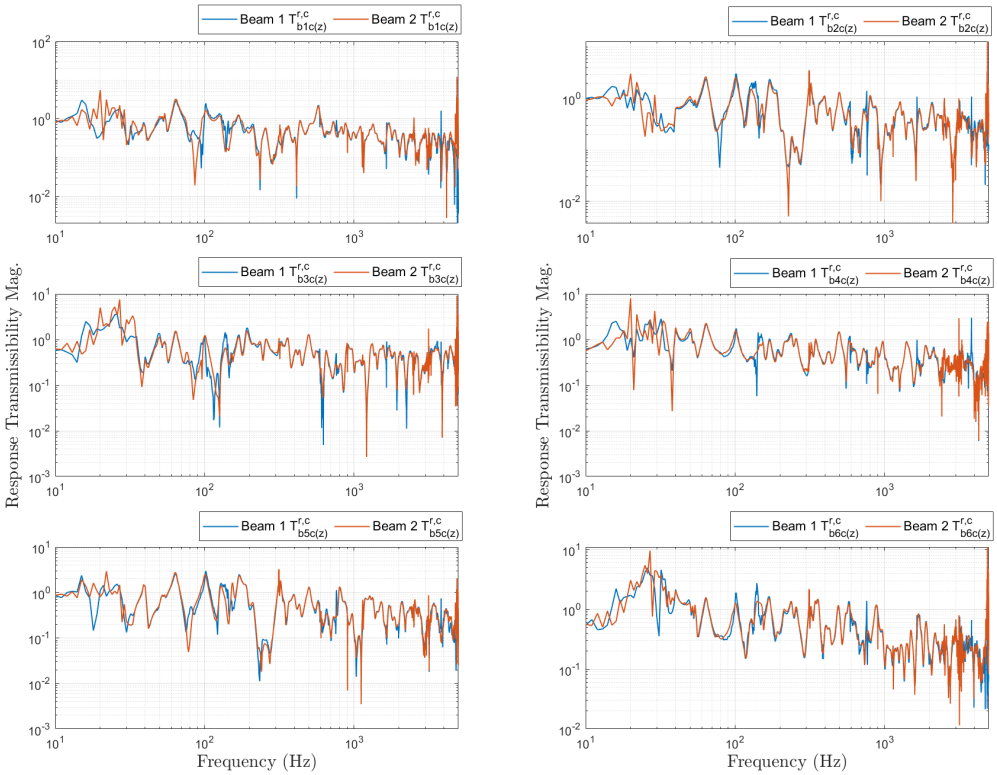

Figure 4.28: Mobility-based $\mathbf{T}_{bc}^{r,c}$ with either beam 1 or 2 coupled to the assembly.

In the above figure $\mathbf{T}_{bc}^{r,c}$ is calculated via mobilities, and determined between each DoF in subset b and the z translation DoF at the interface c. In Fig.4.28, overall all response transmissibilities between each b response and the z-translation at c show good agreement for when either A beam is coupled. In each sub-figure slight differences are visible at very low frequencies (around 10-30Hz), but above this range the response transmissibilities are almost identical for either beam coupled.

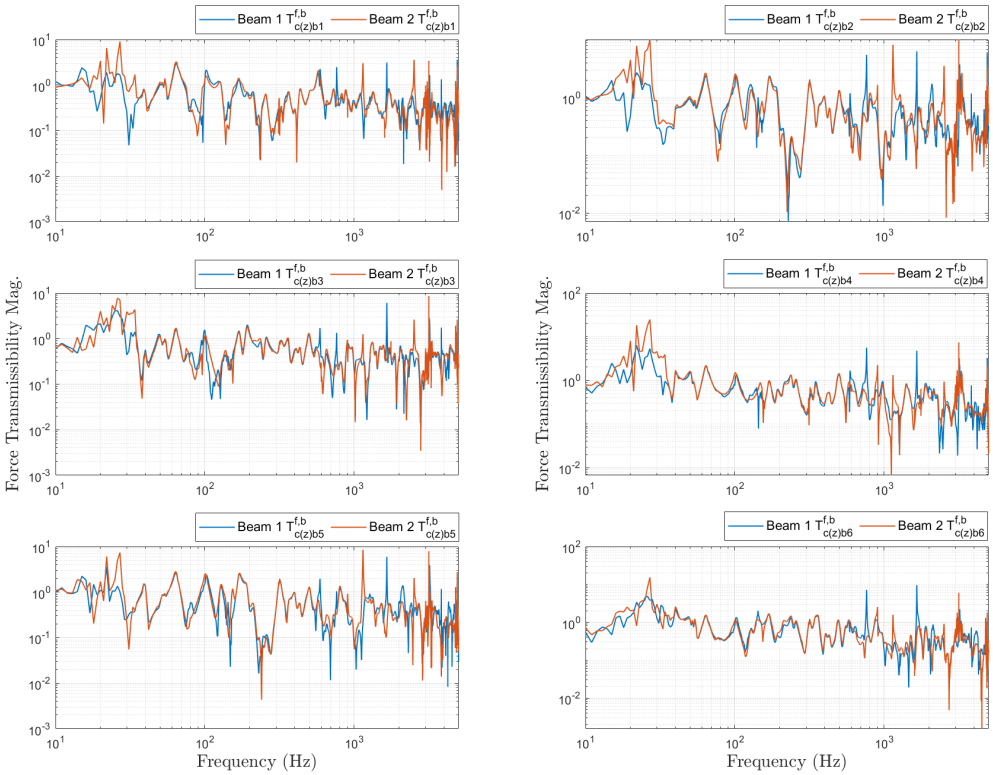

Figure 4.29: Mobility-based $\mathbf{T}_{cb}^{f,b}$ with either beam 1 or 2 coupled to the assembly.

Similarly for the mobility-based $\mathbf{T}_{cb}^{f,b}$ in Fig.4.29, there are six sub-figures plotting the transmissibilities between each DoF in b and the z translation at the interface c. Slight differences are also observed between A beam cases in the 10-30Hz region. In addition, there are some small differences higher up in the frequency range. For example, beam 1 and 2 test scenarios for the sub-figure containing $\mathbf{T}_{c(z)b_2}^{f,b}$ show differences at resonances at 1.2kHz and 1.4kHz. Furthermore, a slight disparity can be observed between 720Hz-1.25kHz for $\mathbf{T}_{c(z)b_4}^{f,b}$. Despite the small errors between either A beam cases, the force transmissibilities are similar to one another for the vast majority of the frequency range. Thus overall it is suggested invariance is also visible when observing the force transmissibility. However when compared to the response transmissibility, Fig.4.28 does shows slightly better agreement between beam cases at higher frequencies. In the next part of this subsection, the force and response transmissibilities are analysed for invariance when certain DoFs at c are not included in their calculation.

The invariance of output-only $\mathbf{T}_{cb}^{f,b}$ and $\mathbf{T}_{bc}^{r,c}$ is also analysed. In Section 4.3.1 the operational definition of these transmissibilities were derived, with definitions given by Eq.4.36 and 4.37.

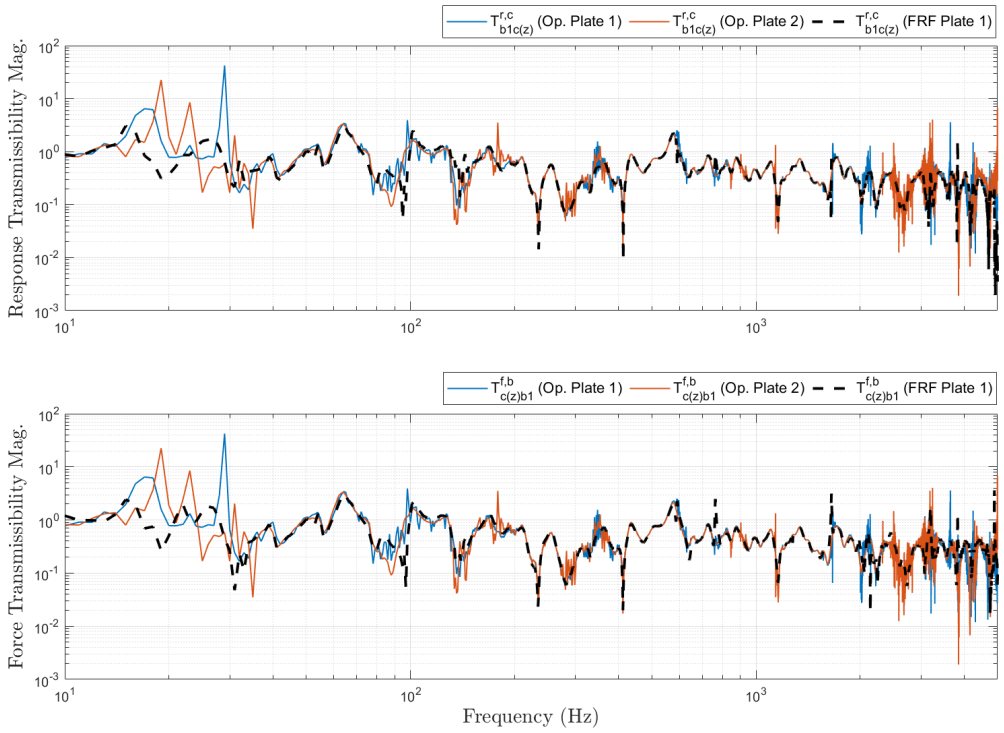

Figure 4.30: $\mathbf{T}_{bc}^{r,c}$ and $\mathbf{T}_{cb}^{f,b}$ determined via operational velocities, compared against validation FRF measurement.

Similarly to the previous experimental example in Fig.4.14, the operational transmissibilities are calculated when either beam 1 or 2 is coupled to the assembly. As the mobility-based transmissibilities were nearly identical when either A component was coupled, for clarity reasons only one of these is used in the above figure to compare the operational transmissibilities to (beam 1). Fig.4.30 shows that the operational transmissibilities have increased noise over their FRF-based counterparts in Fig. 4.29 and 4.28. The above figure also displays the operational versions of $\mathbf{T}_{bc}^{r,c}$ and $\mathbf{T}_{cb}^{f,b}$ as being very similar when either A beam is coupled to the assembly. Furthermore, they also agree well with the FRF-based transmissibility (black dashed line), suggesting the transmissibility of B appears invariant despite which method is used to calculate them. Thus, it is indicated by this figure that the operational transmissibilities are invariant for

this experimental example.

4.4.2 Transmissibility excitation positioning

As was assumed in the previous experimental case studies for this analysis, let's assume A is an active component and B is passive one within the coupled assembly. A comparison is made between the transmissibilities $\mathbf{T}_{bc}^{r,a}$ and $\mathbf{T}_{bc}^{r,c}$ for this assembly, to deduce whether excitation positioning within the active component A has an effect on the transmissibility of the passive component B.

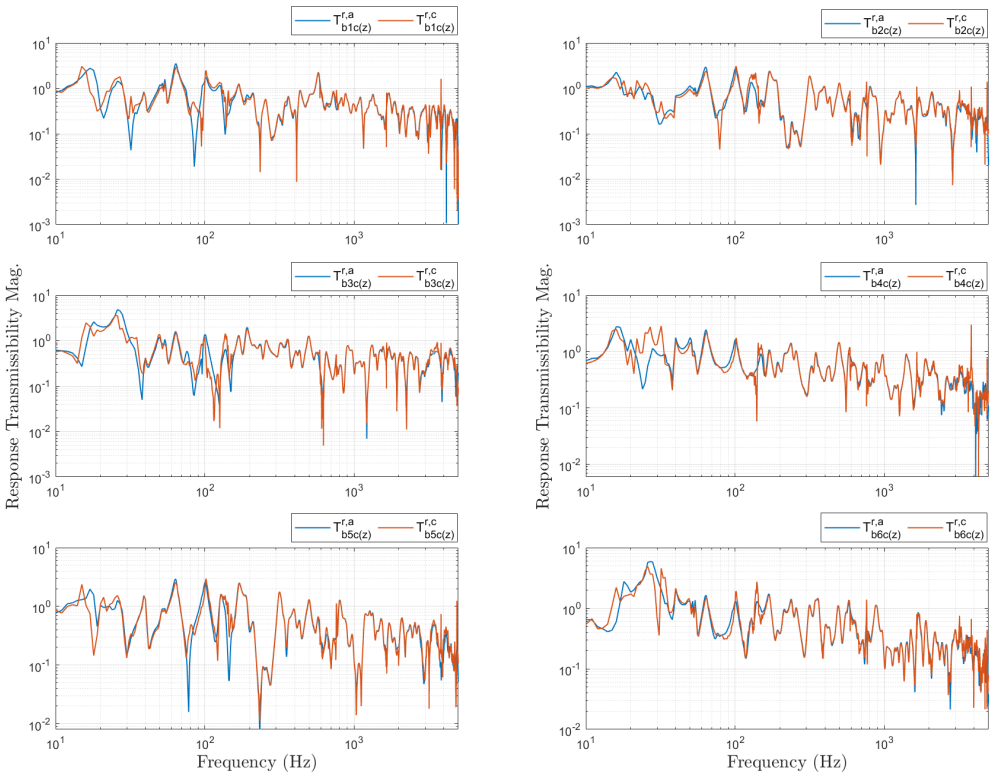

Figure 4.31: Mobility-based $\mathbf{T}_{bc}^{r,a}$ vs. $\mathbf{T}_{bc}^{r,c}$. Each sub-figure shows the transmissibility between the z DoF of interface c and each b response. In reference to rigid-interface test rig, Fig.4.26

In Fig.4.31 there are six sub-figures, each plotting FRF-based transmissibilities $\mathbf{T}_{bc}^{r,a}$ and $\mathbf{T}_{bc}^{r,c}$ determined between every b DoF and the z DoF of the interface c. Similarly to the previous experimental examples, the result for this test rig suggests wherever the excitation location is within the active component (A), the transmissibility of B remains

the same (within experimental error) as $\mathbf{T}_{bc}^{r,a}$ and $\mathbf{T}_{bc}^{r,c}$ appear almost identical to each other. Furthermore, increased noise is apparent from roughly 3kHz and above for $\mathbf{T}_{bc}^{r,a}$ in the previous test examples. It was suggested that this likely due to attenuation induced noise from the isolators, because this transmissibility's excitation is at a and traverses the mount. The above figure does not show increased noise in $\mathbf{T}_{bc}^{r,a}$ for the rigid-interface experiment, indicating that the presence of isolators had an effect on the accuracy of this particular transmissibility. Some small differences are observed in low frequencies between $\mathbf{T}_{bc}^{r,a}$ and $\mathbf{T}_{bc}^{r,c}$ (10-30Hz), but above this range they are almost identical.

In the next part of this sub-section, these transmissibilities are analysed when calculated via operational responses (Eq.4.36 and 4.31).

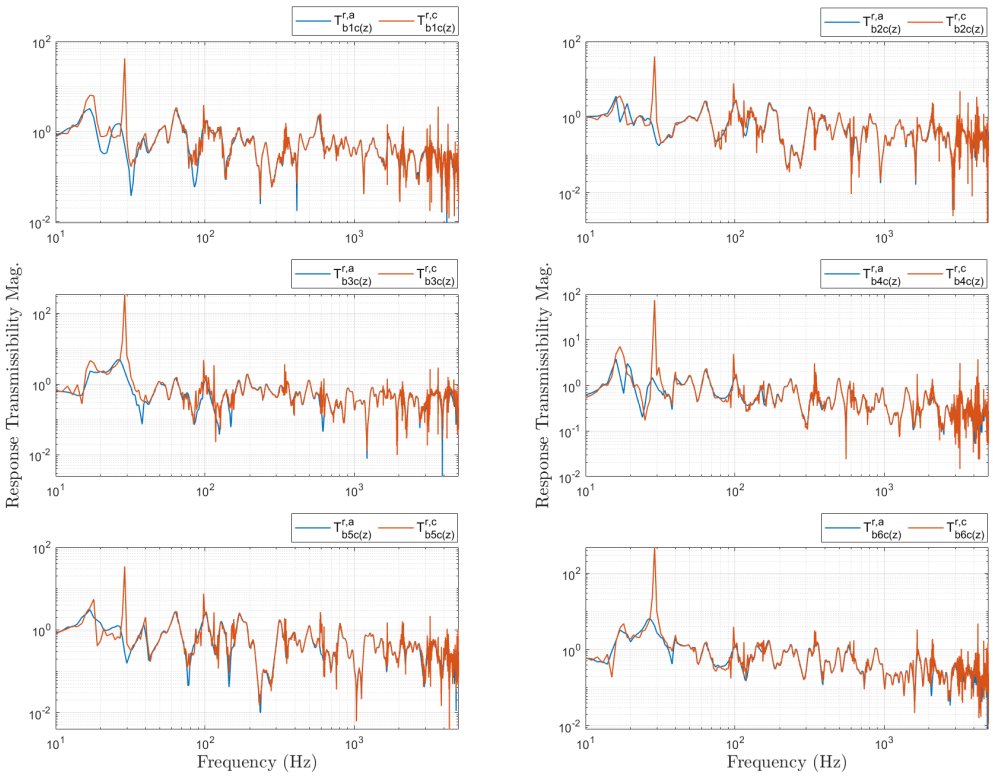

Figure 4.32: Operational $\mathbf{T}_{bc}^{r,a}$ vs. $\mathbf{T}_{bc}^{r,c}$. Each sub-figure shows the transmissibility between the z DoF of interface c and each b response. In reference to rigid-interface test rig, Fig.4.26

In a similar fashion, Fig.4.32 shows $\mathbf{T}_{bc}^{r,a}$ and $\mathbf{T}_{bc}^{r,c}$ are also almost identical when cal-

culated operationally. However some differences are apparent between the two ways of calculating these transmissibilities. Both operational transmissibilities show a small increase in noise, and a large spike at 29Hz can be seen consistently across all sub-figures for $\mathbf{T}_{bc}^{r,c}$ which is likely due to experimental error.

4.4.3 Altering which interface DoFs are included in the transmissibility calculation

In this section, the purpose is to analyse whether transmissibilities are still invariant when DoFs at the interface c are discarded. In a standard calculation of $\mathbf{T}_{cb}^{f,b}$ and $\mathbf{T}_{bc}^{r,c}$ via Eq.4.23 and 4.11 respectively, all c DoFs (x,y,z,α,β,γ) are included in the mobility terms. Instead the transmissibilities will be calculated when only some of these c DoFs are included in the mobility terms.

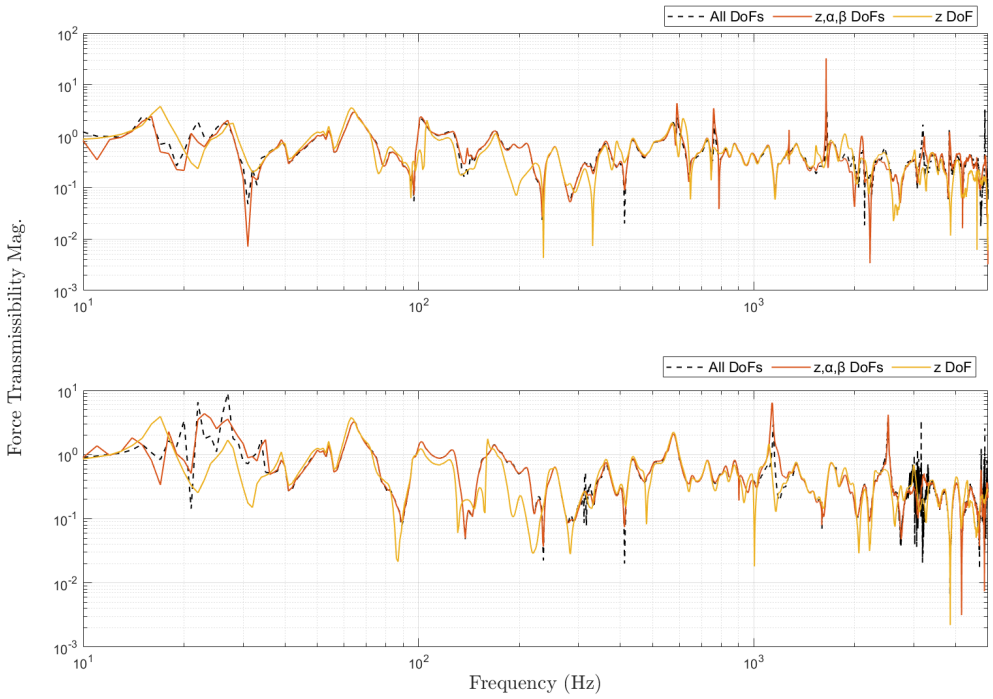

Figure 4.33: Mobility-based $\mathbf{T}_{c(z)b_1}^{f,b}$, determined using all six DoFs at c, translation z with α and β rotational DoFs, and z only. Top sub-figure shows plots of $\mathbf{T}_{c(z)b_1}^{f,b}$ when beam 1 is coupled, while the bottom sub-figure is for beam 2.

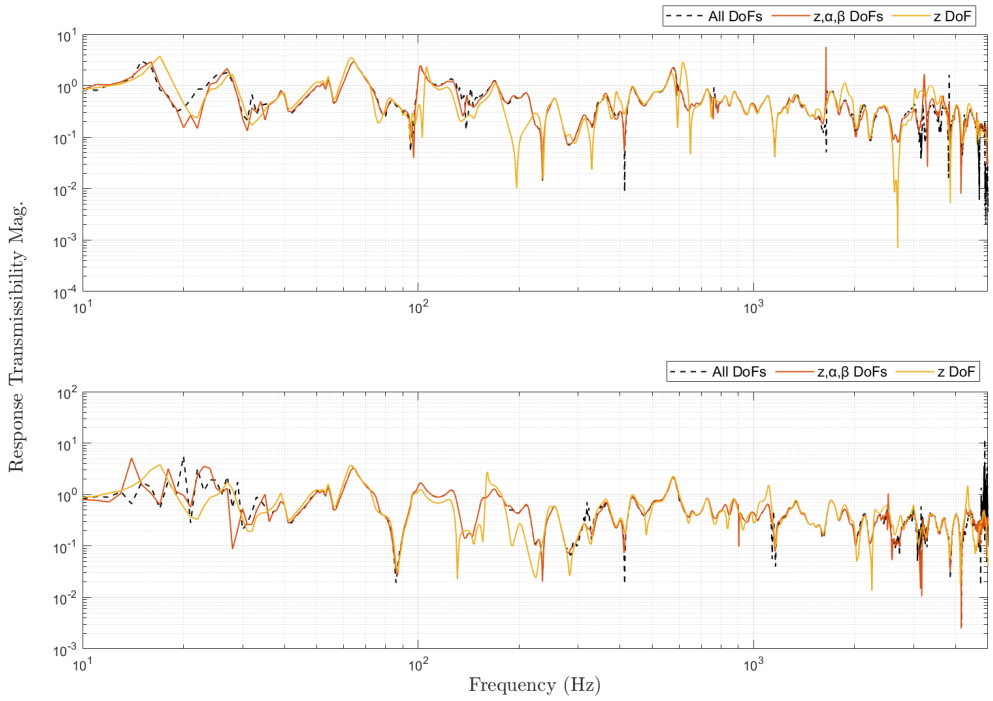

Figure 4.34: Mobility-based $\mathbf{T}^{r,c}_{b_1c(z)}$ determined using all six DoFs, translation z with α and β rotational DoFs, and z only. Top sub-figure shows these plots of $\mathbf{T}^{r,c}_{b_1c(z)}$ when beam 1 is coupled, while the bottom sub-figure is for beam 2.

Fig.4.33 and 4.34 plot $\mathbf{T}^{f,b}_{cb}$ and $\mathbf{T}^{r,c}_{bc}$ respectively, by either using all DoFs, or z, α and β DoFs, or only the z DoF, from the interface c. Each figure contains two sub-figures, the top one plots transmissibilities that were calculated with beam 1 coupled to the assembly, and the bottom one was with beam 2. Both figures indicate that when x, y and γ DoFs have been discarded from calculating the transmissibility (red plot), it is quite similar to the standard case where 'All DoFs' are accounted for from c (dashed black line). For the z only version of $\mathbf{T}^{f,b}_{cb}$ and $\mathbf{T}^{r,c}_{bc}$, similarities to the 'All DoFs' transmissibilities are also visible, but to a lesser degree than the z, α, β transmissibilities. For example, take the bottom subplot of Fig.4.33 where beam 2 is coupled to the system. The z only $\mathbf{T}^{f,b}_{c(z)b_1}$ shows the largest difference to the 'All DoFs' transmissibility between 82-230Hz. With the exception of errors occurring at low frequencies (10-35Hz), and for a few amplified anti-resonance magnitudes (285Hz, 480Hz, 1kHz, 2.05kHz, 2.2kHz), the overall trend of the z only transmissibility follows the 'All DoFs' plot to a satisfactory level. This can also be said for the beam 1 test scenario in the top sub-figure. The z

only transmissibility also shows the largest difference in a similar frequency range of about 100-230Hz, and a few spikes in magnitude at some anti-resonance. The only noticeable difference is the low frequency performance, which appears close to the 'All DoFs' transmissibility. Similar observations of the z only force transmissibility performance can be seen for the same beam scenario of the response transmissibility in Fig.4.34. Overall, the above figures suggest that the z translation DoF is the biggest contributor at c for determining the transmissibilities. This is understandable due to $\mathbf{T}^{f,b}_{c(z)b_1}$ being defined between the z DoF of c and a sensor at b which is orientated to the z-axis.

In the next part of the sub-section, operational versions of response and force transmissibilities are analysed as particular interface DoFs are discarded.

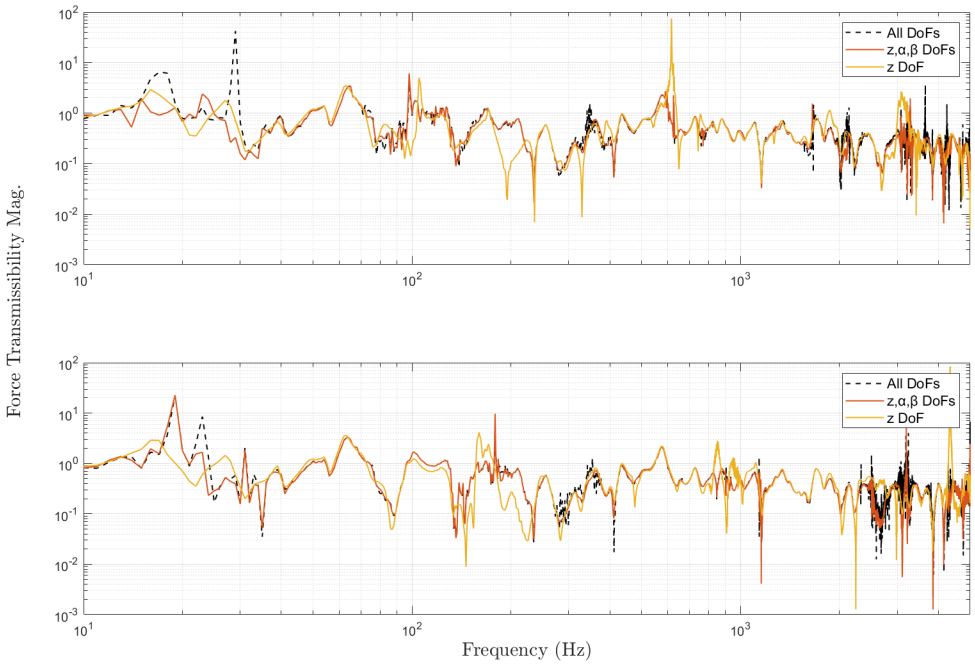

Figure 4.35: Operational $\mathbf{T}^{f,b}_{c(z)b_1}$, determined using all six DoFs at c, translation z with α and β rotational DoFs, and z only. Top sub-figure shows plots of $\mathbf{T}^{f,b}_{c(z)b_1}$ when beam 1 is coupled, while the bottom sub-figure is for beam 2.

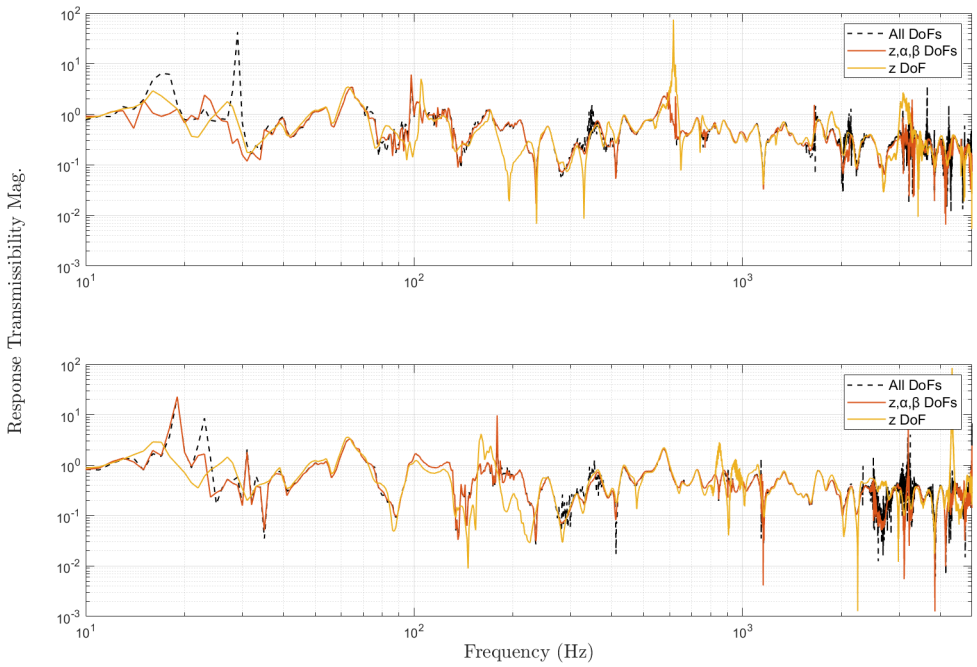

Figure 4.36: Operational $\mathbf{T}^{r,c}_{b_1c(z)}$ determined using all six DoFs, translation z with α and β rotational DoFs, and z only. Top sub-figure shows these plots of $\mathbf{T}^{r,c}_{b_1c(z)}$ when beam 1 is coupled, while the bottom sub-figure is for beam 2.

Firstly, the above figures show that all versions of $\mathbf{T}^{f,b}_{c(z)b_1}$ and $\mathbf{T}^{r,c}_{b_1c(z)}$ to have a small increase in noise over the mobility-based ones, which is seen consistently for output-only data in this experimental example. Trends present in Fig.4.33 and 4.34 appear comparable to those in Fig.4.35 and 4.36. The transmissibilities that only have z, α and β DoFs included appear to be the most accurate and are almost identical to the 'All DoFs' transmissibilities. The plots where only z was used in calculating the transmissibilities all show a satisfactory accuracy, with only a few small instances where it deviates from the 'All DoF' transmissibilities. For example, the same range of 100-230Hz appears to display the areas of largest difference to the 'All DoFs' transmissibilities. In addition, a few spikes in the magnitude of anti-resonances are also present from the mobility-based transmissibilities. For example when examining the bottom sub-figure where beam 2 is coupled to the assembly, $\mathbf{T}^{f,b}_{c(z)b_1}$ has increased anti-resonance magnitudes at 285Hz, 480Hz, and 2.2kHz. These are seen also in the bottom sub-figure of the mobility-based force transmissibility in Fig.4.33. In the higher frequencies (2.5-5kHz)

all versions of the operational force and response transmissibilities show increased noise and larger variance than the mobility-based ones. In this area it is more difficult to discern the affect of particular interface DoFs on the operational transmissibilities. In the low frequencies (10-35Hz), some differences are visible especially between the z only and 'All DoFs' transmissibilities.

4.4.4 Force and response transmissibility relation

The transposition relation between $\mathbf{T}_{cb}^{f,b}$ and $\mathbf{T}_{bc}^{r,c}$, defined earlier by Eq.4.25, is analysed for this rigid interface experimental example. In theory invariance between these two transmissibilities will be visible, as was shown previously in the three-resilient interface experimental example.

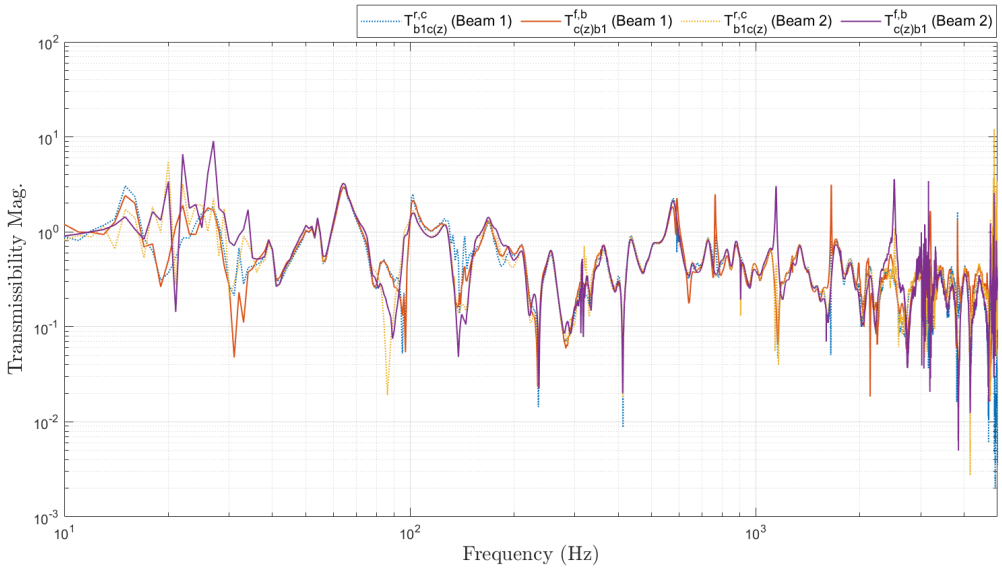

Figure 4.37: Mobility-based $\mathbf{T}_{cb}^{f,b}$ and $\mathbf{T}_{bc}^{r,c}$ for either A beam coupled to the assembly.

Overall, when $\mathbf{T}_{cb}^{f,b}$ and $\mathbf{T}_{bc}^{r,c}$ are calculated when for A component scenario, Fig.4.37 shows there are a lot of similarities across the full frequency range. Some bands such as the 10-37Hz range, display a high variability between all transmissibility plots. Further differences between all four transmissibilities can be spotted at 80-90Hz and 130-150Hz. Between 1-5kHz some large spikes at resonances and anti-resonances begin to emerge for certain transmissibilities, such as at 1.15kHz for Beam 1 $\mathbf{T}_{c(z)b_1}^{f,b}$,

and at 1.65kHz and 2.14kHz for Beam 2 $\mathbf{T}^{f,b}_{c(z)b_1}$. Noise also starts to increase at higher frequencies, particularly around 3kHz and near 5kHz. However, despite some of these small errors at higher frequencies, both force and response transmissibilities for either A case follow very similar trends.

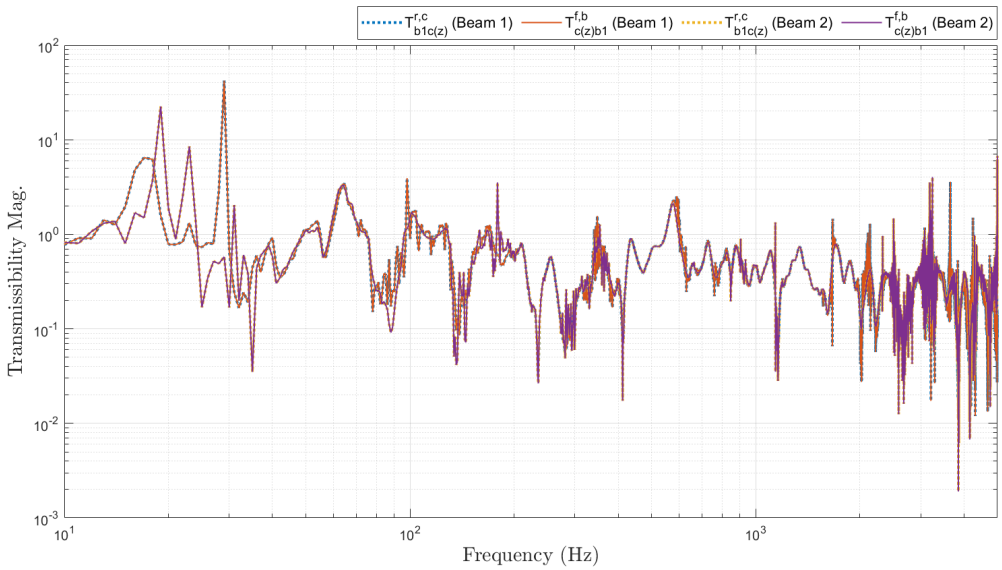

Figure 4.38: Operational $\mathbf{T}^{f,b}_{cb}$ and $\mathbf{T}^{r,c}_{bc}$ for either A beam coupled to the assembly.

The relation by transposition is also examined between operational $\mathbf{T}^{f,b}_{cb}$ and $\mathbf{T}^{r,c}_{bc}$. In Fig.4.38 the operational transmissibilities all appear more closely aligned to each other than the mobility-based route in Fig.4.37. At some frequency ranges, the related force and response transmissibilities determined for a particular A beam case appear to follow each other, i.e for beam 1 $\mathbf{T}^{f,b}_{cb}$ and $\mathbf{T}^{r,c}_{bc}$ follow the same trends between 10-40Hz and 80-90Hz. This is understandable as the operatioanl force transmissibility can only be calculated by taking the transpose of velocities measured for the response transmissibility. This is not like the mobility-based transmissibilities, as the force transmissibility does not require the transpose of the mobility-based response transmissibility. As shown by Eq.4.23, $\mathbf{T}^{f,b}_{cb}$ has the term $\mathbf{Y}_{C_{cb}}$ which uses excitations made at b. In Eq.4.11 $\mathbf{T}^{r,c}_{bc}$ has that mobility term transposed, yielding $\mathbf{Y}_{C_{bc}}$ which uses excitations made c instead. Because of the different force locations, there will be slight variations in the mobility-based transmissibilities. This is why they aren't as closely related as the operational ones. A small increase in noise is visible for the operational transmissibilities

between 280-390Hz, and increasing further along with some artefacts from 2.5kHz upwards. Despite this, over the whole frequency range Fig.4.38 suggests the output-only transmissibilities of B show invariance even when using their related counterpart.

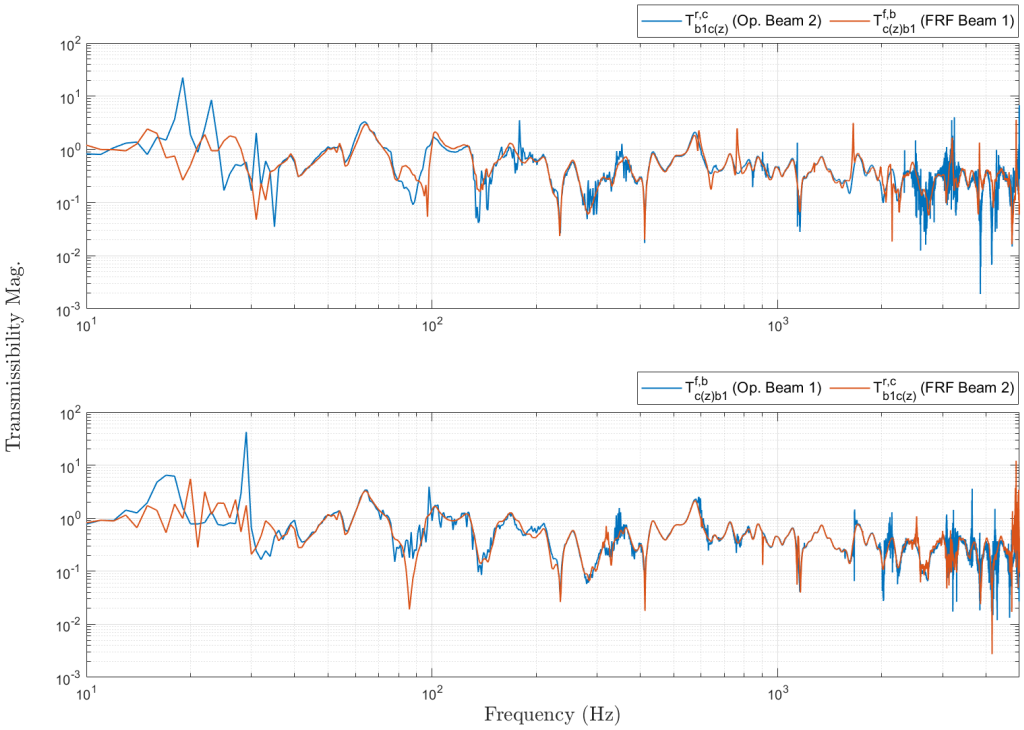

Figure 4.39: Comparison between $\mathbf{T}^{f,b}_{cb}$ and $\mathbf{T}^{r,c}_{bc}$ when calculated operationally or by FRFs. Additionally, different A components are coupled for either FRF or operational transmissibilities.

Above in Fig.4.39, force and response transmissibilities are calculated in opposite ways and using different A components. For example in the top-figure, $\mathbf{T}^{r,c}_{bc}$ is calculated operationally and with beam 2 coupled to the system, and compared against $\mathbf{T}^{f,b}_{cb}$ which is determined using mobilities and with beam 1. Similarly in the bottom sub-figure, $\mathbf{T}^{f,b}_{cb}$ is operational with beam 1 coupled, versus the mobility-based $\mathbf{T}^{r,c}_{bc}$ with beam 2. Both sub-figures show the transposition relation between these transmissibilities irrespective of which A component is coupled, or if they are determined operationally or by mobilities. While the output-only transmissibilities have slightly more noise, such as between 150-350Hz in the top sub-figure and 80-350Hz in the bottom sub-figure, they appear very much inline with the mobility-based transmissibilities

despite using a different A component. Thus it is indicated in the above figure, that invariance can be observed when comparing two related transmissibilities, irrespective of whether they were determined using operational responses or FRFs.

4.5 Transmissibility-based Interface Completeness Criterion

Throughout the analyses made in this chapter it has been demonstrated that a complete interface description is important to ensure a transmissibility for a given subsubstructure is invariant. In some practical scenarios, it may not be possible to have a complete interface description. Earlier in Section 2.8.3, it was shown that the vibroacoustic tool called the Interface Completeness Criterion (ICC) can be used to describe the completeness of the interface. It requires measuring the transfer mobility $\mathbf{Y}_{C_{ba}}$ directly and by the round-trip identity via Eq.3.9, and then conducting a comparison using amplitude or coherence based methods. An issue that can arise practically with this method is determining the round-trip prediction of the transfer mobility. This is because the identity uses measurements of mobilities $\mathbf{Y}_{C_{cc}}$ and $\mathbf{Y}_{C_{ac}}$., In a practical case it may not be possible to obtain these mobilities due to limited room around the interface c. For example in an automotive application, it is possible that interface sensors can be installed at the connection points between the subframe and engine. However, due to the limited space in this area it is not always possible to directly excite the sensors using a roving hammer. This is why in Section 4.3.3, transmissibilities of B were analysed for invariance where sensors were placed at all three connection points, but only two excitations made at two of the interface DoFs were used. It is certainly possible one can measure the mentioned mobilities in laboratory conditions, but in the case where this is not possible, it is explored whether an output-only transmissibility approach to the ICC is viable, termed the 'Transmissibility ICC' (TICC). The original ICC measures the effect of the interface description by comparing a direct measurement of the transfer mobility (which does not use any c DoFs in its calculation), to the

round-trip transfer mobility which does use of the c DoF subset. The TICC method is described in greater detail below, but it uses the same fundamental idea of the ICC by comparing a transmissibility across the coupled assembly without the interface c included, to a similar transmissibility which does use c. Firstly, a diagram showing how this is conducted is presented below.

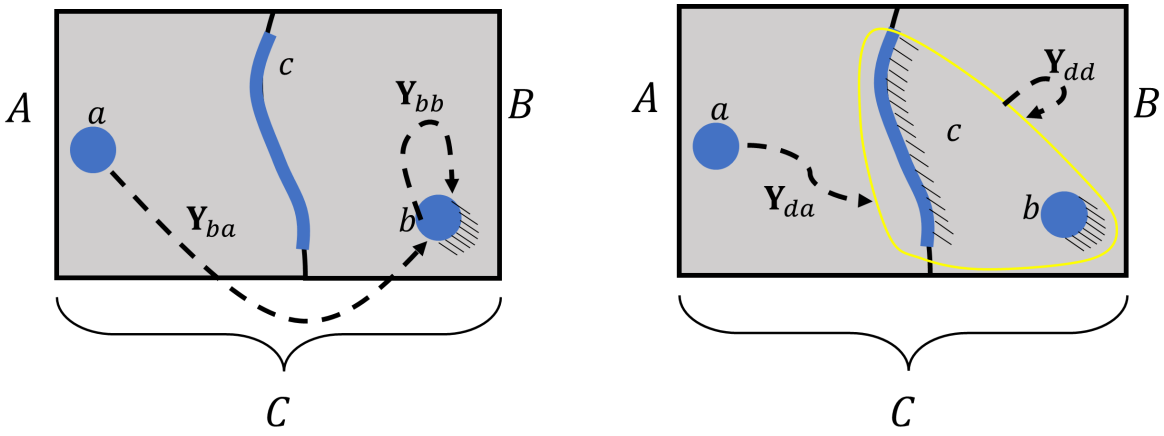

(a) $\mathbf{T}_{ba}^{f,a}$ calculation. (b) $\mathbf{T}_{da}^{f,a}$ calculation.

Figure 4.40: Diagram demonstrating the mobility measurements needed for the mobility-based TICC. In this example the force transmissibilities $\mathbf{T}_{ba}^{f,a}$ and $\mathbf{T}_{da}^{f,a}$ are used.

The diagram in Fig.4.40 illustrates which mobility measurements are required for the force transmissibility TICC. Specifically in this scenario, the two transmissibilities are $\mathbf{T}_{ba}^{f,a}$ and $\mathbf{T}_{da}^{f,a}$. $\mathbf{T}_{ba}^{f,a}$ is simply a force transmissibility between DoFs a and b, i.e. when there is no interface. For $\mathbf{T}_{da}^{f,a}$ in Fig.4.40b, the transmissibility is between DoFs d and a. d is defined as the combination of DoF subsets b and c. Due to the blocking constraint at c, in theory $\mathbf{T}_{da}^{f,a}$ will have a magnitude of 0 (or close to it) if the interface description is complete. On the other hand, $\mathbf{T}_{ba}^{f,a}$ will appear normal and have a magnitude greater than 0. If $\mathbf{T}_{da}^{f,a}$ has an incomplete interface description, in theory the magnitude will have some resemblance to $\mathbf{T}_{ba}^{f,a}$.

Firstly we must demonstrate how the force transmissibilities in Fig.4.40 are defined. By equating Eq. 4.6c and 4.12c we obtain,

$$\mathbf{f}_b = \mathbf{Y}_{C_{bb}}^{-1}\mathbf{Y}_{C_{ba}}\mathbf{f}_a \tag{4.43}$$

The product of the two mobility terms in the above equation yields the following transmissibility,

$$\mathbf{T}_{ba}^{f,a} = \mathbf{Y}_{C_{bb}}^{-1}\mathbf{Y}_{C_{ba}} \tag{4.44}$$

The definition above for $\mathbf{T}_{ba}^{f,a}$ may now be altered. By including c DoFs with b, we simply change the subscripts to d,

$$\mathbf{T}_{da}^{f,a} = \mathbf{Y}_{C_{dd}}^{-1}\mathbf{Y}_{C_{da}} \tag{4.45}$$

As we've discussed in previous chapters, the output-only definition of the force transmissibility can only be obtained by applying a transpose to its related response transmissibility. By equating Eq.4.6a and 4.6c the following is obtained,

$$\mathbf{v}_a = \mathbf{Y}_{C_{ab}}\mathbf{Y}_{C_{bb}}^{-1}\mathbf{v}_b \tag{4.46}$$

The product of mobility terms in the above equation is defined as the following response transmissibility,

$$\mathbf{T}_{ab}^{r,b} = \mathbf{Y}_{C_{ab}}\mathbf{Y}_{C_{bb}}^{-1} \tag{4.47}$$

As we can see this is related to $\mathbf{T}_{ba}^{f,a}$ by transpose. It was pointed out earlier in Section 4.1.4 that during an operational measurement, we must take N amount of linearly independent operational states. As a result, the velocity vectors in Eq.4.46 are now matrices, yielding the following output-only definition of the related response transmissibility,

$$\mathbf{T}_{ab}^{r,b} = \mathbf{V}_a\mathbf{V}_b^{-1} \tag{4.48}$$

$$\mathbf{T}_{ad}^{r,d} = \mathbf{V}_a \mathbf{V}_d^{-1} \tag{4.49}$$

Therefore by transpose of the above equations, the force transmissibilities used in the TICC are defined as,

$$\mathbf{T}_{ba}^{f,a} = (\mathbf{V}_a \mathbf{V}_b^{-1})^{\mathrm{T}} \tag{4.50}$$

$$\mathbf{T}_{da}^{f,a} = (\mathbf{V}_a \mathbf{V}_d^{-1})^{\mathrm{T}} \tag{4.51}$$

Now the relevant force transmissibilities are defined, we may begin applying the TICC theory to a mass spring model.

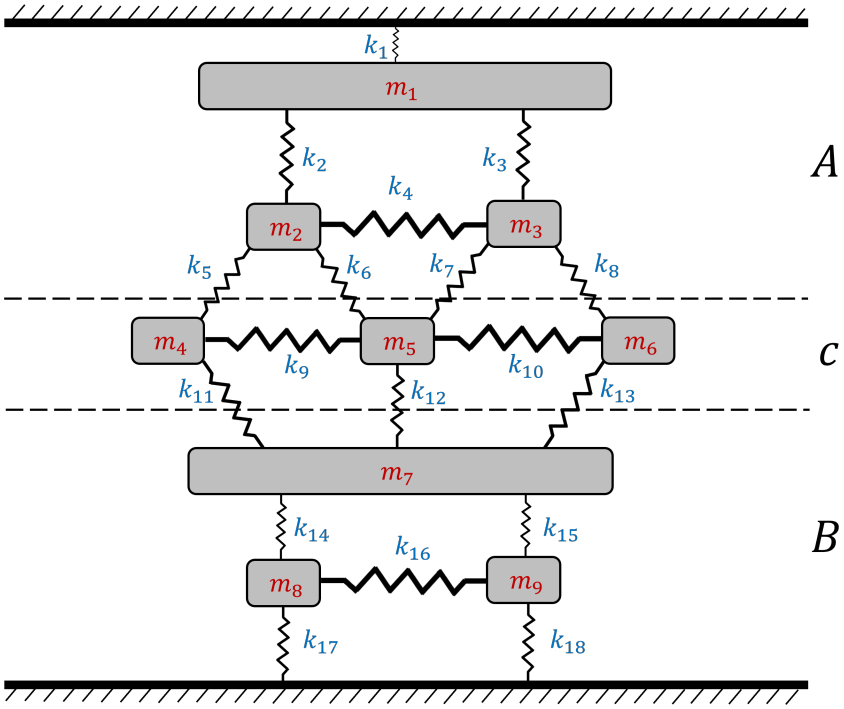

Figure 4.41: Illustration of mass spring model used to test TICC theory.

The MDoF mass spring system shown by Fig.4.41 is divided into sub-structure A and B. It consists of three a DoFs, three interface c DoFs, and three b DoFs. Firstly, the mobility-based force transmissibilities used in Fig.4.40 will be examined, followed

by the output-only versions. The output-only measurement is 'simulated' by applying forces only to DoFs subset a. The force matrix F has N amount of operational states equal the total amount of DoFs in the system (9). This means the problem has been over-determined, and the size of F is 9×9. To ensure linear independence, random force values between 0-1 were applied to the a DoFs.

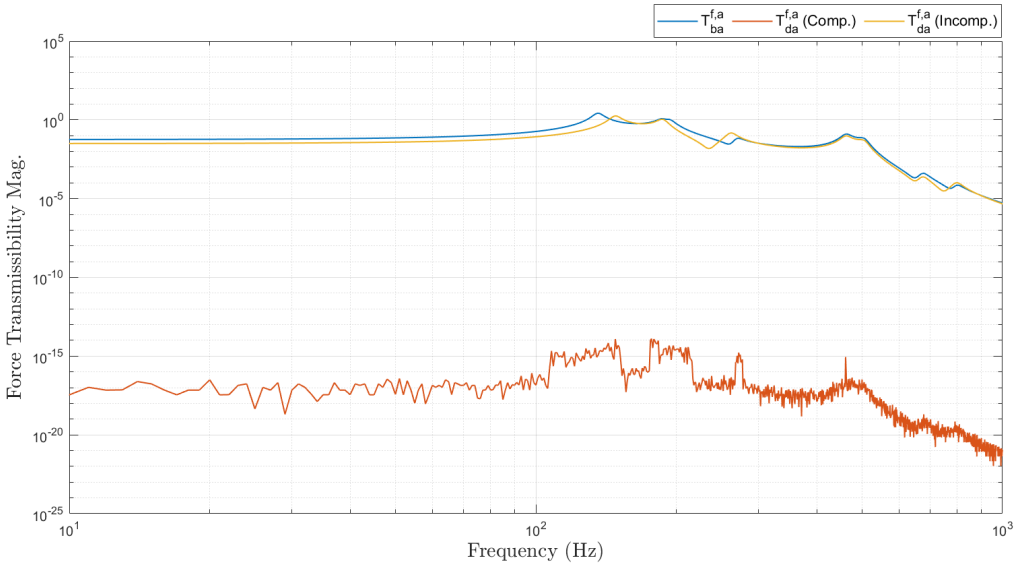

Figure 4.42: Mobility-based $\mathbf{T}_{ba}^{f,a}$ vs. $\mathbf{T}_{da}^{f,a}$ calculated with complete and incomplete interface c descriptions.

Fig.4.42 indicates to confirm the theory discussed earlier in this section. When the interface c is completely characterised, the magnitude of $\mathbf{T}_{da}^{f,a}$ shows an extremely low value, between $10^{-14} - 10^{-21}$ and represents machine error. It also shows that in the presence of an incomplete interface, $\mathbf{T}_{da}^{f,a}$ has a much larger magnitude than if it had a complete interface, and its magnitude is close to $\mathbf{T}_{ba}^{f,a}$. The above transmissibilities will now be examined when determined via operational responses.

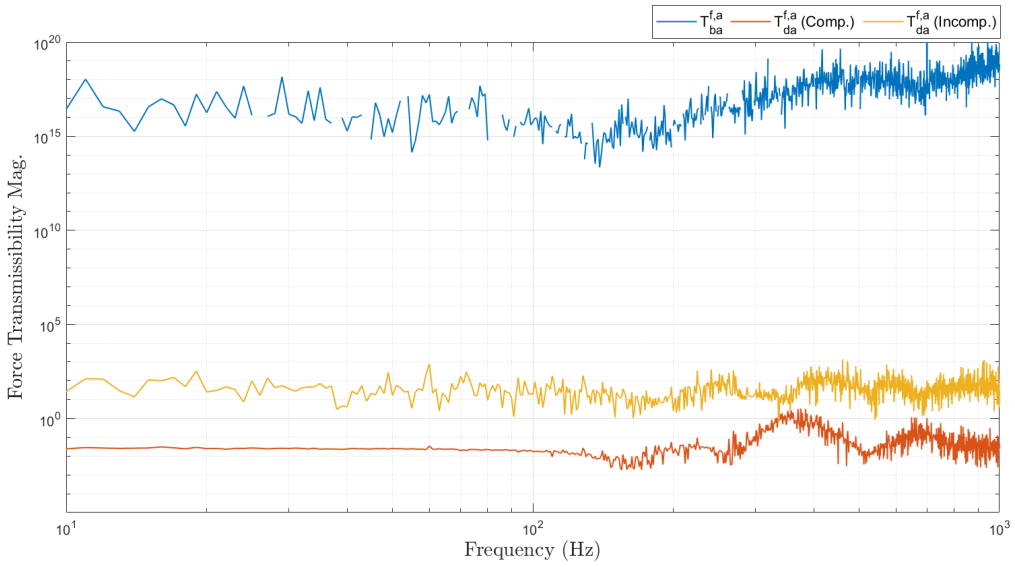

Figure 4.43: Operational $\mathbf{T}^{f,a}_{ba}$ vs. $\mathbf{T}^{f,a}_{da}$ calculated with a complete and incomplete interface c descriptions.

For the operational versions, $\mathbf{T}^{f,a}_{ba}$ has an extremely large magnitude when compared to the mobility case. It is not quite understood why this is the case. Anyhow, the above figure does show some similarities to the mobility-based ones in Fig.4.42. As expected $\mathbf{T}^{f,a}_{ba}$ has the largest magnitude, followed by the complete interface $\mathbf{T}^{f,a}_{da}$, and then the incomplete interface $\mathbf{T}^{f,a}_{da}$ being the lowest. Firstly, when there is a complete interface the magnitude of $\mathbf{T}^{f,a}_{da}$ stays below 1 nearly across the full frequency range. When it has an incomplete interface description the magnitude is much larger and reaches a value of 100 for large portions of the frequency range.

While Fig.4.42, and 4.43 are helpful in confirming the theory of how these transmissibilities will appear, they do not quantify completeness like the amplitude and coherence based ICCs. To identify the extent of completeness, a metric is proposed for the TICC.

$$\text{TICC} = \left| \frac{\mathbf{T}^{f,a}_{ba} - \mathbf{T}^{f,a}_{da}}{\mathbf{T}^{f,a}_{ba}} \right| \tag{4.52}$$

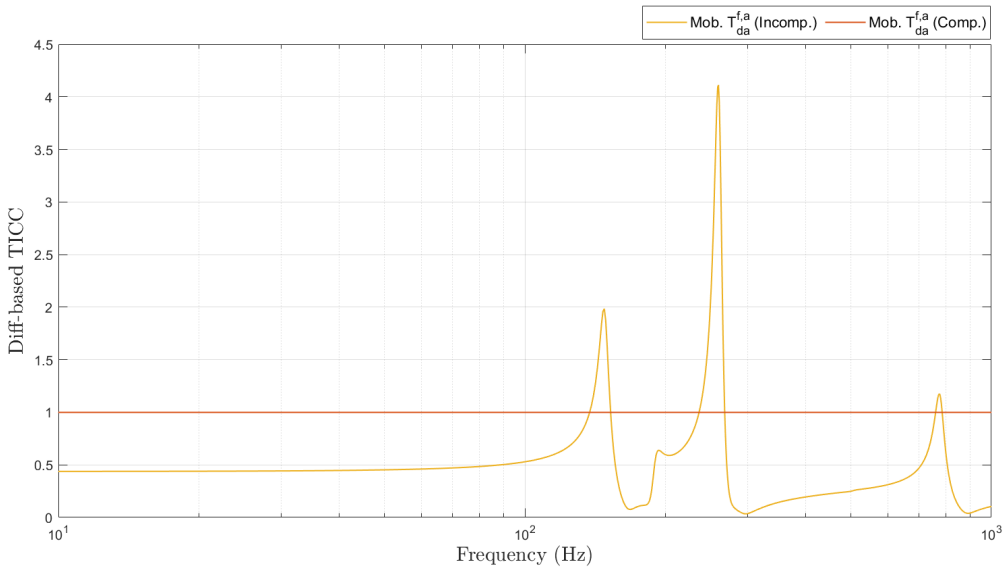

Figure 4.44: TICC difference metric for mobility-based force transmissibility.

The metric proposed for this short study is difference-based, as shown by Eq.4.52. In future studies, different metrics will be explored such as correlation or coherence based methods. In Fig.4.44 the TICC metric for the mobility-based force transmissibilities are shown. Similarly to the amplitude and coherence ICC, a value of 1 is observed across the full frequency range for when $\mathbf{T}_{da}^{f,a}$ has a complete interface description. Likewise, a value of zero indicates incompleteness. For the incomplete interface case of $\mathbf{T}_{da}^{f,a}$, the TICC remains between 0-1 for most of the frequency range. At around 150Hz, 250Hz, and 750Hz the incomplete transmissibility briefly goes over 1. At these distinct frequencies, the incomplete interface case of $\mathbf{T}_{da}^{f,a}$ and $\mathbf{T}_{ad}^{r,d}$ has a larger magnitude than $\mathbf{T}_{ba}^{f,a}$ and $\mathbf{T}_{ab}^{r,b}$, and suggests an amplification.

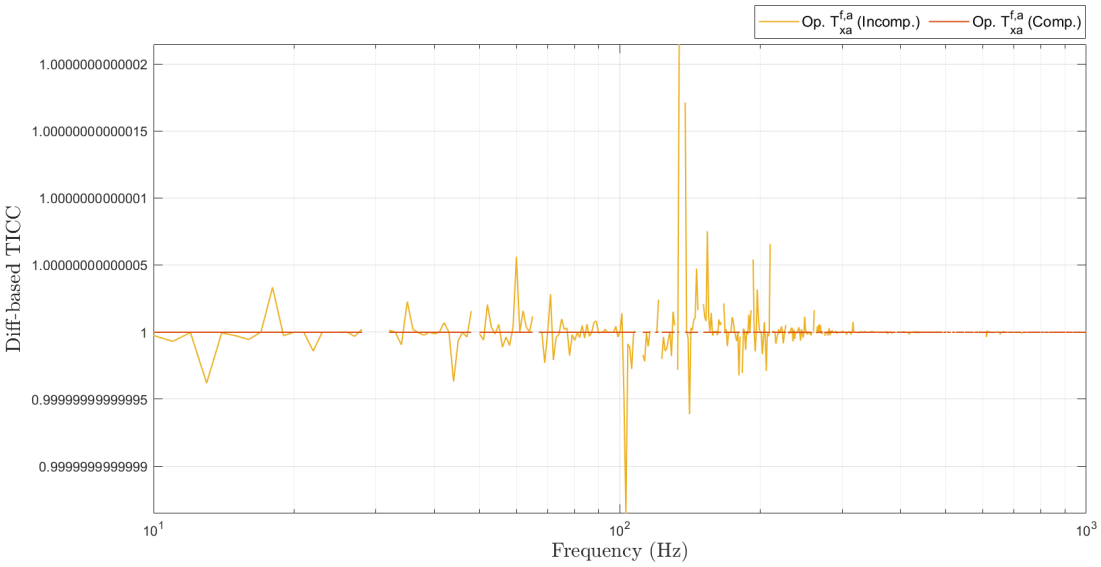

Figure 4.45: TICC difference metric for operational force transmissibility.

In the above figure the difference-based TICC metric is applied to the operational force transmissibilities. The complete interface version of $\mathbf{T}_{da}^{f,a}$ has a value of 1 across the full frequency range. However when there is an incomplete interface description, the metric goes above and below 1 quite frequently, and does not show any familiarity to the mobility-based version. As the magnitude of $\mathbf{T}_{ba}^{f,a}$ is extremely high (between $10^{15} - 10^{20}$, the magnitude of the incomplete $\mathbf{T}_{da}^{f,a}$ is still really far away from it, thus the difference between that and the complete $\mathbf{T}_{da}^{f,a}$ is very small.

4.6 Discussion

Invariance was firstly demonstrated by calculating a transmissibility of B while the component A was interchanged. For the single resilient-interface experiment, mobility-based transmissibilities of B were calculated when two A beams were interchanged differing in length were coupled to system. Additionally, transmissibilities were calculated when no beam was coupled. All three A beam test scenarios yielded transmissibilities of B similar to each other across the frequency range, therefore indicating invariance. Notably, this exercise indicated the interface DoF subset c was sufficiently characterised by a single DoF oriented in the z-axis. For the 'No beam' case force

and response transmissibilities of B were unchanged except between 10-80Hz, which is due to the lack of mass loading. The three resilient-interface experimental example consisted of two plates differing in material properties as sub-structure A. For the single resilient example, mobility-based force and response transmissibilities of B were similar across the full frequency range when either plate was coupled. Some differences were visible at low frequencies in this example too because of the difference in weight and damping between the two, as plate 1 is made out of steel while plate 2 consisted of perspex. The same analysis was conducted on force and response transmissibilities using operational responses, also showing a difference at low frequencies. A check was made to ensure operational transmissibilities didn't deviate from the FRF-based ones, which could be argued as being slightly more reliable. It was found the same trends existed as the FRF-based transmissibilities. In the final experimental example with a rigid interface connection, the same components were used from the single resilient example, except of course the resilient isolator was replaced with a rigid mount. As a consequence the transmission of other translational and moment forces would be more significant, thus characterisation of the interface c by a single DoF facing the z-axis was not sufficient enough to apply the blocking constraints fully. Instead, the c DoF subset was characterised by all three translational DoFs x, y, z, and the rotational DoFs along each plane α, β, γ. In this case, both mobility-based and operational response and force transmissibilities showed close alignment when either A beam was coupled. To summarise, all experimental examples demonstrated the transmissibility of a downstream component (in this case B) is indeed invariant when an upstream sub-structure (A) has been interchanged, on the condition the interface c is sufficiently characterised to provide the necessary blocking constraints.

For the three resilient interface experimental example, the boundaries of where invariance could be observed was tested by changing the number of responses and excitations when calculating transmissibilities. Usually, it is required the number of remote DoFs (a or b) is equal to or greater than the amount of c DoFs. In the case of the mobility-based transmissibilities on the three resilient-interface example, reducing the

number of c DoFs caused invariance to breakdown as the blocking constraints were not applied to all connection points. Additionally in some cases, such as in Fig.4.17, 4.18, reducing the excitations at c DoFs of the inverted term $\mathbf{Y}_{C_{cc}}$ showed invariance was not present at low frequencies, but only visible from around 400Hz and above. Furthermore, when the force transmissibility $\mathbf{T}_{cb}^{f,b}$ was calculated using a different equation (Eq.4.22 - which has the inverted term $\mathbf{Y}_{C_{ac}}$ instead), it was found in Fig.4.20, that reducing the a responses affected invariance, as the requirement of having remote DoFs equal to the number of interface DoFs was not fulfilled. In a similar fashion, this definition of $\mathbf{T}_{cb}^{f,b}$ showed invariance was not visible at lower frequencies, while it was at higher frequencies.

In all three experimental examples, another test for invariance was conducted by observing whether transmissibilities of B were the same as the location of the external force changed within A. Specifically, the response transmissibilities $\mathbf{T}_{bc}^{r,c}$ and $\mathbf{T}_{bc}^{r,a}$ were compared, which in theory are identical. This is due to an assumption when using blocked forces, where the response field in B is identical despite the location of excitations within A (as long as the characterisation of c DoFs is complete). As the interface c is also part of A, it is tested to see whether the external force at c yields the same transmissibility of B when it has been moved to a. All experimental examples showed that, within error, that the two transmissibilities are almost identical. In the single resilient interface and three resilient interface tests, $\mathbf{T}_{bc}^{r,a}$ appeared to show an increase in noise from roughly 3kHz and above, while $\mathbf{T}_{bc}^{r,c}$ did not. As the external force is applied at a for $\mathbf{T}_{bc}^{r,a}$, its transmission path traverses the isolator(s) to reach B. This means it is subjected to isolator attenuation, and at higher frequencies the magnitude of the external force has been decreased close to the level of the noise floor. On the other hand, $\mathbf{T}_{bc}^{r,c}$ has the external force applied at the accelerometer at c, which is located below the resilient mount. This means the transmission path of the external force does not traverse the isolator to determine the transmissibility of B. For the single rigid interface experimental example, both response transmissibilities also appeared almost identical and had the better agreement at higher frequencies than the previous experiments as

$\mathbf{T}_{bc}^{r,a}$ was not contaminated with noise. This makes sense as there is no resilient mount causing the attenuation error.

Additionally on the rigid interface experiment, transmissibilities of sub-structure B were observed when particular DoFs at the interface were left out of its calculation. The goal of this analysis is to observe whether the transmissibilities show invariance even when the interface description is not complete. Three scenarios were tested when calculating the transmissibilities: accounting for all six interface DoFs (which was confirmed as invariant, and serves to validate the other cases), only z translation and rotations α and β, and finally only z. In particular the transmissibilities examined are $\mathbf{T}_{b_1c(z)}^{r,c}$ and $\mathbf{T}_{c(z)b_1}^{f,b}$, which is between the z DoF of c and the first DoF in subset b (also facing the z-axis). Because this transmissibility is between two DoFs facing the z-axis, understandably both mobility-based and operational transmissibilities showed that when only the z translation component was used in their calculation, they appeared to be similar to the case where all c DoFs are accounted for, apart from a few small bands within the full frequency range. The scenario where $\mathbf{T}_{b_1c(z)}^{r,c}$ and $\mathbf{T}_{c(z)b_1}^{f,b}$ were calculated using only z, α and β was even closer to invariant 'All DoFs' transmissibilities for both mobility and operational routes. This indicates that the discarded DoFs x, y, γ had very little effect on $\mathbf{T}_{b_1c(z)}^{r,c}$ and $\mathbf{T}_{c(z)b_1}^{f,b}$. In summary, these particular transmissibilities appear to convey invariance at reasonable level of accuracy by just taking account the dominant z translation at c. If possible it is recommended to account for some rotations as well, as it appears to yield transmissibilities almost identical to the case where all six c DoFs are used.

It is well known that force and response transmissibilities are related by a transposition operation. Therefore in theory, if a particular transmissibility has been deemed invariant, then its related transmissibility will also display invariance. This was tested for the three resilient interface and rigid interface experimental examples. In the case of the mobility-based transmissibilities, the three resilient interface experiment showed some variation at low frequencies (10-100Hz), but overall appear very much in line with one another. At lower frequencies the force and response transmissibilities calculated for

a particular plate case appear to align with each other, but not with the transmissibilities determined for the other plate coupled. This is likely due to the different mass loading provided by the plates as the steel one was much heavier than the perspex plate. For the rigid interface experiment some differences were also visible at low frequencies (10-37Hz). The force and response transmissibilities for a particular A beam scenario did not appear to align with each other like the previous experimental example. It is not yet fully understood why the variance exists here. However above 37Hz all transmissibilities calculated for either A beam showed good agreement, all displaying invariance. It was found in both experimental examples that the operational force and response transmissibilities were almost identical, appearing closer to each other than the mobility-based ones. This is expected, as the operational force transmissibility cannot be directly measured and can only be calculated when taking the transpose of the operational response transmissibility. The mobility-based force transmissibility has slightly more variation to the response transmissibility because you do not need to determine it from the transpose of the mobility-based response transmissibility. You can measure the transposed mobility terms, by applying the external force at the opposite DoF. For example in Eq.4.23, one of the two mobility terms to determine $\mathbf{T}_{cb}^{f,b}$ is $\mathbf{Y}_{C_{cb}}$, which uses an external force applied at b. Meanwhile for its related response transmissibility $\mathbf{T}_{bc}^{r,c}$, the mobility term $\mathbf{Y}_{C_{bc}}$ must be measured; using an external force applied at the interface c instead. Another test on invariance was also made in both experiments by comparing force and response transmissibilities that are calculated in opposite ways. One example being $\mathbf{T}_{bc}^{r,c}$, determined using operational responses and with beam 2 as component A, and plotted against $\mathbf{T}_{cb}^{f,b}$ that was calculated using mobilities and beam 1 as A. It was observed in both experimental examples that the two transmissibilities are very similar to another. Therefore it is strongly indicated that yielding a transmissibility by opposite means of measurement to its related transposed counterpart will show invariance.

Observation of the force transmissibilities illustrated in Fig.4.40 confirmed that when a transmissibility is calculated across the A and B without including any c DoFs, it will

have some magnitude ($\mathbf{T}_{ba}^{f,a}$). It was observed for the mobility-based transmissibilities of $\mathbf{T}_{da}^{f,a}$, that if the c DoFs are included with the b DoFs, then the magnitude will be near 0 as long as the interface c is completely characterised. Additionally, if the interface description is incomplete, then the magnitude will be higher and for the mobility definition quite close to $\mathbf{T}_{ba}^{f,a}$. For the operational versions of $\mathbf{T}_{da}^{f,a}$, the incomplete interface version did have a value much larger than complete case. However when calculating the difference-based TICC metric, there was little difference to distinguish the two interface scenarios because the magnitude of $\mathbf{T}_{ba}^{f,a}$ was so large, that their differences to it were quite similar. For the mobility-based transmissibilities there were some similarities to the original ICC outlined in Section 2.8.3. A value of 1 was seen consistently for the complete interface transmissibilities, while the incomplete version dipped below 1 for the vast majority of the frequency range. A difference to the ICC is that at some frequencies the incomplete interface transmissibilities rise above 1. At these points the incomplete transmissibility magnitude is greater than the transmissibility with no interface included, and suggests some amplification. In a future study, correlation and coherence based metrics will be explored.

Chapter 5

Operational round-trip method

In this chapter the 'Operational round-trip' (ORT) method is introduced, which builds upon the already established Round-trip (RT) method. The ORT enables a mostly-operational approach for predicting a point or transfer mobility, with the main focus of this thesis on the former. The goal of developing the RT method for an output-only scenario is for its applicability to industrial cases. The original round-trip is a highly accurate vibro-acoustic prediction method, but the mobilities within the identity require three FRF measurements, which may limit it to test structures in laboratory conditions. Within industry the use of ambient excitation is usually preferred, for reasons that are explained in detail within this chapter. As pointed out previously in Chapter 4, the combination of two mobilities equates to some generalised transmissibility, which also has an output-only definition by the product of operational responses at two DoF subsets. It is shown that an alternative formulation of the point mobility RT identity can be acquired by replacing two of the three mobility terms with an operational transmissibility. Analyses conducted on the ORT identity's prediction is shown for two experimental examples. These consist of examining the accuracy of the transmissibility term by comparing the FRF-based and operational routes, as well as exploring which conditions yield the most accurate output-only transmissibility, such as the number of operational states and the processing of time-blocks for during an operational measurement. Following on from this is a demonstration of the ORT point mobility prediction, which is

compared to original round-trip and a direct measurement.

Contents

It was previously demonstrated in Chapter 3 the round-trip identity allows a prediction of a point or transfer mobility indirectly. In this chapter, an alternative method of estimating a point mobility indirectly, termed the Operational Round-trip (ORT), is presented by including output-only transmissibilities into the RT point identity. Similarly to previous studies shown in this thesis, the main focus is the prediction of an $M \times M$ driving-point FRF matrix at DoF subset c, which is located at the interface between two sub-structures A and B. The RT method can be used in situations where the driving-point FRFs at a connecting interface cannot be measured directly, usually due to a lack of space meaning apply a roving hammer excitation is impractical. To conduct this indirect measurement, one must apply the controlled and collocated roving hammer excitation to two DoF subsets a and b that are located in adjacent sub-structures, which is either side of the interface DoF subset c. However some issues can also arise with this method. It may be impractical to use due to: the structure being so large that applying a big enough hammer force to yield data with good SNR is difficult, the inability to shut down the structure operationally, and a large number of responses installed on the structure; making the excitation process time consuming. In these situations, methods that simplify the FRF measurement process are usually sought after, especially if they utilise ambient forces (Farrar and III [1997] Orlowitz and Brandt [2017]) over roving hammer excitations. Methods proposed before the RT method synthesised the

$M \times M$ interface matrix from only a single column (modal shape extraction technique using a controlled excitation at a single response within c instead of all DoFs within the subset) as demonstrated by Ashory [1998] Ashory [1999] Silva et al. [2000] Ewins [1980] Maia et al. [1997]. These modal extraction methods are possible if applying an excitation to one DoF within the subset is possible, but usually this is not the case for mounting points of equipment within industry. Another method is System Equivalent Model Mixing (SEMM) that was outlined previously in Section 2.5.2. By mixing measured FRFs of a limited DoF-space from an experimental model, and the increased DoF-space of an equivalent numerical model, a resultant hybrid model is formed which allows the prediction of FRFs at the additional DoFs that are not available in the experimental model. This method is promising but does require the numerical model being a highly accurate representation of the experimental model. While the original RT method does have some problems with its applicability to large industrial structures, it is highly accurate in its in-situ prediction of the point mobility $\mathbf{Y}_{C_{cc}}$, and it is strongly believed that the problems surrounding it applicability to large industrial structures can be easily addressed by the inclusion of output-only transmissibilities into the RT point mobility identity. The reformulation of the RT point identity is derived in detail firstly within Section 5.1. In essence, the alternative definition is possible by replacing two of the three mobility terms in the RT identity with an inverted transmissibility. Alluded to by Moorhouse and Elliott [2013] as well as demonstrated in Chapter 4, the product of two mobilities equates to some transmissibility, which may also be determined by operational velocities and no force reference. An important feature of transmissibilities is that they are 'invariant' (Meggitt and Moorhouse [2020b]), a property that was investigated in the previous chapter and informs how the transmissibilities in the ORT identity should be applied correctly. It is essential that the transmissibility term within the ORT point identity is unaffected by an adjacent active sub-structure. This is only possible when the coupling interface DoFs c applies sufficient blocking, which is achieved only by a 'complete' interface representation (Meggitt and McGee [2024]). It is important because the operational transmissibility needs to be the sole property of the passive

component, rather than being attributed to the coupled assembly as a whole. Another important point to note from the previous chapter in Sections 4.2.2, 4.2.2, and 4.4.2 is the transmissibility of a passive component remains the same regardless of where the external force is applied within an adjacent active sub-structure. This invariance to excitation position is crucial to the ORT method, especially if ambient forces of which no control is possible, are to be used.

To begin, two versions of the ORT identity are dervied in Section 5.1. Each uses either a force or response transmissibility that replaces different mobility terms within the original RT point identity. All experimental examples from Chapter 4, illustrated in Fig.4.4, 4.10, 4.26, are also used in this study for demonstrating the ORT point mobility prediction at interface DoF subset c. The experiment models are relatively small and also set in laboratory conditions, meaning good coherence between DoFs is achieved. In an industrial setting with large structures, it is likely only partial-coherence will exist. Thus in Section 5.2, theory on the processing of time data for partial-coherence is presented. One practical example where the ORT method can be used for fully coherent responses is within the automotive industry. Measuring $\mathbf{Y}_{C_{cc}}$ at the mounting points between a vehicle's engine and sub-frame can be useful in determining the dynamic behaviour at certain frequencies. When plotting the point mobility, resonances and damping characteristics can be identified, which can inform the design of the engine mounts. Usually installing a sensor close to the mounts is possible, but performing a roving hammer excitation at the same location is not. In this scenario, the driving-point FRFs can be predicted indirectly either by the RT method where controlled excitations are applied at two remote DoF subsets (a and b) on either side of the interface c which are easily accessible, or alternatively by using operational forces from the engine to measure the velocities at the interface and remote DoFs using the ORT method. In Section 5.3 the operational transmissibilities used in the ORT identities are compared to equivalent mobility-based measurement. It is essential that the output-only transmissibilities are similar to the mobility-based formulation to obtain the most accurate ORT prediction. Additionally, the accuracy of operational transmissibilities is exam-

ined by exploring different techniques of processing time series data in Section 5.2. In Section 5.4, predictions via the RT and ORT methods are compared to the direct measurement $\mathbf{Y}_{C_{cc}}$.

The setup of experimental assemblies used in this chapter has not changed from Chapter 4. They all consist of an active component A that is resiliently coupled to a passive sub-structure B, a large perspex plate. For the beam-isolator-plate experiment in Fig.4.4, A is a steel beam (pictured in Fig.4.5a) which is coupled to B by one isolator, while the plate-isolator-plate experiment in Fig.4.10 has A as a steel plate (pictured in Fig.4.11a) that is coupled to B by three isolators. As previously stated in the previous chapter, the rigid single interface example from Fig. 4.26 is similar to the single interface experiment, but the resilient mount has been replaced with a rigid one. Additionally, there are no responses installed on the active component A, and three more uni-axial responses have been added to subset b, all facing the vertical z-axis. At the interface c, sensors are orientated in the three translation planes, illustrated in Fig.4.27, where the finite-difference method will be used for complete characterisation of c. For the single-resilient interface and three-resilient interface experiments all of the accelerometers are uni-axial and orientated in the vertical z-axis for all DoF subets. The single-resilient interface only has one sensor at c, while there are three c DoFs for the plate-isolator-plate experiment. During the FRF measurements, excitations were applied at every sensor position, yielding a 7×7 FRF matrix for Fig.4.4, and a 9×9 FRF matrix for Fig.4.10. For Fig.4.26, 20 controlled excitations were applied within A, with the first 9 facing the z axis, 10-18 in the y axis, and 19-20 in x. In addition, 8 excitations were applied at the interface c and 1 each in b (6). After the finite difference approximation, the FRF matrix of the rigid interface experiment is 12×32. The operational tests were also performed using the roving hammer as the source of excitation. These excitations were applied at the same locations as the FRF test, meaning the velocity matrices are the same size as the FRF matrices in each experiment. However instead of a controlled single excitation, impacts were randomised both spatially and temporally for a 20-second period without any force reference. This method of exci-

tation, though somewhat artificial, was chosen to ensure that sufficiently independent states could be generated. The challenges related to realistic operational conditions are of course crucial to the success of the ORT method and will be considered in future studies. In this case, the hammer applies a broadband force to the structure, which is the same as ramping up the frequency of a motor. Furthermore, a motor which is fixed in location cannot create independent operational states, unlike the hammer method where forces are randomised in time and space.

5.1 Operational Round-trip theory

Having introduced the round trip theory in Section 3 and generalised transmissibility concept in Section 2.6.2 and 2.7.2, we are now able to combine both parts and present the ORT identities. As previously shown, the RT identity is defined by Eq.3.7 and similarly by transposition it can also be stated as Eq.3.8. Let us consider A as the active component, and apply a matrix inversion operation to Eq.4.14,

$$(\mathbf{T}_{bc}^{r,a})^{-1} = \mathbf{Y}_{C_{ca}} \mathbf{Y}_{C_{ba}}^{-1}. \tag{5.1}$$

Substituting the response transmissibility from Eq.5.1 into the round-trip identity in Eq.3.8 we have the response-based ORT identity,

$$\mathbf{Y}_{C_{cc}} = (\mathbf{T}_{bc}^{r,a})^{-1} \mathbf{Y}_{C_{cb}}^{\mathrm{T}}. \tag{5.2}$$

Whilst A is in operation, responses are measured at DoFs b and c when calculating $\mathbf{T}_{bc}^{r,a}$ (Eq.4.31), thus yielding the following definition,

$$\mathbf{Y}_{C_{cc}} = (\mathbf{V}_b \mathbf{V}_c^{-1})^{-1} \mathbf{Y}_{C_{cb}}^{\mathrm{T}}. \tag{5.3}$$

Similarly, for relating the force transmissibility to the RT identity, let us apply an inverse

operation to Eq.4.19,

$$\left(\mathbf{T}_{ca}^{f,a}\right)^{-1} = \mathbf{Y}_{C_{ba}}^{-1}\mathbf{Y}_{C_{cb}}^{\mathrm{T}}. \tag{5.4}$$

Substituting the force transmissibility from Eq.5.4 into the round-trip identity in Eq.3.8 we have the force-based ORT identity,

$$\mathbf{Y}_{C_{cc}} = \mathbf{Y}_{C_{ca}}\left(\mathbf{T}_{ca}^{f,a}\right)^{-1} \tag{5.5}$$

Whilst A is in operation, let us recall the transpose relation to a response transmissibility made in Eq.4.26, and the operational transmissibility made in Eq.4.34. Our force-based ORT identity becomes,

$$\mathbf{Y}_{C_{cc}} = \mathbf{Y}_{C_{ca}}(\mathbf{V}_a\mathbf{V}_c^{-1})^{-\mathrm{T}}. \tag{5.6}$$

Excitations made at a allow the operational transmissibility $\mathbf{T}_{bc}^{r,a}$ to be determined, which is included in the ORT identity shown in Eq.5.2. Meanwhile external forces at subset b allow $\mathbf{T}_{ca}^{f,a}$ to be measured in the ORT identity in Eq.5.5. The reason for this, despite $\mathbf{T}_{ca}^{f,a}$ indicating a force applied at a, is because $\mathbf{T}_{ca}^{f,a}$ cannot be measured directly during an operational measurement. Thus, we calculate the related response transmissibility $\mathbf{T}_{ac}^{r,b}$ as shown in Eq.4.26, and then apply a transpose operation to $\mathbf{T}_{ac}^{r,b}$'s definition in Eq.4.34.

The ORT identities in Eq.5.2 and Eq.5.5 show both response and force transmissibilities applied to the RT identity respectively. In both formulas of the ORT method, only one FRF-based measurement is required to predict the interface mobility $\mathbf{Y}_{C_{cc}}$. This is very beneficial in an engineering context. Measuring all three mobility terms in the original RT identity can be costly and time consuming if the test were performed on a large test rig. The ORT identity allows one to measure the single mobility term once at a time of convenience, which can then be used in conjunction with measured velocities

to constantly measure $\mathbf{Y}_{C_{cc}}$ in real-time.

While the transfer mobility prediction of the RT method is not the main focus of this study, it is important to note that operational transmissibilities may also be used in its identity also. To show how this is possible, a derivation of the ORT transfer mobility is provided below.

Let us recall the RT identity in Eq.3.9. By substituting the response transmissibility $\mathbf{T}_{ac}^{r,c}$ in Eq.4.10 into the identity, we yield the following definition,

$$\mathbf{Y}_{C_{ab}} = \mathbf{T}_{ac}^{r,c}\mathbf{Y}_{C_{cb}} \tag{5.7}$$

The output-only definition of the transmissibility term is,

$$\mathbf{T}_{ac}^{r,c} = \mathbf{V}_a\mathbf{V}_c^{-1} \tag{5.8}$$

therefore the ORT definition of $\mathbf{Y}_{C_{ab}}$ is defined as,

$$\mathbf{Y}_{C_{ab}} = \mathbf{V}_a\mathbf{V}_c^{-1}\mathbf{Y}_{C_{cb}} \tag{5.9}$$

Similarly, we may define the transposed version of the transfer mobility (Eq.3.10) with an operational transmissibility. Recalling the definitions in Eq.4.16 and 4.17, the combinations of these two equations yields a force transmissibility,

$$\mathbf{T}_{ca}^{f,a} = \mathbf{Y}_{C_{cc}}^{-1}\mathbf{Y}_{C_{ca}} \tag{5.10}$$

Substituting the above definition for $\mathbf{T}_{ca}^{f,a}$ into the $\mathbf{Y}_{C_{ba}}$ RT transfer mobility identity,

$$\mathbf{Y}_{C_{ba}} = \mathbf{Y}_{C_{cb}}^{\mathrm{T}}\mathbf{T}_{ca}^{f,a} \tag{5.11}$$

This force transmissibility is also used in a form of the point mobility ORT identity in

Eq.5.6. The ORT form of the transfer mobility prediction is therefore defined as,

$$\mathbf{Y}_{C_{ba}} = \mathbf{Y}_{C_{cb}}^{\mathrm{T}}(\mathbf{V}_a\mathbf{V}_c^{-1})^{\mathrm{T}} \tag{5.12}$$

5.2 Analysis of output-only transmissibilities using alternative time block processing methods

In this section, the operational transmissibility terms used in the ORT identities are analysed by altering the time block processing. In the experimental examples presented in this chapter, responses are coherent and the source of excitation is stationary. In this scenario, the method of processing differs to when there is only partial coherence. Theory of processing time data in this case is covered first, followed by three methods of time-block processing for coherent and stationary sources.

For example, let us recall the operational definition of $\mathbf{T}_{bc}^{r,a}$ in Eq.4.31 and reorder it so $\mathbf{V}_b$ is the subject,

$$\mathbf{V}_b = \mathbf{T}_{bc}^{r,a}\mathbf{V}_c \tag{5.13}$$

By post-multiplying both sides of the above equation by $\mathbf{V}_c^{\mathrm{H}}$, the following definition is obtained,

$$\mathbf{V}_b\mathbf{V}_c^{\mathrm{H}} = \mathbf{T}_{bc}^{r,a}\mathbf{V}_c\mathbf{V}_c^{\mathrm{H}} \tag{5.14}$$

On both sides of this equation an average is taken over N amount of operational states, but as they cancel out it has been omitted for clarity reasons. The product of velocities between b and c on the LHS equates to a matrix of averaged cross-spectral densities $\langle\mathbf{S}_{bc}\rangle$, while on the RHS the velocity matrix at c multiplied by its transposition yields a matrix of averaged auto-spectral densities $\langle\mathbf{S}_{cc}\rangle$,

$$\langle \mathbf{S}_{bc} \rangle = \mathbf{T}_{bc}^{r,a} \langle \mathbf{S}_{cc} \rangle \tag{5.15}$$

and therefore,

$$\mathbf{T}_{bc}^{r,a} = \langle \mathbf{S}_{bc} \rangle \langle \mathbf{S}_{cc} \rangle^{-1} \tag{5.16}$$

This is one method of calculating operational transmissibilities when only partial coherence is achieved between responses. Another method of calculating operational transmissibilities when only partial coherence is achieved, is to take the velocities for individual operational states and apply a least squares solution. Thus for a given operational state i, the definition in Eq.5.14 may be rewritten as,

$$\mathbf{v}_b^i (\mathbf{v}_c^i)^{\mathrm{H}} = \mathbf{T}_{bc}^{r,a} \mathbf{v}_c^i (\mathbf{v}_c^i)^{\mathrm{H}} \tag{5.17}$$

which can also be written as,

$$\mathbf{S}_{bc}^i = \mathbf{T}_{bc}^{r,a} \mathbf{S}_{cc}^i \tag{5.18}$$

Thus for this example of processing for partial coherence, the response transmissibility is defined as,

$$\mathbf{T}_{bc}^{r,a} = \left(\mathbf{S}_{bc}^1, \quad \mathbf{S}_{bc}^2, \quad \cdots \right) \left(\mathbf{S}_{cc}^1, \quad \mathbf{S}_{cc}^2, \quad \cdots \right)^+ \tag{5.19}$$

In the above equation the multiplication between the cross-spectral density vector and the pseudo-inverse (denoted $^+$ in the superscript) of the auto-spectral vector, means there is a multiplication of the individual elements for each ith operational state and added all together. A comprehensive outline of the pseudo-inverse matrix operation may be found earlier in Section 2.9, and shown mathematically by Eq.2.74. In the remaining part of this section, the theory behind the time block processing when full

coherence and steady-state source behaviour is achieved will be covered.

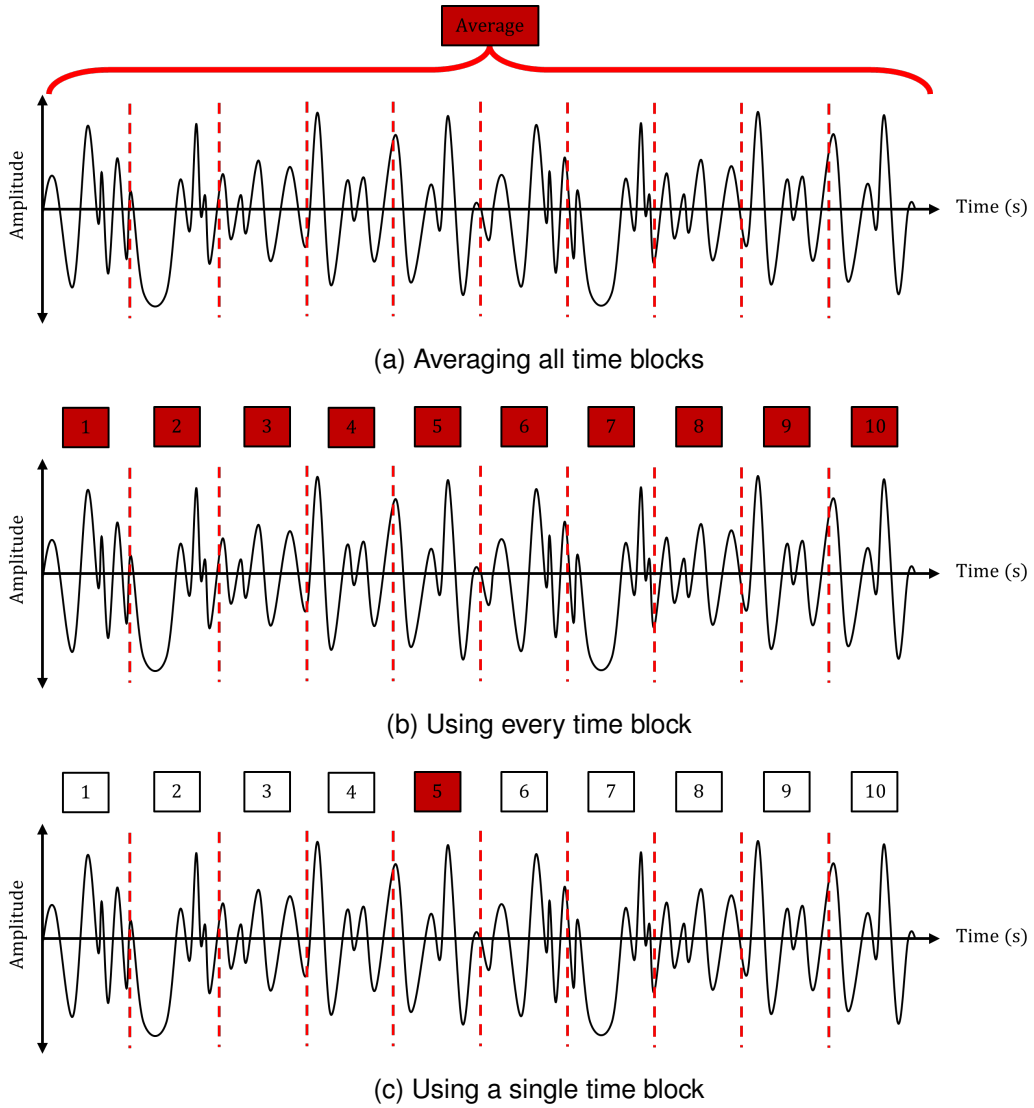

Figure 5.1: Time block processing methods for an operational measurement.

As detailed earlier in this chapter, the operational forces used in the experimental examples are simulated by randomly applied excitations (both in time and location). A roving hammer (which in this case has no force reference) applied an excitation at a number of randomly chosen points in the active component for a duration of 20 seconds. In conjunction with a Hanning window (66.7% overlap), each time block recorded is 1 second long, generating 20 time blocks for a given operational excitation. Fig. 5.1 illustrates three different methods of processing the blocks to generate an operational transmissibility. These are, for each operational state measurement: averaging over all time blocks, using all time blocks with no averaging, and only using one time block.

The first method is the most common and generally considered the most accurate. However, the other methods may also be of interested in the context of computational limitations, especially in real-time.

Fig.5.1a displays a classical method of processing time domain date in vibro-acoustics (Janssens et al. [1999]), and presented in the equation below,

$$\begin{pmatrix} \langle v_1 \rangle \\ \langle v_2 \rangle \\ \vdots \\ \langle v_k \rangle \end{pmatrix} = \begin{pmatrix} \sqrt{\langle S_{11} \rangle} \\ \sqrt{\langle S_{22} \rangle} \\ \vdots \\ \sqrt{\langle S_{kk} \rangle} \end{pmatrix} \odot \begin{pmatrix} e^{-j0} \\ e^{-j\angle\langle S_{12} \rangle} \\ \vdots \\ e^{-j\angle\langle S_{1k} \rangle} \end{pmatrix} \tag{5.20}$$

For the averaged case, the operational velocity vector is calculated by auto and cross-spectral densities. Specifically, the cross-spectrum angle for each of the response signals (k) is allocated to the phase of a corresponding auto-spectrum by an element wise product $\odot$. Additionally, the auto and cross-spectral densities over all time blocks are averaged. This operational will simply be referred to from onwards as 'time-averaged'. This formulation assumes that all elements the velocity vector are coherent with one another, such that a single column of the cross-spectrum contains sufficient phase information. It is important to have reliable phase referencing, as it is essential when dealing with matrix inversions involving complex spectra (Meggitt [2017]). For example, for a transmissibility using b and c DoF subsets (say $\mathbf{T}_{bc}^{r,a}$), across N amount of operational states, the velocity matrices take the form,

$$\mathbf{V}_c = [\langle v_c^1 \rangle | \langle v_c^2 \rangle | \cdots | \langle v_c^N \rangle |] \tag{5.21}$$

$$\mathbf{V}_b = [\langle v_b^1 \rangle | \langle v_b^2 \rangle | \cdots | \langle v_b^N \rangle |] \tag{5.22}$$

where the superscript denotes the column vector of velocities measured for a given operational state. In the second method shown by Fig.5.1b, when no time-averaging is applied the velocity matrices take the form,

$$\mathbf{V}_c = [|v_c^{1,1}, v_c^{1,2}...v_c^{1,20}|v_c^{2,1}, v_c^{2,2}...v_c^{2,20}|\cdots|v_c^{N,1}, v_c^{N,2}...v_c^{N,20}|] \tag{5.23}$$

$$\mathbf{V}_b = [|v_b^{1,1}, v_b^{1,2}...v_b^{1,20}|v_b^{2,1}, v_b^{2,2}...v_b^{2,20}|\cdots|v_b^{N,1}, v_b^{N,2}...v_b^{N,20}|] \tag{5.24}$$

where the superscript denotes the particular operational state and time block. In the final alternative method as shown by Fig.5.1c, only 1 block out of the 20 is chosen for FFT. In this example we take the 5th block, therefore yielding the following definitions,

$$\mathbf{V}_c = [v_c^{1,5}, v_c^{2,5}\cdots v_c^{N,5}] \tag{5.25}$$

$$\mathbf{V}_b = [v_b^{1,5}, v_b^{2,5}\cdots v_b^{N,5}] \tag{5.26}$$

In this section, operational transmissibilities used in the ORT identities ($\mathbf{T}_{ca}^{f,a}$, $\mathbf{T}_{bc}^{r,a}$) are calculated using the alternative 1 block or all blocks no averaging methods, and compared against FRF-based transmissibilities as validation. In the case of the Fourier spectrum being taken for 1 time block (Fig.5.1c), the velocity matrix of the system is 7×7 for Fig.4.4 case study, 9×9 for Fig.4.10, and 12×32 for Fig.4.26. On the other hand when the Fourier spectrum is taken for all time blocks with no time-averaging applied (illustrated in Fig.5.1b), the system velocity matrix is 7×160 for Fig.4.4, 7×180 for Fig.4.10, and 12×640 for Fig.4.26. This is due to 20 time blocks taken for each excitation position.

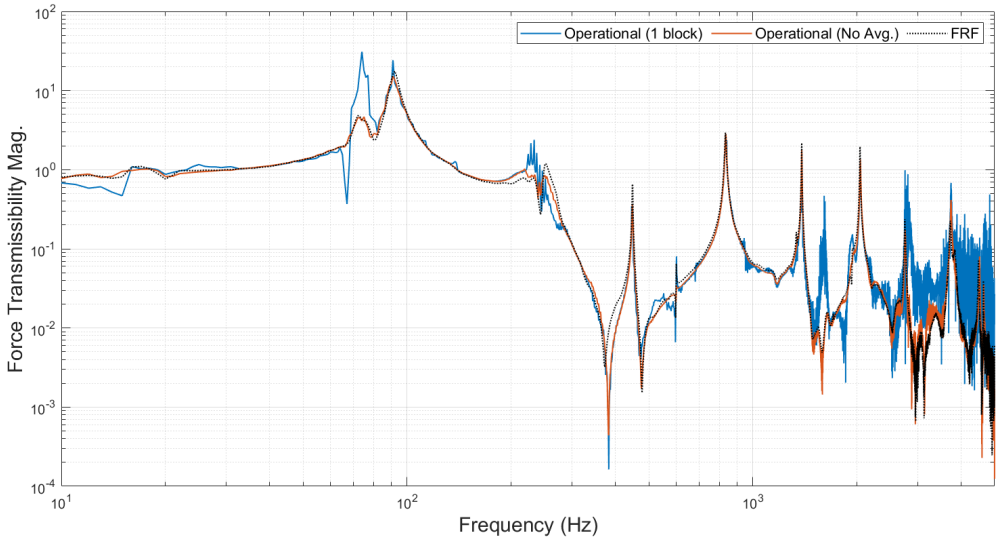

(a) $\mathbf{T}_{ca}^{f,a}$

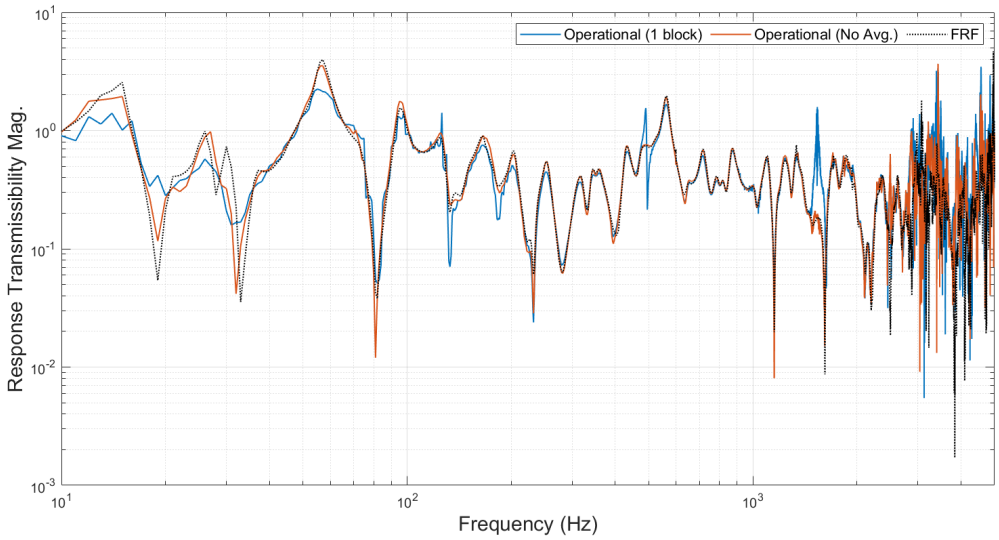

(b) $\mathbf{T}_{bc}^{r,a}$

Figure 5.2: Operational $\mathbf{T}_{ca}^{f,a}$ and $\mathbf{T}_{bc}^{r,a}$ calculated using 1 time block or all time blocks with no averaging. In reference to single-interface test rig, Fig.4.4.

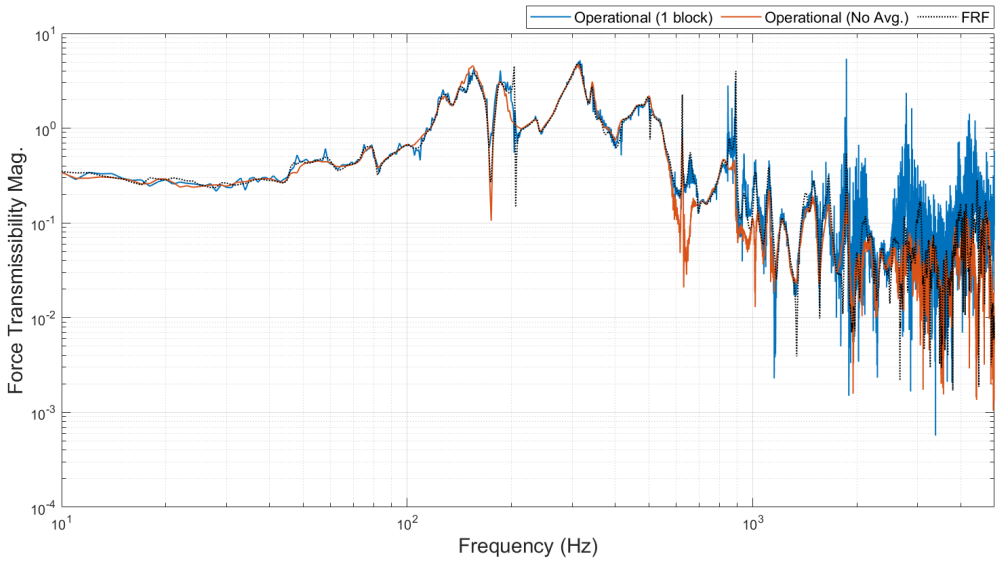

(a) $\mathbf{T}_{ca}^{f,a}$

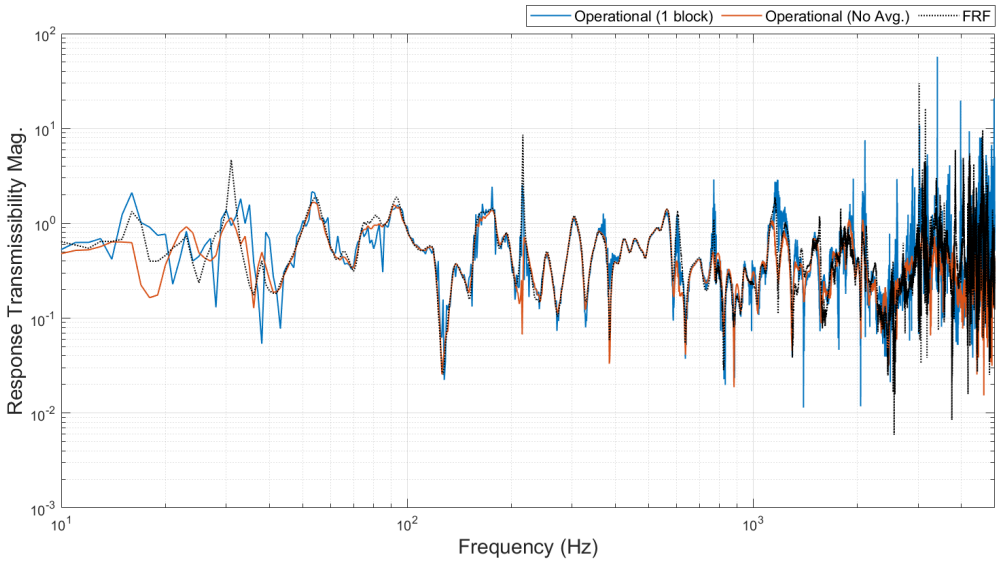

(b) $\mathbf{T}_{bc}^{r,a}$

Figure 5.3: Operational $\mathbf{T}_{ca}^{f,a}$ and $\mathbf{T}_{bc}^{r,a}$ calculated using 1 time block or all time blocks with no averaging. In reference to three-interface test rig, Fig.4.10.

Firstly, let us consider the processing methods for the resilient single-interface experimental example (Fig.4.4), as shown by Fig.5.2. Force and response transmissibilities are calculated using either the FFT of one block, or all blocks with no time-averaging. Overall, both transmissibilities show there is good agreement between the alternative processing methods and the FRF-based route. In Fig.5.2a, both methods perform well overall, with the 1 block processing showing a few small artefacts below 2kHz.

However from 3kHz and above this processing method yields a force transmissibility which increases significantly in noise. While all plots shown an increase in this region, this processing certainly has the largest increase. In the case of the response transmissibility in Fig.5.2b, the no average and 1 block cases both appear to show similar accuracy throughout the whole frequency range. In the region of 3-5kHz, both methods appear to have comparable amounts of noise. It should be noted however that the FRF-based transmissibility also shows increased noise in this region as well, suggesting an inherent error for the measurement of this particular transmissibility on this experimental example - most likely attenuation based error as shown by analyses made in the previous chapter.

Let us also consider the resilient three-interface experimental example from Fig.4.10. For the force transmissibility in Fig.5.3a, the 1 block FFT case shows good agreement against the FRF measurement up to around 2kHz. Above this there is a large amount of noise, similar to the previous experimental example in Fig.5.2a. The all blocks no time-average processing also agrees with the FRF-based one, and shows much less noise from 2kHz and above. The response transmissibility in Fig.5.3b also shows a similar trend for both processing methods to the single-interface example. In general there is good agreement with the FRF-based transmissibility for the majority of the frequency range, other than an increase in noise for all plots from around 2.5kHz and above. This further suggests this transmissibility is subject to attenuation based error for the resilient three-interface experiment as well.

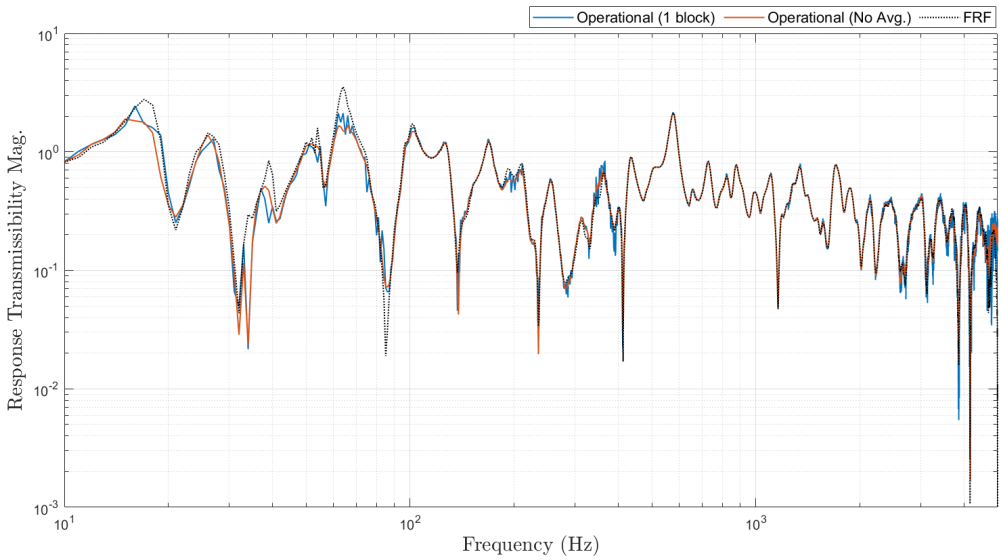

(a) Using all 20 operational states.

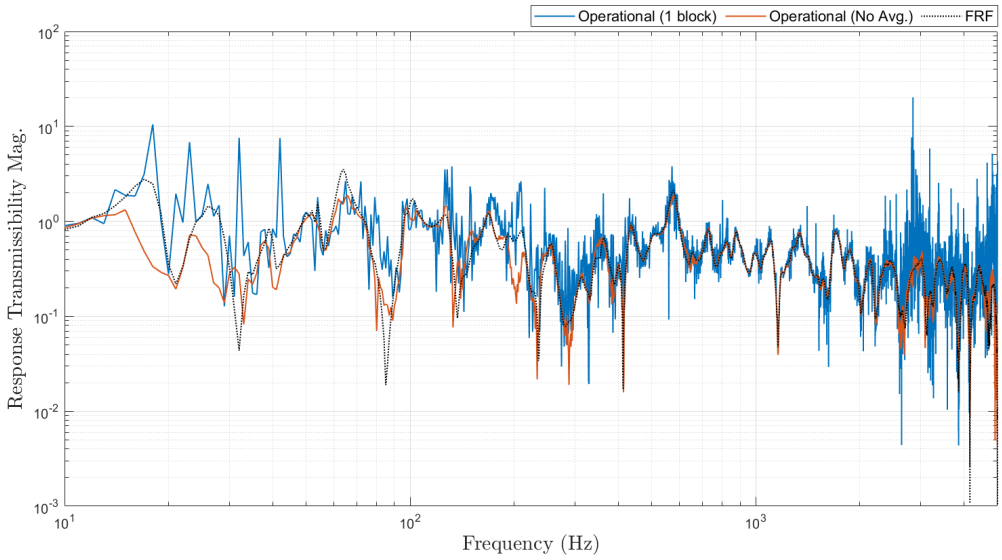

(b) Equating the number of operational states to DoFs in subset c, 6.

Figure 5.4: Operational $\mathbf{T}_{bc}^{r,a}$ calculated using 1 time block or all time blocks with no averaging. In reference to rigid-interface test rig, Fig.4.26.

In the above figure, analysis is conducted on the alternative processing methods for a rigid-interface experimental example (Fig.4.26). The techniques were tested when over-determined (more operational states than the number of DoFs in subset c), and when the number of operational states equates the amount of c DoFs. Fig.5.4a indicates both methods are highly accurate when over determined, appearing very much in line with the FRF measurement. On the other hand, Fig.5.4b suggests when the

number of operational states is equal to amount of c Dofs, the 1 block technique in particular is very sensitive to noise across the majority of the frequency range. However when all blocks with no time-averaging is used, noise is also present but far less than the 1 block processing. This makes sense, as shown in the previous chapter, that matrix inversion error occurs when the inverted term is ill-conditioned. Despite their errors, both processing methods do follow the trend of the FRF-measurement generally. It should be noted that although the inverse approach is prone to ill-conditioning, regularisation techniques are usually employed to combat it as demonstrated by Thite and Thompson [2003a] Thite and Thompson [2003b]. Truncated singular value decomposition and Tikhonov regularisation techniques were tested during this study, but did not make an improvement to warrant their inclusion.

5.3 Output-only vs. FRF measurement of transmissibilities used in the ORT identities

In this section, conventional FRF-based transmissibilities are compared with output-only ones determined using the most commonly used technique previously shown in Eq.5.20 (multiple block averaging). Importantly, the output-only transmissibilities are calculated without any force reference, and done so using complex response (velocity) spectra. To assess the accuracy of the operational transmissibilities in the ORT identity using the standard time-averaged approach, while also without introducing additional error/variability due to changing excitation positions, the 'ambient' forces were applied to the same sets of DoFs used in the FRF test. Rather than applying a single excitation, as done for the FRF test, a series of random excitations (both in time and location around the the DoF) were applied for a period of 20 seconds using a roving hammer.

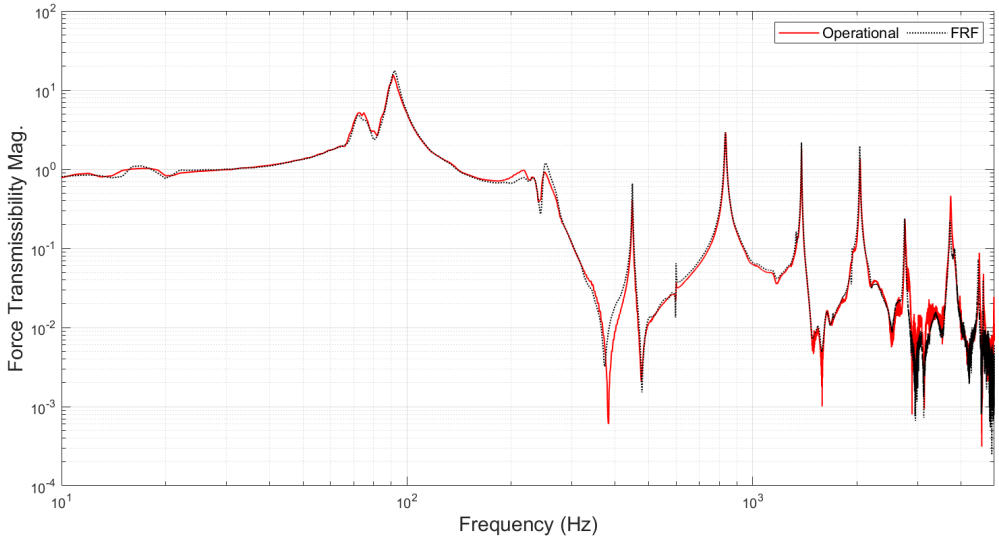

(a) $\mathbf{T}_{ca}^{f,a}$

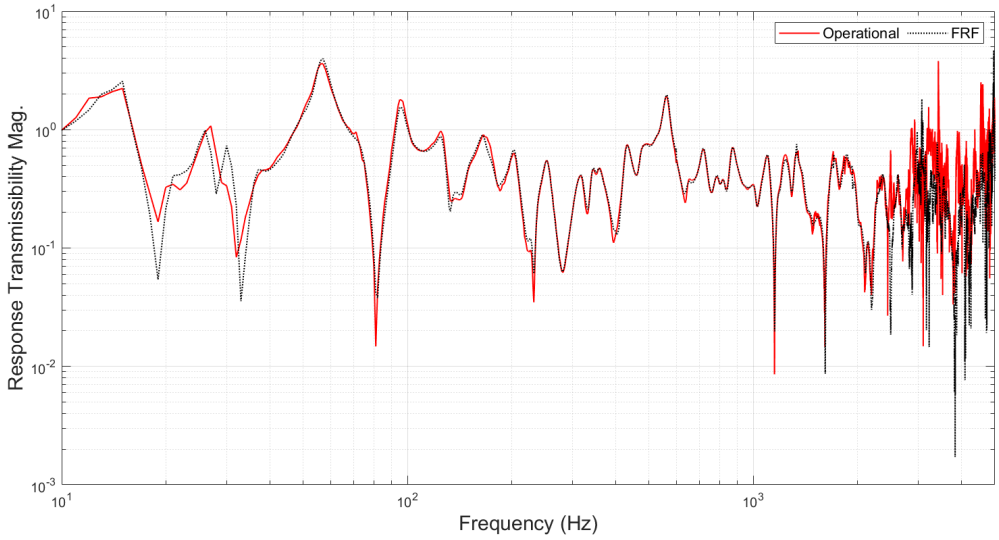

(b) $\mathbf{T}_{bc}^{r,a}$

Figure 5.5: FRF vs operational $\mathbf{T}_{ca}^{f,a}$ and $\mathbf{T}_{bc}^{r,a}$. In reference to single-interface test rig, Fig.4.4.

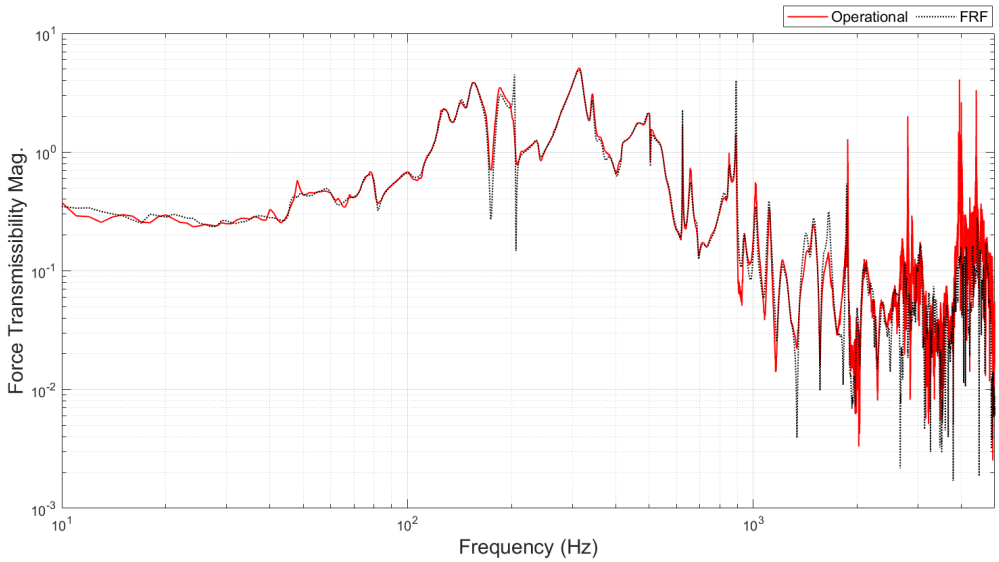

(a) $\mathbf{T}_{ca}^{f,a}$

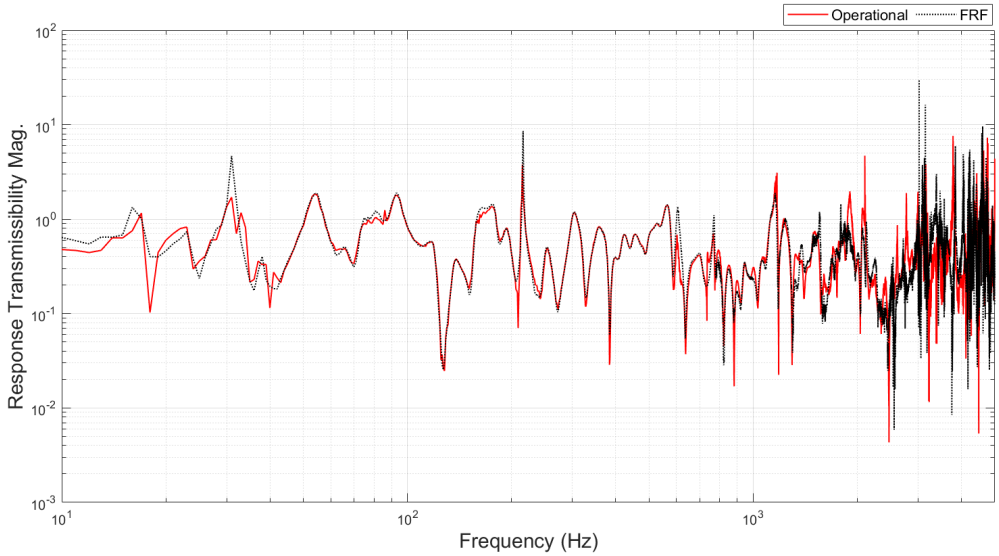

(b) $\mathbf{T}_{bc}^{r,a}$

Figure 5.6: FRF vs operational $\mathbf{T}_{ca}^{f,a}$ and $\mathbf{T}_{bc}^{r,a}$. In reference to three-interface test rig, Fig.4.10.

In reference to the resilient single-interface assembly, Fig.5.5 shows the operational transmissibilities agree well with the FRF-based ones, and overall show less noise and artefacts to the alternative processing methods in Fig.5.2. Both operational and FRF-based measurements of $\mathbf{T}_{ca}^{f,a}$ show a small increase in noise between 3-5kHz. In comparison, Fig.5.5b shows operational and FRF-based $\mathbf{T}_{bc}^{r,a}$ have a greater amount of noise in the 3-5kHz region. To calculate this transmissibility (see Eq.4.14), we use

$\mathbf{Y}_{C_{ca}}$ which traverses the isolator, and so at higher frequencies it is subject to noise. The inversion of $\mathbf{Y}_{C_{ca}}$ has the effect of amplifying this noise. On the other hand, $\mathbf{T}_{ca}^{f,a}$ requires the inversion of $\mathbf{Y}_{C_{bc}}$ (see Eq.4.19), which is not affected by the isolators attenuation.

Let us also consider the three-interface test rig from Fig.4.10. Similarly to the single-interface experimental example, Fig.5.6 shows good agreement between the output-only transmissibilities and the FRF-based ones. For the operational transmissibility in Fig.5.6a, noise begins to emerge from around 2kHz and above. In the next set of figures, this will be made clear that this is largely attributed to the amount of operational states used (in this case 3). The FRF-based $\mathbf{T}_{ca}^{f,a}$ also shows noise in this region but to a lesser than the output-only one. Meanwhile in Fig.5.6b, the FRF plot shows even more noise than the force transmissibility from 2kHz and above. As detailed before, this is due to the amplification of noise when inverting $\mathbf{Y}_{C_{ca}}$, which traverses the isolator and is affected by its attenuation. Overall, the operational $\mathbf{T}_{bc}^{r,a}$ agrees well with the FRF-based one up to around 2.5kHz.

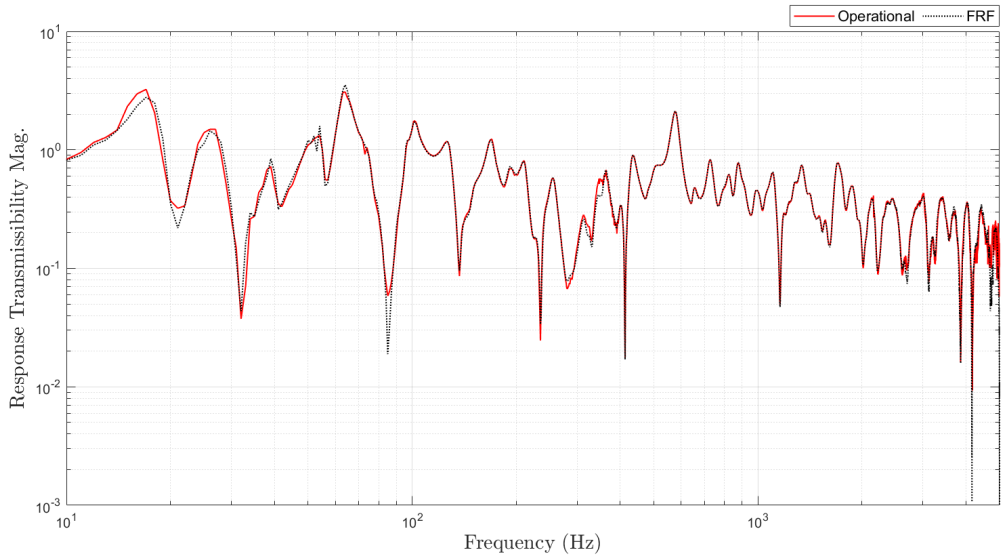

Figure 5.7: FRF vs operational $\mathbf{T}_{bc}^{r,a}$. In reference to rigid-interface test rig, Fig.4.26.

For the rigid-interface experimental example in Fig.4.26, no responses are installed within A, meaning the measurement of $\mathbf{T}_{ca}^{f,a}$ is not possible. Thus, all analysis on the

rigid connection experiment is conducted only on the response transmissibility $\mathbf{T}_{bc}^{r,a}$. Fig.5.7 displays the best agreement between response transmissibilities. While all experimental examples indicate the operational $\mathbf{T}_{bc}^{r,a}$ is similar to the FRF measurement, the increased noise in 3-5kHz region present in the other experimental examples is not observed for this case. This is because there no isolator is used at the connection point between A and B, meaning no attenuation based error exists.

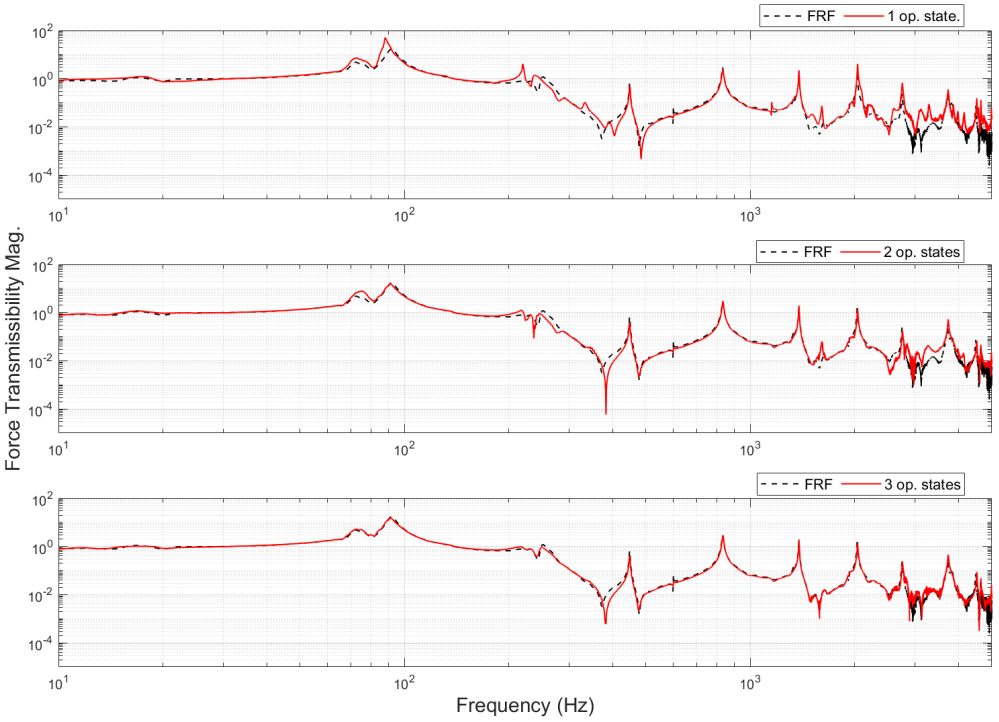

(a) $\mathbf{T}_{ca}^{f,a}$

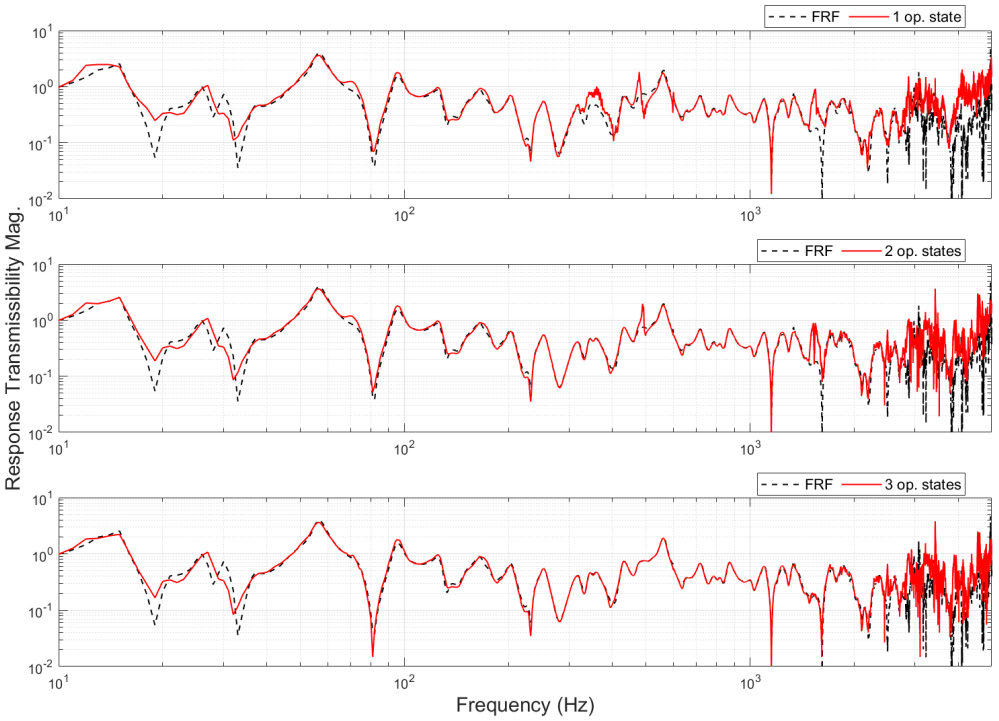

(b) $\mathbf{T}_{bc}^{r,a}$

Figure 5.8: Operational transmissibilities $\mathbf{T}_{ca}^{f,a}$ and $\mathbf{T}_{bc}^{r,a}$. Number of operational states changed incrementally, and compared against FRF-measurement. In reference to single-interface test rig, Fig.4.4.

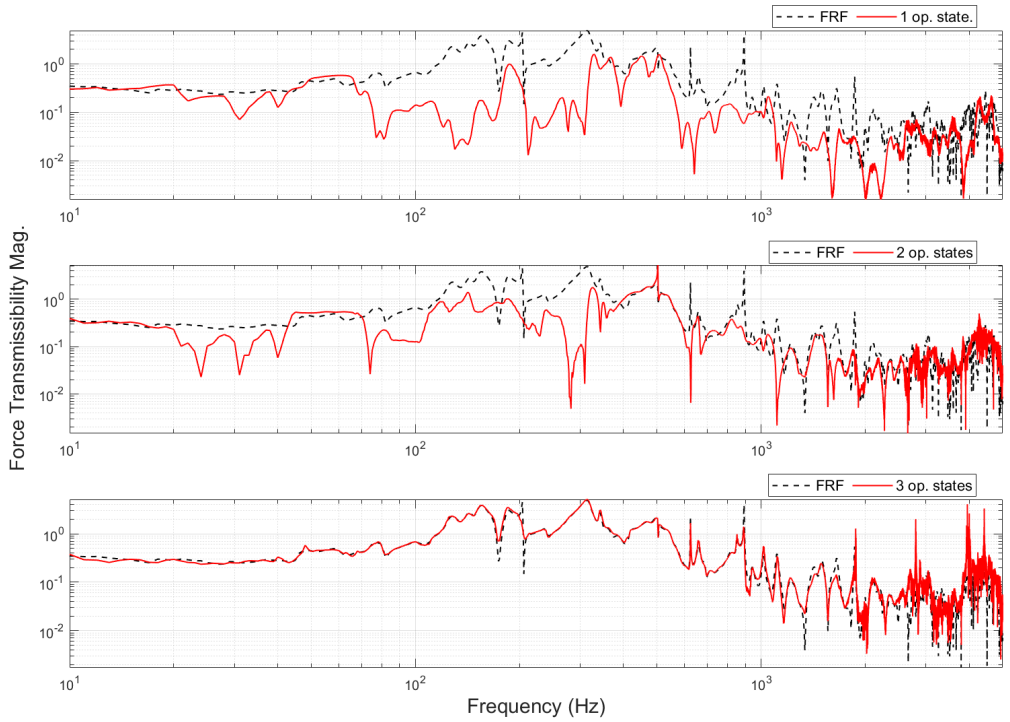

(a) $\mathbf{T}_{ca}^{f,a}$

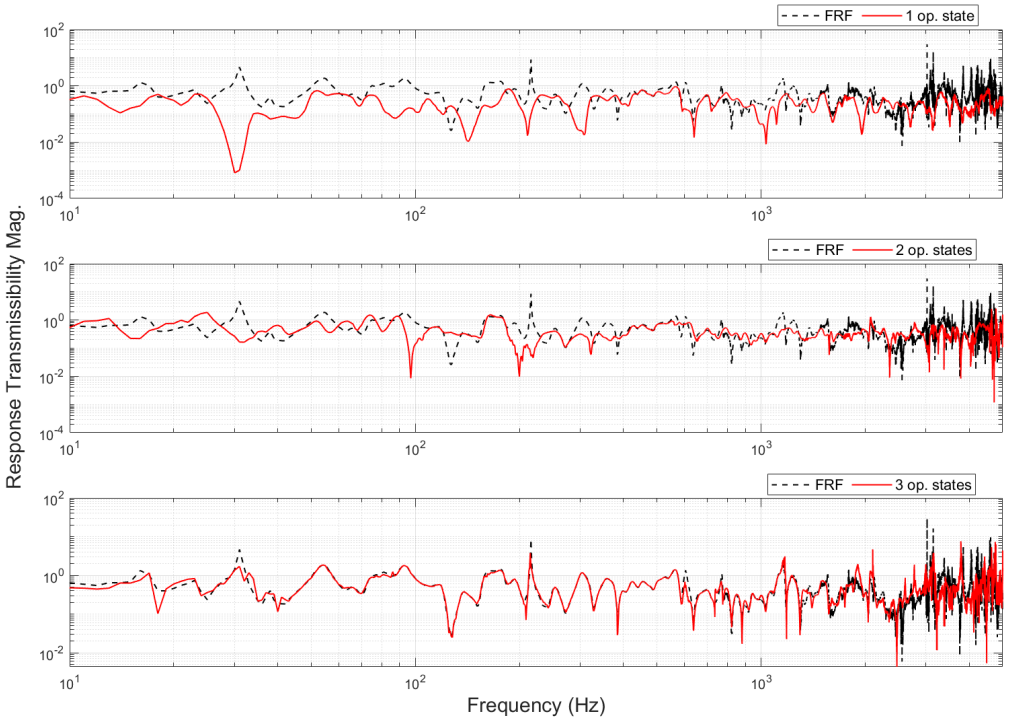

(b) $\mathbf{T}_{bc}^{r,a}$

Figure 5.9: Operational transmissibilities $\mathbf{T}_{ca}^{f,a}$ and $\mathbf{T}_{bc}^{r,a}$. Number of operational states changed incrementally, and compared against FRF-measurement. In reference to three-interface test rig, Fig.4.10.

Shown in Fig.5.8 are the FRF and operational transmissibilities obtained using an increasing number of operational states (1 from the top sub-figure, 2 in the middle, and 3 in the bottom one). For the single DoF interface experiment considered here, a single operational state within a should be sufficient to obtain the transmissibility as it equates to the amount of interface c DoFs (1). However, additional DoFs can be included to over-determine the problem. For $\mathbf{T}_{ca}^{f,a}$ shown in Fig.5.8a, using 3 operational states shows the smoothest plot and most precise transmissibility. When compared to the 1 operational state plot in the top sub-figure, using 3 shows less artefacts in the range of 1.2-5kHz, as well as better representation of resonances at 3.75kHz and 4.5kHz, and anti-resonances at 2.95kHz and 3.1kHz. Meanwhile for the operational response transmissibility used in Eq.5.1, Fig.5.8b shows increasing the number of excitations at a similarly smooths the plot (to a slightly lesser degree than Fig.5.8a), while also making the resonances at 350Hz, 560Hz, and 1.7kHz more intelligible. A key difference to $\mathbf{T}_{ca}^{f,a}$, is that $\mathbf{T}_{bc}^{r,a}$ shows a much greater amount of noise from around 2.5-5kHz, which is exacerbated as the number of operational states increases. As the noise floor is already reached with 1 operational state, additional states will only add more noise.

In the previous chapter, the accuracy of operational transmissibilities was examined by reducing the number of operational states below the required amount. To calculate an output-only transmissibility that is line with an equivalent FRF-based measurement, the number of operational states must be greater than or equal to the amount of interface DoFs c. For the same experimental example in Fig.4.22, $\mathbf{T}_{b}^{r,c}c$ is calculated using 3 operational states, which equates to the three Dofs within c. This was confirmed to be in line with an already established invariant FRF-based $\mathbf{T}_{b}^{r,c}c$, and was compared to the same transmissibility when only 1 or 2 operational states were used. It was indicated by this figure that 1 operational state was insufficient at low frequencies but reasonable as the frequency increases. When 2 operational states were used the accuracy was increased at low frequencies, and it was indicated that having 1 operational state below the required amount would suffice. In this section, we will examine a similar transmissibility, $\mathbf{T}_{bc}^{r,a}$, which is used in the ORT method. In theory the same

trends should be observed for this transmissibility as well.

Identically to Fig.5.8, Fig.5.9 shows the operational transmissibilities with an increasing amount of operational states used from top to bottom. It is clear for both Fig.5.9a and 5.9b, when 1 operational state is used, the output-only transmissibilities do not match the FRF-based ones. In the case of 2 operational states, there are certainly some inaccuracies but begins to follow the FRF measurement much closer. In the bottom sub-figures where 3 operational states were used, we achieve the best result and the operational transmissibilities show good agreement with the FRF-based ones. When the number of operational states equate to the number of c DoFs, noise increases for the operational transmissibilities from around 3kHz. For the force transmissibility in the single-interface case study (Fig.5.8a), noise does not increase as much as the three-interface example in Fig.5.9a. This is likely due to the matrix inversion of $\mathbf{V}_c$ (see Eq. 5.6), as the matrix is now square. Increased noise at three operational states is also observed in Fig.5.9b, which is also likely for the same reason (see Eq.5.3).

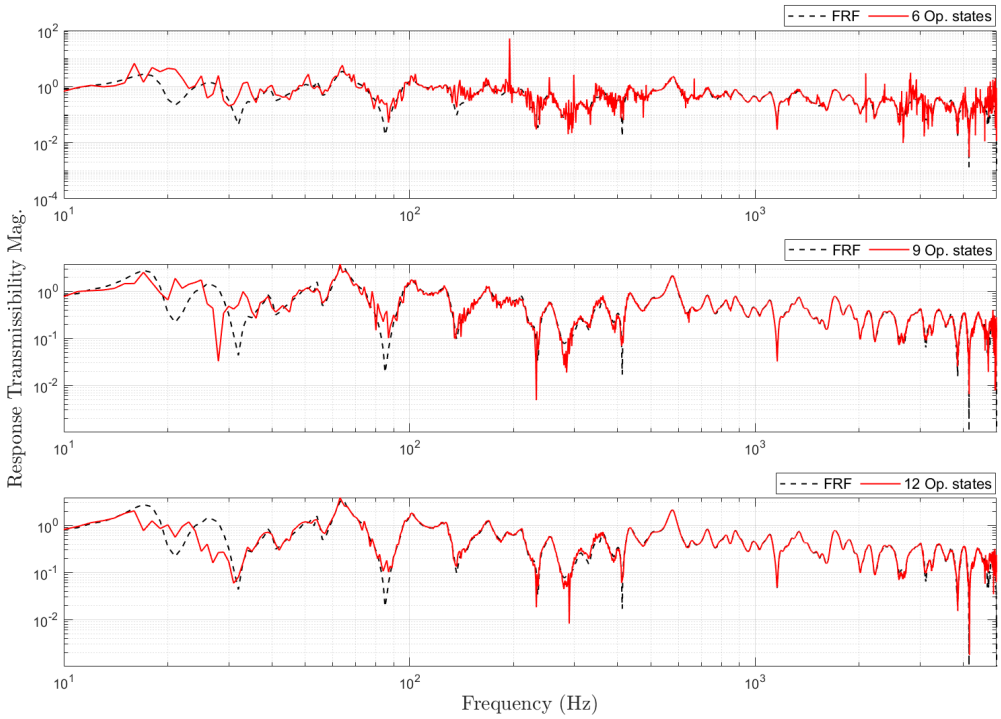

Figure 5.10: Operational $\mathbf{T}_{bc}^{r,a}$. Number of operational states used changed incrementally and compared against FRF-measurement. In reference to rigid-interface test rig, Fig.4.26.

For the rigid-interface example, the accuracy of the output-only response transmissibility is analysed when over-determined. In the top sub-figure of Fig.5.10, the operational states of output-only $\mathbf{T}_{bc}^{r,a}$ is equal to the number of c DoFs. Once again an increase in noise can be observed, which is attributed to $\mathbf{V}_c$ being square and thus causing matrix inversion error. This is occurs when a matrix is ill-conditioned, which makes it very sensitive to input changes when inverted. However when the problem is over determined, noise is reduced as shown by the middle sub-figure, and even more so in the bottom sub-figure when the number of operational states is double the amount of c DoFs.

It was shown in the previous chapter the number of remote responses was changed in the output-only transmissibility calculation. By adding an extra response, an extra row is included to the matrix $\mathbf{V}_b$ or $\mathbf{V}_a$ for $\mathbf{T}_{bc}^{r,a}$ and $\mathbf{T}_{ca}^{f,a}$ respectively. This has no effect on the transmissibilities already established. As we already know no changes will take place to the transmissibilities, no extra analysis is conducted on the remote responses. On the other hand, adding or removing interface c DoFs will effect the rows of $\mathbf{V}_c$ which does have the effect of changing the operational transmissibilities. The reason being that the inversion of $\mathbf{V}_c$ applies a set of physical constraints, and by adding or removing c points we alter the blocking constraints, which in turn affects the transmissibility term. It should be noted that the transmissibilities calculated for all experimental examples use all available remote and interface responses.

5.4 ORT prediction vs. direct measurement

Now that we have verified the accuracy of the output-only transmissibilities and determined a suitable processing approach, we are able to incorporate them within the ORT identities shown in Eq. 5.3 and 5.6. We begin by comparing the performance of both ORT identities and the RT identity for the single interface experiment, followed by the three resilient-interface experiment, and finally the rigid-interface example. Each result is plotted alongside the directly measured $\mathbf{Y}_{C_{cc}}$, obtained from an FRF

test. In Section 5.3, transmissibilities in the ORT identities were shown to be accurate when the amount of operational states was equal to the number of c DoFs, and even more so over determined. Therefore in this section, the ORT predictions for single resilient-interface and rigid-interface examples are over determined, while the three resilient-interface experiment equates the number of operational states to amount of c DoFs. Additionally, no difference in accuracy was found when the amount of remote responses changed, therefore all are included for all three experimental case studies. The mobility terms in the ORT and RT identities use all excitations and remote responses available.

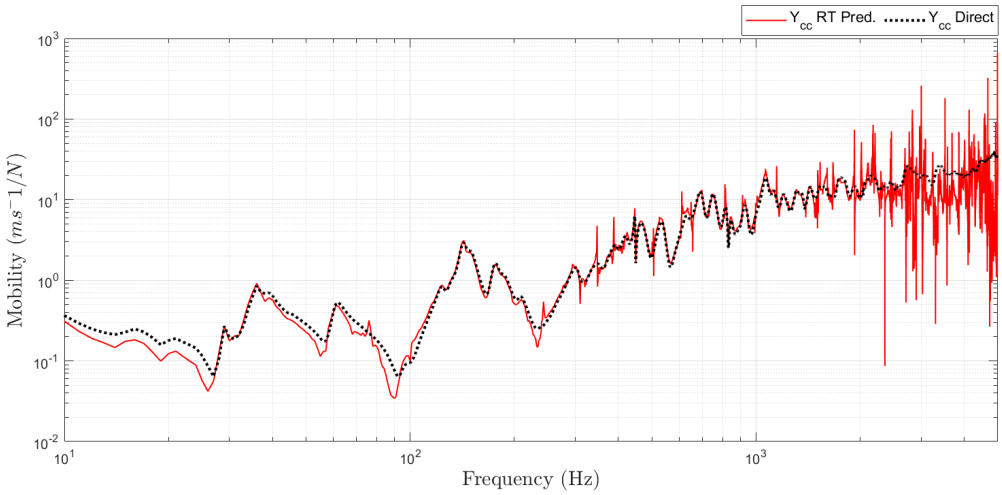

(a) Round-trip prediction vs. direct measurement.

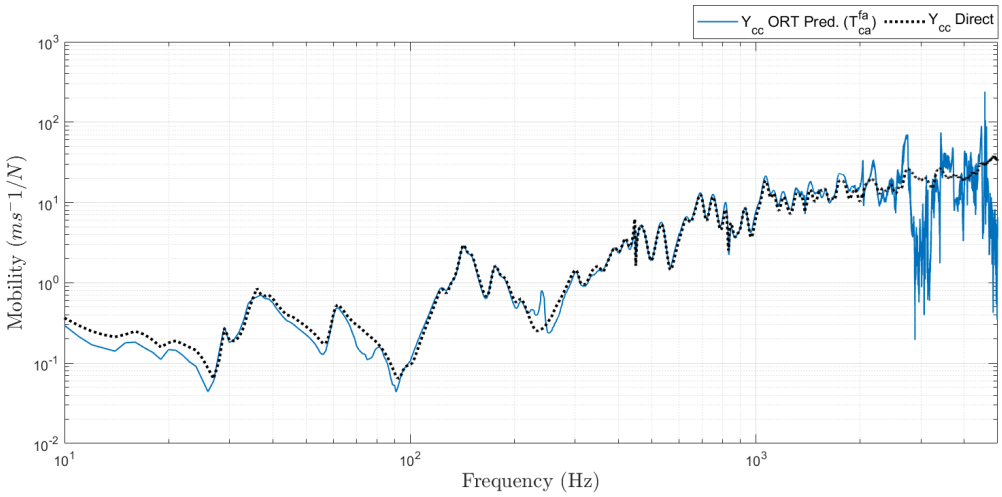

(b) Operational Round-trip prediction using $\mathbf{T}_{ca}^{f,a}$ vs. direct measurement.

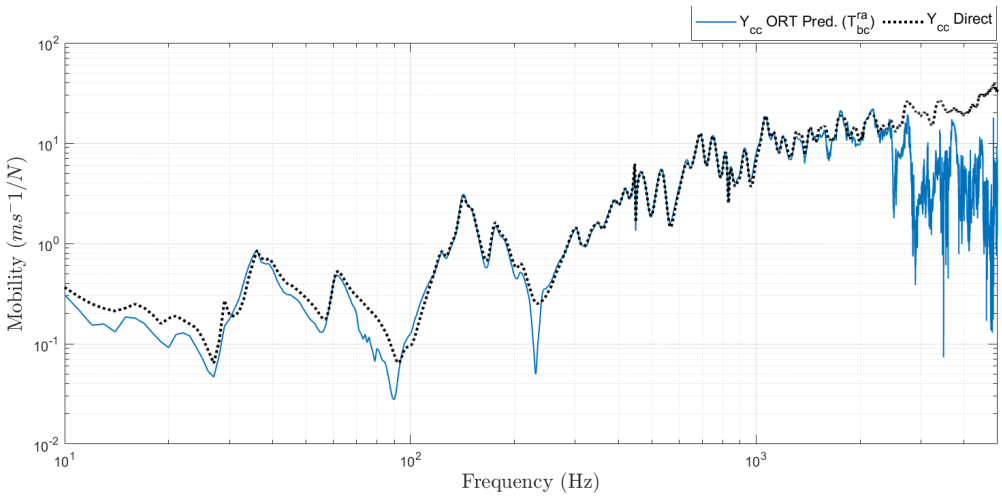

(c) Operational Round-trip prediction using $\mathbf{T}_{bc}^{r,a}$ vs. direct measurement.

Figure 5.11: RT & ORT predictions vs. direct $\mathbf{Y}_{C_{cc}}$ for single resilient-interface test rig, Fig.4.4.

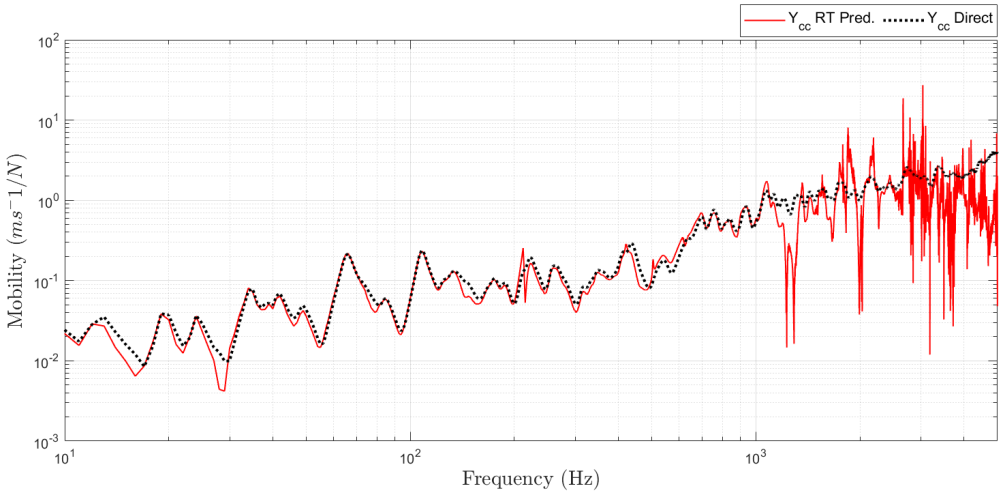

(a) Round-trip prediction vs. direct measurement.

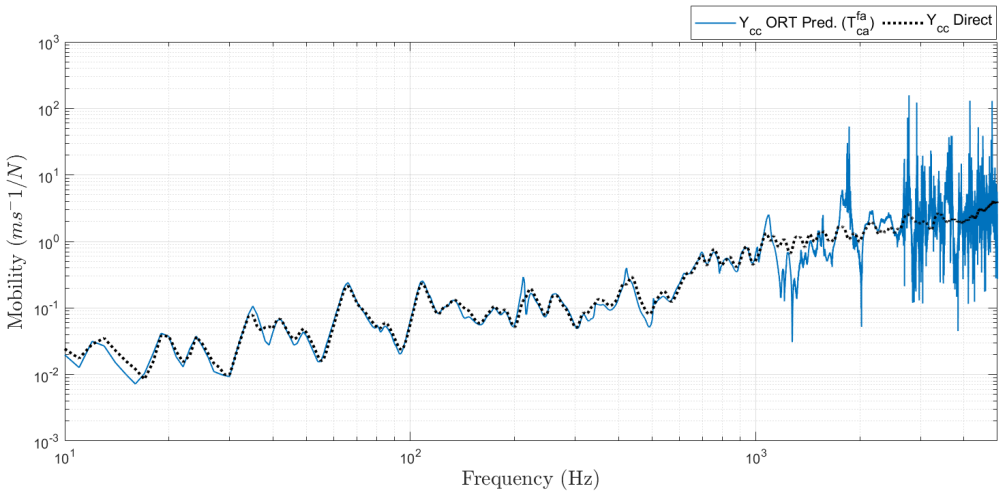

(b) Operational Round-trip prediction using $\mathbf{T}_{ca}^{f,a}$ vs. direct measurement.

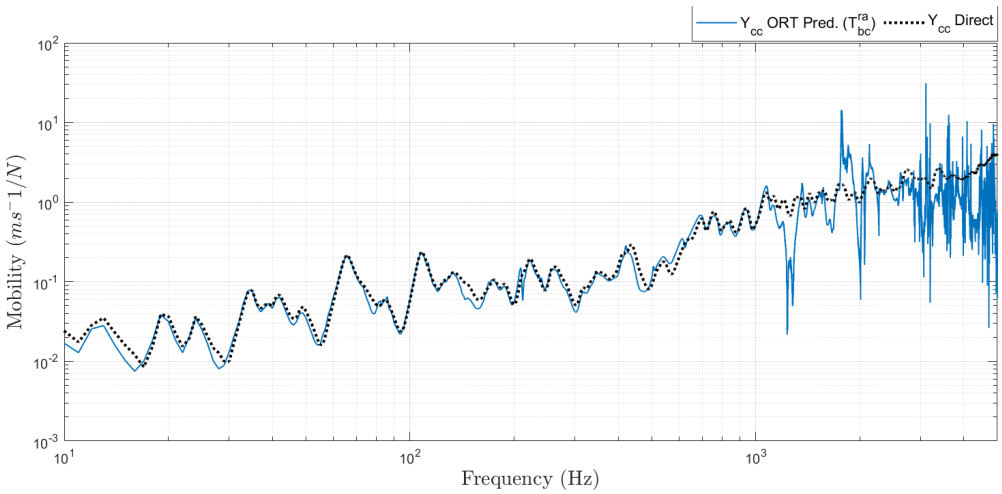

(c) Operational Round-trip prediction using $\mathbf{T}_{bc}^{r,a}$ vs. direct measurement.

Figure 5.12: RT & ORT predictions vs. direct $\mathbf{Y}_{C_{cc}}$ for three resilient-interface test rig, Fig.4.10.

In the single resilient-interface experiment, Fig.5.11a generally shows good agreement between the RT identity and direct $\mathbf{Y}_{C_{cc}}$ up to 3kHz. A series of small artefacts begin to emerge from 310Hz, and increase in number and magnitude from 1.9kHz. These are likely due to inconsistencies in the measured FRF matrices, especially $\mathbf{Y}_{C_{ba}}$, whose inverse must be taken. The accuracy of the RT prediction begins to decrease as noise increases from 3-5kHz. In Fig. 5.11b, the inclusion of operational force transmissibility $\mathbf{T}_{ca}^{f,a}$ into the RT formula yields a point mobility prediction with less artefacts and noise. Similarly to Fig.5.11a noise also increases from 3kHz, but to a lesser degree. The accuracy of the $\mathbf{T}_{ca}^{f,a}$ ORT prediction falls from 2.75kHz. Unlike Fig.5.11a artefacts do not emerge between 310Hz-2.75kHz. The operational response transmissibility version of the ORT identity plotted in Fig.5.11c also shows good agreement to the direct $\mathbf{Y}_{C_{cc}}$, displaying a similar overall accuracy to its force transmissibility counterpart. Equivalently to Fig.5.11b the amount of artefacts are less than the RT prediction. All $\mathbf{Y}_{C_{cc}}$ predictions appear to be most precise between 100Hz-2kHz, with the exception of the anti-resonance at 230Hz for Fig.5.11c. The $\mathbf{T}_{bc}^{r,a}$ ORT prediction shows the largest decrease in accuracy from around 2.5kHz, which as stated previously, is due to the effect of isolator-induced noise.

For the three resilient-interface experimental example, we present the RT & ORT predictions of $\mathbf{Y}_{C_{cc}}$ in Fig.5.12. Similarly to the single resilient-interface example, Fig.5.12a generally shows good agreement between the RT prediction and direct measurement up to around 1kHz. Noise begins to affect the RT prediction from 2.5kHz and above. On the other hand, the $\mathbf{T}_{ca}^{f,a}$ ORT prediction shows similar agreement overall with the direct measurement. Correspondingly to the RT prediction, the accuracy of the ORT begins to decrease from 1kHz and above. Noise also occurs from 2.5kHz, although with increased magnitude compared to the RT method. For the $\mathbf{T}_{bc}^{r,a}$ ORT prediction in Fig.5.12c, we see a similar performance in the 10Hz-1kHz range. Once again, accuracy begins to decrease above 1kHz, with noise appearing from 3-5kHz.

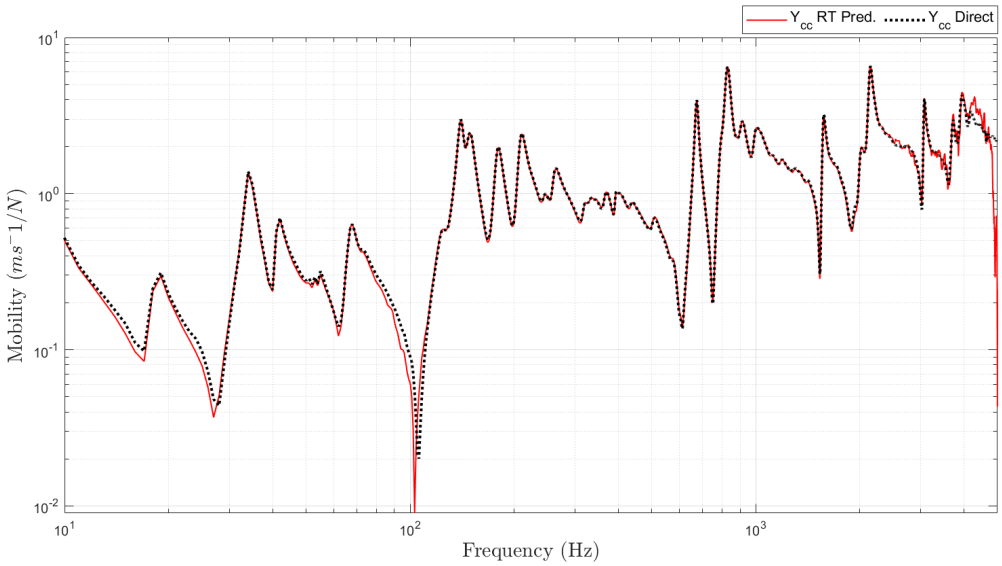

(a) Round-trip prediction vs. direct measurement.

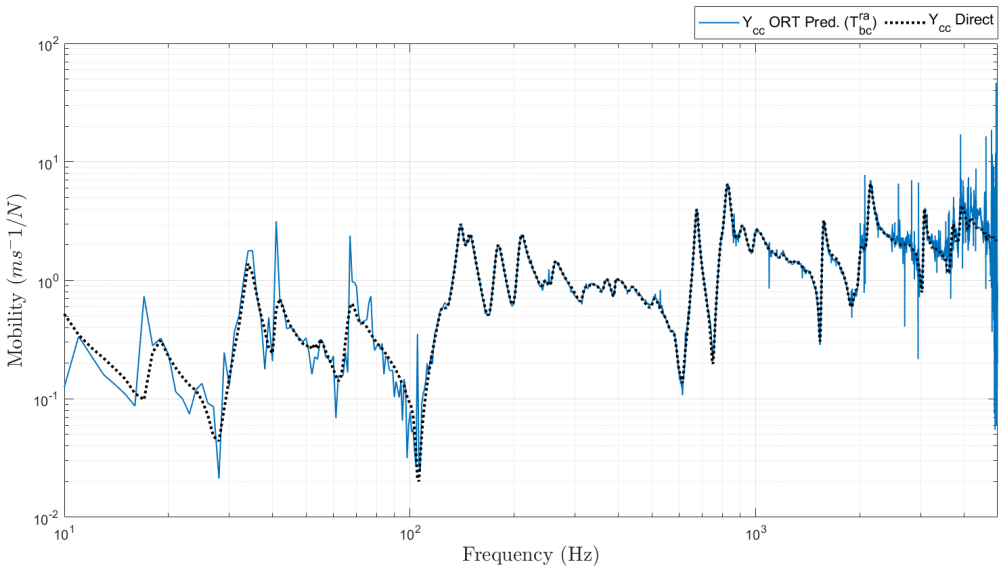

(b) Operational Round-trip prediction using $\mathbf{T}_{bc}^{r,a}$ vs. direct measurement.

Figure 5.13: RT & ORT predictions vs. direct $\mathbf{Y}_{C_{cc}}$ for rigid-interface test rig, Fig.4.26.

Earlier in this chapter is was explained that the ORT identity using $\mathbf{T}_{ca}^{f,a}$ cannot be used for the rigid-interface experimental example, as there are no responses installed on A. Therefore, only the Eq.5.3 ORT identity can be compared against the RT prediction and direct $\mathbf{Y}_{C_{cc}}$. Fig.5.13a appears as a highly accurate prediction for this experimental example across the full frequency range. Very little noise and virtually no artefacts are present for the RT method. The ORT prediction using $\mathbf{T}_{bc}^{r,a}$ also agrees well with the direct measurement. However, between 10-110Hz artefacts are present and accuracy

is slightly reduced. In the range 110Hz-2.5kHz the ORT prediction is highly accurate and very few artefacts or noise can be observed. From 2.5kHz and above noise and artefacts increase again, although the general trend of the prediction appears to follow the direct $\mathbf{Y}_{C_{cc}}$.

5.5 Discussion

In this chapter, an operational extension of the RT identity termed the ORT identity was derived and unveiled as a credible alternative. By combining a remote transfer mobility and operational response measurements whilst a coupled assembly is excited by unknown internal forces, the point mobility at an interface c can be predicted accurately.

In Section 5.2 the alternative methods of processing time domain data is analysed: taking the FFT of 1 block, or all blocks without time-averaging. Overall across all experimental examples, these techniques produced operational transmissibilities that agreed well with the FRF-based measurements. Although the 1 block processing was prone to increased noise at higher frequencies of $\mathbf{T}_{ca}^{f,a}$, the overall accuracy achieved was sufficient. All techniques for determining $\mathbf{T}_{bc}^{r,a}$ on the resilient interface experiments had shown to be accurate, with increased noise at higher frequencies attributed to attenuation based error. This was further proven as the rigid-interface experimental example did not show noise in the same frequency range (3-5kHz). Additionally for the rigid-interface example, both processing techniques were highly accurate when heavily over-determined. As expected when the amount of operational states equated the number of DoFs in c, increased error in the transmissibility was visible - attributed to the matrix inversion of $\mathbf{V}_c$ which is ill-conditioned. In general, the all block no time-averaging processing was the more accurate alternative across the case studies, but not as accurate as the standard time-averaged approach shown in the next section. What this part of the study has shown is that the alternative approaches are promising, and may serve as an alternative when computational power is limited. This can be

important in real-time calculation of operational transmissibilities, and is an area of future work.

In Section 5.3 it was found for the single resilient and rigid interface experiments that over-determining, i.e. increasing the number of operational states above the number of interface DoFs c, yielded the most accurate operational transmissibility when compared to the FRF-based measurement. In the three resilient-interface test rig, it was shown when the number of operational states was the same as the amount of c DoFs (3 in this example), there was good agreement with the FRF-based transmissibilities, but caused an increase in noise which was attributed to a matrix inversion error of an ill-conditioned $\mathbf{V}_c$ matrix. Further indicating the most accurate means of using the operational transmissibilities in the ORT identities was to over-determine the problem. Having a square $\mathbf{V}_c$ matrix would still yield a sufficiently accurate prediction but at the cost of small increase in error.

It was found for all case studies in Section 5.4, that there is good agreement between the ORT method and the directly measured point mobility. For the single resilient-interface experiment, both versions of the ORT identity displayed fewer artefacts overall and slightly less noise than the RT method in higher frequencies. All prediction methods displayed a drop in accuracy from roughly 2.5kHz upwards, with the response transmissibility ORT identity showing the least accurate prediction in this region due to the effect of isolator-induced noise. For the three resilient-interface example, all prediction methods displayed a similar performance, where the accuracy began to decrease from 1kHz upwards across the board. In both of these resilient interface experimental examples, noise occurs from roughly 2.5 - 5kHz. For the rigid-interface experiment, the force transmissibility ORT identity could not be used as there were no responses installed on A, thus only a comparison between the response transmissibility ORT and the RT could be made. It was found for this case study that the RT method was the most accurate, showing virtually no noise or artefacts. The $\mathbf{T}_{bc}^{r,a}$ ORT identity did also accurately prediction $\mathbf{Y}_{C_{cc}}$ but was contaminated by noise and artefacts at high frequencies.

While the ORT method still requires one mobility to be measured, the inclusion of operational transmissibilities indicates this is potentially more convenient in an industrial setting. There are fewer mobility terms to be measured via roving hammer, while also having identical accuracy to the RT method in the resilient interface case studies. For rigid interface assemblies within industry it is indicated that the ORT can predict the driving-point interface FRFs but at the cost of noise and artefacts at high frequencies. One possible application for the ORT method is in real-time prediction. The single mobility term in the identity can be measured once beforehand, and used in conjunction with real-time measured responses to monitor the point mobility $\mathbf{Y}_{C_{cc}}$. However, further investigation is needed before definitively proving that possibility.

Chapter 6

Identification of transmission paths & unknown bridges

In this chapter the singular values (SVs) of mobilities and transmissibilities, obtained using the SVD, are examined to detect transmission paths between source and receiver sub-structures using the "bottleneck" effect. Additionally, SVs are also examined in detecting an unknown mechanical bridge which circumvents the bottleneck. The theory, which is outlined in the beginning of this chapter, suggests observing the SVs of output-only transmissibilities may be possible in achieving the detection of known transmission paths and unknown mechanical bridges. This is particularly beneficial for industrial applications. This is firstly tested on a mass-spring model, and finally a experimental example.

Contents

One of the main implementations of the SVD within the field of vibro-acoustics is noise suppression, particularly in OMA (Araújo and Laier [2014]). Its uses have been ex-

tended over the years into other applications, such as identifying modes within in a system and determining which of those has the greatest energy contribution (Barton [2023] Barton et al. [2023]). In this chapter another application of the SVD is introduced for the context of coupled assemblies; identifying known transmission paths and any changes due to mechanical bridges using a bottleneck effect. The bottleneck effect is a well known phenomenon in the science and engineering, it refers to a situation where the performance, capacity, or throughput of a system is constrained or limited by a single component or process. This component or process, known as the "bottleneck" may either be of concern, such as the in the context of computing, but in others it may be sought after in order to determine the maximum efficiency or output of the system, much like the narrow neck of a bottle restricts the flow of liquid. In this chapter and in the context of vibro-acoustics, the bottleneck effect can be used for restricting multiple excitation mechanisms of a source to a limited subset of interface DoFs at a connection point, thus allowing the identification of known transmission paths between source and receiver sub-structures. In an industrial application, the radiated sound measured to a receiver may be greater than predicted, despite appropriate measures taken in attenuating sources (such as compressors or generators) with isolators. One possibility is this is caused by an unknown mechanical bridge between source and receiver, circumventing the attenuation measures. If the size, weight and space around the source allows, it may be possible to visually inspect and dismantle the source, but this may take time. As shown throughout this thesis, output-only methods are increasingly sought after in industrial applications. In the method shown in this chapter, an experimental alternative which seeks to detect known transmission paths and any unknown mechanical bridges via an output-only method is presented. However some analysis is conducted before attempting to reach that possibility, by presenting an EMA technique. In the EMA route, singular values (SVs) are analysed from the SVD applied to mobilities on a simple mass-spring system. Theory of the method is outlined in greater detail in the upcoming section, but in essence the amount of SVs for mobilities and transmissibilities are observed to see if there is a correlation between

the restricted amount of interface DoFs and mechanical bridges. The findings of the initial study are used to validate the method in a more "manual" sense. As the end goal is for the method to work in an output-only case, analysis of SVs is firstly conducted on FRF-based transmissibilities, and then finally operational transmissibilities. In the final part of the study, the method is tested on an experimental example.

6.1 Theory

For the detection of transmission paths and mechanical bridges, we start by considering a coupled assembly consisting of a source and receiver sub-structure which are rigidly connected at a single point serving as the bottleneck.

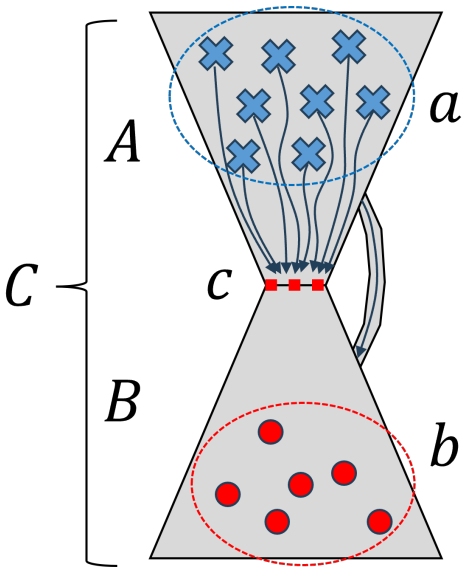

Figure 6.1: Illustration of experimental setup to detect transmission paths and bridges.

In the above figure, an example of a coupled assembly setup to analyse transmission paths is illustrated. Component A represents a source that contains multiple force mechanisms, coupled to a receiver sub-structure B via a rigid point connection. At the connection point between the sub-structures lies a subset of interface DoFs, c. While the source A will have multiple excitation mechanisms, the calculated responses in the receiver b are due to forces exerted by the c DoFs. Essentially, the b DoFs are not directly affected by the source excitations at DoF subset a and have been

'bottlenecked' by the c DoFs. The question that this chapter seeks to answer is: if we examine the SVs of either a mobility or transmissibility, can we determine how many transmission paths exist between the c DoFs and the responses at b? Additionally, if this is possible, will an extra SVs appear when a mechanical bridge exists? To answer these questions, the proposed method is initially applied to mobilities. Firstly, we begin with the definition of the SVD to some mobility $\mathbf{Y}$,

$$\mathbf{Y} = \mathbf{U}\mathbf{\Sigma}\mathbf{V}^{\mathrm{H}} \tag{6.1}$$

As pointed out previously in Section 2.9, a matrix where the SVD is applied may be either square or rectangular. Let's assume for this example that $\mathbf{Y}$ is rectangular and is $M \times N$. $\mathbf{\Sigma}$ will therefore also be rectangular with the size $M \times N$, containing the SVs σ ordered in descending order along its diagonal, $\sigma_1 > \sigma_2 > \sigma_3 > \ldots$. All other elements within $\mathbf{\Sigma}$ have a value of 0. The size of $\mathbf{U}$ will be $M \times M$, consisting of left singular vectors u_i. On the other hand, $\mathbf{V}$ is $N \times N$ and made up of right singular vectors v_i. $\mathbf{U}$ and $\mathbf{V}$ are both unitary (square and complex matrices) and of the form,

$$\mathbf{U} = \Big[\mathbf{u}_1, \mathbf{u}_2 \ldots \mathbf{u}_M\Big] \tag{6.2}$$

$$\mathbf{V} = \Big[\mathbf{v}_1, \mathbf{v}_2 \ldots \mathbf{v}_N\Big] \tag{6.3}$$

One explanation of what the SVD does, is that it splits up $\mathbf{Y}$ into a sum of ordered single rank r matrices $\mathbf{A}_i$,

$$\mathbf{Y} = \sum_{i=1}^{r} \mathbf{A}_i = \sum_{i=1}^{r} \sigma_i \mathbf{u}_i \mathbf{v}_i^{\mathrm{H}} \tag{6.4}$$

$\mathbf{A}_i$ matrices corresponding to first and highest value SVs represent the most important contributions within the force/velocity space. In relation to the detection of transmis-

sion paths, they essentially reveal how many independent modes or DoFs contribute to the coupled assemblies response for a given source excitation. For example, if there are 4 interface DoFs in c, then at most there are 4 independent transmission channels through the interface. The rank r in turn will be limited, which means up to 4 dominant SVs are obtained. $\mathbf{A}_i$ matrices corresponding to the final and smallest value SVs represent the least important contributions, which will most likely be noise. If a mechanical bridge is made between the source and receiver that circumvents the bottleneck, a new transmission channel is created. I.e. the additional path allows an energy transfer from the source, independent of c. This results in an additional dominant SV, because r has been increased. In the next section, this theory will be applied to three coupled mass-spring models, each being almost identical to one another, but increasing in the number of c DoFs. This part of the study is to determine if the theory works on the most ideal system. The first mass-spring system will be the simplest, containing only a single c interface DoF, and will have the SVs of mobilities $\mathbf{Y}_{C_{ba}}$, $\mathbf{Y}_{C_{xa}}$, $\mathbf{Y}_{C_{bc}}$ analysed. While this is the not the end goal, it is important to establish whether the theory works in EMA sense before the eventually moving onto an output-only technique. This is because of the controlled conditions set by a roving hammer test, and reduces the likelihood of experimental errors occurring, therefore yielding more accurate results. Following this, the SVs of mobility-based transmissibilities $\mathbf{T}_{ba}^{r,a}$, $\mathbf{T}_{bc}^{r,a}$, $\mathbf{T}_{da}^{r,a}$ are analysed on a mass-spring system with two c DoFs, and finally the operational variants on a three c DoF system. These transmissibilities are defined as,

$$\mathbf{T}_{ba}^{r,a} = \mathbf{Y}_{C_{ba}}\mathbf{Y}_{C_{aa}}^{-1} = \mathbf{V}_b\mathbf{V}_a^{+} \tag{6.5}$$

$$\mathbf{T}_{da}^{r,a} = \mathbf{Y}_{C_{da}}\mathbf{Y}_{C_{aa}}^{-1} = \mathbf{V}_d\mathbf{V}_a^{+} \tag{6.6}$$

$$\mathbf{T}_{bc}^{r,a} = \mathbf{Y}_{C_{ba}}\mathbf{Y}_{C_{ca}}^{-1} = \mathbf{V}_b\mathbf{V}_c^{+} \tag{6.7}$$

Subscripts denoted d are defined as the combined subsets of b and c. It should be noted that the inverted operational velocity matrices in the above equations are denoted with a pseudo-inverse. In Chapter 4, part of the analysis conducted suggested over-determination yields more accurate operational transmissibilities. This was demonstrated further for transmissibilities used in the ORT identities (Section 5.3). In most industrial settings OMA is preferred, meaning transmissibilities will most likely be calculated using operational responses. In this instance, complex internal force mechanisms of the source can be bottlenecked by the c DoFs. This is certainly more practical than applying multiple controlled roving hammer impacts on the source, which means having to shut down the assembly (not always possible). One goal of this study is to determine whether the theory mentioned can be applied to industrial scenarios using output-only transmissibilities.

6.2 Mass-spring model example

To begin analysing the detection of transmission paths and unknown bridges, the most fundamental model is constructed - a mass-spring model system. In this section three are constructed; In the first only 1 c DoF exists, followed by 2 c DoFs, and finally 3 c DoFs. In the 1 c DoF model, the SVs of $\mathbf{Y}_{C_{ba}}$, $\mathbf{Y}_{C_{bc}}$, and $\mathbf{Y}_{C_{da}}$ are examined. In the next model the analysis of SVs for those mobility terms and transmissibilities $\mathbf{T}_{ba}^{r,a}$, $\mathbf{T}_{da}^{r,a}$, $\mathbf{T}_{bc}^{r,a}$ calculated via FRFs and output-only responses is conducted. Finally in the 3 c DoF example, the mobilities are omitted and only the SVs of the mentioned transmissibilities will be analysed via FRFs and operational responses, for reasons that will be explained later on. Additionally, for each model a bridge between A and B is made using a spring. The question that these mass-spring model examples seek to clarify is: do any of these mobilities or transmissibilities show the number of dominant SVs corresponding to the amount of transmission paths?

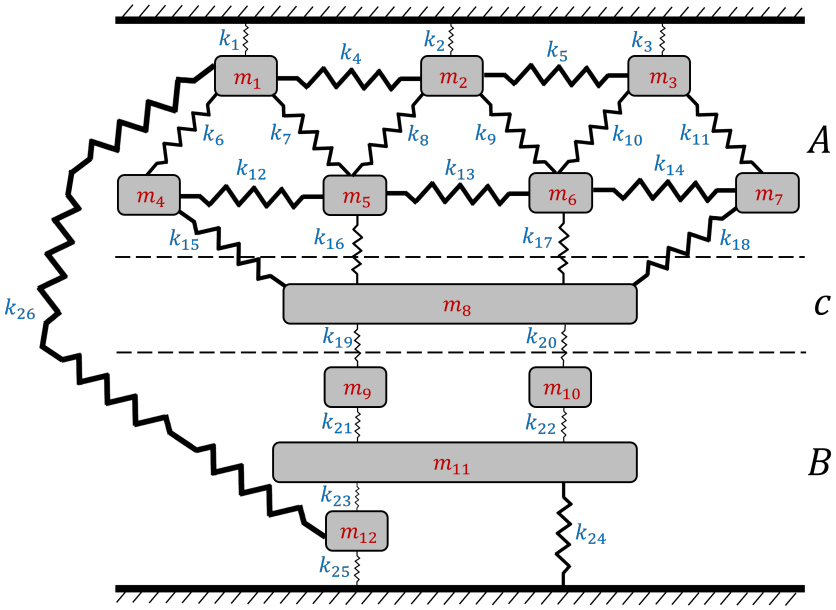

Figure 6.2: Single DoF interface mass-spring system.

Fig.6.2 has 1 interface c DoF. Within the source A lies 7 masses where the excitation DoFs are applied. In the receiver B there are 4 masses where the responses are measured.

Mass (kg)		***Spring*** (N/m)	
$m_1 - m_7$	0.03	$k_1 - k_{14}$	1×10^5
m_8	0.01	$k_{15} - k_{20}$	5×10^3
$m_9 - m_{10}$	0.03	$k_{21} - k_{23}$	1×10^5
m_{11}	0.05	k_{24}	1.5×10^5
m_{12}	0.015	k_{25}	1×10^5
		k_{26}	5×10^4

Table 6.1: Single DoF interface Mass-spring system values. Damping ratio $\zeta = 0.05$.

In theory when there is no bridge circumventing the bottleneck, the amount of dominant SVs should be 1 as it will correlate with the amount of transmission paths from the bottleneck DoF subset c. Additionally when a bridge does exist (as shown by spring k_{26}), there will be 2 dominant SVs. One question of this study is: what kind of mobility or transmissibility is inline with this theory? We will begin to answer this question, by firstly observing the SVs of $\mathbf{Y}_{C_{ba}}$.

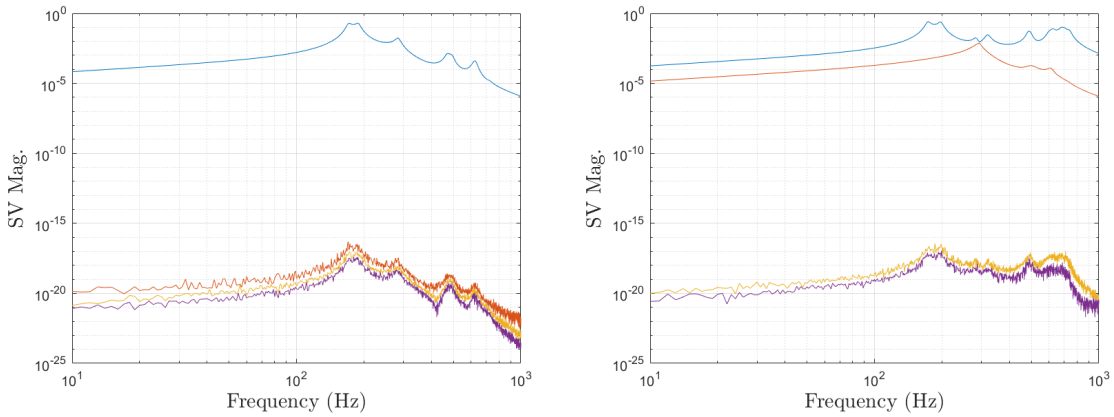

(a) No bridge (b) Bridged

Figure 6.3: Singular values of $\mathbf{Y}_{C_{ba}}$ for a single c DoF interface mass-spring system.

$\mathbf{Y}_{C_{ba}}$ is analysed with and without a bridge in Fig.6.3b and 6.3a respectively. The latter figure displays the SVs when the bridge, spring k_{26}, is not present, while former shows the SVs when bridge k_{26} is connected between the source DoF m_1, and receiver DoF m_{13}. In this case, the number of dominant SVs of $\mathbf{Y}_{C_{ba}}$ correspond to the amount of transmission paths through the bottleneck (1), and also when the bridge is present (2). In the next set of figures, the SVs of $\mathbf{Y}_{C_{da}}$ and $\mathbf{Y}_{C_{bc}}$ are analysed.

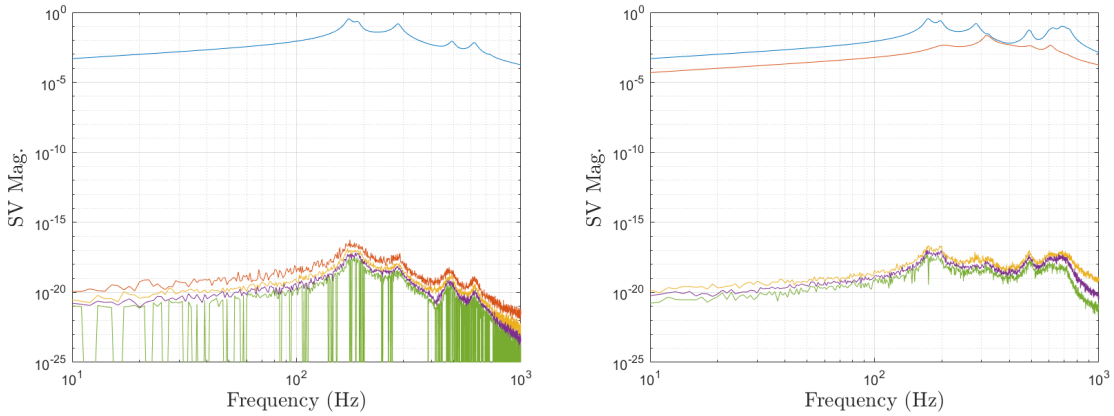

(a) No bridge (b) Bridged

Figure 6.4: Singular values of the mobility $\mathbf{Y}_{C_{da}}$ for a single DoF interface mass-spring system.

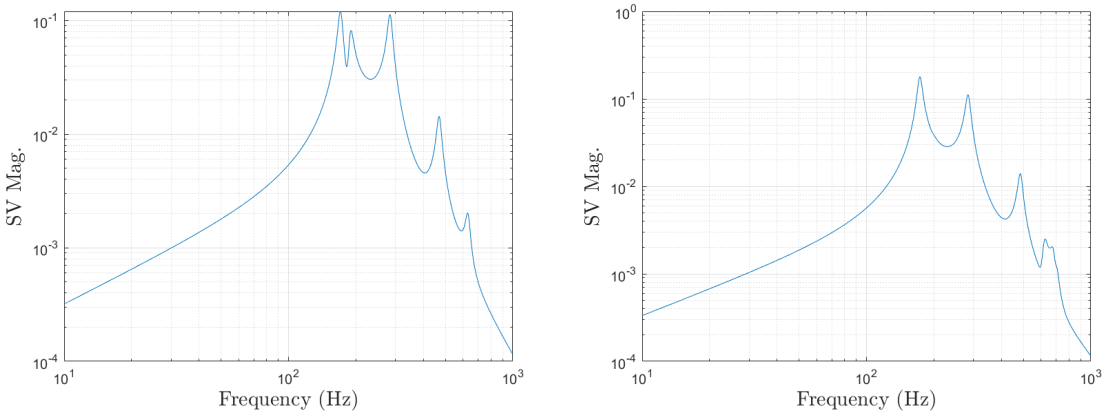

(a) No bridge (b) Bridged

Figure 6.5: Singular values of the mobility $\mathbf{Y}_{C_{bc}}$ for a single DoF interface mass-spring system.

The amount of dominant SVs for $\mathbf{Y}_{C_{da}}$ in Fig.6.4 also correlate to the number of transmission paths. There is 1 dominant SV when there is no bridge, and 2 when there is. For Fig.6.5, $\mathbf{Y}_{C_{bc}}$ only displays 1 SV, even if a bridge is present or not. As $\mathbf{Y}_{C_{bc}}$ is a 4×1 matrix, the size of the singular value matrix Σ will be the same. The number of σ's within this matrix corresponds to its smallest dimension, which in this case is due to the single c DoF. Therefore, only one σ is present in the Σ matrix for $\mathbf{Y}_{C_{bc}}$. This suggests that observing a mobility or transmissibility which uses the bottleneck c DoFs, may not be suitable. In order to observe the correct number of transmission paths and unknown bridges, the amount of SVs within Σ must be greater than number of DoFs within the bottleneck subset c. This is investigated further in the next mass-spring model where 2 c DoFs will be used. As $\mathbf{Y}_{C_{bc}}$ in the next example will be 4×2, it is expected there will only be 2 SVs.

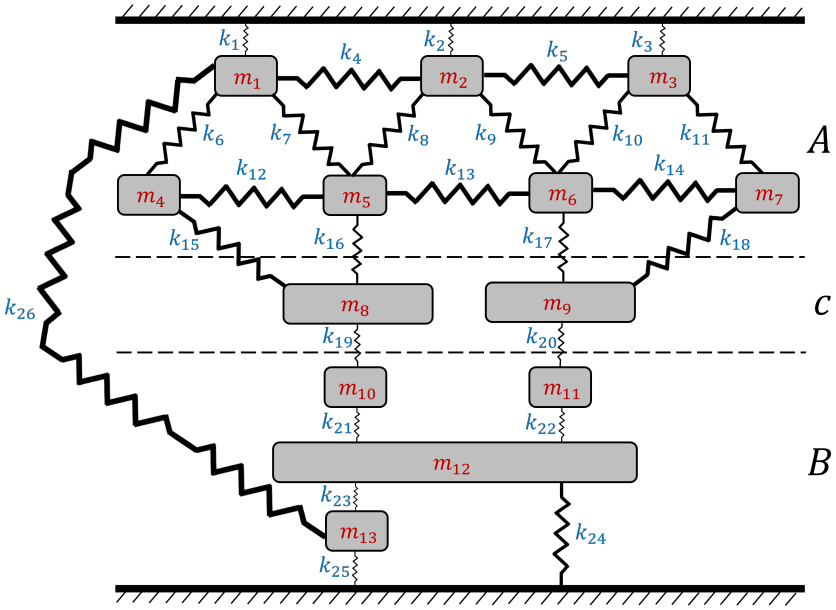

Figure 6.6: Two DoF interface mass-spring system

As shown in the above figure, an additional c DoF has been added to the interface subset. The mass and spring values for this system are given in the table below.

Mass (kg)		***Spring*** (N/m)	
$m_1 - m_7$	0.03	$k_1 - k_{14}$	1×10^5
$m_8 - m_9$	0.01	$k_{15} - k_{20}$	5×10^3
$m_{10} - m_{11}$	0.03	$k_{21} - k_{23}$	1×10^5
m_{12}	0.05	k_{24}	1.5×10^5
m_{13}	0.015	k_{25}	1×10^5
		k_{26}	5×10^4

Table 6.2: Two DoF interface Mass-spring system values. Damping ratio $\zeta = 0.05$

It is expected the number of dominant SVs will increase by one in both bridged and non-bridged scenarios for $\mathbf{Y}_{ba}$ and $\mathbf{Y}_{xa}$ as shown in the previous example. Σ for both of these quantities will be 4×7 and 6×7 respectively. As the number of σ is larger than the amount of bottleneck c DoFs, in theory there should be a number of dominant SVs corresponding to the amount of transmission paths. In the presence of a bridge (k_{26}), Σ will not increase, but as shown by the previous example, a small SV will turn dominant due to the increased energy transfer from source to receiver. For the remaining mass-spring models, the SVs of transmissibilities calculated via mobilities and operational responses will be analysed in addition to the mobilities just covered in the 1 c DoF

example. It should be noted that the output-only transmissibilities were calculated by simulating operational forces to the source sub-structure. As we have already outlined previously, such as in Section 4.1.4, an operational force matrix will be constructed due to N amount of linearly independent states, which in this case is equal to the total number of DoFs in the coupled system (13 in the 2 c DoF model, and 14 in the 3 c DoF model). Therefore for the upcoming model, the operational force matrix $\mathbf{F}$ is 13×13. As we're only applying the operational forces to a DoFs, the first 7 rows of $\mathbf{F}$ have a random value between 0-1, while the remaining rows (representing DoFs b and c) have values of 0.

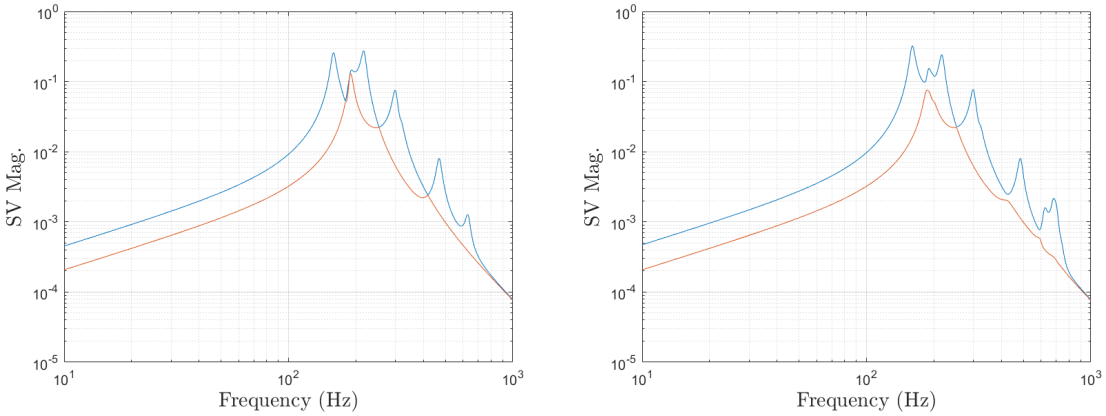

(a) No bridge (b) Bridged

Figure 6.7: Singular values of the mobility $\mathbf{Y}_{C_{bc}}$ for a double DoF interface mass-spring system.

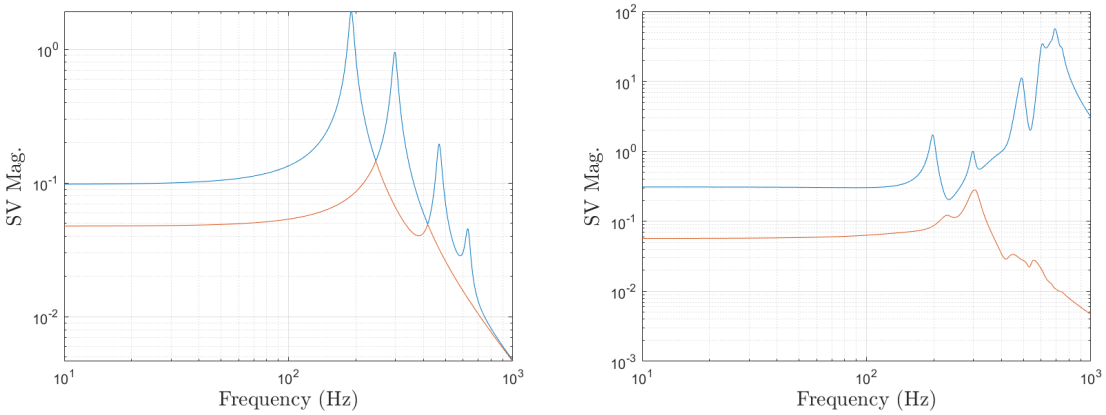

(a) No bridge (b) Bridged

Figure 6.8: SVs of mobility-based $\mathbf{T}_{bc}^{r,a}$, for a double c DoF mass-spring system.

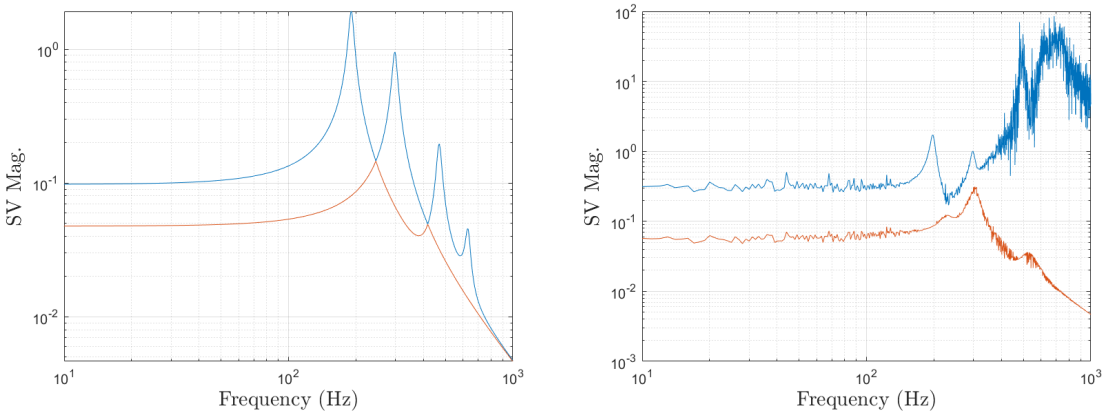

(a) No bridge (b) Bridged

Figure 6.9: SVs of output-only $\mathbf{T}_{bc}^{r,a}$, for a double c DoF mass-spring system.

Firstly, we will examine the mobility and transmissibility between subsets b and c, $\mathbf{Y}_{C_{bc}}$ and $\mathbf{T}_{bc}^{r,a}$. In Fig.6.7 2 SVs are visible when no bridge exists, which correlates with the number of transmission paths to B. However, as expected, only 2 SVs are visible for the bridged case. The SVs of $\mathbf{T}_{bc}^{r,a}$, calculated via mobilities or operational responses in Fig.6.8 and 6.9 respectively, also show just 2 in the bridged case as well. Looking back to the single interface model, $\mathbf{Y}_{C_{bc}}$ displayed the same trend, where the non-bridged and bridged cases showed just 1 SV. This is because of the dimensions of Σ for the quantities using the bottleneck DoFs c. As outlined earlier in this section, when using the reduced bottleneck DoFs, the amount of SVs will correspond to how many DoFs are in c, which is not suitable for detecting a bridge. For this possibility, the smallest dimension of Σ must be greater than c. This is why $\mathbf{Y}_{C_{ba}}$ and $\mathbf{Y}_{C_{da}}$ in the previous mass-spring model were able to account for the extra dominant SV when a bridge was present - the smallest dimension of these matrices is much greater c, i.e. $\sigma_n > c$. In the following figures, the SVs of the mobility and transmissibility between DoFs b and a ($\mathbf{Y}_{C_{ba}}$ and $\mathbf{T}_{ba}^{r,a}$) are examined.

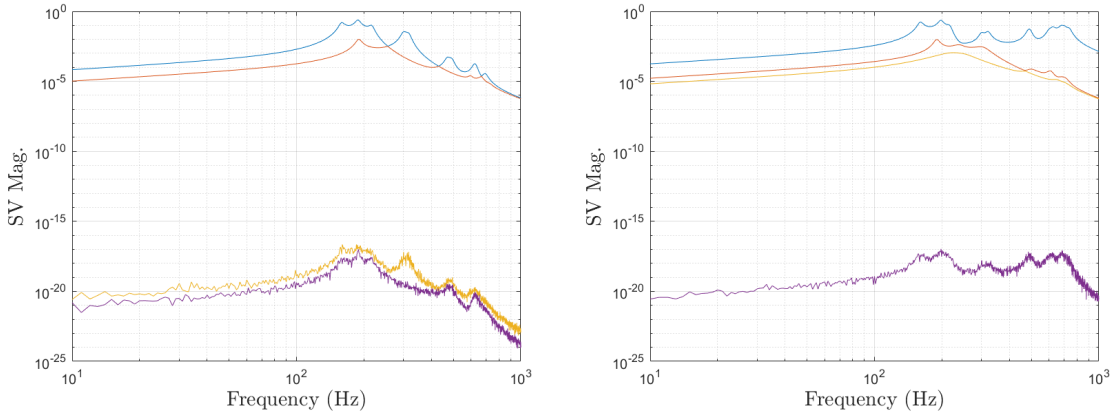

(a) No bridge (b) Bridged

Figure 6.10: SVs of $\mathbf{Y}_{C_{ba}}$, for a double c DoF mass-spring system.

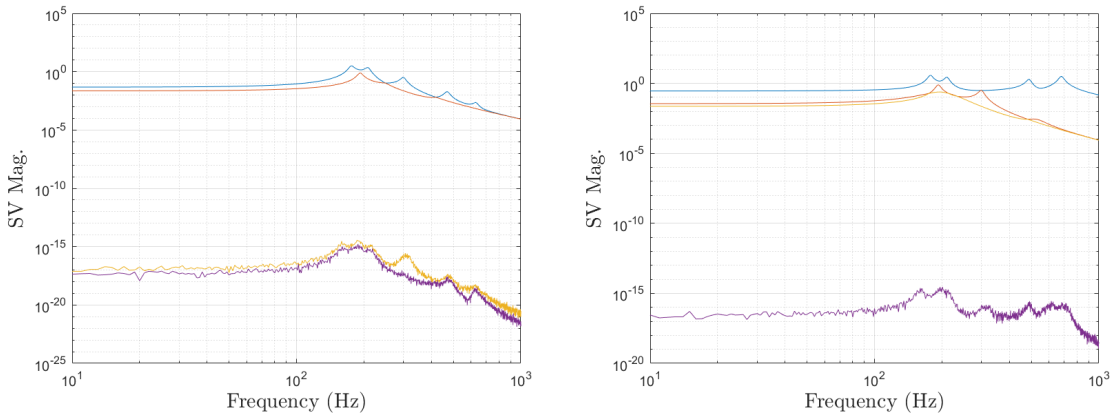

(a) No bridge (b) Bridged

Figure 6.11: SVs of mobility-based $\mathbf{T}_{ba}^{r,a}$, for a double c DoF mass-spring system.

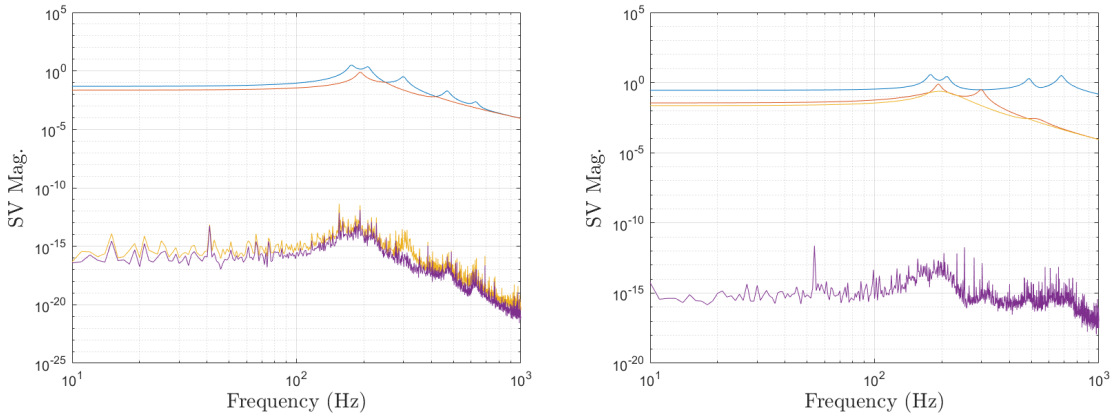

(a) No bridge (b) Bridged

Figure 6.12: SVs of output-only $\mathbf{T}_{ba}^{r,a}$, for a double c DoF mass-spring system.

In Fig.6.10 the dominant SVs of $\mathbf{Y}_{C_{ba}}$ corresponds to the number of transmission paths to the responses b in both bridged and non-bridged cases. Similarly, for the mobility-based and operational $\mathbf{T}_{ba}^{r,a}$ shown in Fig.6.11 and 6.12 respectively, 2 dominant SVs are present in the non-bridged case, and 3 when a bridge exists. While the magnitudes of the dominant SVs for $\mathbf{Y}_{C_{ba}}$ are slightly reduced to $\mathbf{T}_{ba}^{r,a}$, the trends are very similar. So far for the 1 and 2 c DoF mass-spring models, $\mathbf{Y}_{C_{ba}}$ and $\mathbf{T}_{ba}^{r,a}$ are correlating with the amount of transmission paths to the responses in b, for both bridged and non-bridged scenarios. In final set of figures for the 2 c DoF mass-spring model, we will observe the SVs of the mobility and transmissibility between the combined subset d and a, $\mathbf{Y}_{C_{da}}$ and $\mathbf{T}_{da}^{r,a}$.

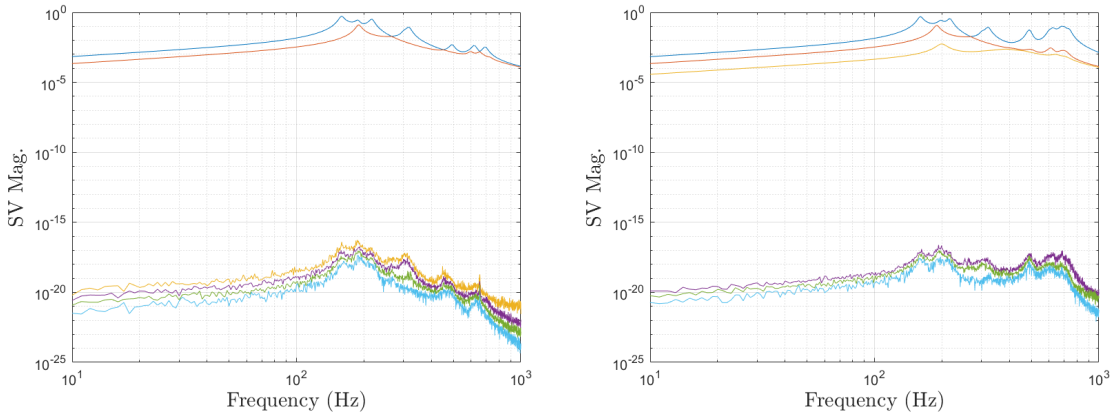

(a) No bridge (b) Bridged

Figure 6.13: SVs of $\mathbf{Y}_{C_{da}}$, for a double c DoF mass-spring system.

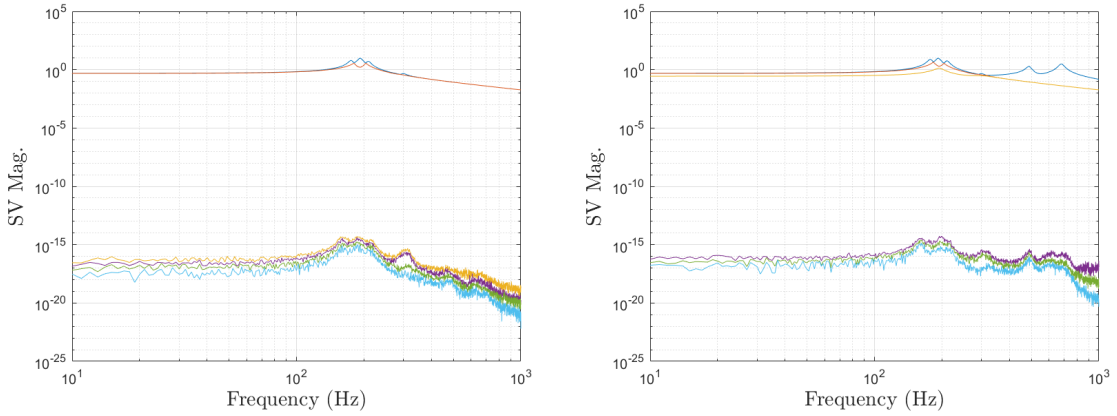

(a) No bridge (b) Bridged

Figure 6.14: SVs of mobility-based $\mathbf{T}_{da}^{r,a}$, for a double c DoF mass-spring system.

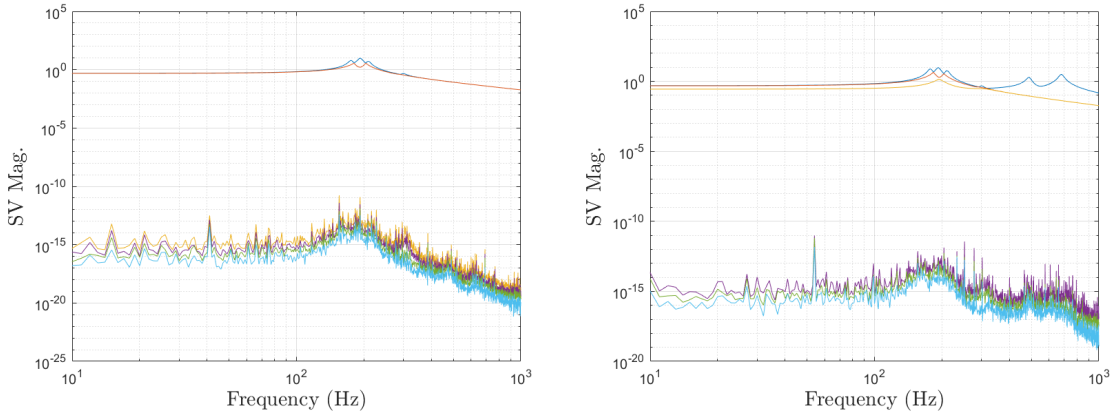

(a) No bridge (b) Bridged

Figure 6.15: SVs of output-only $\mathbf{T}_{da}^{r,a}$, for a double c DoF mass-spring system.

For the mobility $\mathbf{Y}_{C_{da}}$, Fig.6.14 shows 2 dominant SVs when there is no bridge, and 3 when there is a bridge. This same trend is also visible for the mobility-based and output-only transmissibility $\mathbf{T}_{da}^{r,a}$. So far the dominant SVs of $\mathbf{Y}_{C_{ba}}$, $\mathbf{T}_{ba}^{r,a}$, $\mathbf{Y}_{C_{da}}$ and $\mathbf{T}_{da}^{r,a}$ for the 1 and 2 c DoF models have corresponded to the number of transmission paths to b responses in both bridged and non-bridged cases. Furthermore, across both mass-spring examples the dominant SVs of a mobility and transmissibility using the same DoF subsets appear very similar to each other. Therefore in the next mass-spring model, the SVs of the mobilities will be omitted. While the quantities between subsets b and c ($\mathbf{Y}_{C_{bc}}$ and $\mathbf{T}_{bc}^{r,a}$) do show the same amount of SVs as transmission paths in the non-bridged cases, an extra SV is not visible for when there is a bridge across the mass-spring examples presented. A main focus of this study is being able to detect a mechanical bridge between the source and receiver sub-structure. This means using these quantities isn't helpful for this task, and thus will also be omitted from the analysis of the 3 c DoF mass-spring model.

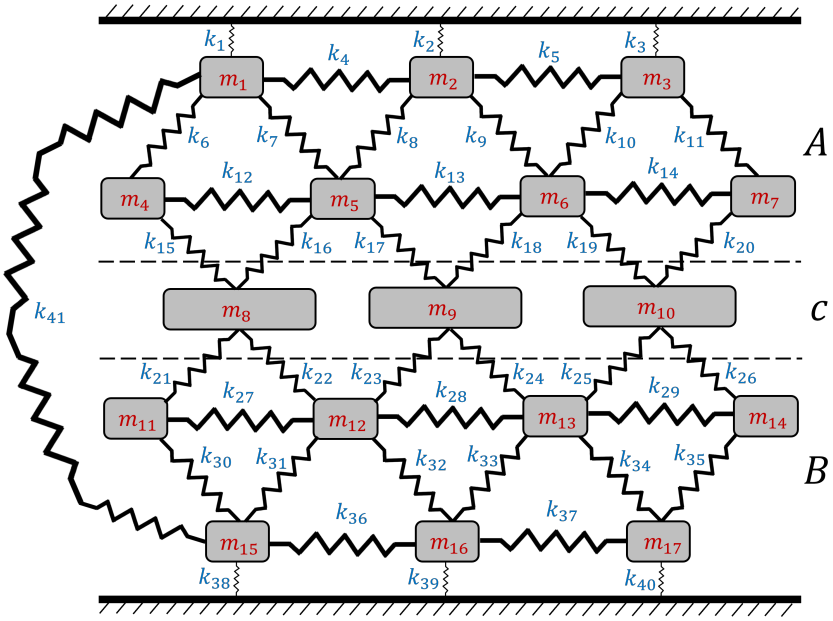

Figure 6.16: Triple DoF interface mass-spring system

The dominant SVs of $\mathbf{T}_{ba}^{r,a}$ and $\mathbf{T}_{da}^{r,a}$ have so far corresponded with the transmission paths to b responses, from the point of view of the interface c DoFs. For the 3 c DoF mass-spring model, the B sub-structure has an increased amount of masses so that the bottleneck remains at the interface DoFs. The mass and spring values for the model presented in Fig.6.16 are as follows in the table below.

Mass (kg)		***Spring*** (N/m)	
$m_1 - m_7$	0.03	$k_1 - k_{14}$	1×10^5
$m_8 - m_{10}$	0.01	$k_{15} - k_{26}$	5×10^3
$m_{11} - m_{17}$	0.03	$k_{27} - k_{40}$	1×10^5
		k_{41}	5×10^4

Table 6.3: Three DoF interface Mass-spring system values. Damping ratio $\zeta = 0.05$.

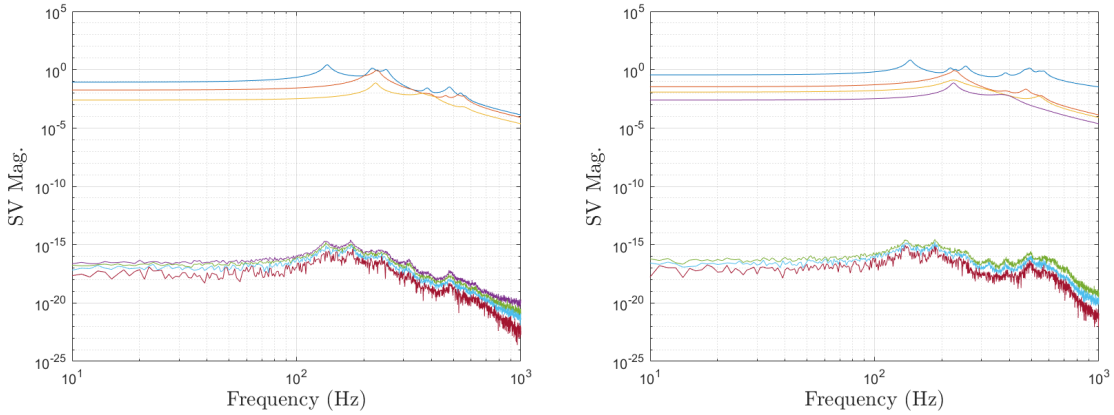

(a) No bridge (b) Bridged

Figure 6.17: SVs of mobility-based $\mathbf{T}_{ba}^{r,a}$, for a triple c DoF mass-spring system.

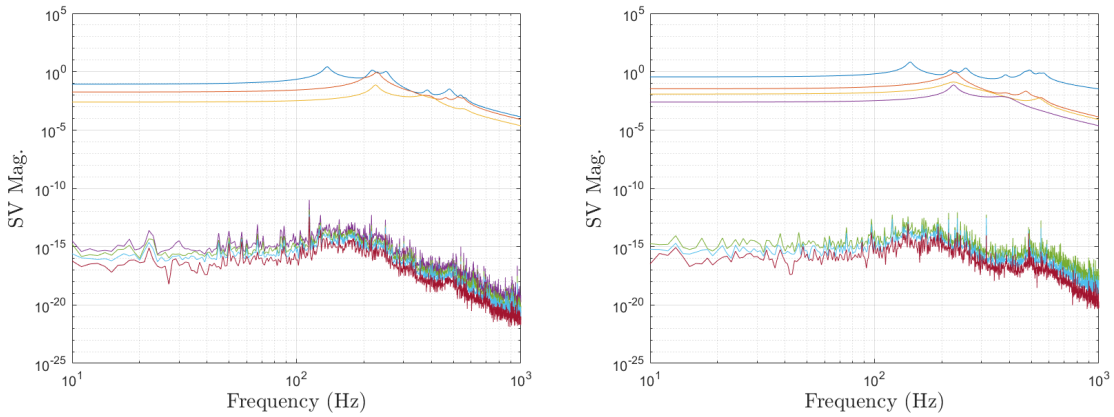

(a) No bridge (b) Bridged

Figure 6.18: SVs of output-only $\mathbf{T}_{ba}^{r,a}$, for a triple c DoF mass-spring system.

For the 3 c DoF model, the dominant SVs for both mobility-based and output-only measurements of $\mathbf{T}_{ba}^{r,a}$ correspond to the number of transmission paths for non-bridged and bridged cases. In Fig.6.17a there are 3 dominant SVs, and 4 for the bridged case in Fig.6.17b. Identically, as shown in the below figures, the number of dominant SVs of mobility-based and operational $\mathbf{T}_{da}^{r,a}$ also correspond to how many transmission paths exist for bridged and non-bridged scenarios.

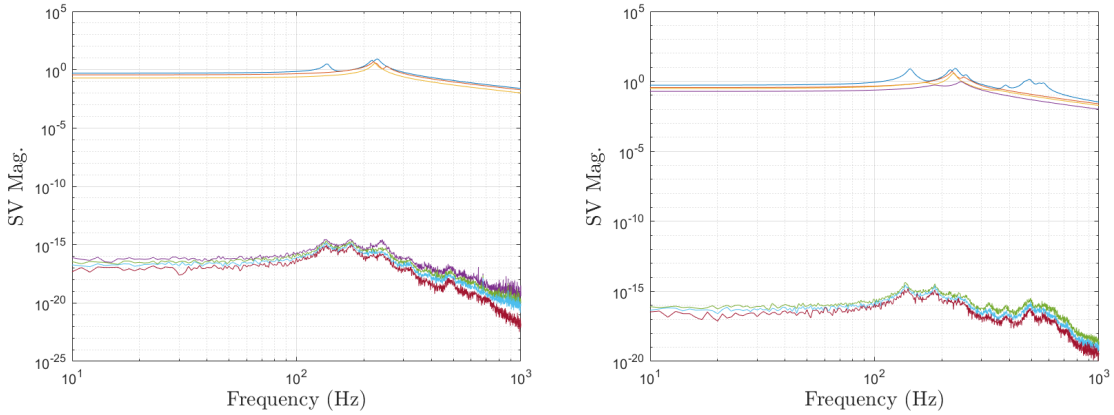

(a) No bridge (b) Bridged

Figure 6.19: SVs of mobility-based $\mathbf{T}_{da}^{r,a}$, for a triple c DoF mass-spring system.

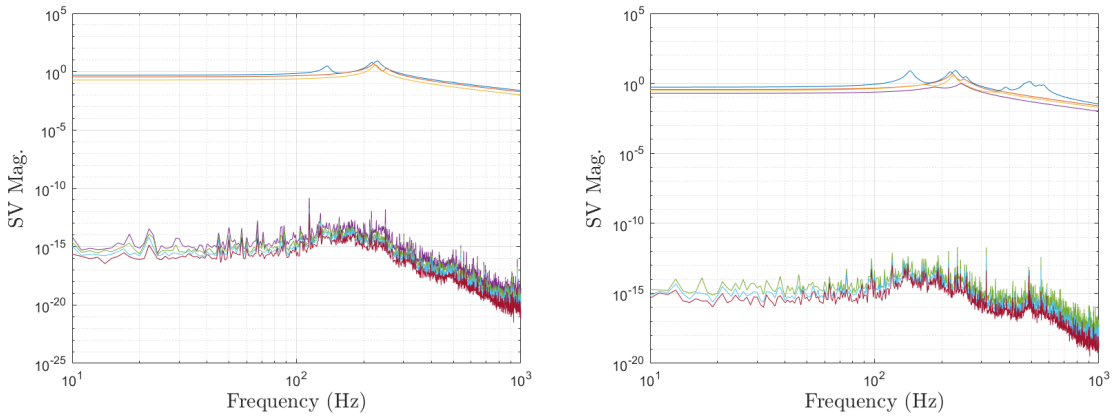

(a) No bridge (b) Bridged

Figure 6.20: SVs of output-only $\mathbf{T}_{da}^{r,a}$, for a triple c DoF mass-spring system.

This mass-spring system study has indicated out of all quantities across the mass-spring models presented, the ones that use b and a, or d and a DoF subsets, have correlated to the number of transmission paths from c. Additionally these transmissibilities have displaying an extra dominant SV when a bridge circumventing the bottleneck exists. Furthermore, it is suggested by this study that using operational transmissibilities between these subsets is a viable option in the detection of transmission paths and unknown bridges. This is tested for an experimental model in the next section.

6.3 Experimental model example

In this section, the SVs of mobilities and operational transmissibilities used in the mass-spring model examples are analysed on an experimental model.

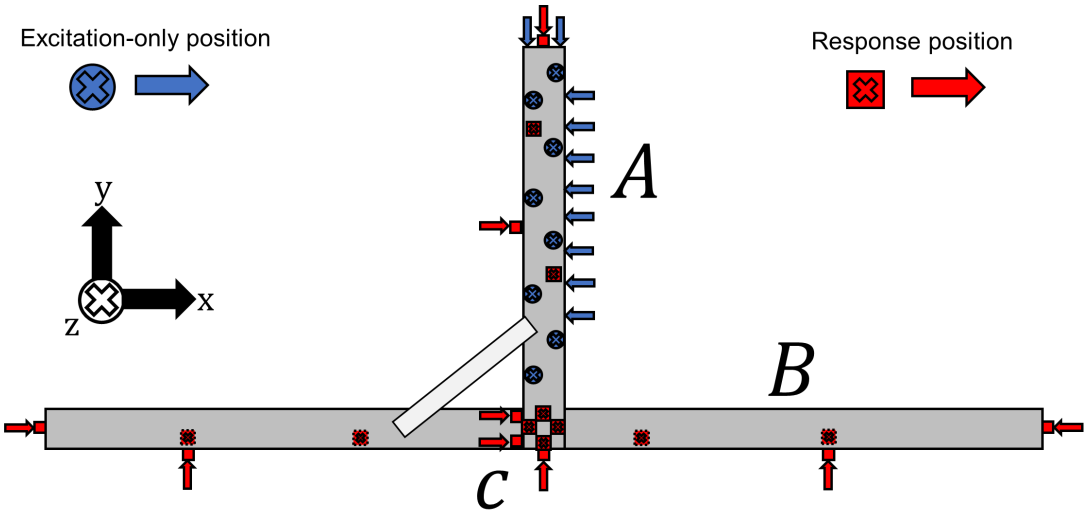

Figure 6.21: Top-down diagram of experimental example setup. Vertical bar A is the source component, rigidly connected at a point to the horizontal bar B which is the receiver.

In Fig.6.21, a 2D top-down diagram of the experimental coupled assembly used is presented. It consists of two steel beams rigidly connected at a single point. The A beam is a source sub-structure, while B is a receiver component. During the FRF test, 18 controlled excitations were applied: 8 in the z-axis, 2 in the y-axis, and 8 in the x-axis. During this test, the source had no sensors installed. On the receiver beam there are 8 uni-axial responses, denoted b: 4 facing the z-axis, and 2 in the x and y axes. At the rigid connection lies 7 uni-axial responses, denoted as the interface DoFs c. Excitations were applied in the same way as previous operational measurements shown in this thesis in order to conduct the finite difference approximation. This is shown in Fig.4.27. However, it was found during this study that applying the finite difference to the interface yielded SVs that did no correspond with trends of bridged and non-bridged cases in the mass-spring model. Thus the results shown for this experimental study were not processed with the finite difference method. During the

operational measurement, forces were applied using an impact hammer in a random fashion for a 20 seconds without a force reference, and at the exact same 18 locations during the FRF measurement. b responses and the c DoFs are in the same location. During the operational measurement, 4 uni-axial sensors were installed in A, denoted as subset a. For both tests, a bridge was made between the source and receiver by super glueing a thin aluminium beam across. To begin, we will analyse the SVs of $\mathbf{Y}_{C_{ba}}$.

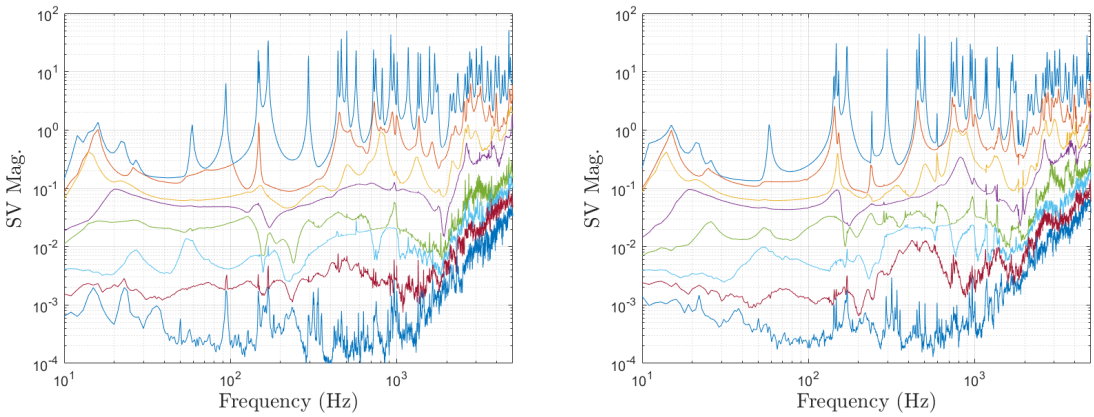

(a) No bridge (b) Bridged

Figure 6.22: SV magnitudes of $\mathbf{Y}_{C_{ba}}$, for an experimental assembly.

For this experimental study, SV analysis is conducted differently to the mass-spring examples. This is because, as demonstrated in Fig.6.22, it is more difficult to discern the differences between bridged and non-bridged SVs. In the mass-spring model, there is a clear distinction between dominant and non-dominant SVs. This is expected with an idealised model. This however, does not translate to the experimental structure presented in this study.

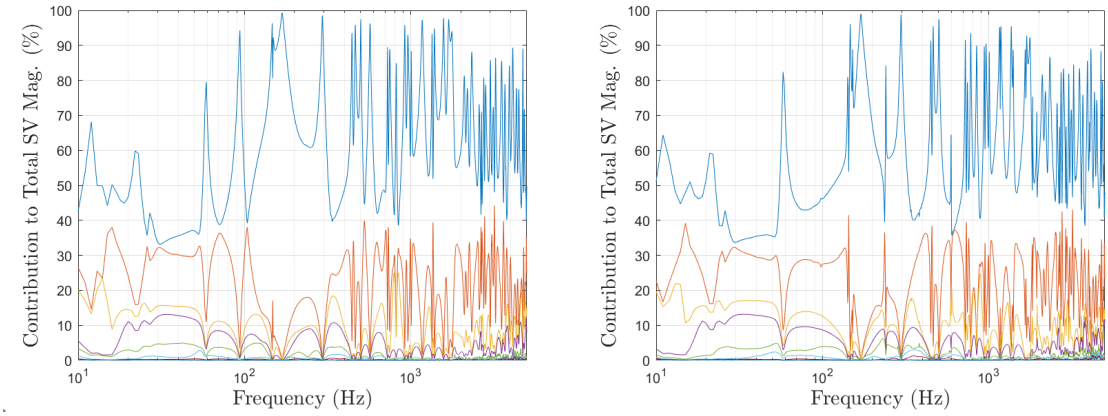

(a) No bridge (b) Bridged

Figure 6.23: Normalised SV magnitudes of $\mathbf{Y}_{C_{ba}}$, for an experimental assembly.

To analyse the small differences between bridged and non-bridged tests, the SVs are normalised. This is carried out by a summation of all SV magnitudes and dividing each SV by the total magnitude. Each is then multiplied by 100 to give the percentage contribution to the total magnitude, as shown by Fig.6.23. The smallest singular values show a small increase in magnitude between tests. However, it is difficult to understand just by how much when comparing bridged and non-bridged SV figures. Therefore some quantification is needed.

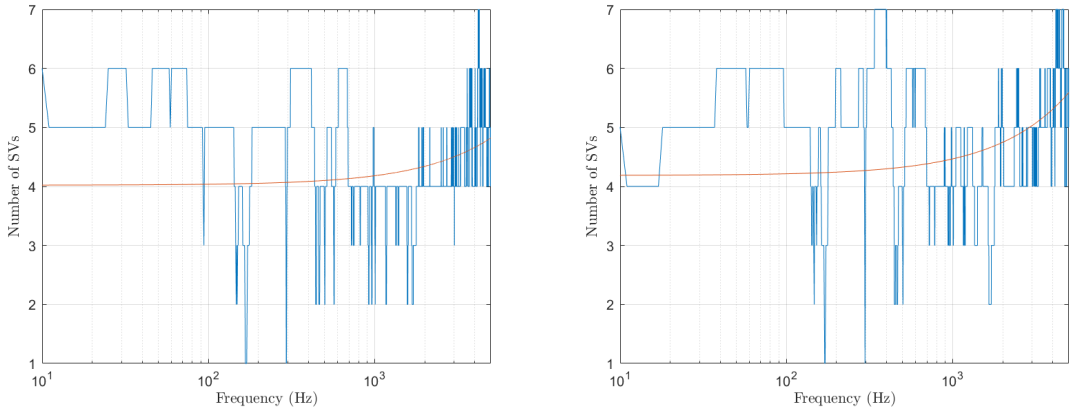

(a) No bridge (b) Bridged

Figure 6.24: Number of significant SVs for $\mathbf{Y}_{C_{ba}}$ at all frequencies between 10Hz - 5kHz, as shown by the blue plot. Red plot is the line of best fit, representing the overall trend of significant SVs across the frequency range. In reference to the experimental model in Fig. 6.21.

To understand by how much the lowest singular values are contributing by, a percentage threshold is take on the normalised SVs. At say 5% and above, is what we will call the 'Significant SVs'. At this cut-off we can assess how many singular values are above 5% of the total SV magnitude. In other words, if the lowest singular values have a higher magnitude contribution to the total, in say a bridged test, then more significant SVs will be observed. In Fig.6.24, the number of significant SVs are plotted against frequency for bridged and non-bridged tests. For the mobilities presented in this study, a threshold of 1% is taken. In addition, a line of best fit is included (in red) to help understand the rate of change in the number of significant SVs across the frequency range. When observing the line of best fit for the non-bridged case, Fig.6.24a shows that for 99% of the normalised SVs there are 4 SVs from 10Hz and ramps up to around 4.8 by 5kHz. For the bridged case as shown by Fig.6.24b, a slightly higher number at 10Hz of about 4.2 significant SVs can be observed, which ramps up to 5.6 by 5kHz. Furthermore, more frequencies show a value of 7 in the bridged test. It is indicated by Fig.6.24b there is a small increase in energy for the bridged test.

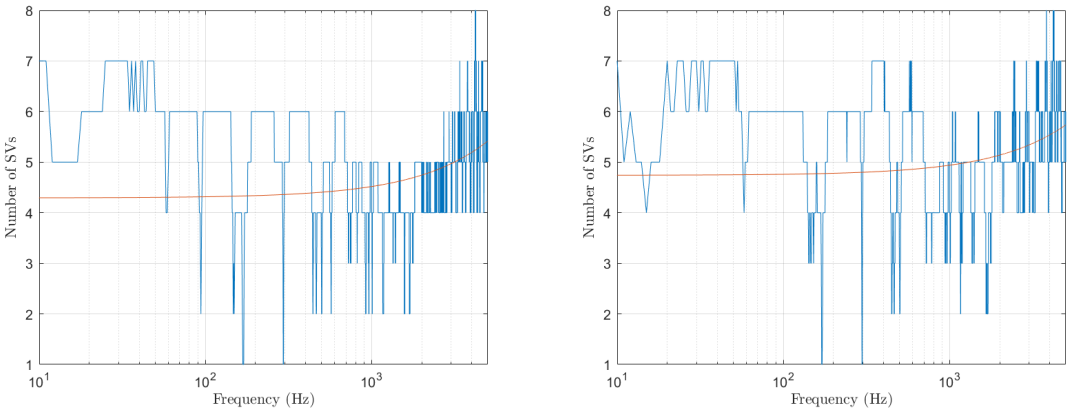

(a) No bridge (b) Bridged

Figure 6.25: Number of significant SVs for $\mathbf{Y}_{C_{da}}$, on an experimental assembly.

In the case of $\mathbf{Y}_{C_{da}}$ the singular values show a similar picture. When the bridge is present, Fig.6.25b shows more points in the frequency range that reach between 5 significant SVs and above. This is why the line of best fit has been raised for the bridged case, starting at a value of 4.8, compared to 4.2 in the non-bridged test.

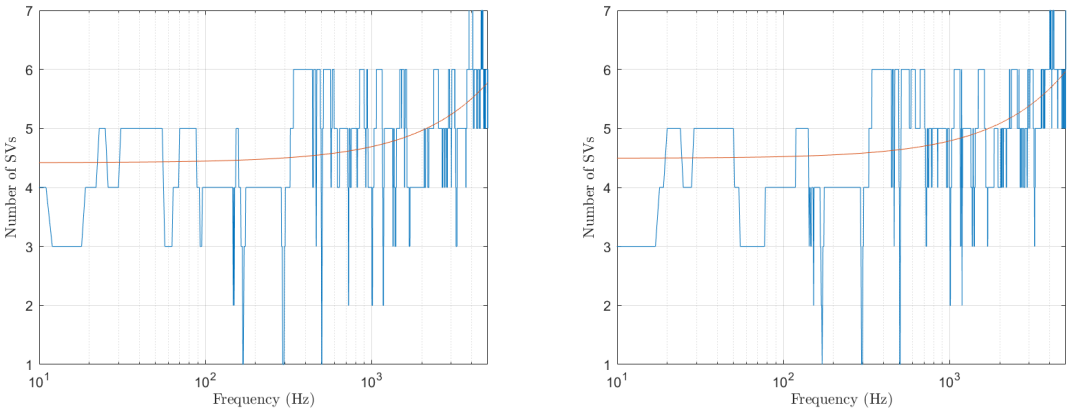

(a) No bridge (b) Bridged

Figure 6.26: Number of significant SVs for $\mathbf{Y}_{C_{bc}}$, on an experimental assembly.

In Fig.6.26 the SVs of $\mathbf{Y}_{C_{bc}}$ show no notable difference between bridged and non-bridged tests. When a bridge is present, the previous mobilities showed an increase in the amount of significant SVs at multiple frequencies, but has not been observed for $\mathbf{Y}_{C_{bc}}$. This is further indicated by the line of best fit, which shows virtually no difference in both tests. In the previous mass-spring models, there was also no difference in the number of SVs appearing. So far the SVs of $\mathbf{Y}_{C_{da}}$ and $\mathbf{Y}_{C_{ba}}$ have shown a noticeable difference between bridged and non-bridged tests - similarly to the mass-spring model study.

For the remainder of this section, the operational transmissibilities analysed in the mass-spring models will be examined. For the following figures, a significant SV threshold of 2% was chosen. Firstly, we compare the above mobility with a transmissibility using the same subsets, $\mathbf{T}_{bc}^{r,a}$.

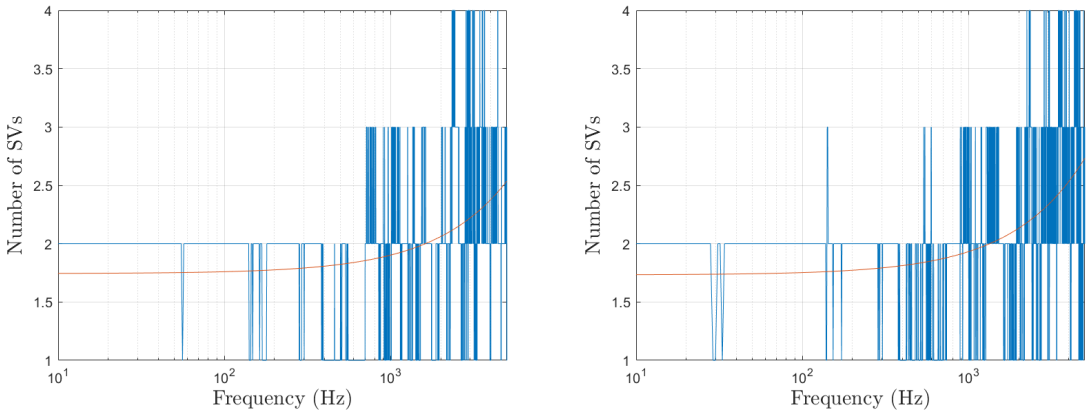

(a) No bridge (b) Bridged

Figure 6.27: Number of significant SVs for output-only $\mathbf{T}_{bc}^{r,a}$, on an experimental assembly.

The number of significant SVs of $\mathbf{T}_{bc}^{r,a}$ is less overall, because of the dimension of the singular value matrix. The amount of SVs is equal to the smallest dimension of the original matrix. For example, the mobility matrix $\mathbf{Y}_{C_{ba}}$ is 8×18, and therefore will have 8 SVs in the SV matrix. Comparing against $\mathbf{Y}_{C_{bc}}$, a similar trend is observed. In Fig.6.27, the difference between the amount of significant SVs from bridged and non-bridged cases is very small. This is further supported when observing the line of best fit, which shows almost no change. If the line of best fit is ignored, there is still very little to distinguish between the bridged and non-bridged tests. It appears that the experimental SVs of $\mathbf{T}_{bc}^{r,a}$ and $\mathbf{Y}_{C_{bc}}$ are comparable to the mass-spring results.

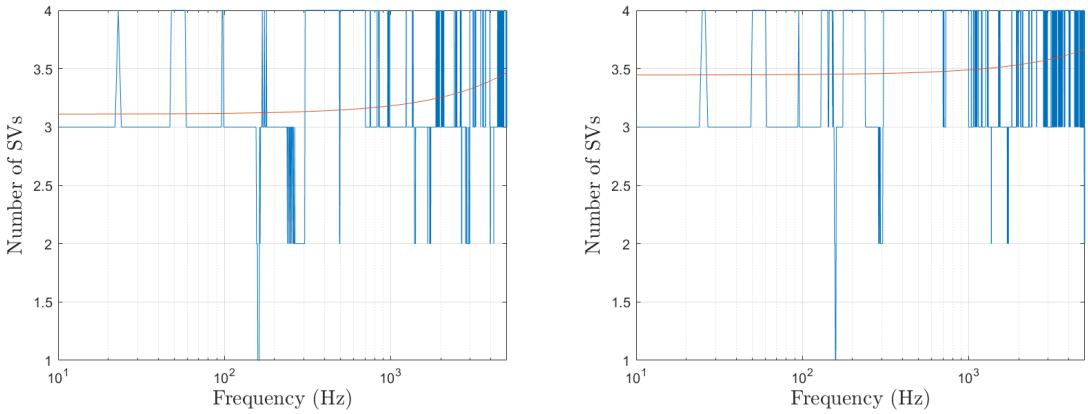

(a) No bridge (b) Bridged

Figure 6.28: Number of significant SVs for output-only $\mathbf{T}_{ba}^{r,a}$, on an experimental assembly.

For the significant SVs of $\mathbf{T}_{ba}^{r,a}$, the above figure shows there are more points in the frequency range reaching a maximum of 4 SVs. Additionally, the line of best fit begins at 3.1 and nearly 3.5 for non-bridged and bridged test respectively. Like the mobility between these subsets of DoFs, $\mathbf{Y}_{C_{ba}}$, there is not much difference in the low frequencies, but there are more points higher in the frequency range that have a value of 4.

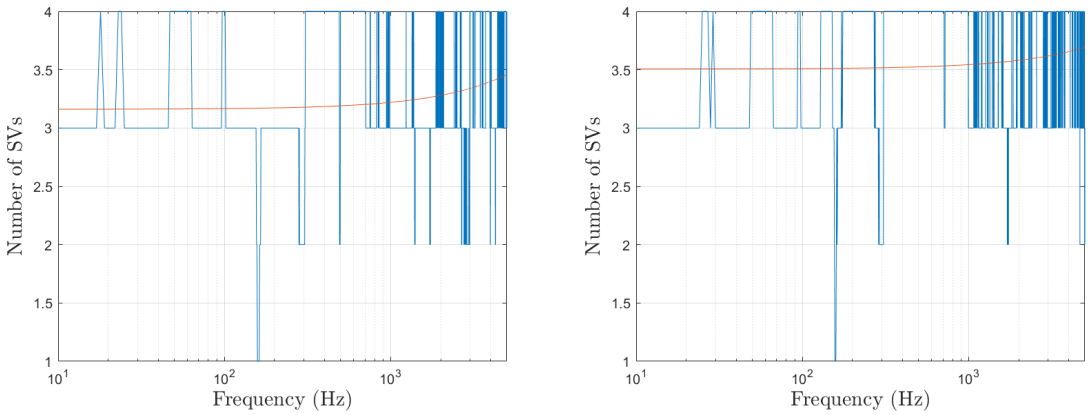

(a) No bridge (b) Bridged

Figure 6.29: Number of significant SVs for output-only $\mathbf{T}_{da}^{r,a}$, on an experimental assembly.

Finally for $\mathbf{T}_{da}^{r,a}$, a similar trend is observed to previous figure for $\mathbf{T}_{ba}^{r,a}$. At more frequencies we can see a maximum of 4 significant SVs for the bridged test, and when

observing the line of best fit it begins at a value of 3.5 compared to 3.1 for the non-bridged test in Fig.6.29a.

6.4 Discussion

Across all mass-spring model examples, $\mathbf{Y}_{C_{ba}}$, $\mathbf{Y}_{C_{da}}$, $\mathbf{T}_{ba}^{r,a}$, $\mathbf{T}_{da}^{r,a}$ showed the number of dominant SVs consistently correlated with the transmission to b responses. When a bridge was made between the source and receiver sub-structures, the rank r of these quantities increased, resulting in an extra dominant SV. This part of the study indicated the most reliable quantities to observe are between b and a, as well as between d (combined b and c DoF subsets) and a. Additionally, it was suggested that the operational transmissibilities using these DoF subsets may be used in detecting the number of transmission paths from the bottleneck, and any bridges between source A and receiver B.

However, when observing the SVs of the experimental study a different trend was visible. For all mobilities and transmissibilities analysed there was not a clear distinction between SVs, as they were all grouped closer to each other. I.e. dominant SVs were not distinguishable from the rest. Therefore the exact number of transmission paths could not be correlated to how many dominant SVs were present in the figures. To understand how the SVs behave under bridged and non-bridged conditions, all SVs of the mobilities and transmissibilities analysed were normalised to the total magnitude. This yielded a % contribution of each SV. At a particular threshold of the total magnitude (1% for the mobilities, and 2% for transmissibilities), it was determined how many SVs were above the cut-off. It was found in the bridged scenario, the smallest SVs increased in magnitude for $\mathbf{Y}_{C_{da}}$, $\mathbf{Y}_{C_{ba}}$, $\mathbf{T}_{ba}^{r,a}$, and $\mathbf{T}_{da}^{r,a}$, and therefore the number of significant SVs increased when compared to the non-bridged test.

In summary, the mass-spring model examples indicated it may be possible to determine the amount of transmission paths and bridges by observing how many dominant SVs are present. These quantities appear to be able to “see” all transmission

through the bottleneck and a bridge circumventing the interface DoFs. It was suggested in the mass-spring examples that the theory also applied to $\mathbf{T}_{ba}^{r,a}$ and $\mathbf{T}_{da}^{r,a}$ in a simulated operational measurement. An output-only measurement is beneficial for industrial scenarios, where the source component in a coupled assembly (such as generator or compressor) has multiple excitation mechanisms. If it is rigidly coupled at a point to a receiver structure, the bottlenecking effect on the operational forces through a restricted number of DoFs at the point interface c, may yield dominant SVs that correlate to the number of transmission paths. This is advantageous as no explicit knowledge of the forces within the source is required when calculating an operational transmissibility. It was found in the operational experimental study that output-only $\mathbf{T}_{ba}^{r,a}$ and $\mathbf{T}_{da}^{r,a}$ were able to detect a bridge, however a clear distinction between dominant SVs and the smallest SVs was not seen and made it difficult to discern the exact amount of transmission paths from the bottleneck. An explanation for this is that in the mass-spring models, the responses at b are largely governed by a much reduced number of dominant modes or DoFs. At certain frequencies, a smaller amount of specific resonant modes related to the c DoFs dominate the responses at b. As a result this leads to a significant contribution from a few singular values, corresponding to physical modes where energy transfer is highly efficient. The mass-spring systems exhibit clean, idealised behaviour without the complexities of damping, material heterogeneities, or boundary imperfections. This simplification makes it easier for dominant modes to emerge at specific frequencies. Additionally, because there are relatively few modes at play, there is a lower chance of modal overlap (where multiple modes contribute similarly to the response at a given frequency). This leads to a clear separation of SVs, particularly near resonances. For a continuous system such as the experimental assembly, coupling between modes can occur often, contributing to a less pronounced hierarchy of singular values. Additionally, real beams have a theoretically infinite number of modes or DoFs. While practically only a finite number of modes contribute significantly in the frequency range of interest, there will still be far more modes than in the mass-spring model.

An idea for further work is to construct an analytical model which has more modes than mass-spring example and far fewer than experimental assembly. This can help link the understanding between the two examples presented in this study, and suggest how many modes the theory is restricted to. For the experimental example in Fig.6.22, it is clear there is less of a distinction between the SVs (spacing between them decreases) as frequency increases. It is not yet understood why this occurs, and requires further investigation. Lastly, another area is to observe the effect of stiffness created by the bridge on the SVs. If the relative stiffness of the bridge is greater than the material of the coupled assembly, the overall magnitude of the SVs will be greater and thus make it easier to detect a change.

Chapter 7

Conclusions

In this thesis, one of the main objectives was to investigate whether a novel approach of including invariant operational transmissibilities can be used to enhance prediction methods, specifically the RT method. Another aim was to investigate if they could also be used in vibro-acoustic analysis methods, such as identifying transmission paths and unknown bridges within coupled assemblies.

Before undertaking the first objective, the sensitivities of the RT method were examined. This study was carried out to examine potential sources of error before incorporating operational transmissibilities. As mentioned previously, the RT identity provides a very convenient means of reconstructing the driving-point mobility at a connecting interface DoF subset (c). However, it was found that when utilising the same amount of remote DoFs (a and b) for reconstruction, a large spike in error would occur. The source of this error is largely attributed to the inverted term $\mathbf{Y}_{ab}^{-1}$, which when having a large condition number, made small errors on the input amplified when inverted. This matrix inversion is well known and is a common theme throughout the research presented. This error was easily circumvented by reducing either only a or b, making the mobility term rectangular, allowing the use of the least squares pseudo-inverse. An interesting revelation from this study was that increasing or decreasing the number of interface c DoFs in the line setup did not effect the accuracy of the driving-point

prediction, suggesting there is some flexibility in how line interfaces are described.

In the experimental study, the same spike in error attributed the inversion of a square $\mathbf{Y}_{ab}^{-1}$ term was also observed. However, as it was highlighted in the discussion section of that chapter, some limitations were observed with the example due to the sparse array of sensors on either side of the interface. In the FE model, 77 a and b DoFs were used either side of the interface c, while in the experiment there were only 8 a and 12 b DoFs. It was shown in the FE model that after a certain threshold in the amount of remote DoFs in one subset, there was a sudden drop in error. In this case FE model case, this appeared after 12 DoFs. Granted, having nearly the same amount as in the FE model is impractical in real-world applications. In a future study, the remote DoF subsets resolution should be increased to observe this theoretical drop seen in the numerical model. In the final part of this chapter, the reconstructed transfer mobility was also analysed for sensitivities. Four distinct pairs of a and b DoFs were chosen around each of the sub-structures, revealing at certain resonances/modes that an increase in amplitude at the a responses corresponded with an elevation in error. In order to understand which pairs of a responses and b excitations yielded the least error, a plot was constructed of a vs b with their error represented by a heat map. For the pairs that showed the smallest error, the reconstructed transfer mobility was compared against a direct measurement and indeed confirmed the difference at certain resonances was reduced. While the analysis conducted on this formulation of the RT identity was not the main focus, it has provided a foundation for a more rigorous sensitivity analysis in future work. A final point that should be for this chapter is that while the interface description in both FE and experimental models was incomplete, this study still revealed significant findings while only the dominant z-axis was used for c. Accounting for other translations and rotations is another areas for future work as it will improve the accuracy of the predictions. However, this is more straightforward through an FE model than an experimental model.

This thesis also investigated the invariance of both mobility-based and operational transmissibilities. In particular the latter is of significant relevance to the ORT method

presented in the chapter afterwards. As a whole a comprehensive understanding was provided for the characteristics of transmissibilities under certain measurement conditions. Three experimental coupled assembly were used to examine invariant transmissibilities: a single resilient-interface, three resilient-interfaces, and a single rigid connection. With each experiment, complexity increased with the goal of unveiling the tests of invariance that were applicable in a simple test rig could be applied to those more representative of industrial ones. These tests for invariance included: excitation positioning, the interchanging of an adjacent sub-structure, characterisation of interface DoFs (c), and the number of remote DoFs used in their calculation.

The first and simplest check for invariance that was tested in all three examples was to interchange A and observe whether the transmissibilities of B were the same. In the first two examples, it was demonstrated that the transmissibilities of B were invariant when only a single z-axis accelerometer beneath each isolator was used, suggesting this sufficed for a complete characterisation of the interface DoFs (c). Some excitations of a DoFs were applied near the edge, therefore inducing a moment force β. Despite the presence of this rotation, the z-axis dynamics dominated. This was alluded to in a paper co-authored by myself, and was confirmed by these examples. However, future studies could explore forces applied in other planes to further test this invariance on coupled assemblies with resilient connections. Additionally, when either mass or damping was altered by the interchanged A component, it was revealed that invariance was visible for the vast majority of the frequency range, except for very low frequencies. In the rigid connection example, excitations were applied in x, y, and z, which also induced moment forces α, β, γ. The transmission of translational and moment forces are much greater in this example, thus c was characterised by the finite-difference approximation method to account for all 6 DoFs. It was found in this study that the z force was still the largest contributor at the interface DoF, and that the transmissibilities of B were still accurate when only the z DoF was accounted for.

For testing invariance of transmissibilities of B for different force locations within A, two transmissibilities ($\mathbf{T}_{bc}^{r,c}$ and $\mathbf{T}_{bc}^{r,a}$) were analysed. Specifically, the excitation posi-

tioning was test at either the a DoFs or directly at the c interface DoFs. An important assumption when using incorporating the blocking constraint definitions from blocked force method, is the response field in the adjacent sub-structure to where the force is applied will yield an identical response field. All experimental examples showed that (within error) the two transmissibilities are very similar. Some error due to noise was present at higher frequencies for $\mathbf{T}_{bc}^{r,a}$ in the resilient experiment examples. This is due to the excitation at a traversing the isolators, which lead to higher attenuation in this frequency range, and thus reaching the noise floor. For $\mathbf{T}_{bc}^{r,c}$ the noise at higher frequencies was not observed, as the c DoF excitation was applied beneath the isolator and thus the transmission of the force input was not subject to attenuation-based error. This was later confirmed in the rigid connection example, where the two transmissibilities were almost identical and noise did not contaminate $\mathbf{T}_{bc}^{r,a}$ at high frequencies.

In the final test for invariance, the number of remote DoFs (a or b) and interface (c) DoFs were varied on the three resilient-interface. It was confirmed that the number of c DoFs must be equal to or greater than the number of remote DoFs to ensure invariance. Reducing the number of c DoFs resulted in transmissibilities (both mobility-based and operational) that were no longer invariant. This occurred because the blocking constraints were not fully applied to all connection points, and primarily affected low frequencies. Invariance did re-emerge at higher frequencies. Additionally, reducing the number of remote DoFs while maintaining sufficient c DoFs did not invariance. However, when the remote DoFs were reduced specifically in an inverted term, such as $\mathbf{Y}_{Cac}^{-1}$, invariance was lost. For the operational transmissibilities, equating the number of operational states to the c DoFs yielded an invariant transmissibility at the cost of noise at higher frequencies. Interestingly, when the operational state was reduced to 1 below the requirement, invariance emerged for the majority of the frequency range except at the low end. Furthermore, noise did not appear to contaminate higher frequencies due to the minimisation of error via the pseudo-inverse. As expected, over-determination improved transmissibility accuracy.

At the end of this chapter, the possibility of using the TICC for assessing the complete-

ness of interfaces was explored, in particular by an output-only method to serve as an alternative to the EMA strategy for the original ICC. The mass-spring model for which this idea was tested on revealed there was clear distinction in magnitudes between a transfer transmissibility $\mathbf{T}_{ba}^{f,a}$ across the coupled assembly and $\mathbf{T}_{da}^{f,a}$, which included the blocking interface DoFs in its calculation. The inclusion of interface DoFs that had a complete description showed a transmissibility with a magnitude close to zero. However, if the interface was not complete there was a significant rise in magnitude. This was the case for both mobility-based and operational transmissibilities. However, issues were apparent in the metric proposed for the output-only case. While the possibility of an output-only approach is promising, future work needs to address its use on an experimental assembly while also testing different metrics such as a correlation or coherence based approach.

These foundational insights into invariant transmissibilities had informed their use in the next chapter, the ORT method. In this study it was validated that the ORT has the potential to serve as a practical alternative in predicting interface point mobilities. It was revealed across all experimental examples, that the ORT method achieved accurate predictions that are comparable to the original RT method while also requiring fewer FRF measurements, a significant advantage for industrial applications. Particularly in the single resilient-interface, it was confirmed that over-determination by increasing the operational states over the number of c DoFs, made the prediction more accurate when compared to the RT method. While the ORT point reconstruction was accurate across the majority of the frequency range, a common theme throughout out was a reduction in accuracy at high frequencies. In the three resilient-interface example noise was present in this part of the range, which is attributed to the fact the transmissibilities used had operational states applied above the isolator (a). In the rigid connection example, noise was present in the higher frequencies but was certainly reduced, confirming attenuation based error did not effect the prediction. However, high frequency artefacts were present. While the RT method across the resilient interface models was very similar in performance to the ORT, it displayed a highly accurate prediction with

little error in the rigid connection case. Overall, the ORT method displayed a robust prediction of the interface point mobility and suggests the possibility of being a useful tool within in industry. Its identity shows promise for real-time monitoring, where the operational transmissibilities can be constantly measured in conjunction with a pre-measured mobility. This application however warrants a future study on an industrial size test rig to realise its potential for industry.

For the final objective of this thesis, it was investigated whether the relationship the SVs of transmissibilities would introduce a novel way of detecting transmission paths and unknown bridges. By constraining the interface DoFs to a reduced amount of DoFs, the many excitations within the source component A would be bottlenecked by c. In the mass-spring model examples, it was firstly indicated this was possible by observing the dominant SVs of mobilities, and later for mobility-based and operational transmissibilities. In particular, the most reliable quantity was $\mathbf{T}_{da}^{r,a}$, as it correlated the number of transmission paths from the interface as well as bridges circumventing the c. This part of the study revealed there is potential in an SVD-based method of transmission path detection. However in the experimental example, some divergences from the idealised model appeared. For continuous systems, theoretically there are an infinite number of modes and they exhibit exhibit more complex dynamic behaviour such as damping and modal coupling. This is is why there was not a clear distinction between dominant SVs and the smallest SVs. This made quantifying the number of transmission paths challenging. However it was possible to detect a bridge. By taking a threshold, say 1% of the total magnitude, the number of SVs above it were counted and revealed there was an increase in SVs counted when a bridge was formed. These findings emphasise the complexities of real-world systems, and forms the foundation for future work. In particular, it is proposed that an 'in-between' model, such as a numerical one which has more modes than the mass-spring model but less than the experimental example, would bridge the understanding.

For the final remarks, this research has demonstrated the diverse possibilities for operational methods in coupled systems by the use of the transmissibility concept. In

particular, the challenges of point mobility prediction and the analysis of transmission paths and bridges were addressed thoroughly. The insights gained have enhanced the understanding of transmissibilities on coupled assemblies, especially via output-only methods, while also potentially paving the way for real-time monitoring, diagnostics, and design optimisation for real-world engineering applications.

Bibliography

R.J. Allemang, R.S. Patwardhan, M.M. Kolluri, and A.W. Phillips. Frequency response function estimation techniques and the corresponding coherence functions: A review and update. *Mechanical Systems and Signal Processing*, 162:108100, 2022.

R.A.B. Almeida, A.P.V. Urgueira, and N.M.M. Maia. The use of transmissibility properties to estimate frfs on modified structures. *Shock and Vibration*, 17(4-5):749679, 2010.

I.G. Araújo and J.E. Laier. Operational modal analysis using svd of power spectral density transmissibility matrices. *Mechanical Systems and Signal Processing*, 46 (1):129–145, 2014.

M.R. Ashory. Correction of Mass-loading Effects of Transducers and Suspension Effects in Modal Testing. In *Proceedings of the 16th International Modal Analysis Conference*, volume 3243 of *Society of Photo-Optical Instrumentation Engineers (SPIE) Conference Series*, page 815, 1998.

M.R. Ashory. *High quality modal testing methods*. PhD thesis, Imperial College London, 1999.

M. Aykan and M. Çelik. Vibration fatigue analysis and multi-axial effect in testing of aerospace structures. *Mechanical Systems and Signal Processing*, 23(3):897–907, 2009.

L. Barton. *Decomposed vibro-acoustic frequency response functions for the prediction*

of radiated sound. PhD thesis, School of Science, Engineering & Environment - University of Salford, 2023.

L. Barton, A.S. Elliott, and J. Smith. Prediction of radiated structural noise using decomposed vibro-acoustic frequency response functions. *Forum Acusticum*, 2023. doi: 10.61782/fa.2023.1125.

Y. Bobrovnitskii. A theorem on the representation of the field of forced vibrations of a composite elastic system. *Acoustical Physics*, page 507–510, Sep 2001.

A. Brandt. *Noise and vibration analysis: Signal analysis and experimental procedures*. Wiley, 2011. ISBN 978-1-118-96218-3.

R. Brincker, L. Zhang, and P. Andersen. Modal identification of output-only systems using frequency domain decomposition. *Smart Materials and Structures*, 10(3):441, 2001.

S. Chesné and A. Deraemaeker. Damage localization using transmissibility functions: A critical review. *Mechanical Systems and Signal Processing*, 38(2):569–584, 2013.

A. Cunha and E. Caetano. Experimental modal analysis of civil engineering structures. *Sound and Vibration*, 40, 06 2006.

M. Van der Seijs, D. Van den Bosch, D. Rixen, and D. de Klerk. An improved methodology for the virtual point transformation of measured frequency response functions in dynamic substructuring. *Proceedings of the 4th International Conference on Computational Methods in Structural Dynamics and Earthquake Engineering (COMPDYN 2013)*, 2014.

C. Devriendt, F. Magalhães, W. Weijtjens, G. De Sitter, A. Cunha, and P. Guillaume. Structural health monitoring of offshore wind turbines using automated operational modal analysis. *Structural Health Monitoring*, 13:644–659, 11 2014.

M.F. Dimentberg, K.V. Frolov, and A.I. Menyailov. *Vibroacoustical Diagnostics for Machines and Structures*. Wiley. ISBN 9780863801167.

C. Draeger and M. Fink. One-channel time-reversal in chaotic cavities: Theoretical limits. *The Journal of the Acoustical Society of America*, 105(2):611–617, 1999.

A.S. Elliott and A.T. Moorhouse. Characterisation of structure borne sound sources from measurement in-situ. *Euronoise*, page 1477–1482, 2008.

A.S. Elliott, G. Pavić, and A.T. Moorhouse. Measurement of force and moment mobilities using a finite difference technique. *The Journal of the Acoustical Society of America*, 123(5):3312–3312, 2008. doi: 10.1121/1.2933757.

A.S. Elliott, A.T. Moorhouse, and G. Pavić. Moment excitation and the measurement of moment mobilities. *Journal of Sound and Vibration*, 331(11):2499–2519, 2012.

A.S. Elliott, A.T. Moorhouse, T. Huntley, and S. Tate. In-situ source path contribution analysis of structure borne road noise. *Journal of Sound and Vibration*, 332(24): 6276–6295, 2013.

A.S. Elliott, N. Sanei, and M. Glesser. Combining structural modification with in-situ transfer path analysis to solve noise and vibration problems. page 427 – 434, 2019.

D.J. Ewins. On predicting point mobility plots from measurements of other mobility parameters. *Journal of Sound and Vibration*, 70(1):69–75, 1980.

D.J. Ewins. *Modal Testing: Theory, Practice, and Application*. Mechanical engineering research studies. Research Studies Press, 2000. ISBN 9780471975182.

F. Fahy and P. Gardonio. *Sound and structural vibration (2nd Edition)*. Academic Press, 2007. ISBN 978-0-12-373633-8.

C.R. Farrar and G.H. James III. System identification from ambient vibration measurements on a bridge. *Journal of Sound and Vibration*, 205(1):1–18, 1997.

O. Guasch, C. García, J. Jové, and P. Artís. Experimental validation of the direct transmissibility approach to classical transfer path analysis on a mechanical setup. *Mechanical Systems and Signal Processing*, 37(1):353–369, 2013.

M. Haeussler, T. Mueller, and E. Pasma. Component tpa: benefit of including rotational

degrees of freedom and over-determination. Technical report, VIBES.technology, 2020.

P.C. Hansen. *Rank-Deficient and Discrete Ill-Posed Problems: Numerical Aspects of Linear Inversion*. Society for Industrial and Applied Mathematics", 1998.

H. Helmholtz. *Handbuch der physiologischen Optik*. Andesite Press, 1867. ISBN 9781296569389.

ISO 20270:2019. Acoustics — characterization of sources of structure-borne sound and vibration — indirect measurement of blocked forces. Standard, International Organization for Standardization, 2019.

ISO 7626-1:2011. Mechanical vibration and shock — experimental determination of mechanical mobility. Standard, International Organization for Standardization, 2011.

M.H.A. Janssens, J.W. Verheij, and D.J. Thompson. The use of an equivalent forces method for the experimental quantification of structural sound transmission in ships. *Journal of Sound and Vibration*, 226(2):305–328, 1999.

J. Jové and O. Guasch. Direct response and force transmissibilities in the characterization of coupled structures. *Journal of Sound and Vibration*, 407:1–15, 2017.

W.L. Hallauer Jr. *Introduction to linear time-invariant dynamic systems for students of engineering*. A.T. Still University, 2016.

G. Kerschen, M. Peeters, J. C. Golinval, and C. Stéphan. Nonlinear modal analysis of a full-scale aircraft. *Journal of Aircraft*, 50(5):1409–1419, 2013.

S. Klaassen and M. Van der Seijs. Introducing semm: A novel method for hybrid modelling. In *Dynamics of Coupled Structures, Volume 4*, pages 117–125, 2018. ISBN 978-3-319-74654-8.

S.W.B. Klaassen, M.V. van der Seijs, and D. de Klerk. System equivalent model mixing. *Mechanical Systems and Signal Processing*, 105:90–112, 2018.

Y.E. Lage, M.M. Neves, N.M.M. Maia, and D. Tcherniak. Force transmissibility versus

displacement transmissibility. *Journal of Sound and Vibration*, 333(22):5708–5722, 2014.

S.S. Law, J. Li, and Y. Ding. Structural response reconstruction with transmissibility concept in frequency domain. *Mechanical Systems and Signal Processing*, 25(3): 952–968, 2011.

J. Li, T. Bao, and C.E. Ventura. An automated operational modal analysis algorithm and its application to concrete dams. *Mechanical Systems and Signal Processing*, 168, 2022.

W. Liu and D.J. Ewins. Transmissibility properties of mdof systems. *Proceedings of the 16th International Modal Analysis Conference (IMAC XVI)*, pages 847–854, 1998.

J.N. Macduff and J.R. Curreri. *Vibration Control*. McGraw-Hill, 1958.

F. Magalhães, Á. Cunha, E. Caetano, and R. Brincker. Damping estimation using free decays and ambient vibration tests. *Mechanical Systems and Signal Processing*, 24 (5):1274–1290, 2010.

F.X. Magrans. Method of measuring transmission paths. *Journal of Sound and Vibration*, 74(3):321–330, 1981.

N.M.M. Maia and J.M.M. Silva. *Theoretical and experimental modal analysis*. Research Studies Press Ltd., 2003.

N.M.M. Maia, J.M.N. Silva, and A. Ribeiro. Some applications of coupling/uncoupling techniques in structural dynamics part 2: Generation of the whole frf matrix from measurements on a single column-the mass uncoupling method (mum). *Proceedings of the 15th International Modal Analysis Conference*, 2, 1997.

N.M.M. Maia, J.M.M. Silva, and A.M.R. Ribeiro. The transmissibility concept in multi-degree-of-freedom systems. *Mechanical Systems and Signal Processing*, 15(1): 129–137, 2001.

N.M.M. Maia, M. Fontul, and A.M.R. Ribeiro. Transmissibility of forces in multiple-

degree-of-freedom systems. *Proceedings of International Conference on Noise and Vibration Engineering (ISMA 2006)*, 09 2006.

N.M.M. Maia, R.A.B. Almeida, A.P.V. Urgueira, and R.P.C. Sampaio. Damage detection and quantification using transmissibility. *Mechanical Systems and Signal Processing*, May 2011a.

N.M.M. Maia, A.P.V. Urgueira, and R.A.B. Almeida. *Whys and Wherefores of Transmissibility*. 09 2011b.

J.C. Maxwell. On the calculation of the equilibrium and stiffness of frames. *The London, Edinburgh, and Dublin Philosophical Magazine and Journal of Science*, 27 (182):294–299, 1864.

J.W.R. Meggitt. *On in-situ methodologies for the characterisation and simulation of vibro-acoustic assemblies*. PhD thesis, Acoustics Research Centre, University of Salford, 2017.

J.W.R. Meggitt and R.C. McGee. On the limitations of transmissibility functions for damage localisation: the influence of completeness. *Structural Health Monitoring*, 2024.

J.W.R. Meggitt and A.T. Moorhouse. In-situ sub-structure decoupling of resiliently coupled assemblies. *Mechanical Systems and Signal Processing*, 117:723–737, 2018.

J.W.R. Meggitt and A.T. Moorhouse. On the completeness of interface descriptions and the consistency of blocked forces obtained in situ. *Mechanical Systems and Signal Processing*, 145, 2020a.

J.W.R. Meggitt and A.T. Moorhouse. Finite element model updating using in-situ experimental data. *Journal of Sound and Vibration*, 489:115675, 2020b.

J.W.R. Meggitt, A.S. Elliott, A.T. Moorhouse, and L. Heng-Yi. In situ determination of dynamic stiffness for resilient elements. *Proceedings of the Institution of Mechanical Engineers, Part C: Journal of Mechanical Engineering Science*, 12 2015.

J.W.R. Meggitt, A.S. Elliott, A.T. Moorhouse, A. Jalibert, and G. Franks. Component replacement transfer path analysis. 09 2020.

J.W.R. Meggitt, A.S. Elliott, A.T. Moorhouse, A. Jalibert, and G. Franks. Component replacement tpa: A transmissibility-based structural modification method for in-situ transfer path analysis. *Journal of Sound and Vibration*, 499:115991, 2021.

A.T. Moorhouse. Vibro-acoustic measurement methods in condition monitoring. volume 1, page 74 – 84, 2012.

A.T. Moorhouse and A.S. Elliott. The “round trip” theory for reconstruction of green’s functions at passive locations. *The Journal of the Acoustical Society of America*, 134(5):3605–3612, 2013.

A.T. Moorhouse and G. Seiffert. Characterisation of an airborne sound source for use in a virtual acoustic prototype. *Journal of Sound and Vibration*, 296(1):334–352, 2006.

A.T. Moorhouse, A.S. Elliott, and T.A. Evans. In situ measurement of the blocked force of structure-borne sound sources. *Journal of Sound and Vibration, 325 (4-5)*, page 679–685, 2009.

A.T. Moorhouse, T.A. Evans, and A.S. Elliott. Some relationships for coupled structures and their application to measurement of structural dynamic properties in-situ. *Mechanical Systems and Signal Processing*, pages 1574–1584, 2011.

A.T. Moorhouse, A.S. Elliott, and J.W.R. Meggitt. Virtual acoustic prototyping - a story of four decades. 08 2022.

Domen Ocepek, Miha Kodrič, Gregor Čepon, and Miha Boltežar. On the estimation of structural admittances from acoustic measurement using a dynamic substructuring approach. *Applied Acoustics*, 180:108115, 2021.

G.J. O’Hara. Mechanical Impedance and Mobility Concepts. *The Journal of the Acoustical Society of America*, 41(5):1180–1184, 1967.

E. Orlowitz and A. Brandt. Comparison of experimental and operational modal analysis on a laboratory test plate. *Measurement*, 102:121–130, 2017.

R. Oshana. 3 - overview of embedded systems development life cycle using dsp. In *DSP Software Development Techniques for Embedded and Real-Time Systems*, pages 35–58. Newnes, 2006.

M.A. Panza. A review of experimental techniques for nvh analysis on a commercial vehicle. *Energy Procedia*, 82:1017–1023, 2015.

E. Pasma, S.W.B. Klaassen, L. Nieuwenhuijse, M.V. Van der Seijs, and D. Lennström. Application of system equivalent model mixing (semm) to model the structural dynamic properties of a complex vehicle component using numerical and experimental data. 09 2018.

B. Peeters and G. De Roeck. Reference-based stochastic subspace identification for output-only modal analysis. *Mechanical Systems and Signal Processing*, 13(6): 855–878, 1999.

R. Penrose. A generalized inverse for matrices. *Mathematical Proceedings of the Cambridge Philosophical Society*, 51(3):406–413, 1955.

A. Preumont. *Vibration Control of Active Structures: An Introduction*, volume 246. 02 2018.

C. Rainieri and G. Fabbrocino. *Operational Modal Analysis of Civil Engineering Structures: An Introduction and Guide for Applications*. Springer, 06 2014. ISBN 978-1-4939-0767-0.

L. Ramos, L. Marques, P. Lourenco, G. De Roeck, A. Costa, and J. Roque. Monitoring historical masonry structures with operational modal analysis: Two case studies. *Mechanical Systems and Signal Processing*, 24:1291–1305, 07 2010.

S.S. Rao. *Mechanical Vibrations*. Pearson Prentice Hall, 2004. ISBN 9780131207684.

J. Rayleigh. *The Theory of Sound*, volume 2. Cambridge MA: Macmillan, 1878. ISBN 9781139058087.

A.M.R. Ribeiro, J.M.M. Silva, and N.M.M. Maia. On the generalisation of the transmissibility concept. *Mechanical Systems and Signal Processing*, 14(1):29–35, 2000. ISSN 0888-3270.

A.M.R. Ribeiro, M. Fontul, J.M.M. Silva, and N.M.M. Maia. Transmissibility matrix in harmonic and random processes. 06 2002.

A.M.R. Ribeiro, M. Fontul, N.M.M. Maia, and J.M.M. Silva. Further developments on the transmissibility concept for multiple degree of freedom systems. 09 2005.

D.J. Rixen. How measurement inaccuracies induce spurious peaks in frequency based substructuring. In *International modal analysis conference IMAC-XXVI*, 01 2008.

J.M. Roesset, R.V. Whitman, and R. Dobry. Modal analysis for structures with foundation interaction. *Journal of the Structural Division*, 99:399–416, 1973.

Z. Saeed, S.W.B. Klaassen, C.M. Firrone, T.M. Berruti, and D.J. Rixen. Experimental joint identification using system equivalent model mixing in a bladed disk. *Journal of Vibration and Acoustics*, 142(5):051001, 2020.

R.P.C. Sampaio, N.M.M. Maia, A.M.R. Ribeiro, and J.M.M. Silva. Damage detection using the transmissibility concept. *Proceedings of the 6th International, Congress on Sound and Vibration (ICSV6)*, pages 2559–2568, 1999.

R.P.C. Sampaio, N.M.M. Maia, R.A.B. Almeida, and A.P.V. Urgueira. A simple damage detection indicator using operational deflection shapes. *Mechanical Systems and Signal Processing*, 72-73:629–641, 2016.

S. Sattinger. A method for experimentally determining rotational mobilities of structures. *Shock and Vibration Bulletin*, pages (50) 17–27, 1980.

M.J. Schulz, A.S. Abdelnaser, P.F. Pai, M.S. Linville, and J. Chung. Detecting structural

damage using transmittance function. *International Modal Analysis Conference, Orlando, Florida*, pages 638–644, 1997.

J.M.M. Silva, N.M.M. Maia, and A.M.R. Ribeiro. Cancellation of mass-loading effects of transducers and evaluation of unmeasured frequency response functions. *Journal of Sound and Vibration*, 236(5):761–779, 2000.

R. Snoeys, P. Sas, W. Heylen, and H. Van der Auweraer. Trends in experimental modal analysis. *Mechanical Systems and Signal Processing*, 1(1):5–27, 1987.

G. Steenackers, C. Devriendt, and P. Guillaume. On the use of transmissibility measurements for finite element model updating. *Journal of Sound and Vibration*, 303 (3):707–722, 2007.

A.N. Thite and D.J. Thompson. The quantification of structure-borne transmission paths by inverse methods. part 1: Improved singular value rejection methods. *Journal of Sound and Vibration*, 264(2):411–431, 2003a.

A.N. Thite and D.J. Thompson. The quantification of structure-borne transmission paths by inverse methods. part 2: Use of regularization techniques. *Journal of Sound and Vibration*, 264(2):433–451, 2003b.

F.S. Tse, I.E. Morse, and R.T. Hinkle. *Mechanical vibrations: theory and applications (2nd Edition)*. Allyn and Bacon, 1978. ISBN 0-205-05940-6.

A.P.V. Urgueira, R.A.B. Almeida, and N.M.M. Maia. Experimental estimation of frfs using the transmissibility concept. *23rd International Conference on Noise and Vibration Engineering 2008, ISMA 2008*, 3:1807–1814, 2008.

A.P.V. Urgueira, R.A.B. Almeida, and N.M.M. Maia. On the use of the transmissibility concept for the evaluation of frequency response functions. *Mechanical Systems and Signal Processing*, 25(3):940–951, 2011.

M.V. van der Seijs, D. de Klerk, and D.J. Rixen. General framework for transfer path

analysis: History, theory and classification of techniques. *Mechanical Systems and Signal Processing*, 68-69:217–244, 2016.

A.S. Veletsos and C.E. Ventura. Modal analysis of non-classically damped linear systems. *Earthquake Engineering & Structural Dynamics*, 14(2):217–243, 1986.

J.W. Verheij. *Multi-path sound transfer from resiliently mounted shipboard machinery - Experimental methods for analyzing and improving noise control*. PhD thesis, 05 1982.

T.E. Vigran. *Building Acoustics*. Taylor & Francis, 2008. ISBN 9780203931318.

K. Wienen, M. Sturm, A.T. Moorhouse, and J.W.R. Meggitt. Generalised round-trip identity - for the determination of structural dynamic properties at locations inaccessible or too distant for direct measurement. *Journal of Sound and Vibration*, 511: 116325, 2021.